UNIVERSITY OF SOUTHAMPTON

FACULTY OF NATURAL AND ENVIRONMENTAL SCIENCES

School of Chemistry

Electrochemical Surface Enhanced Raman Spectroscopy of a Beacon Probe Immobilized on Au Electrodes

by

Yung-Chun Lin

Thesis for the degree of Doctor of Philosophy

Apr 2018

DECLARATION OF AUTHORSHIP

I, YUNG-CHUN LIN

declare that the thesis entitled

ELECTROCHEMICAL SURFACE ENHANCED RAMAN SPECTROSCOPY OF A BEACON PROBE IMMOBILIZED ON AU ELECTRODES

and the work presented in the thesis are both my own, and have been generated by me as the result of my own original research. I confirm that:

- this work was done wholly or mainly while in candidature for a research degree at this University;
- where any part of this thesis has previously been submitted for a degree or any other qualification at this University or any other institution, this has been clearly stated;
- where I have consulted the published work of others, this is always clearly attributed;
- where I have quoted from the work of others, the source is always given.

  With the exception of such quotations, this thesis is entirely my own work;
- I have acknowledged all main sources of help;
- where the thesis is based on work done by myself jointly with others, I have made clear exactly what was done by others and what I have contributed myself;

Signed:

Date: 4th Apr 2018

Acknowledgements

I am grateful to my supervisor Phil Bartlett and my advisor Andrea Russell for all of their advice. It is impossible for me to finish this thesis without the endless patience and support from Professor Bartlett on my road to pursue the PhD degree.

It is my pleasure to work with researchers from Chemistry, Optoelectronics Research Centre and the visiting scientists. I owe a debt of gratitude to the help and expertise provided by Tom Brown and his research group; James Richardson and Nittaya Gale for the synthesis of the oligonucleotides; Zilong Wang, Kevin Huang and Jun-Yu Ou for the valuable opinions of the nanophotonics; Jiawen Hu, Xiaodong Lin and Victor Costa Bassetto for the insightful discussions of SERS; Lorriane Praut and Penny Spake in the faculty office for their considerate advice on my visa issue and miscellaneous administrative works.

I acknowledge those people in the SERS group and the electrochemistry group including for their encouragement and the help—Rachel Gao, Rob Johnson, Evanthia Papadopoulou, Marta Meneghello, Danai Panagoulia, Alex Keeler, David Cook, Jack Branch, Gabriela Kissling, Charlie Cummings, Firas Al-Lolage, Peter Richardson, Mara Serrapede, Maciek Sosna, Thomas Foley, Saiful 'Arifin Shafiee, Hairul Hisham Hamzah, Andy Naylor and Mike Huang

I appreciate Patrick Hendra, for his pioneering research of SERS and the engineering of the spectroelectrochemical cells; Alistair Clarke for the gold film deposition and the instruction of the SEM operation; Sumeet Mahajan and Steven Bell for the valuable discussion and the guidance of the thesis correction. Gratitude goes to the Ministry of Education in Taiwan for helping and providing the funding for the work. Also thanks to my colleagues in the Forensic Science Centre of Kaohsiung City Government Police Department for their covering during my study to UK.

Finally, I would like to thank my family for their sacrifice and support, especially to my wife Yu-Ching, who spent her precious time to accompany me these years.

UNIVERSITY OF SOUTHAMPTON

ABSTRACT

FACULTY OF NATURAL AND ENVIRONMENTAL SCIENCES

Chemistry

Doctor of Philosophy

ELECTROCHEMICAL SURFACE ENHANCED RAMAN SPECTROSCOPY OF A BEACON PROBE IMMOBILIZED ON AU ELECTRODES

By Yung-Chun Lin

The aim of this thesis is to investigate the factors, and possible mechanisms, involved in the electrochemical SER response of a reporter dye attached to an immobilized oligonucleotide on the negatively charged Au surface. This work used a 5'-thiol anchored beacon and a partial self-pairing oligonucleotide, instead of a linear strand probe, to study the sensing process. The observation of the SERS intensity of the 3'-labelled dye at the negatively charged Au surface is similar to that of the hybridized duplex of the linear probe at low surface coverage.

By competitive adsorption of mercaptohexanol together with the beacon probe in the immobilization solution, 3 times lower coverage than reported previously was achieved to ensure low intramolecular interactions between the beacon probe. A number of electrochemical methods were also utilized to observe the Raman intensity of the Texas Red-labelled beacon probe and the results interpreted in terms of the configuration changes of the beacon probe.

The potential dependent Raman enhancement of the reporter itself, Texas Red, was later found to have a similar response to the labelled beacon probe. A detailed discussion with respect to absorption of the Texas Red, orientation, potential tuning of the LSPR, the interference from hydrogen evolution, the electronic Stark effect and the charge-transfer enhancement is presented, to understand the possible contributions to the potential dependence Raman enhancement. As a result, a molecule-to-metal charge-transfer mechanism was found to explain the most relevant dependence of the enhancement on electrode potential.

The potential dependent Raman response of the corresponding beacon probe was compared as a function of the time scale of the modification, the alkyl chain length of mercaptoalkanol from C2, C4, C6 and C9 and the preparation method used (backfilling or co-adsorption). The possible surface states are proposed to explain the electrochemical SERS response of the system.

Contents

Chapter 1 Introduction

1.1 DNA Analysis

Deoxyribonucleic acid (DNA) is the molecule that contains most of the genetic information of all known organisms and many viruses. Since DNA holds the blueprint to construct the RNA and proteins for expressing the organism's reproduction, growth and development and response to stimuli, the pathogen like Hepatitis virus B has to infect the host hepatocytes in its lysogenic lifecycle by inserting their DNA into the host DNA for the stable virus propagation[1,2]. In contrast, genetic diseases are caused by a disorder in DNA sequences like substitution, deletion or addition which cause the subsequent protein modification or dysfunction in protein assembly. The essential role of DNA in both pathogen-caused diseases and genetic disorders makes DNA analysis one of the popular topics in the research disciplines. New analytical techniques for DNA have led to new understanding of the interactions of DNA with other molecules and have also inspired the new development of clinical diagnostics. Other demands from forensic sciences and environmental monitoring also drive the development of DNA analysis. The main features required for next generation DNA analysis commonly include rapidity in data acquisition and precise interpretation, on-site analysis, low cost and high sensitivity.

In the case of the biological samples found at a crime scene, the DNA extracted from these samples are usually trace, degraded and mixed with other contaminants. Forensic scientists have to isolate the nucleic acid from its matrices such as soil or fabrics. The issue of trace nucleic acids was overcome with the aid of the polymerase chain reaction (PCR) in the mid-1990s[3–5], about a decade after the PCR discovery[6]. PCR uses cyclic amplification reactions of the target fragment of nucleic acid[7]. The resultant amplified product can reach ca. 10^6 yield in 30 cycles which solves the trace issue of forensic DNA samples. A PCR cycle contains three stages as shown in Figure 1.1. The first stage is the denaturation of the double-stranded DNA (dsDNA) at 95 ℃. The second stage is annealing two short oligonucleotides (often referred to as primers) to the target region among the denatured long DNA fragments (often referred to as the template) at around 56 ℃. The third stage is an elongation of the target region using the *Taq* DNA polymerase at 72 ℃. The polymerase starts the replication at the end of the primer in the 5' to 3'

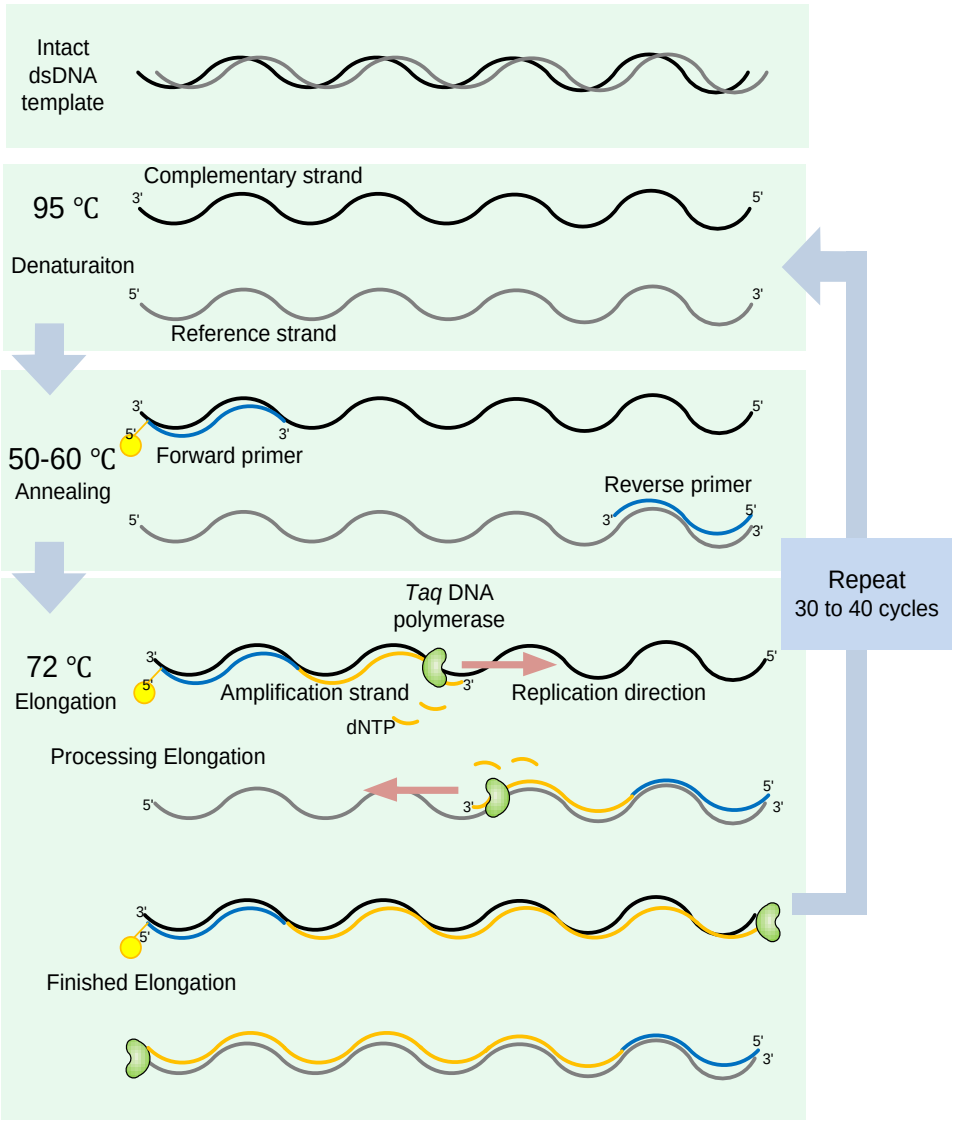

Figure 1.1 Schematic of polymerase chain reaction (PCR) in the conventional forensic STR typing. One PCR cycle contains three thermal steps in the order denaturation at 95℃, annealing at 50 to 60℃ and elongation at 72℃. The sequence of the forward primer is identical to the reference strand from 5' to 3 at the correspondent position and hence binds to the complementary strand. The tag on the 5'end of forward primer is a fluorescent molecule used as the reporter. This reporter can emit fluorescence stimulated by the laser beam at the characteristic wavelength. The PCR reactants include template DNA, primers, *Taq* DNA polymerase, deoxynucleotide triphosphate (dNTP), magnesium chloride and monovalent ion like potassium. Magnesium ions act as the co-factor of the polymerase during the elongation step[7]. Monovalent ions shield the negatively charged phosphate backbone of DNA and weaken the electro-repulsion force between the primers and the template.

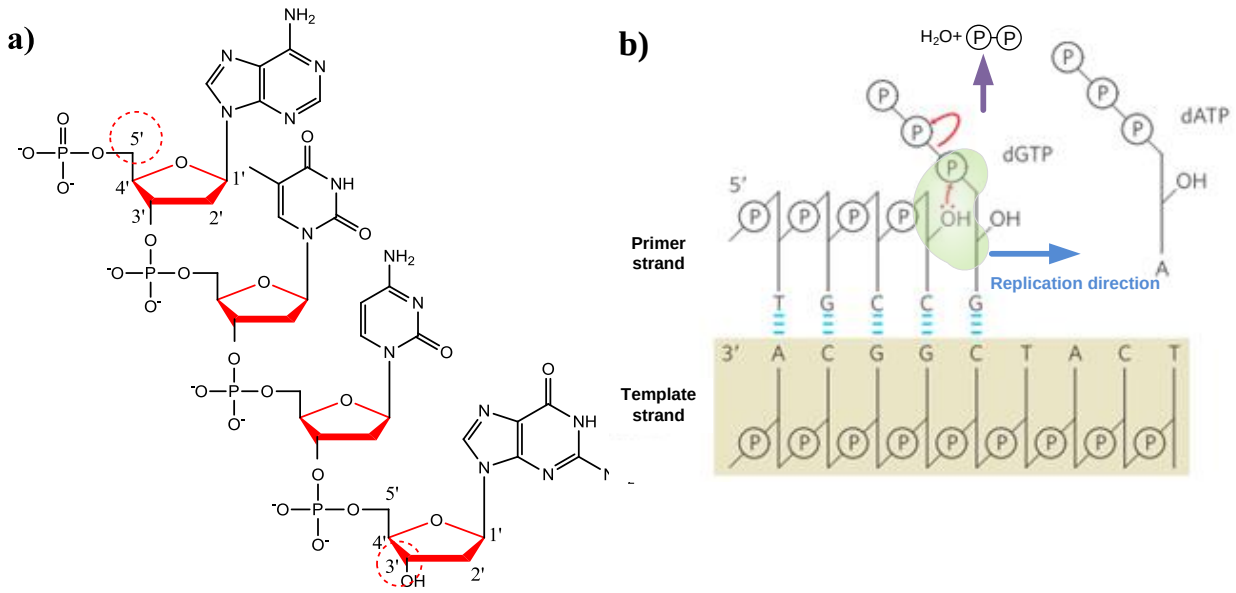

Figure 1.2 Molecular structure of a tetranucleotide has 4 nucleotides linked by 3 phosphate diester bonds at the 3' and 5' carbon of each pentose (red backbone in the Figure) except the termini. a) The 5' to 3' was denoted as the direction of synthetic reaction catalysed by the DNA polymerase from the residual group of phosphate at 5' end toward the hydroxyl group at 3' end. b) *Taq* DNA polymerase acts on the 3'-OH group to join the phosphate group on the paring nucleotide of the synthetic DNA strand. This joining reaction removes one oxygen on the dNTP which has three phosphates on its 5' position and produces H_2O and diphosphates as the by-products. (Adapted from LEHNINGER PRINCIPLES OF BIOCHEMISTRY 6E by David L. Nelson and Michael M. Cox, Copyright ©2013 by WH Freeman and Company. Used with permission by the publisher.)

direction. The numbered annotation 5' to 3' represents the carbon of pentose which is attached to the triphosphate group or hydroxyl group respectively as shown in Figure 1.2. The replication incorporates the deoxynucleotide triphosphates (dNTP) which are complementary, binding to the template with the Watson-Crick pairing. The length of the product strand elongates during the amplification and stops when the temperature increases to 95 ℃ at the denaturation stage of the next cycle. *Taq* DNA polymerase is chosen due to its thermal stability at 95 ℃ and was isolated first from the thermophilic bacteria named *Thermus aquaticus*[8]. Before the *Taq* polymerase was introduced for *in vitro* amplification, it was necessary to add polymerase after every melting step because the DNA polymerases extracted from most organisms are inactivated at 60 to 80 ℃. This was time-consuming and inconvenient.

Taq DNA polymerase is the essential catalyst in the one-pot PCR reaction and maintains its reactivity in the replication step even after heating at 95 ℃ to keep the 'reaction chain' working

during repeated thermal cycles. The PCR reaction yields two-fold amplification of the product (often referred to as the amplicon) every cycle on average, and the final PCR achieves 10^6 amplification of the target after 30 cycles. Capillary electrophoresis can then be used to separate the amplicon based on the length of each selected genetic marker.

Forensic scientists select the genetic markers (also referred to as loci) which are highly variable among individuals and usually less than 300 bp in length in *Homo sapiens*. This is because genomic DNA is degraded into 300 to 500 bp fragments[9] on average and to 200 bp fragments in extremely degraded samples. The second reason is that the enzyme works better to amplify shorter fragments, loci lengths longer than 300 bp would have lower amplification efficiency compared to other shorter loci in multiplex PCR, which amplifies several loci simultaneously. This phenomenon, called 'preferential amplification', becomes more apparent in degraded samples and hence results in the generation of lower amounts of longer loci. These two reasons mean that the length of genetic markers less than 300 bp has better amplification yields for degraded DNA in multiplex PCR. Among the genes in the human genome, the short tandem repeat (STR) is one of the most widespread markers and its allele length meets the forensic requirement of less than 300 bp in average. STR (also referred to as microsatellite) has a repeat motif composed of 2, 3, 4 or 5 nucleotides. The number of repeats of the motif determines the alleles length and normally ranges from 5 to 20 as shown in Figure 1.3. STR alleles among 16 loci in the human genome can be amplified in the multiplex PCR to achieve the individualization

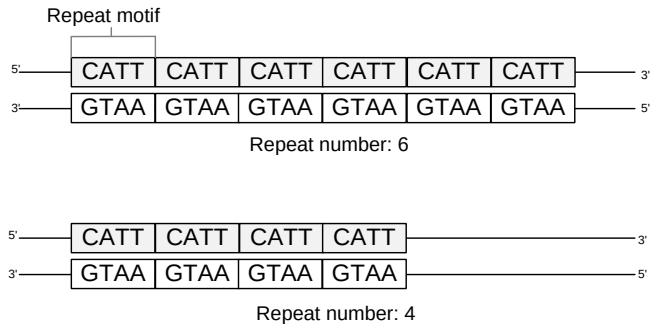

Figure 1.3 A schematic of a genotype of the short tandem repeat (STR) locus. This instance of STR is composed of the tetranucleotide "CATT" as the repeat motif. The allele of the STR is determined by the repeat number. In the heterozygote case, as shown in the figure above, the allele is 6 and 4 respectively and was noted as (6,4) (which is equivalent to (4,6)). Since the paired chromosomes of the gamete are obtained from its parents during the meiosis, if each allele of the gamete differs from each other, this genotype is called heterozygous genotype. When the locus possesses two identical alleles like (6, 6) or (4, 4), the genotype is described as homozygous genotype.

probability to 10^{-18} in the global population. This statistic assessment means the specific allele's combination would only occur in one individual among 10^{18} people[5].

The conventional method of STR analysis uses multiplex PCR to amplify the target sequences and then to discriminate the amplicon by the fragment length using capillary electrophoresis[10]. Since the polymerase synthesises the copy strand from the 3' end of the primers, the fluorescent dyes (6-FAM, VIC, NED and PET) are attached to the 5' end of the forward primer. The corresponding copy strand is amplified via the *Taq* polymerase in the elongation stage. Since the mobility of the labelled PCR product in capillary electrophoresis is proportional to its length, the length of the PCR product at each locus can be designed to separate them in the elution time scale by adjusting the length of the flanking region of the locus. Those loci's amplicon designed with shorter flanking region results in shorter product and hence is faster to elute than the longer ones. A typical electropherogram of 9947A DNA[11], a known standard control, is shown in Figure 1.4. The charge coupled diode (CCD) used as the detector collects the fluorescent signal of the amplicon from the window of the capillary. Since the mobility of the amplicon differs from each allele of the correspondent locus, the resultant electropherogram contains 16 loci distributed in 4 dye channels[10].

In contrast to STR, single nucleotide polymorphism (SNP) is another option as a genetic marker for forensic scientists. A single nucleotide polymorphism has single nucleotide variation on each locus. For example, two SNP sequences of DNA fragments obtained from distinct individuals are AA**C**CGA and AA**T**CGA which contains single sequence differences in the third nucleotide from the left. In this case, there are two alleles (C and T) on this locus. On average SNP occurs at one in every 1330 bases in the human genome[12]. In the case of a SNP locus amplified by the PCR technique, the length of the specific primer to hybridise the SNP locus could normally be confined to a 20 to 30 mer and hence the size of the amplification product is normally less than 60 bp. The short length of the probes or primers for SNP detection mainly reduces the problem of sample degradation. As a result, SNP has a higher tolerance than the STR to the degradation caused by the environment. The differences between SNP and STR are summarized in Table 1.1.

As most SNPs are bi-allelic, the allele frequencies of the SNP alleles are much higher than the STR alleles. This implies that to reach the same individualization probability of 10^{-18} requires more SNP loci than STRs. Allele frequency of an allele is the ratio of the number of individuals that possess the allele to the population size, and the matching probability is the product of the genotype frequency at each locus.

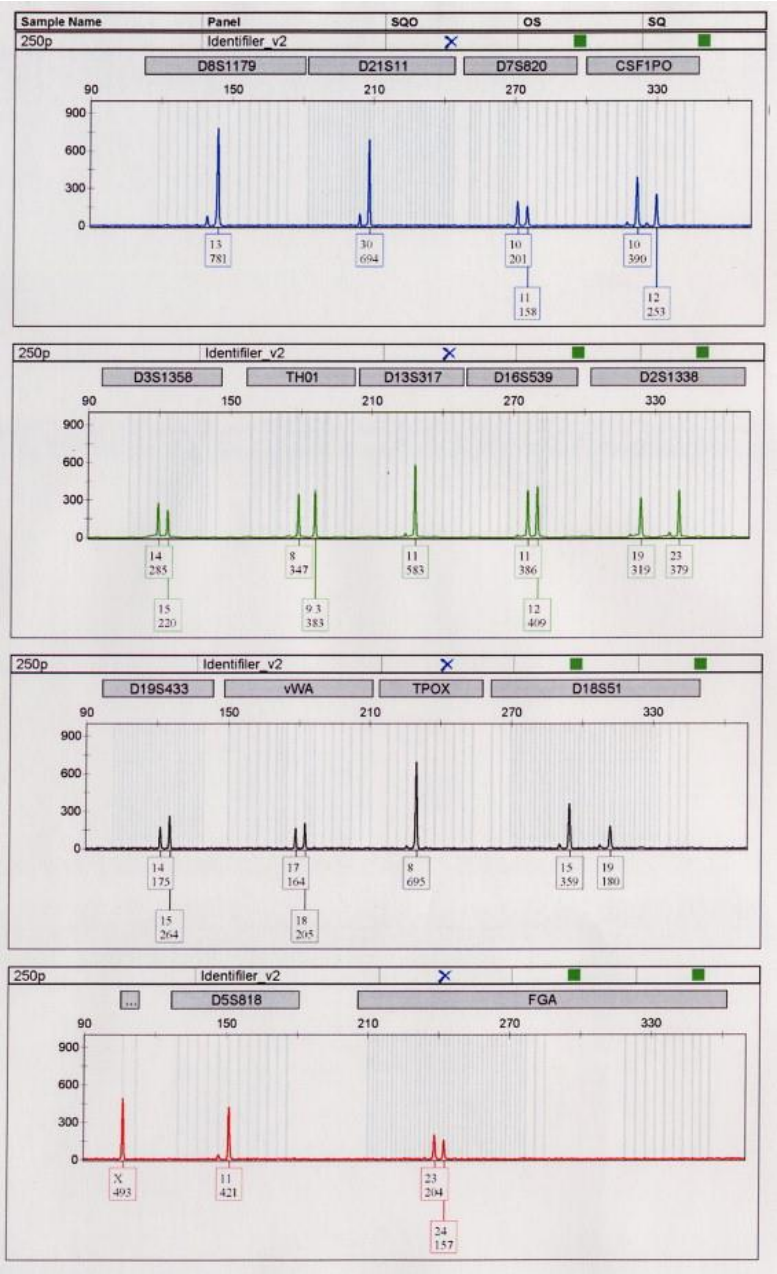

Figure 1.4 The electropherogram of amplified 9947A DNA (Promega Co, USA) with AmpF*l*STR Identifiler kit (Applied Biosystem, USA). Adapted from Tsukada *et al*.[11] The 9947A is a typical cell line as a standard control in forensic DNA typing. The 4 fluorescent channels from top to bottom are 6-FAM (blue), VIC (green), NED (yellow, expressed in black for easier visualisation) and PET (red).(Reprinted from Ref.[11], Copyright© (2009) with permission from Elsevier)

Table 1.1 Comparison of STR and SNP markers, Adapted from Ref.[13] with permission, Copyright ©2011 of Elsevier.

Characteristics	Short Tandem Repeat (STR)	Single Nucleotide Polymorphism (SNP)
Occurrence in human genome	~1 in every 15 kb	~1 in every 1.3 kb
General informativeness	High	Low; only 20% to 30% as informative as STRs
Mutation rate	~1 in 10^3	~1 in 10^8
Marker type	2, 3, 4, 5 nucleotide repeat markers with many alleles	Mostly bi-allelic markers with 6 possibilities (A/G, C/T, A/T, C/G, T/G and A/C).
Number of alleles per marker	Usually 5 to 20	Typically 2 (some tri-allelic SNPs exist)
Multiplex capability	>10 markers with multiple fluorescent dyes	Difficult to amplify more than 50 SNPs well
Amplicon size	~75 to 400 bp	less than 100 bp
Ability to predict ethnicity (biogeological ancestry)	Limited	Some SNPs associated with ethnicity
Phenotypic information	No	Possible to predict some hair colours, etc.

For the bi-allelic SNP loci mentioned earlier, if the allele frequency of allele C is p and for allele T is q, the genotype frequency is p^2 for the homozygote CC and q^2 for the homozygote TT. Conversely, in the case of heterozygous CT or TC, its genotype frequency is $2pq$. A comparison of the gene frequency of STRs and SNPs is shown in Table 1.2. All the statistical data in Table 1.2 was observed in American Caucasians from two research groups[14,15]. The three loci are selected on chromosome 11 and the TH01 (6, 7) allele is chosen from highest allele frequencies of 2 non-microvariant (no deletion of the repeat motif) alleles for the brief comparison. The rs901398 and rs2076848 are both bi-allelic SNP loci on chromosome 11. The genotype frequencies of both SNPs are higher than TH01 loci. Even combining the result of rs901398 and rs2076848, the matching probability is given by 0.483 times 0.411 as 0.199. The matching probability value of 2 SNP loci is still poorer than a TH01 (STR) locus (0.077). As a result, the required number of SNP loci to meet the individualization standard has to increase to ca. 45 to yield the equivalent random match probabilities of the 13 core STR[16].

Table 1.2 Comparison the genotype frequency in the selected heterozygote of 1 STR and 2 SNP loci. The statistical data is adapted from the investigation in American Caucasians based on Budowle *et al.*[14] for TH01 and Amigo *et al.*[15] for rs901398 and rs2076848.

DNA profile		Allele frequency from population			Genotype frequency for locus	
Locus	Allele	Times allele observed	Size of the population	Frequency	Formula	Number
TH01	6	46	203	p= 0.226	$2pq$	0.077
(STR)	7	35	203	q= 0.172		
rs901398	C	269	657	p= 0.409	$2pq$	0.483
(SNP)	T	388	657	q= 0.591		
rs2076848	T	192	661	p= 0.710	$2pq$	0.411
(SNP)	A	469	661	q= 0.290		

The mini-sequencing (also known as SNaPshot) assay[13], one of the most conventional SNP analyses, adopts a similar strategy except for single-base extension PCR. Figure 1.5 depicts the 4 steps of SNaPshot. The first phase performs the PCR to amplify an outer region of nucleotide containing an SNP locus and hence the amplicon can be used as template for the second step. The exonuclease and shrimp alkaline phosphatase are then used to inactivate the primers and deoxynucleotides (dNTP) in the former PCR reaction otherwise these two reactants would give rise to interference reactions at the second step. The second step applies the inner SNP primer to bind the adjacent sites next to the SNP position. Then 4 fluorescent dye-labelled dideoxynucleotides (ddNTP) are added to conduct the second PCR reaction via thermostable polymerase. Due to the lack of hydroxyl group on the 3' carbon in the ribose of ddNTP, the polymerase stops replicating at the distal position during the reaction as shown in Figure 1.5. The paired ddNTP is synthesized onto the 3' end of the SNP primer and forms the single base extension. The single base extended primer is then injected into the capillary electrophoresis and is discriminated by the primer length based on its mobility and the fluorescence of the labelled dye.

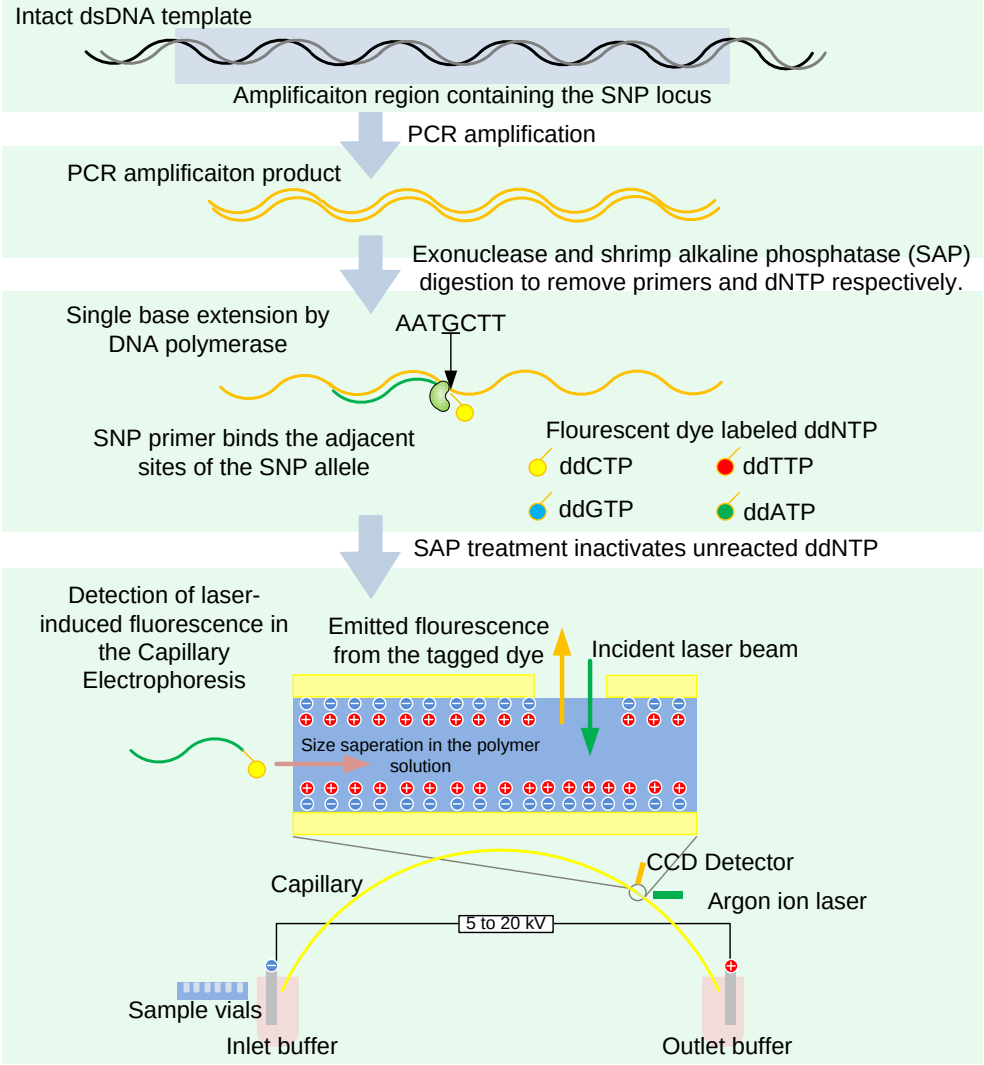

Figure 1.5 A schematic of mini-sequencing (also referred as SNaPshot) of the SNP analysis[8]. The first PCR amplification reacts on the external region containing the SNP locus. The primers in the first PCR and the dNTP are digested by an exonuclease, and the shrimp alkaline phosphatase (SAP) individually. The two components may continue the unwanted side PCR reaction in the following single-base extension. The third step incorporates a SNP primer which is adjacent to the distinct nucleotide. Then the fluorophore-labelled deoxyoligonucleotide (ddNTP) is paired to the allele position by the polymerase. Again, unreacted ddNTP has to be digested by SAP. Finally, the single base extended SNP primer is injected electrokinetically into the capillary electrophoresis at a potential of 15 kV. The capillary leaves the uncoated region to allow the laser to stimulate and to collect the emission of the fluorescence. The emitted photons striking on the CCD detector are transmitted as current signals to the PC. The polymer solution filled in the capillary acts as the sieving matrix for the single-stranded DNA. The components of the polymer solution are 4% linear dimethyl acrylamide, 8 M urea, 5% 2-pyrrolidione[17]. Another function of the polymer solution is reducing the electroosmotic flow which lowers both the resolution and reproducibility.

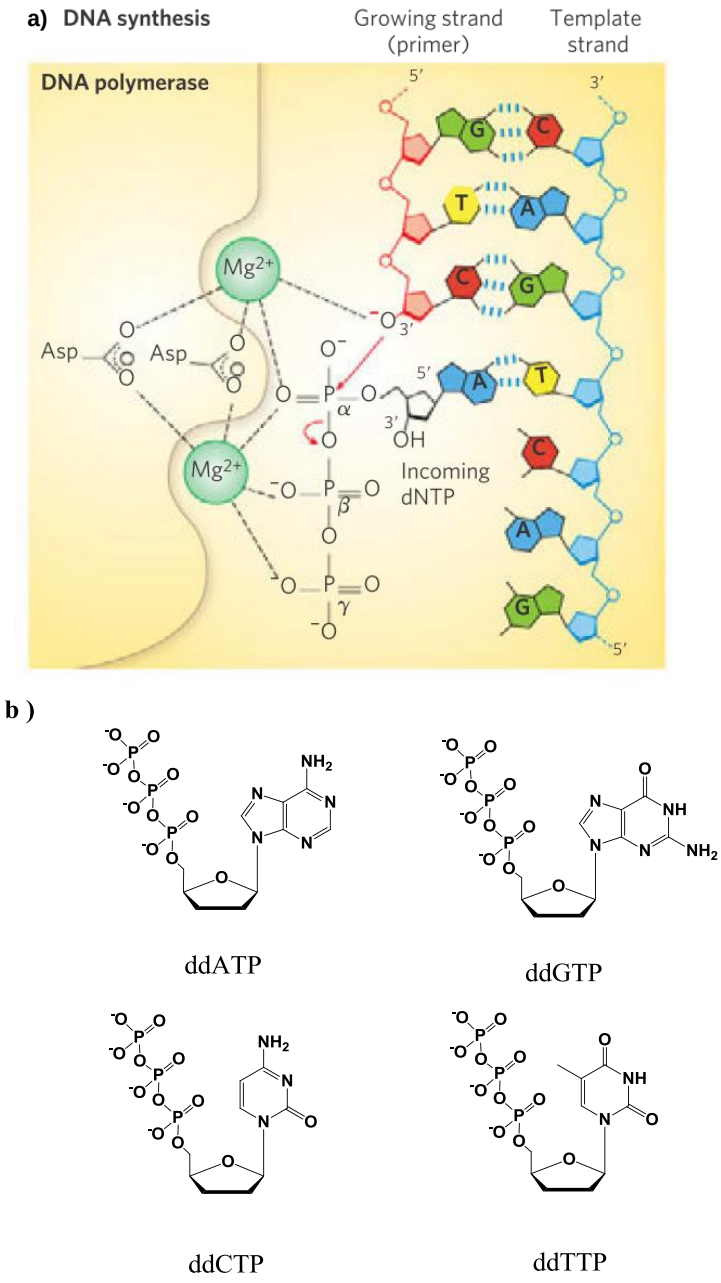

Figure 1.6 a) Adapted from Lehninger *et al*[18]. An illustration of the polymerization reaction catalysed with the DNA polymerase I. DNA polymerase I activity requires a single unpaired strand to act as a template and a primer strand to provide a free hydroxyl group at the 3′ end, to which a new nucleotide unit is added. Each incoming nucleotide is selected in part by base pairing to the appropriate nucleotide in the template strand. The reaction product has a new free 3′ hydroxyl, allowing the addition of another nucleotide. b) The structure of the dideoxynucleotides (ddNTP) which lack the hydroxyl moiety at the C3 on the ribose ring. The ddNTP stop the following polymerization reaction and only ligates to the end of the annealing primer shown in Figure 1.4. (From LEHNINGER PRINCIPLES OF BIOCHEMISTRY 6E by David L. Nelson and Michael M. Cox, Copyright ©2013 by WH Freeman and Company. Used with permission by the publisher.)

In order to avoid the off-scale and relevant artifacts in the separation steps, the quantitation of nucleic acid is essential to ensure the amount of DNA template loaded into the following multiplex PCR is 0.25 to 1 ng. Lower or higher amounts of DNA template not only result in weak or overloading signals, but cause imbalance in amplification between the loci. However, this quantitation step takes an additional 2 h before the ca. 3 h multiplex PCR. Conventional analysis of STR and SNP markers has the pitfalls of the time-consuming PCR and high cost of the commercialized kit when compared to the surface-enhanced Raman spectroscopy (SERS) based detection. The surface-enhanced Raman spectroscopy is a rapidly growing research topic since its discovery, and gains more insightful understanding after 2000 as the nanoscale fabrication of the SERS active substrate can be higher controlled[19]. The introduction of SERS would be discussed in Section 1.2. The advantages of SERS applied in the biosensing has been reviewed by several authors[20–23]. There are three major advantages of SERS over the conventional analytical techniques. First, the resolution of a Raman band is up to ca. 1.5 to 7 cm^{-1} between the desktop and portable Raman spectrometers, which is higher than that of the electronic emission band of fluorescent dyes, around 20 to 30 nm (ca. 500-600 cm^{-1}). Hence the selectivity of the Raman spectroscopy is better as long as the Raman bands do not overlap. Consequently, the SERS is one of the options in the multiplex detection systems[24]. Second, the SERS technique has an enhancement factor ranged from 10^4 to 10^8 and may increase to 10^{11} to 10^{14} when combined with the technique of the surface-enhanced resonance Raman scatterings (SERRS). The sensitivity of SERRS is close to the level of single molecule detection[20,24–26]. The third advantage of SERS used in the biosensing is based on that to the most biomolecules, and the relevant reactions are in aqueous solution. However, the water molecule has an enormous infrared activity which may mask the infrared signals of the biomolecules of interest. In contrast, the Raman activity of water is relatively small and less interfere the detection of the biomolecules[24].

Due to the SERS active substrates has to be fabricated as the periodically ordered nanostructure[19], there are highly diverse developments in both of the geometry and size aspects[19,22]. The SERS active substrates used in this study developed in Bartlett's group is the sphere segment void (SSV). The details of SSV fabrication carried out by the electrodeposition on the nanosphere template would be given in Section 2.1[27]. The SSV substrate has advantages compared to the conventional nanoparticle SERS substrate which has a more homogenous surface structure and with ease to measure the universal and reproducible SERS signals[28]. The nanoparticles as the SERS substrate has higher SERS enhancement than the SSV substrate. However, due to the

nanoparticle SERS enhancement is triggered by the aggregation between the nanoparticles, the control of the aggregation is hard to control an equal distance between each nanoparticle and hence the analysts need to select the "hot spot" to gain the appropriate SERS signals which result in the non-universal signal sampling. Based on the pitfalls of nanoparticle substrate, more researchers trying to modify the surface of nanoparticles, one example is to coat an inert shell of silicon dioxide on the metal nanoparticle and depositing the coinage metal outside to form a core-shell structure[29]. However, the fabrication of the aggregation-improved nanoparticle is relatively time-consuming requires high skills compared to the SSV substrate used in this study.

The DNA detection as mentioned earlier also attracts SERS scientists to design various sensing systems on the discrimination of DNA sequences in the diagnostic either forensic fields. Several reviews focused on the biosensing application of SERS[20,24,30–33]. The works of Graham's group are worth mentioned studies based on the metal nanoparticle substrates. The Graham's group has established the SERRS detection limits of 8 and later 13 Raman dyes commonly used in the hybridization sensing at 10^{-10} to 10^{-12} M level[34,35]. They followed this fundamental results further developed the 5 plex DNA detection system contained human at dual excitation wavelengths (514 and 633 nm)[36]. Additionally, both Mirkin[37] and Vo-Dinh's group[38] have reported SERRS based DNA detection assays. Mirkin and co-workers[37] fabricated the chip that can discriminate single nucleotide polymorphisms between 6 viruses at the limit of detection of 20 fmol.[37] Their chip thus possessed the high capacity, rapid and ultrasensitive virus detection. Based on the similar scheme, Vo-Dinh's group[38] used their SERS chip to detect of the breast cancer gene (BRCA-1). In this system, they immobilised the probe on a silver surface and then hybridised the target onto that surface. Finally, they used labelled probes to generate SERRS signals where the hybridisation occurred, thus indicating the presence of the breast cancer gene (BRCA-1).

Compared to the DNA sensing systems of the metal nanoparticle based SERS substrates, Mahajan *et al.*[39]designed a dithiol-anchored oligonucleotide as the probe on the sphere segment voids (SSV) Au electrode which has SERS activity at 633 nm excitation. The analyte, the 5'-labelled PCR amplicon produced by the asymmetric amplification hybridised with the immobilised probe. The hybridization is similar to the PCR mentioned earlier but has the advantage of removing the non-paring amplicon by rinsing with high stringency buffers. The Raman intensity of the Raman label, Texas Red, was a function of the negative sweeping potential. Mahajan's[39] and later Corrigan's work[40] both indicated that the potential-driven Raman intensity of the Texas Red label can be used to discriminate the sequence variation of SNP and

STR, the two genetic markers of forensic importance. Although their works still used PCR amplicon as the analyte, no quantitation step is needed and hence the time is saved in the analysis. The overall advantages of the electrochemical SERS DNA detection system posses the ease of fabrication, lost cost, reproducible and homogenous Raman response when compared to the metal nanoparticle based SERS DNA detection systems.

1.2 Raman Spectroscopy and Surface Enhanced Raman Scattering

When light irradiates molecules, the molecule undergoes several interactions with the incident light and results in absorption or emission. The net variance of the adsorption and emission compared to the incident light can be measured by a detector. From the perspective of energy, this process can be described as an energy exchange among the radiation and the molecule. In adsorption the irradiated molecule gains energy from the incident light and is excited to a higher energy state by storing the energy in the corresponding excited state. In emission the molecule releases the excess energy and drops down to a lower energy state. If there is no electronic state transition, the energy changes occur among the molecular vibrational and rotational quantum levels. The Raman shift refers to these interactions and the "net frequency shift" between the incident and the emitted light. However, rotational transitions can only be resolved in high resolution in the gas phase and are, therefore, not relevant to the vibrational spectra of the liquid-solid phase discussed in this thesis.

The light emitted from the molecule after absorbing the incident radiation is in the form of scattered light that is measured by the spectrometer. Figure 1.6 shows the three types of the scattering on the scale of the energy. As mentioned earlier, the energy (frequency) of the emitted light is compared to the energy (frequency) of the incident light. The case of no net energy (frequency) change between the incident and emitted light is referred to as the elastic scattering. If there is a change in frequency between the incident and emitted light, this is referred to as the inelastic scattering. Raman scattering is one of the examples of the inelastic scattering. In Raman spectroscopy, the energy is often expressed in wavenumber with unit of cm^{-1} which is the reciprocal of the wavelength. If the molecule gains energy from the incident light, the shift in the wavenumber (equivalent to a decrease of the frequency) and is called the Stokes shift. If the molecule loses energy to the incident light, the shift in the wavenumber is called the anti-Stokes shift. Figure 1.7 shows the Raman spectrum of chloroform recorded with an incident 514.5 nm laser, the intensity of the Rayleigh scattering is denoted in the centre of the spectrum. Note, in reality that is several orders of magnitude large as in Raman spectroscopy. Only about 1 in $10^7$of

the incident photons that collide with the molecules undergoes the Stokes shift (to the right side of the spectrum). An even lower number of photons emerge with an anti-Stokes shift (left side of the spectrum). Most con-

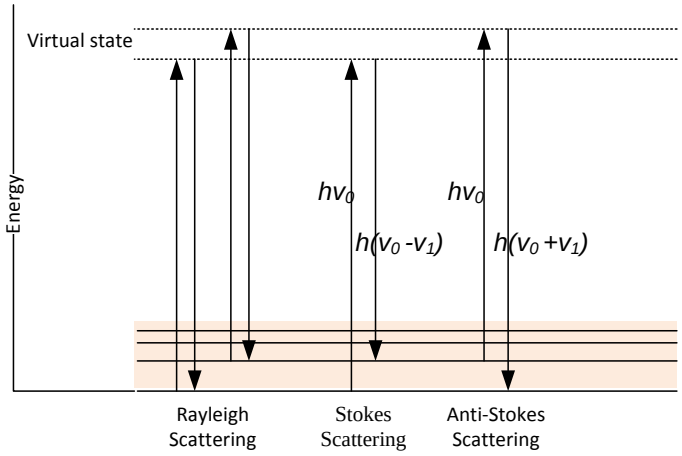

Figure 1.6 Energy correlation of the scattering phenomenon. Rayleigh scattering is an elastic scattering process due to both the incident and emitted energies being equal. Raman scattering, composed of Stokes (lowering energy) and anti-Stokes (gaining energy) scattering, is a type of the inelastic scattering process.

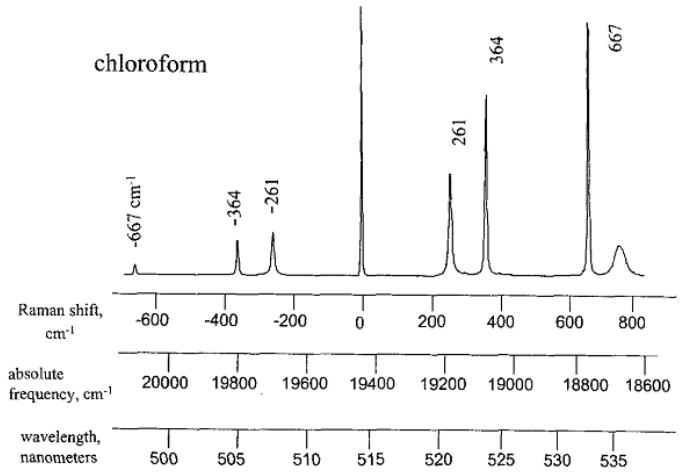

Figure 1.7 Adapted from McCreery[41]. Raman spectrum of room-temperature chloroform obtained with 514.5 nm light. Rayleigh scattering at zero Raman shift is heavily attenuated by a band reject filter and is several orders of magnitude more intense than the Raman scattering. The x-axis is shown in three different scales but is typically plotted as Raman shift in reciprocal centimetres about the laser frequency (19,435 cm^{-1} in this case). Although the Stokes Raman to the right is a negative frequency shift, convention assigns Stokes Raman shifts as positive numbers. (Adapted with permission from Ref. [41], Copyright© 2000 of John Wiley & Sons)

ventional Raman spectroscopy measures the Stokes shift because the anti-Stokes spectrum is weak and not easy to observe. Each molecule has its electric field created by the electrons in the orbitals and the protons in the nuclei. While the incident light strikes the molecule, the electric field of the light will distort the molecular electric field and the extent of distortion can be expressed in terms of the polarizability which is proportional to the electric field of the incident light. The polarizability is a property of the molecule and the polarization will depend on the polarizability of the molecule and the field. Figure 1.8 shows the correlation between the vibrations and the resultant change of polarizability. For the vibrational energy levels, only when the polarizability changes during a particular vibration can the molecule gain or lose energy to cause the Stokes or anti-Stokes shift observed in the Raman spectrum. This is the Raman selection rule. The selection rule also applies to liquid samples. Since the Raman scattering of water is weak, aqueous samples can be studied with Raman spectroscopy.

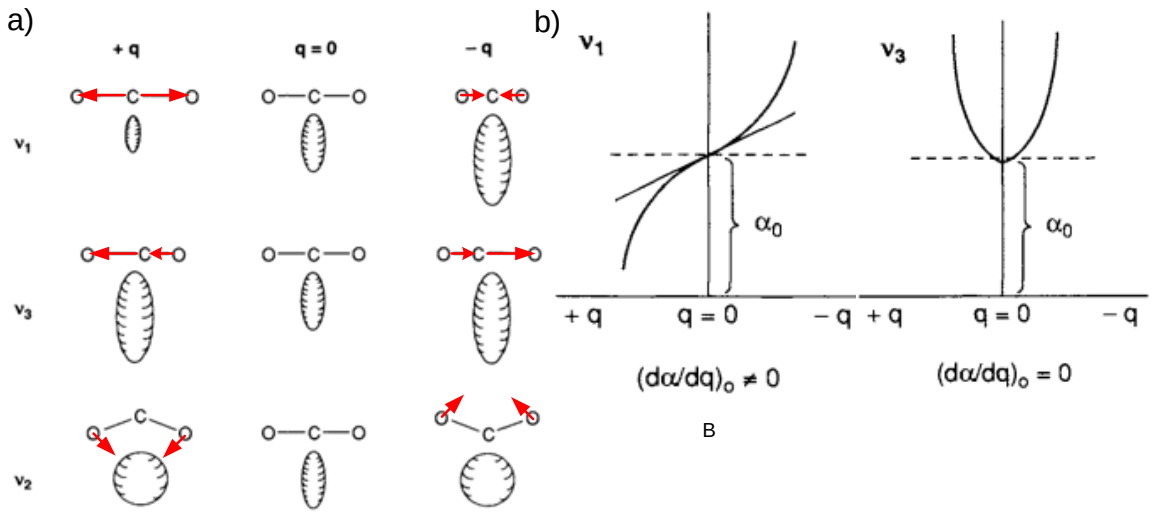

Figure 1.8 Modified from Ferraro *et al.*[42]. a) The ellipsoid represents the changes in polarizability during vibration of CO_2 molecule. The arrows indicate the vibrational direction. b) Difference between v_1 and v_3 vibrations in CO_2 molecule. (Reprinted with permission from Ref. [42]. Copyright© 2003. Elsevier.)

The Raman spectrum contains valuable information about the vibration energy levels and can help to identify the molecular structure from the characteristic Raman shifts. Unfortunately, in most cases the conventional Raman spectrum is weak (1 in 10^7 incident photons) and requires the high purity and high concentration of molecules and high incident laser power to be observed. However, the discovery of surface-enhanced Raman scattering (SERS) by Fleischmann and co-workers[43] gave a new perspective to Raman spectroscopy. It was noted that the Raman scattering of pyridine was much stronger when it was adsorbed on a roughened silver electrode. Today

most authors accept that the major enhancement is the primiry result of localised surface plasmon resonance (LSPR) driven by the collective oscillation of local dipoles on the metal nanostructures driven by the incident laser[44,45]. A minor enhancement is caused by charge transfer (CT), this is also referred to as chemical enhancement.

Charge transfer merely contributes an enhancement up to a 100 in SERS and has been the topic of much debate since the beginning of SERS around 1977. Pyridine (Py) was noted for the potential dependent intensity of its Raman bands at the silver electrode by Jeanmaire and Van Duyne[46]. They first inferred that neutral pyridine had a fixed end-on orientation by the depolarization ratio. The enhanced intensity of the Raman bands can then be divided into two groups. The first group of Raman bands have weaker intensity at 0.0 V and grew to a peak intensity at -0.6 V (vs. SCE) while the second group have non-observable Raman intensity at 0.0 V and then eventually reached a maximum intensity at -0.8 V. The 1.5 to 3 times stronger Raman intensity observed in both groups at more negative potential cannot be explained solely by the electromagnetic enhancement. This characteristic intensity response was studied by other teams. Tian's team[47,48] compared the quantum calculation using density functional theory for pyridine and metal clusters, including Ag, Au and Pt, with the experimental results. They concluded that the enhanced intensities were the result of two collective contributions. The first is the chemical bonding between the pyridine and the metal. The second is due to the fact that the electronic structure of adsorbed pyridine has two adjacent excited states higher than the lowest unoccupied molecular orbital (LUMO) which participate in charge transfer enhancement at more negative potential and result in the two groups of enhanced bands[49]. The other team led by Lombardi[50] proposed a SERS theory of charge transfer enhancement by correlating the effect with extra excited state in the molecular-metal system tuned by the Fermi level of the metal electrode. This potential dependent energy state lay, and was tuned between, the LUMO and highest occupied molecular orbital (HOMO) of the probe molecule[51]. When the optimal state (also referred to as a charge transfer state), tuned by the electrochemical potential, is resonant with the excitation frequency the strongest Raman intensity will be observed. They later classified the probe molecules that show distinct charge transfer behaviour into two groups, based on the dependence of peak potential on excitation frequency. Both Tian's and Lombardi's work indicate the critical role of the molecular orbitals and hence show that the charge transfer enhancement is molecule-specific and is not universal in SERS. However, these experiments are, arguably, one of the

clearest proofs that CT is real and that it plays a non-negligible role in the magnitude of the SERS enhancement[52]. This is discussed in greater depth in Chapter 4.

In contrast, the electromagnetic enhancement is a universal feature of SERS. The electromagnetic enhancement is driven by localised surface plasmon resonance (LSPR)[44]. The surface plasmons originate from the free electrons in the conduction band of the metal beneath the surface. When light excitation irradiates in nanoscale metal structures, like nanoparticles, the free electrons can be polarised by and oscillate with the electric field of the transmitted light to form a dipole oscillator. At the same time, a restoring force of Coulomb interaction provides a damping factor for this oscillation. The two interactions produce a surface plasmon resonance (SPR) whose oscillation frequency is characterised by absorption and scattering of light. Therefore one can probe the surface plasmon resonance by measuring the reflectance spectrum. When the incident light is tuned to a characteristic frequency that enable the surface plasmons to coupling in and out efficiently, the resultant complex of light and plasmon is referred to as a

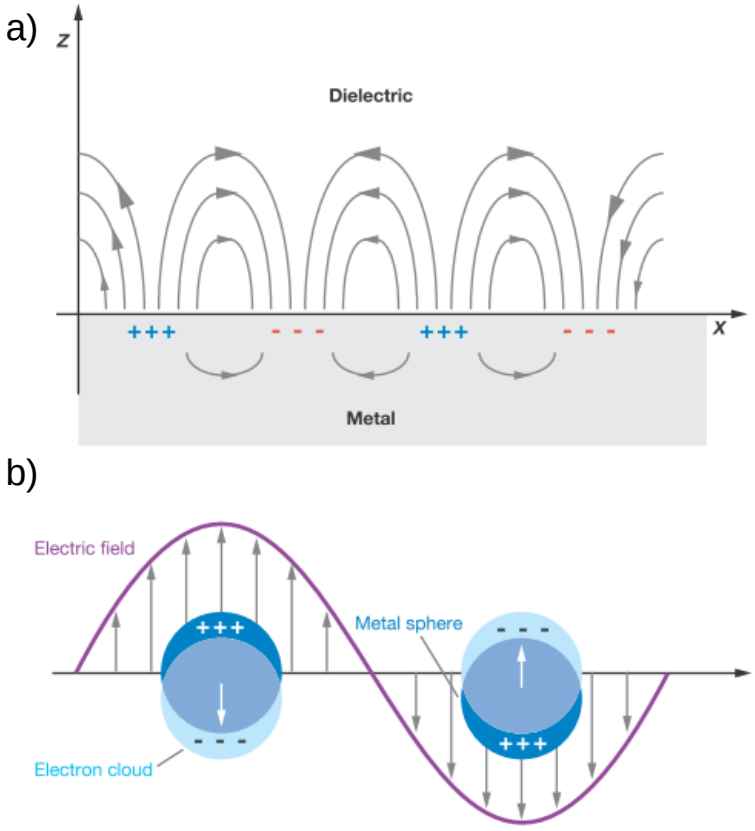

Figure 1.9 Adapted from Willet *et al.*[44] Schematic diagrams illustrating a surface plasmon polaritons (or propagating plasmon) a) and a localized surface plasmon b). (Reprinted from Ref. [44] with permission, Copyright @ 2008 Annual Reviews)

surface plasmon polariton (SPP). The Coulomb interaction weakens as the dimension of the metal structure increases and, as a result of the weakened damping, there is a red shift of the reflectance spectrum[53].

The SPPs that propagate, and eventually dissipate, on a planar metal surface are called propagating plasmons[54]. Conversely, an ordered nanostructure can act as a grating and contribute constructive interference between the incident radiation and the SPR, to do with the scale of the grating-like structure should have an appropriate geometry and an average dimension less than half wavelength of excitation radiation.

On a flat surface, a higher electron density of surface plasmon gives a greater dipole momentum than an optical field traversing above the surface, so it is hard to observe the coupling with the incident light. The momentum difference between the electromagnetic wave and the incident light can be compensated mainly by several techniques[55]. Either a grating or high refraction index prism can be used to match the momentum. The third technique is to pattern the metal surface a periodic ordered structure at the subwavelength scale of the excitation light. When the surface has orderly arrangements, the optical field can be confined to scatter to higher momentum states. The surface plasmon polaritons can be further divided into the propagating SPPs which depend on the incident angle of light and the localized SPPs which are independent to the incident angle. Localised surface plasmon, has a characterized frequency which generates the enhanced electromagnetic field in the vicinity of the interface and hence enables the resonance with the corresponding excitation and the Raman scattered radiation [44,56].

The resonance frequency of a LSPR varies with the dielectric constant of the metal, the dielectric constant of the contacting environment and the surface geometry of the structure. The resonance frequency of plasmons on silver and gold is located in the visible region of the spectrum which makes them suitable for use with the visible and near-infrared (NIR) laser excitation that is conventionally used in Raman scattering. For use as a SERS substrate, the surface plasmons must resonate in the energy region that matches the incident laser.

Aggregated, regular sized, nanoparticles are a common SERS substrate. However, aggregation is not easily controlled and is not ordered due to the dominant effect of random Brownian motion. This reduces the homogeneity of aggregation and makes it hard to collect a stable SERS signal from different location surface or from sample to sample. In the present work we chose to use

"spherical segment void" (SSV) surface and to utilize their defined geometry. The basic method is to fill the gap between the ordered arrangement of polystyrene nanospheres (typically 600 nm in diameter) by Au electrodeposition. Then to dissolve the polystyrene nanospheres with dimethylformamide (DMF) to leave the spherical segment void substrate. Further experimental details are given in Section 2.1; the following introduction focuses on how the optimal LSPR is formed on the SSV substrates.

Cintra *et al.*[27] studied SERS of SSV substrates using benzene thiol to form a monolayer through covalent binding with Au. They varied the thickness of the deposited Au film by control of the charge during the deposition by chronoamperometry. The diameter of the nanospheres was varied from 350 nm to 800 nm. In the case of the 600 nm diameter nanospheres, a thickness of 0.8 times the diameter of the 600 nm nanosphere was found optimal for SERS when using a 633 nm laser.

The plasmonics of the substrates were investigated using reflectance spectroscopy as reported in a detailed study by Kelf *et al.*[54] They found that the maximum enhancement was related to the collective contributions of the delocalized Bragg plasmons and localised Mie plasmons as shown in Figure 1.10. The Bragg plasmons are the plasmons propagating on the metal surface which are Bragg scattered from the openings of the cavities. The Mie plasmon is the plasmons confined within the cavities and is modelled after Mie scattering theory which originally was computed on spherical metal nanoparticles.[57] Bragg and Mie plasmons eventually dissipate because of the resistance of the metal. The Bragg plasmons can be distinguished from the Mie plasmons by the dependence of their reflection spectra on the incident angle. The dispersion of the plasmons is investigated by recording the reflectance spectrum for different incident angles and sample azimuthal orientations and for varied sample thickneses $\bar{t}$, where $\bar{t}$ is the ratio of the film thickness to template sphere diameter as shown in Figure 1.11. The results can be divided into groups

$0<\bar{t}<0.4$: Bragg plasmons were seen, becoming increasingly intense as the corrugation deepens. The Bragg plasmons disappear as the top surface breaks up into islands.

$0.4<\bar{t}<0.6$: Mie plasmons appeared at high energies around $\bar{t}=0.35$ and continuously red shift (shift to lower energy) at increasing thickness. The Mie modes are almost independent of azimuthal angle as they are localised. Mie plasmons are observed dropping down from short

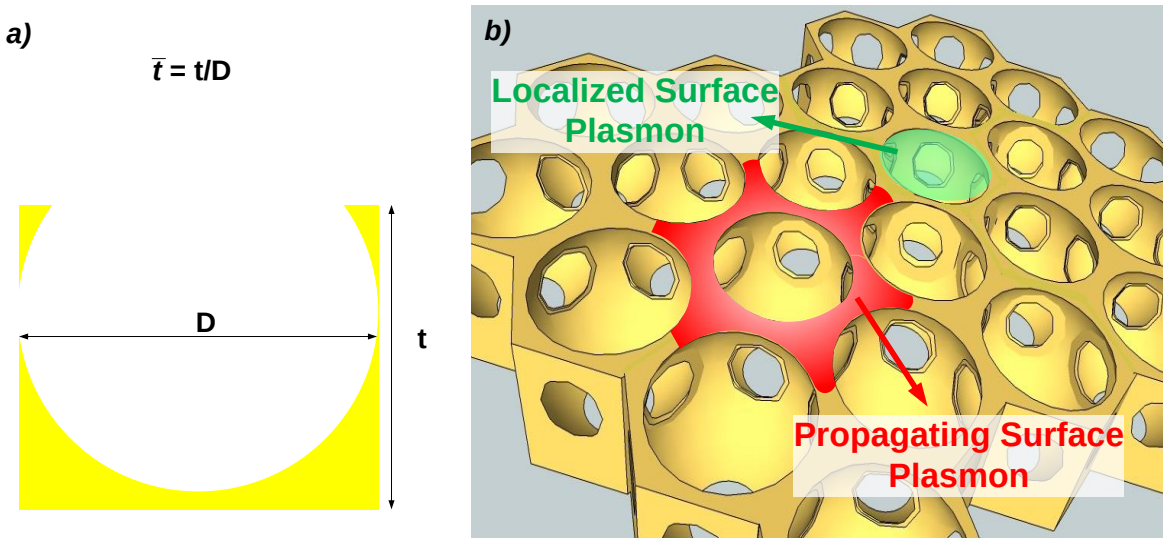

Figure 1.10 Schematic modified from Kelf *et al.*[54] a) A schematic of the of the geometric factor, $\bar{t}$, which is the ratio of thickness to the diameter of the template nanosphere. b) Representative illustration of the plasmons on the SSV surface. The delocalized surface plasmons termed Bragg plasmons exist on the flat surface and propagated across the surface. The localized plasmons exists inside the void have energies that are highly dependent on the nanostructured geometry. They are independent of the incident angle of the excitation light and sample orientation because they are localized.(Reprinted from Ref. [54] with permission, Copyright ©2006 The American Physical Society)

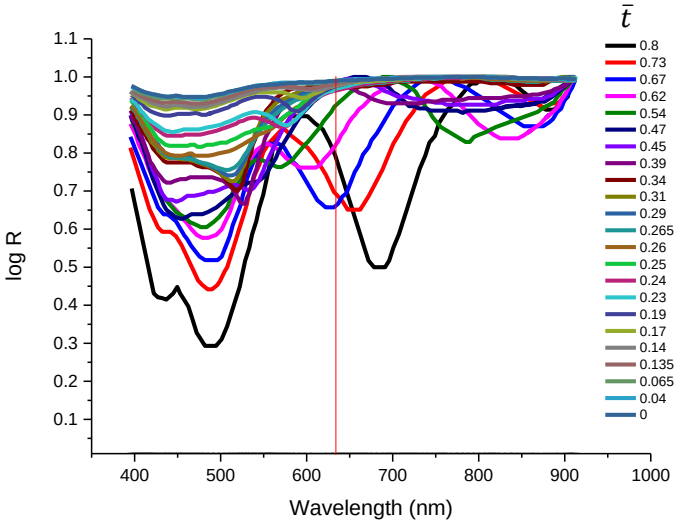

Figure 1.11 Schematic modified from Cintra *et al.*[27] The reflectance spectra was overlaid to demonstrate the dependence on the geometric factor, $\bar{t}$, which is the ratio of thickness to the radius of the template nanosphere. The vertical line indicates the excitation wavelength of the laser at 632.8 nm. The dips of the curve shows the Mie plasmon modes have red-shift as the thickness in creases. (Modified from Ref.[27]. with permission, Copyright© (2006) of the Royal Society of Chemistry.)

wavelength with increasing film thickness. The high coupling as they mix with the Bragg modes is clearly visible, creating complex dispersion relations.

$0.6<\bar{t}<1.1$: As the sample thickness reaches void encapsulation the Mie plasmon modes become better confined within the cavities. Bragg plasmons reappear and coexist on the top surface of the film, coupling with these Mie plasmons.

Kelf's and Cintra's work proved that the Mie plasmon could be tuned by varying the thickness to mix with the Bragg plasmons to achieve an optimal enhancement in SERS. Around $\bar{t}= 0.8$ is optimum because it allows efficient coupling of the incoming laser light and efficient coupling out of the Raman scattered light in the geometry of the Raman microscope when using the 633 nm laser for the Au SSV substrate. In fact for air and solution the optimum is going to be slightly different because of difference in reflective index of air and solution alters the plasmon energy.

1.3 Oligonucleotides on Charged Surfaces and Electrochemical Melting

Hybridization and denaturation (often referred to as melting) are the core reactions in nucleic acid chemistry. Hybridization describes the process by which two complementary single-stranded DNA molecules (ssDNA) bind with each other through the hydrogen bonds between the bases. Among the four bases in DNA, adenine (A) pairs to thymine (T) and cytosine (C) pairs to guanine (G) by hydrogen bonding and consequently forms double-stranded DNA. The pairings (A-T and C-G) are referred to as Watson-Crick binding. A clear instance of DNA hybridization is when the forward primer hybridises to the target template in the annealing stage of PCR as described in Section 1.1. In the case of denaturation, denaturation can be tuned by the temperature which is applied in the first stage of PCR. Denaturation can also be controlled by hexlicase in the prokaryotic organism as well, for example, genomic DNA has to be unwound and denaturated into single strands by the helicases at the first step of DNA replication[58]. Scientists implement hybridization and denaturation in the *in vitro* reactions to select, or isolate, the region of interest for discrimination in the biosensors. Most design strategies for DNA biosensors contain at least the hybridization step to begin a specific binding with the analyte sample. Before the hybridization step, melting is usually performed to dissociate the target dsDNA.

DNA melting takes place when the environment temperature increases to around 70 to 100 ℃. The denaturation temperature and the time depend on the length of dsDNA, the GC content and the ionic strength of the solution. In a typical PCR melting stage at 95℃ most of the genomic DNA will denature in 20 min. The hydrogen bonds of dsDNA between the paired bases break eventually and hence separates the double strands to ssDNA accompanied with the increase absorbance at 260 nm[59]. The lower absorbance of dsDNA at 260 nm results from the electronic coupling of the individual nucleotides in the nucleic acids. The absorbance at the spectrum region is proportional to the dipole strength, the square of the magnitude of the transition dipole moment. The dipole moments in the A-T or C-G pairs are both aligned parallel to the base plane as the calculation reported by Srinivasan *et al.* [60]. When the orientation of transition dipole is in side-by-side geometry is qualitatively similar to that of the bases the base stacking in double-

stranded DNA, the mixing of the transitions in different regions of the spectrum results in transfer of dipole strength from absorption bands in the lower-energy region to bands at higher energies. The high-energy bands of the nucleotide bases occur too far into the UV to be measured conveniently, whereas the low-energy bands occur in the more accessible region around 260 nm. The loss of dipole strength in the 260-nm region is therefore seen experimentally as lower absorbance which also is referred to as hypochromism[61–63].

The melting temperature (T_m) is defined as the midpoint temperature during the transition between dsDNA and ssDNA when the DNA strands are half in the ssDNA state. The T_m depends on the composition sequence of the strand since the larger number of hydrogen bonds in GC-rich oligonucleotides leads to higher T_m (3 hydrogen bonds for G-C against 2 for A-T). The T_m value predicts the dsDNA stability and is used in real time PCR to perform high resolution melting analysis to discriminate different sequences. Thermal-based melting analysis has been integrated with microarray, lab-on-chip systems, and has been applied in clinical diagnostics, and forensic science[64]. Conventional melting analysis follows the reactions in phosphate buffer or sodium chloride solution which is stable for biological applications.

Compared to homogeneous solution assays, the use of solid surfaces has advantages such as the ease of processing, temperature control and electric field manipulation. For example, thermal solid phase microextraction has been applied in many isolation steps of chemical reactions. The thermal conductivity is also higher and temperature changes more rapid on a solid surface compared to a liquid phase. Additionally, the application of an external electrical field at the solid surface, by contrast, has been reported to accelerate the immobilisation reaction of oligonucleotides in low ionic strength solution and hence provides an option to switch the physical or chemical properties of the surface. Another example is to tune the surface hydrophobicity and the adsorption of the organic molecules both of which have been shown to be switchable by using an external electric field[65]. Based on these features and on the manipulation aspects, there are more studies aimed at the development of the biosensors at the liquid-solid interface.

However, understanding of the conformations of oligonucleotides at charged surfaces is still a challenge for chemists. The early researches adopted the dropping mercury electrode (DME) or

hanging mercury drop electrode (HMDE) as a model surface. This is a liquid-liquid interface which can be formed reproducibly. Paleček showed that the surface denaturation of adsorbed dsDNA occurred in the potential region around -1.0 to -1.5 V (vs. Ag/AgCl) at the mercury electrode[66]. Later Heller's group[67] reported work on an array of platinum electrodes with pulsed current at biased positive potential. Two oligonucleotides, 19 and 22-mers, were immobilised in a hydrogel on the electrode surface instead of in indirect contact with the platinum. The platinum array accelerated hybridization by a factor of 25 times over the rate at the open circuit potential (OCP). Differential denaturation of either 19-mers or 22-mers was performed at negative potential and varied with the sequence composition. Electrochemical melting was used to detect the single nucleotide polymorphism imposing 0.6 μA and 1.5 μA, 0.1 sec on, 0.2 sec off for 150 cycles. Most of the previous work chose a mono-thiol anchoring moiety to tether the DNA on the charged surface; this limits the observation for the possible denaturation of dsDNA at more negative potential because the reductive desorption of the thiol occurs earlier than the denaturation.

The first observation of the electrical conformation switching of a monolayer of dsDNA was reported by Kelly *et al.*[68] using electrochemical atomic force microscope (EC-AFM). 15-mers dsDNA were anchored through a thiol to a polycrystalline gold electrode and their average height was measured in a confined area as a function of the applied electrode potential. 50 mM phosphate buffer (pH 7) in 0.1 M Mg_2Cl solution was used as the electrolyte. The height decreased from 6.5 nm to 2 nm when the potential shifted from +350 to +600 mV (vs. Ag wire). This change corresponds to a transition of the dsDNA from an upright position towards a horizontal position on the surface. In subsequent work reported by Wackerbarth *et al.*[69], the height of the HS-10A (ssDNA) oligonucleotide was measured on single crystal gold electrodes at negative potential. In this case, the aqueous buffer was 0.01 M phosphate buffer (pH 7.1). Scanning tunnelling microscopy (STM) showed an ordered morphology related to stretching of the ssDNA that appeared at -0.61 V. The elongated state maintained as the potential swept back to -0.21 V (vs. SCE). The thiol-gold bond broke around -0.67 V and caused desorption of the thiol-anchored oligonucleotides. These studies demonstrated the primary behaviour for thiol-anchored ssDNA in an electric field at the solid-liquid interface.

Rant and co-workers[70] have evaluated the effect of ionic strength, temperature and electrochemical potential on tethered ssDNA and dsDNA. Their work provides the latest

promising model for oligonucleotides at charged surfaces and is worth discussing in detail. They chose a 72 mer oligonucleotide with a 5'-monothiol anchor and a 3'- fluorophore (Cy3) label and measured the response to excitation based on the fluorescence energy transfer to the Au surface. The fluorescence is quenched when the fluorophore approaches the Au surface and, conversely, emerges when the fluorophore leaves the Au surface. A complementary strand oligonucleotide was hybridised with the Cy3-labelled probe in the case of dsDNA. The fluorescence of ssDNA and dsDNA were then measured in various conditions including the ionic strength, temperature and potential stepping. The fluorescence was used to estimate the distance of the 3' end of the immobilized probe to the Au surface. To ensure the immobilised probe has freedom to orient during potential sweeping, they used a pulsed negative potential to desorb some of the probe and re-passivated with mercaptohexanol until the maximum difference of fluorescence for ssDNA is reached. The potential window in their study is -0.6 to +0.1 (vs. Pt). The estimated distance of the Cy3 label was further interpreted as the extension of dsDNA and ssDNA on the charged Au surface.

In the electrical double-layer on a charged electrode, the distribution of ions is more compact at the surface of the Helmholtz layer and extends further out into the electrolyte at moderate ionic strength. The thickness of the double-layer scales with the Debye length (l_D) given by

$$l_D = \left(\frac{\varepsilon_r \varepsilon_0 k_B T}{2 n_i^0 z^2 e^2}\right)^{1/2} \quad (1.1)$$

where n_i^0 is the numerical concentration of ions i in the bulk solution, ε_r the dielectric constant, ε_0 the permittivity of vacuum, z the charge on the ion, e the electron charge, k_B the Boltzmann constant, and T the temperature in Kelvin. For a monovalent electrolyte like NaCl, z = 1 and for 0.1 mM solution the l_D is around 30 nm, and is 0.3 nm for 1 M solution as shown in Figure 1.11. This distance describes that the extent of the electric field surrounding the tethered DNA which is inhomogeneous and depends on the ionic strength of electrolyte. Even the charge density in the diffuse part of double-layer produces an inhomogeneous and intense electric field up to several kV cm^{-1}, the major potential In addition, Rant *et al.* [70] used the persistence length (l_0), which describes the stiffness of a molecule, to characterise the conformations of dsDNA and ssDNA and has been adapted to describe the polyelectrolyte models[71]. The persistence length (as shown in Figure 1.12 a)) is defined as the minimum length for which correlations in the direction of the

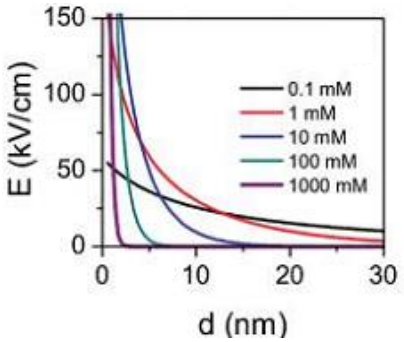

Figure 1.11 Adapted from Kaiser *et al.*[70] Electric field *E* in electrolyte solution plotted as a function of the distance *d* from a surface which is biased at 100 mV. Curves are calculated for solutions containing varied concentrations of monovalent salt. (Reprinted with permission from Ref [70]. Copyright© (2010) American Chemical Society)

tangent are lost, which means that the longer the persistence length, the stiffer the strand. For a chain molecule like an oligonucleotide, the persistence length reflects the flexibility of the ssDNA or dsDNA under common physiological conditions. The persistence length of dsDNA is accepted to be around 50 nm whereas for ssDNA it is only 2 to 3 nm where there is no electrostatic contribution from the ionic electrolyte. This pronounced difference is reflected in the conformation in an electric field. Following the concept of persistence length, Rant's group[70] applied the electrostatic persistence length (l_e) to explain the ionic strength effect on the conformation of ssDNA. The total persistence length l_p of a charged polymer can be written as

$$l_p = l_0 + l_e \tag{1.2}$$

where l_0 and l_e are the bare persistence length and electrostatic contributions to the polymer's total persistence length, respectively.

The electrostatic persistence length, l_e, was estimated based on a bead-spring model that assumes the polyelectrolyte, in this case the oligonucleotide, is composed of the beads with every bead linked by a spring as shown in Figure 1.12 b). Every bead has a negative charge, *e* and the monovalent cations in the solution shield the negative charge based on the Debye length l_D. The electrostatic persistence length, l_e, is given by

$$l_e = \frac{l_B}{4}\lambda^2 l_D^2 \tag{1.3}$$

where l_B , the Bjerrum length

$$l_B = \frac{e^2}{4\pi\varepsilon\varepsilon_0 k_B T} \tag{1.4}$$

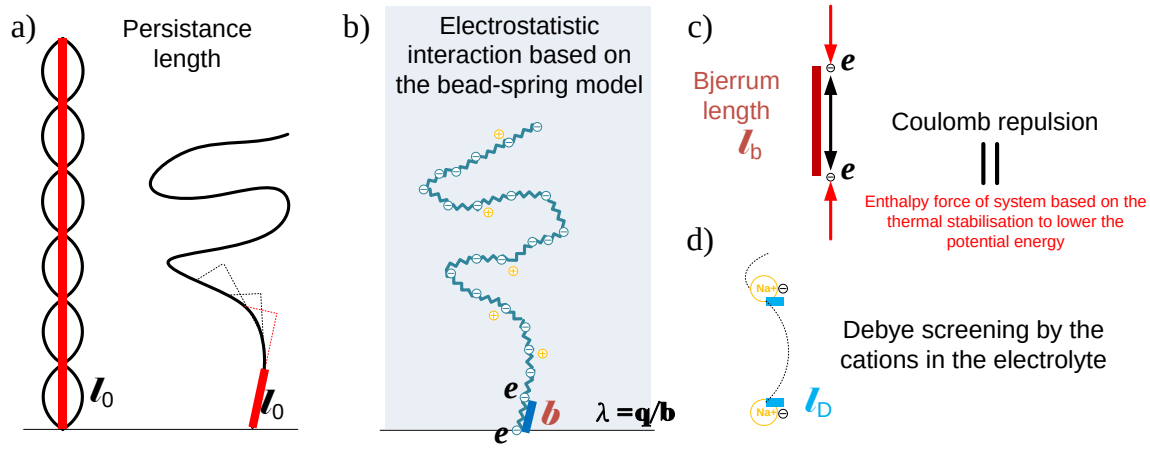

Figure 1.12 Schematic representations of the parameters related to the DNA conformation on the surface. a) The persistence length represents the minimum length of which correlations in the direction of the tangent are lost. b) The bead-spring model to describe the electrostatic interaction at the polyelectrolyte. Each bead has a negative charge, *e*, while separated by a spring unit length, *b*. The line charge density λ means the residual charge, *q,* after screening by the cations. The medium contains counter cations and the Debye screening effect depends on the concentration of cations (electrolyte). c) The Bjerrum length represents the balancing length between two interactions of Coulomb repulsion and thermal stabilisation in the system to lower the potential energy. d) A schematic demonstrates the charged beads of a polyelectrolyte model screened by the cations and the unscreened portion would sense the electrostatic interaction of electric double layer from the surface.

where *e* is the charge of both beads in the medium with dielectric constant ε and ε_0 that of the oligonucleotide. The Bjerrum length is the distance between two charges at which the Coulomb energy is equal to the thermal energy, k_BT. For the oligonucleotide in water at room temperature l_b is 0.7 nm. λ is the line charge density in C m^{-1} where is defined as the ratio of two charges, *q,* to their distance apart, *b*. l_D is the Debye screening length in nm mentioned above and shown in the Figure 1.12 b), c) and d). By estimating the overall contribution to the electrostatic factors above, they conclude that for ssDNA exposed to an electrical field, l_e is 34 nm in 1 mM NaCl. In the case of dsDNA, since the l_0 of dsDNA is 50 nm, which is much larger to l_e, the electrostatic contribution to the persistence length would become significant ($l_e > l_0$) only in solutions of very low salinity (Cs=10 mM), but the double helix is thermally unstable at this ionic strength so that double strands promptly dissociate into single strands. This dissociation mainly results from the collapse of the Watson-Crick pairing in a physiological condition when the ionic strength is around 10 mM and is enhanced at lower salinity due to the increase of the repulsion between the

phosphate backbones. Here equation (1.2) describes how the electrostatic affects the persistence length in ssDNA, but is unable to explain the dissociation directly. Rant finally concluded that the electrostatic effects dominated the oligonucleotide interaction at low to intermediate ionic buffer concentration. DNA was attracted to the positively charged surface and repelled from the surface under minor negative charge. The conformation of ssDNA is more sensitive at low to intermediate ionic strength and those negative charges of the phosphate backbone not screened by the cations would be attracted or repelled from the surface by the surface charge. The conclusions of their work are summarised in Figure 1.13.

In contrast to Rant's observation of the conformation of the oligonucleotide on the charged surface, Bartlett and co-workers[39] demonstrated the first electrochemical denaturation of dsDNA monitored with SERS. The major difference from Rant's work is that in Bartlett's work, three dithiolate hexaethylene glycol (HEG) anchors were used to attach the probe oligonucleotide to the surface and then to widen the potential window to a lower cathodic potential limit of ca. -1.2 V (vs. Ag/AgCl). Due to the major SERS response is enhanced based on the electromagnetic mechanism on the Raman tag on the vicinity of the surface, SERS provides an alternative perspective of the oligonucleotide conformation compared with the fluorescent tags used in Rant's works..

By using the electrochemical SERS-melting technique, Mahajan *et al*[39]. were able to discriminate the CFTR gene mutations of cystic fibrosis, a type of single nucleotide polymorphism (SNP). Corrigan *et al.*[40] further simultaneously screened the alleles of two short tandem repeats (STRs) used in forensics.

So far, the electrochemical SERS-melting technique has been demonstrated to discriminate the allele of STR or SNP. However, the mechanism of SERS-melting has not been studied intensively from the respect of fundamental research. Johnson *et al.*[31] investigated the mechanism and concluded that electrochemical melting was not due to a localised variation in pH at the electrode surface. This was done by co-adsorption of the p-mercaptobenzoic acid and

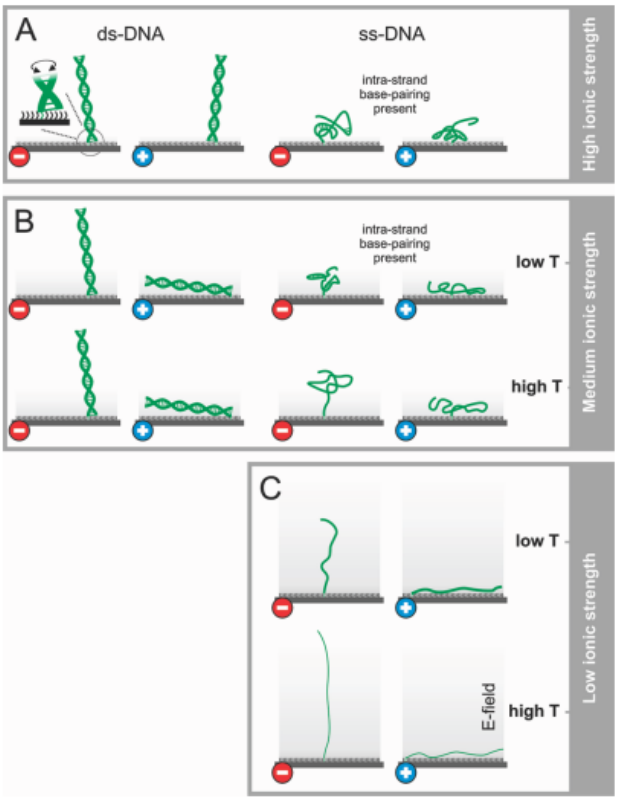

Figure 1.13 Adapted from Kaiser *et al.*[70] Schematic representation of the DNA conformation on negatively and positively charged surfaces in electrolytes of varying ionic strength. *T* represents the temperature which is low for *T* less than 16 ℃, intermediate *T* for 14 to 34 ℃, and high for above 49 ℃. The ionic strength was defined low at 1 mM (C) , medium for 10 to 100 mM (B), and high above 1 M (A). (Reprinted with permission from Ref. [70] Copyright© (2010) American Chemical Society)

using the SERS of the carboxyl group to reflect the protonation. This feature enables one to monitor the electrochemical melting and pH simultaneously. Johnson *et al.*[32] further showed that the electrochemical melting is not driven by the electrostatic repulsion by using a probe-target duplex composed of peptide nucleic acid (PNA) which has a neutral peptide backbone in place of the negatively charged phosphate backbone of DNA.

Even though distinct forms of electrochemical denaturation have been reported over 40 years since the first work in 1974, there is still not an explicit model to explain most of the

fundamentals. Consequently, more extensive studies are required to understand the mechanisms of electrochemical melting of dsDNA tethered at gold electrodes. This is the aim of this thesis and we focus on the investigation of the electrochemical melting using surface-enhanced Raman spectroscopy. Chapter 2 discusses the materials and methods in this work. Chapter 3 describes the primary observation of the SERS response of a beacon probe to potential perturbations including linear potential sweep and potential steps. Chapter 4 discusses the intrinsic surface enhanced Raman spectrum of bare Texas Red, rather than being attached to the 3' end of the beacon probe. The potential induced Raman intensity of Texas Red was compared both from the literature and experimental results. Chapter 5 follows the critical factors found in Chapter 4 to examine the influence of the excitation wavelength on the potential induced Raman intensity of Texas Red-labelled beacon probe. The passivation reagents and pH were selected to explore their influence on the Raman intensity of Texas Red-labelled beacon probe during the potential perturbation.

1.4 References

(1) Beck, J.*World J. Gastroenterol.* **2007**, *13*, 48.
(2) Koshy, R.; Koch, S.; Freytag von Loringhoven, A.; Kahmann, R.; Murray, K.; Hofschneider, P. H.*Cell* **1983**, *34*, 215.
(3) Sajantila, A.; Budowle, B.; Ström, M.; Johnsson, V.; Lukka, M.; Peltonen, L.; Ehnholm, C.*Am. J. Hum. Genet.* **1992**, *50*, 816.
(4) Comey, C. T.; Budowle, B.; Adams, D. E.; Baumstark, A. L.; Lindsey, J. A.; Presley, L. A.*J. Forensic Sci.* **1993**, *38*, 13402J.
(5) Sajantila, A.; Pacek, P.; Lukka, M.; Syvänen, A. C.; Nokelainen, P.; Sistonen, P.; Peltonen, L.; Budowle, B.*Forensic Sci Int* **1994**, *68*, 91.
(6) Saiki, R.; Scharf, S.; Faloona, F.; Mullis, K.; Horn, G.; Erlich, H.; Arnheim, N.Enzymatic amplification of beta-globin genomic sequences and restriction site analysis for diagnosis of sickle cell anemia. *Science (New York, N.Y.)*, 1985, *230*, 1350–1354.
(7) Eckert, K. A.; Kunkel, T. A.*Nucleic Acids Res.* **1990**, *18*, 3739.
(8) Chien, A.; Edgar, D. B.; Trela, J. M.*J. Bacteriol.* **1976**, *127*, 1550.
(9) Butler, J. M.; Shen, Y.; McCord, B. R.*J. Forensic Sci.* **2003**, *48*, 1054.
(10) Butler, J. M.*Fundamentals of Forensic DNA Typing*; Elsevier: San Diego, 2010.
(11) Tsukada, K.; Harayama, Y.; Kurasawa, Y.; Kasahara, K.*Forensic Sci. Int. Genet.* **2009**, *2*, 108.
(12) Lewin, B.*Genes IX*; 9th ed.; Jones and Bartlett Publishers: Sudbury, MA, 2008.
(13) Butler, J. M.*Advanced Topics in Forensic DNA Typing: Methology*; Elsevier: San Diego, CA, 2011.
(14) Budowle, B.; Moretti, T. R.; Baumstark, A. L.; Defenbaugh, D. A.; Keys, K. M.*J. Forensic Sci.* **1999**, *44*, 1277.
(15) Amigo, J.; Phillips, C.; Lareu, M.; Carracedo, Á .*Int. J. Leg. Med.* **2008**, *122*, 435.
(16) Chakraborty, R.; Stivers, D. N.; Su, B.; Zhong, Y. X.; Budowle, B.*Electrophoresis* **1999**, *20*, 1682.
(17) Madabhushi, R. S.*Electrophoresis* **1988**, *19*, 224.
(18) Lehninger, A. L.; Nielson, D. L.; Cox, M. M.*Lehninger Principles of Biochemistry*; 6th ed.; W.H.Freeman: New York, NY, 2012.
(19) Lin, X. M.; Cui, Y.; Xu, Y. H.; Ren, B.; Tian, Z. Q.*Anal. Bioanal. Chem.* **2009**, *394*, 1729.
(20) Bantz, K. C.; Meyer, A. F.; Wittenberg, N. J.; Im, H.; Kurtuluş, O.; Lee, S. H.; Lindquist, N. C.; Oh, S.-H.; Haynes, C. L.*Phys. Chem. Chem. Phys.* **2011**, *13*, 11551.
(21) Cialla, D.; März, A.; Böhme, R.; Theil, F.; Weber, K.; Schmitt, M.; Popp, J.*Anal. Bioanal. Chem.* **2012**, *403*, 27.
(22) Fan, M.; Andrade, G. F. S.; Brolo, A. G.*Anal. Chim. Acta* **2011**, *693*, 7.
(23) McNay, G.; Eustace, D.; Smith, W. E.; Faulds, K.; Graham, D.*Appl. Spectrosc.* **2011**, *65*, 825.
(24) Smith, W. E.*Chem. Soc. Rev.* **2008**, *37*, 955.
(25) Nie, S.*Science (80-.).* **1997**, *275*, 1102.
(26) Kneipp, K.; Wang, Y.; Kneipp, H.; Perelman, L. T.; Itzkan, I.; Dasari, R. R.; Feld, M. S.*Phys. Rev. Lett.* **1997**, *78*, 1667.
(27) Cintra, S.; Abdelsalam, M. E.; Bartlett, P. N.; Baumberg, J. J.; Kelf, T. A.; Sugawara, Y.; Russell, A. E.*Faraday Discuss.* **2006**, *132*, 191.
(28) Mahajan, S.; Baumberg, J. J.; Russell, A. E.; Bartlett, P. N.*Phys. Chem. Chem. Phys.* **2007**, *9*, 6016.
(29) Li, J. F.; Huang, Y. F.; Ding, Y.; Yang, Z. L.; Li, S. B.; Zhou, X. S.; Fan, F. R.; Zhang, W.; Zhou, Z. Y.; Wu, D. Y.; Ren, B.; Wang, Z. L.; Tian, Z. Q.*Nature* **2010**, *464*, 392.
(30) Faulds, K.; Smith, W. E.; Graham, D.*Analyst* **2005**, *130*, 1125.
(31) Qian, X.-M.; Nie, S. M.*Chem. Soc. Rev.* **2008**, *37*, 912.
(32) Vo-Dinh, T.; Wang, H. N.; Scaffidi, J.*J. Biophotonics* **2010**, *3*, 89.
(33) Schlücker, S.*Angew. Chemie - Int. Ed.* **2014**, *53*, 4756.
(34) Faulds, K.; Barbagallo, R. P.; Keer, J. T.; Smith, W. E.; Graham, D.*Analyst* **2004**, *129*, 567.

(35) Stokes, R. J.; Macaskill, A.; Johan Lundahl, P.; Ewen Smith, W.; Faulds, K.; Graham, D.*Small* **2007**, *3*, 1593.
(36) Faulds, K.; Mckenzie, F.; Smith, W. E.; Graham, D.**2007**, 1829.
(37) Cao, Y. C.; Jin, R.; Mirkin, C. a.*Science* **2002**, *297*, 1536.
(38) Pal, A.; Isola, N. R.; Alarie, J. P.; Stokes, D. L.; Vo-Dinh, T.*Faraday Discuss.* **2006**, *132*, 293.
(39) Mahajan, S.; Richardson, J.; Brown, T.; Bartlett, P. N.*J. Am. Chem. Soc.* **2008**, *130*, 15589.
(40) Corrigan, D. K.; Gale, N.; Brown, T.; Bartlett, P. N.*Angew. Chemie - Int. Ed.* **2010**, *49*, 5917.
(41) McCreery, R.*Raman Spectroscopy for Chemical Analysis*; John Wiley & Sons: New York, NY, 2000.
(42) Ferraro, J. R.; Nakamoto, K.; Brown, C. W.*Introductory Raman Spectroscopy*; 2nd ed.; Elsevier: San Diego, CA, 2003.
(43) Fleischmann.M.; Hendra, P. J.; McQuilla.A.J.*Chem. Phys. Lett.* **1974**, *26*, 163.
(44) Willets, K. A.; VanDuyne, R. P.*Annu. Rev. Phys. Chem.* **2007**, *58*, 267.
(45) Smith, E.*Modern Raman Spectroscopy*; Wiley: New York, NY, 2005.
(46) Jeanmaire, D. L.; VanDuyne, R. P.*J. Electroanal. Chem.* **1977**, *84*, 1.
(47) Wu, D. Y.; Hayashi, M.; Chang, C. H.; Liang, K. K.; Lin, S. H.*J. Chem. Phys.* **2003**, *118*, 4073.
(48) Wu, D. Y.; Hayashi, M.; Lin, S. H.; Tian, Z. Q.*Spectrochim. Acta - Part A Mol. Biomol. Spectrosc.* **2004**, *60*, 137.
(49) Wu, D. Y.; Li, J. F.; Ren, B.; Tian, Z. Q.*Chem. Soc. Rev.* **2008**, *37*, 1025.
(50) Lombardi, J. R.; Birke, R. L.; Lu, T.; Xu, J.*J. Chem. Phys.* **1986**, *84*, 4174.
(51) Lombardi, J. R.; Birke, R. L.*Acc. Chem. Res.* **2009**, *42*, 734.
(52) LeRu, E. C.; Etchegoin, P. G.*Principles of Surface-Enhanced Raman Spectroscopy and related plasmonic effects*; Elsevier: Amsterdam, The Netherlands, 2008.
(53) Sonnefraud, Y.; Leen Koh, A. L.; McComb, D. W.; Maier, S. A.*Laser Photonics Rev.* **2012**, *6*, 277.
(54) Kelf, T. A.; Sugawara, Y.; Cole, R. M.; Baumberg, J. J.; Abdelsalam, M. E.; Cintra, S.; Mahajan, S.; Russell, A. E.; Bartlett, P. N.*Phys. Rev. B - Condens. Matter Mater. Phys.* **2006**, *74*, 1.
(55) Barnes, W. L.; Dereux, A.; Ebbesen, T. W.*Nature* **2003**, *424*, 824.
(56) Mahajan, S.; Abdelsalam, M.; Suguwara, Y.; Cintra, S.; Russell, A.; Baumberg, J.; Bartlett, P.*Phys. Chem. Chem. Phys.* **2007**, *9*, 104.
(57) *The Mie Theory*; Hergert, W.; Wriedt, T., Eds.; Springer Series in Optical Sciences; Springer Berlin Heidelberg: Berlin, Heidelberg, 2012; Vol. 169.
(58) Krebs, J.*Lewin's Genes X*; Jones and Bartlett Publishers: Sudbury, MA, 2009.
(59) Bloomfield, V. A.; Crothers, D. M.; Tinoco, I.*Nucleic acids : structures, properties, and functions*; University Science Books: Sausalito, CA, 2000.
(60) Srinivasan, A. R.; Sauers, R. R.; Fenley, M. O.; Boschitsch, A. H.; Matsumoto, A.; Colasanti, A.V; Olson, W. K.*Biophys Rev* **2009**, 13.
(61) Tinoco, I.*J. Am. Chem. Soc.* **1960**, *82*, 4785.
(62) Tinoco, I.*J. Am. Chem. Soc.* **1961**, *5*, 6063.
(63) Parson, W. W.*Modern Optical Spectroscopy*; Springer-Verlag: Berlin, 2007.
(64) Wittwer, C. T.*Hum. Mutat.* **2009**, *30*, 857.
(65) R. Lahann, J.; Mitragotri, S.; Tran, T. N.; Kaido, H.; Sundaram, J.; Choi, I. S.; Hoffer, S.; Somorjai, G. A.; Langer, R.*Science* **2003**, *299*, 371.
(66) Paleček, E.*Electroanalysis* **2009**, *21*, 239.
(67) Sosnowski, R. G.; Tu, E.; Butler, W. F.; O'Connell, J. P.; Heller, M. J.*Proc. Natl. Acad. Sci. U. S. A.* **1997**, *94*, 1119.
(68) Kelley, S. O.; Barton, J. K.; Jackson, N. M.; McPherson, L. D.; Potter, A. B.; Spain, E. M.; Allen, M. J.; Hill, M. G.*Langmuir* **1998**, *14*, 6781.
(69) Wackerbarth, H.; Marie, R.; Grubb, M.; Zhang, J.; Hansen, A. G.; Chorkendorff, I.; Christensen, C. B.V; Boisen, A.; Ulstrup, J.*J. Solid State Electrochem.* **2004**, *8*, 474.
(70) Kaiser, W.; Rant, U.*J. Am. Chem. Soc.* **2010**, *132*, 7935.

(71) Dobrynin, A.V.; Rubinstein, M.*Prog. Polym. Sci.* **2005**, *30*, 1049.

Chapter 2 Experimental Methods and Materials

2.1. Fabrication of Sphere Segment Void (SSV) Substrates

2.1.1. Assembly of Polystyrene Nanospheres

The work employs sphere segment void (SSV) substrates as the SERS substrates. These were originally developed by Abdelsalam *et al.*[1] Sphere segment void (SSV) substrates with surface enhanced Raman scattering (SERS) acitivity were fabricated by the electrodeposition of gold through the close-packed polystyrene nanospheres.

All solvents and chemicals were of reagent quality and were used without further purification. All solutions were freshly prepared using reagent-grade water (18 MΩ cm) from a Whatman RO80 system coupled to a Whatman ‘‘Still Plus’’ system. Polystyrene nanospheres (Thermo Scientific) were supplied as a 1 wt % solution in water (certified mean diameter of 600 nm by the National Institute Standard Technology, USA).

Gold coated slides were prepared by evaporating 10 nm of chromium, followed by 200 nm of gold onto 1 mm thick glass microscope slides (760 mm to 260 mm in width and length) (VWR, USA). The chrome-gold coated slide was cut into 8 pieces (190 mm × 130 mm), and each was immersed in Piranha solution (H_2SO_4 / H_2O_2= 3/1) for 20 min. The slides were rinsed with plenty of deionized H_2O (2Putrite select water system) for 5 min. Due to the highly corrosive hazards of Piranha solution, the cleaning step had to be operated in the fume cupboard and safety spectacles and gloves must be worn.

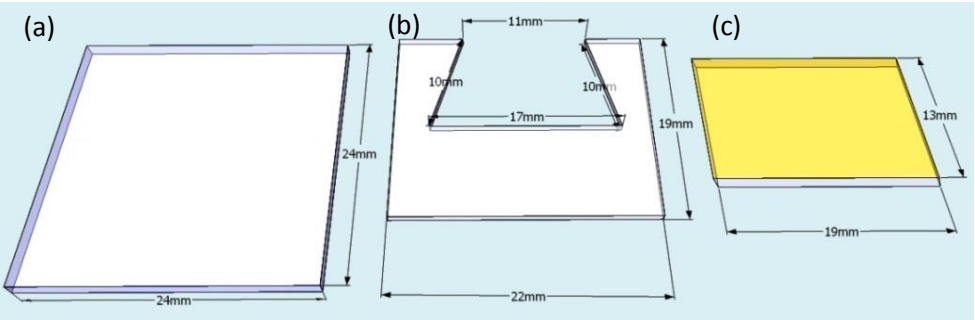

Figure 2.1 Dimensions and shapes of three components of the film-spaced cell. (a) Coverslip (b) Parafilm® (c) Chrome-gold coated slide.

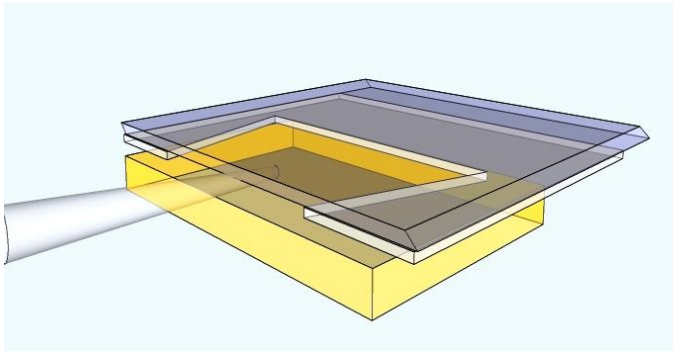

Figure 2.2 Illustration of the injection site of the colloidal solution. The cell was constructed with three components arranged from top to bottom: coverslip, Parafilm® and chrome-gold coated slide. The Parafilm seals the coverslip and the chrome-gold coated slide on heating to become translucent.

A film-spaced cell was made as shown in Figure 2.2. Parafilm® (Sigma-Aldrich, UK) was cut to a trapezoidal shape as shown in Figure 2.1. The trapezoidal shape assists the subsequent polystyrene particle assembles from the centre toward its corners[34]. The coverslip (24 mm × 24 mm, thickness 17 mm, Menzel, Germany) and Parafilm® spacer were put on the chrome-gold slide and placed on a heating stage at 60 ℃. The Parafilm® spacer softened and became translucent to seal the coverslip and the chrome-gold coated glass slide; it was then left to cool to room temperature. The thickness of Parafilm® spacer is estimated to be less than 100 micron. This thin gap enables the capillary force to assist the packing of the polystyrene nanoparticles. Polystyrene nanospheres (1 wt % solution in water, ThermoFisher Scientific, USA) were adjusted to 1.4 wt % by centrifuging at 600 rpm for 10 min and discarding the suspension liquid. The nanosphere solution was injected into the gap between the coverslip and chrome-gold coated slide as shown in Figure 2.2. The cell was tapped gently to spread the colloidal solution evenly and was incubated in the fridge at 14 ℃ for 36 h. Since the packing occurs at the boundary of the solution and the adjacent air, the evaporation of water in the colloidal solution, capillary, and gravitational forces drive the polystyrene particle packing from top down[2]. The evaporation rate relies on the saturated vapour pressure of water at the environmental temperature. Brownian motion is related to the viscosity, the temperature of the liquid, and the size of polystyrene particles. Lower temperature reduces the Brownian motion of the polystyrene particles and slows the evaporation. The cooperative conditions above result in the assembly of polystyrene particles in a hexagonal close packing monolayer on the gold substrate.

2.1.2. Electrodeposition

The coverslip was removed from the polystyrene-packed gold coated slide by mild heating a 55 ℃. Nail varnish (Rimmel, UK) was then used to cover the surface except for a 2 × 14 mm rectangular at the bottom of the template, where the spheres were well-packed and the connect area for the potentiostat connection.

Gold deposition on the polystyrene-packed gold coated slide was carried out at -0.73 V *vs.* SCE in 10 mL of cyanide-free gold plating solution (Metalor technology, ECF 60) containing 5 µl of brightener (Metalor technology, E 3) which increases the surface smoothness[3]. A platinum gauze (20 × 20 mm) was used as the counter electrode and a homemade saturated calomel electrode (SCE) as the reference electrode. The chronoamperometry was acquired on the potentiostat PGSTAT 320 (Metrohm Autolab, The Netherlands) in a typical three electrode configuration.

The Au deposition curve for a SSV structure on the polystyrene packed Au electrode is shown in Figure 2.4. The deposited thickness of the SSV structure was tuned by the charge (integrated current with time by the GPES software) as shown in Figure 2.3. The initial current decreased and rebounded for the formation of the electric double layer, followed by the nucleation of gold atoms on the surface within the first 5 to 10 s. The current reached a minimum at the half-height of the nanosphere diameter (0.5 *D*) due to the lowest surface area. The deposition charge was controlled to ca. 1.54 times the minimum current to achieve a 480 nm deposited thickness which has optimized SERS enhancement at 633 nm excitation according to Cintra *et al.*[4].

After deposition, the substrates were cleaned with copious amounts of water and then dried with nitrogen. The deposited SSV substrates were then immersed into dimethylformamide (DMF) to dissolve the polystyrene nanospheres for 3 h. The substrates are dried with nitrogen and used freshly for the following modification or measurement.

The geometric surface features recorded with scanning electron microscope (SEM) are shown in Figure 2.4 and illustrated in Figure 2.5. The top view (Figure 2.4 a)) reflects a partial imperfect packing on the left between the nanospheres possibly due to the uneven crystal edge or step edge on the Au film. The 52° tilted image in Figure 2.4 b) shows the triangular pillar and holes between the rim of each void, as reported by Cole *et al.*[5], which is related to the plasmon hybridization between the rim mode and cavity mode when the deposited thickness is increased to 0.54 *D*–0.8 *D*

and additional absorption bands around 550 to 680 nm observed in the reflectance spectrum (see the Figure 1.11). This results in SERS activity at 633 nm excitation as discussed in Section 1.2.

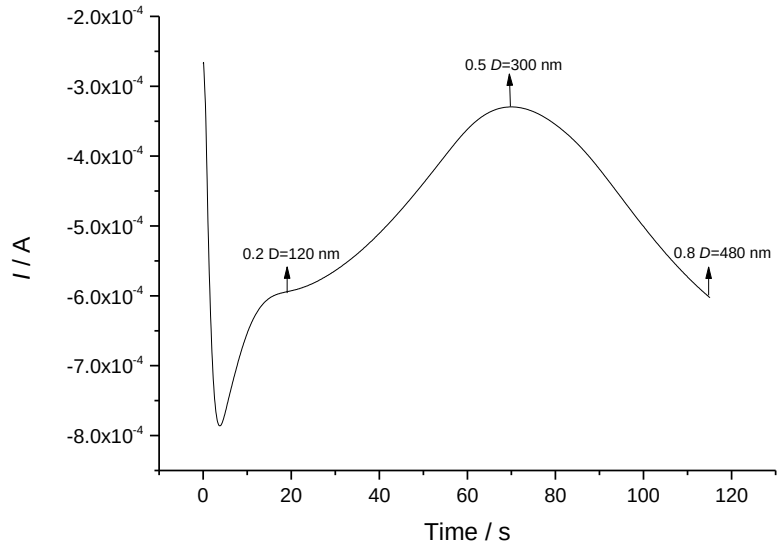

Figure 2.3 Deposition transition for 600 nm polystyrene sphere template packed on a gold substrate fabricated by the method described in Section 2.1.1. The Au deposition was performed on the potentiostat PGSTAT 320 (Metrohm Autolab, The Netherlands). The chronoamperometry was held at -0.73 V vs. SCE. *D* stands for the diameter of the nanosphere. Three varied thicknesses are depicted on the curve at 0.2 *D*, 0.5 *D* (minimum) and 0.8 *D* (end). The geometric area was ca. 0.21 cm^2.

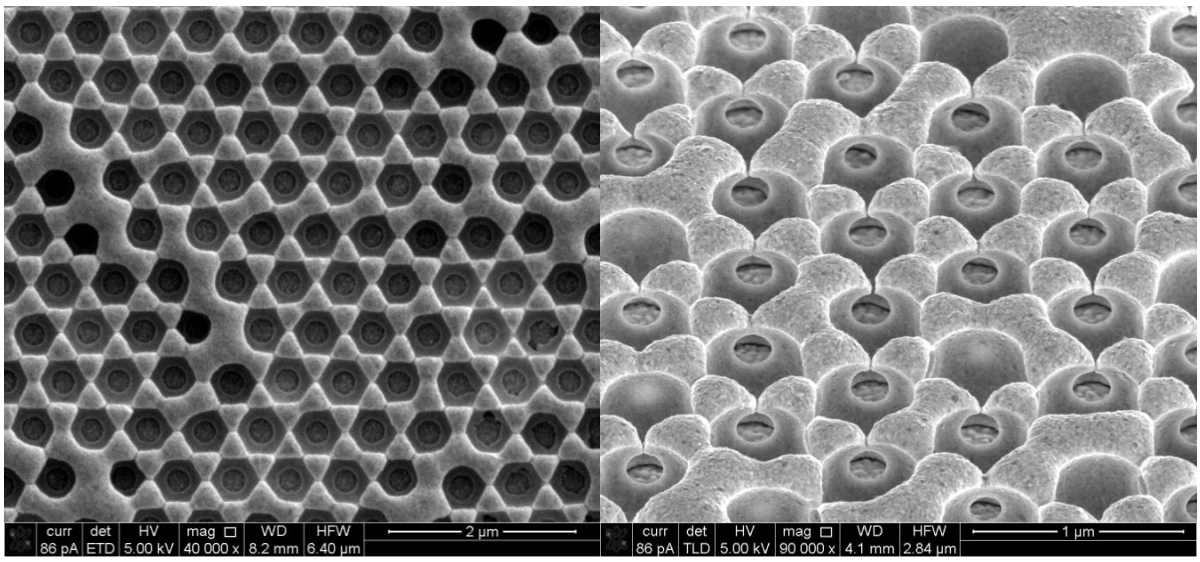

Figure 2.4 SEM images of the SSV substrate. The substrate was made following the protocol in Section 2.1.2 to deposit Au via control the charge to achieve a thickness of 480 nm. Left top-view, and right 52° tilting view. The top-view shows the hexagon-close packed array. The tilted image shows the pillars and the holes between the spherical voids.

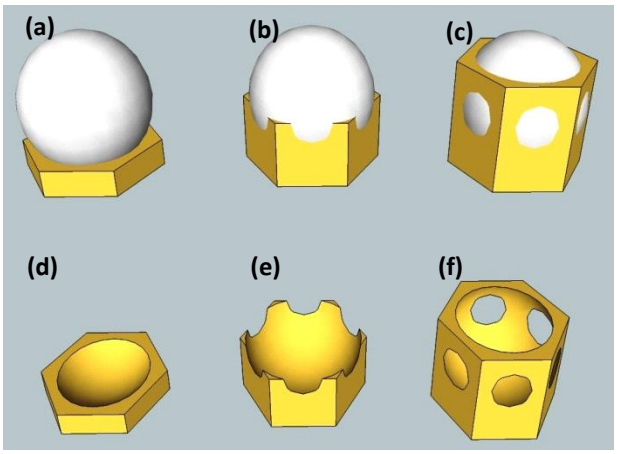

Figure 2.5 A schematic of growth of the deposit thickness through the nanosphere template using Sketchup (Google Inc, USA). The 3D unit cell is 600 nm as the diameter of the sphere and $300\sqrt{3}$ nm as the radius of the hexagon cylinder. The scale of the radius of the hexagon is based on the dimension measurement from Figure 2.4. The thickness varies from (a) 120 nm, (b) 300 nm, (c) 480 nm during the deposition progress. (d) (e) (f) shows the corresponding void after removal of the sphere by dissolving in dimethylformamide. (b) and (e) correlate to the minimum of the current in Figure 2.3 and (c) and (f) correspond to the end of the deposition.

The SSV surfaces fabricated in this these are all fabricated in 480 nm deposit thickness using 600 nm nanosphere template unless otherwise stated.

2.2. Probe Immobilization and Surface Coverage

2.2.1. Oligonucleotides and Immobilization

All the oligonucleotides in this study were synthesized by ATDBio (ATDBio, Southampton, UK). TH01 locus was selected from the short tandem repeat markers used in human individual identification and has the allele distribution from 3 to 14. TH01 stands for the first intron of human tyrosine hydroxylase. This locus, a short tandem repeat marker, possesses a tetranucleotide motif of AATG. One of the featured alleles is the 9.3 which is a microvariant allele composed of $[AATG]_6ATG[AATG]_3$ and has an extra deletion of adenine on the seventh repeat motif. The target sequence was chosen from the website of the National Center for Biotechnology Information (NCBI, USA).

The sequence and modification of the 35-mer TH01 probe is depicted in Table 2.1. It was modified on the 3' end of the oligonucleotide modified with Texas Red which was linked to the oligonucleotide via the 15-atom spacer, aminohexyl modification (C7) and N-hydroxysuccinimide (NHS) amide which was coupled by the reduction of primary amine with N-hydroxysuccinimide ester. Such a long spacer is necessary to avoid disturbing the hybridization when a relatively large molecule like Texas Red is linked to the DNA.

The 5' end oligonucleotide linker was composed of hexaethylene glycol (HEG) as spacers and three disulfide bridges. The three di-thiol groups formed six thiol-gold bonds on the Au surface and enhanced the strength of binding to the gold[6] at significant negative potentials, down to -1.3 V. The modification structure of the 5' linker and 3' reporter are shown in Figure 2.6.

The immobilisation of the beacon probe was carried out on the SSV chips immersed into the Texas Red-labelled beacon probe solution containing varied ionic strength electrolytes in the absence or

Table 2.1 Sequence and modification for the beacon probe. The TH01 sequence was adapted from the Entrez website of the National Center for Biotechnology Information (NCBI, USA) and was synthesised by ATDBio (Southampton, UK).

Sequence Label	Sequence	Length (bases)	Modifications
Beacon Probe	CGCGATCCCTGTTCCTCCCTTATTTCCCGATCGCG	35	3'-C7 amino-NHS-Texas Red, 5'-HEG spaced 3 disulfides

.

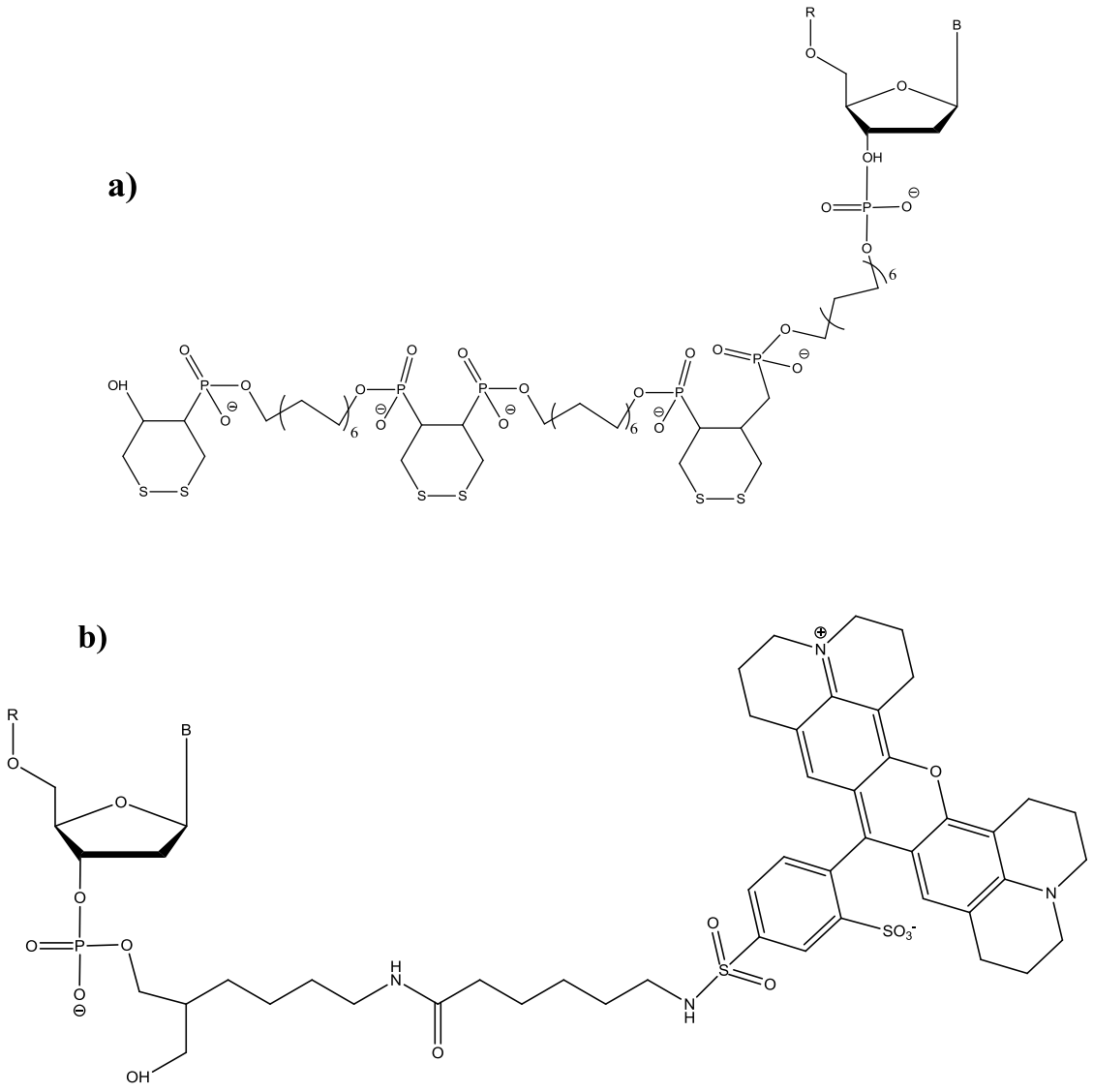

Figure 2.6 The synthesized Texas Red-labelled beacon probe for ATDBio (ATDBio, Southampton, UK). The structures contain (b) 3' end of oligonucleotide modified with Texas Red by the C7 amino linker coupled with NHS amide and (a) 5' end of oligonucleotide linking to the anchor group that contains hexamethylene glycol spacers and three disulfide bridges. B stands for the base moiety on the C1 position of the nucleotide.

presence of mercaptohexanol as described in the Section 3.2. To avoid intramolecular interaction between the DNA probes strands and the gold surface, mercaptohexanol was used to lower non-specific adsorption and hence lower the density of the beacon probe by co-adsorption on the gold surface to form a self-assembled monolayer (SAM)[7,8]. The surface density of the beacon probe can be tuned by the co-adsorption of mercaptohexanol or by changing the ionic strength. This is discussed in Sections 3.2 and 5.2.

2.2.2. Surface Coverage

The surface excess of the immobilized oligonucleotide was determined by using Steel's method[9]. Steel *et al.*[9] reported a DNA quantitation method based on the adsorption of cations to the negatively charged anionic phosphate of the oligonucleotide in low ionic strength electrolyte. These cations are readily exchanged with other cations[10,11]. When an electrode modified with DNA is placed in a low ionic strength electrolyte containing a multivalent redox cation, the redox cations exchange with the original monovalent cations (sodium ions in our preparation) and become electrostatically bound at the oligonucleotide. The amount of adsorbed cationic redox marker can then be measured by using chronocoulometry by serial addition of the redox markers to reach the equilibrium adsorption[12]. Crystal structure and STM data for the interaction of the ruthenium hexamine with DNA was reported to show that this metal complex adsorbed on DNA through electrostatic interactions by Ho *et al.*[13] and Grubb *et al.*[14] Details of the charge and correlated configurations are illustrated in Figure 2.7. The measured charge is the sum of the double layer charge, diffusive charge and absorbed charge. The charge for the double-layer, Q_{dl}, is measured in the absence of electroactive species. Diffusive charge (Q_{diff}) and absorbed charge (Q_{ads}) are obtained in the presence of redox indicators. For a gold electrode modified with immobilized oligonucleotides, the ruthenium hexamine cations associate electrostatically with the phosphate moieties of the nucleotides and also exist around the electrode surface where the charge transfer is possible. The ruthenium hexamine is reduced from the +3 to +2 form when the potential steps from 0.1 to -0.4 V. The reducing charge can be obtained by subtracting the charge for double-layer charging measured in the absence of ruthenium hexamine at 10 mM Tris buffer (pH 7.2).

The measured charge can be derived from the integrated Cottrell equation as

$$Q = \frac{2nFAD_0^{1/2}C_0^*}{\pi^{1/2}} t^{1/2} + Q_{dl} + nFA\,\Gamma_0 \qquad (2.1)$$

where n is the number of electrons per molecule for reduction, F the Faraday constant, A the electrode surface area (cm^2), D_o the diffusion coefficient (cm^2/s), C_0* the bulk concentration (mol/cm^3) of the redox marker, Q_{dl} the charge for the electric double-layer (Coulomb), and $nFA\,\Gamma_0$ the charge from the reduction of Γ_0 (mol/cm^2) of adsorbed redox marker. Here the redox marker is the ruthenium hexamine cation. The charge in the absence and presence of the redox indicator is shown in Figure 2.8. The expression for the transient charge is composed of three terms. The first

term on the right hand side is the diffusive charge Q_{diff} which is the integral of current *vs.* t from the Cottrell equation (2.2). This equation describes the current measured when the analyte diffuses to the electrode in a simple redox event[41].

$$i = \frac{nFAD_0^{1/2}C_0^*}{\pi^{1/2}} t^{-\frac{1}{2}} \tag{2.2}$$

The second term on the right hand side is Q_{dl}, the charge for the double-layer. The last term on the right hand side is the charge for the adsorbed species Q_{ads} which is $nFA\,\Gamma_0$. In the saturated state the adsorbed ruthenium hexamine provides complete charge compensation for the immobilized DNA. The saturated surface density of the probes is converted from the surface excess of redox indicators with the relationship,

$$\Gamma_{DNA} = \Gamma_0 \left(\frac{Z}{m}\right) N_A \tag{2.3}$$

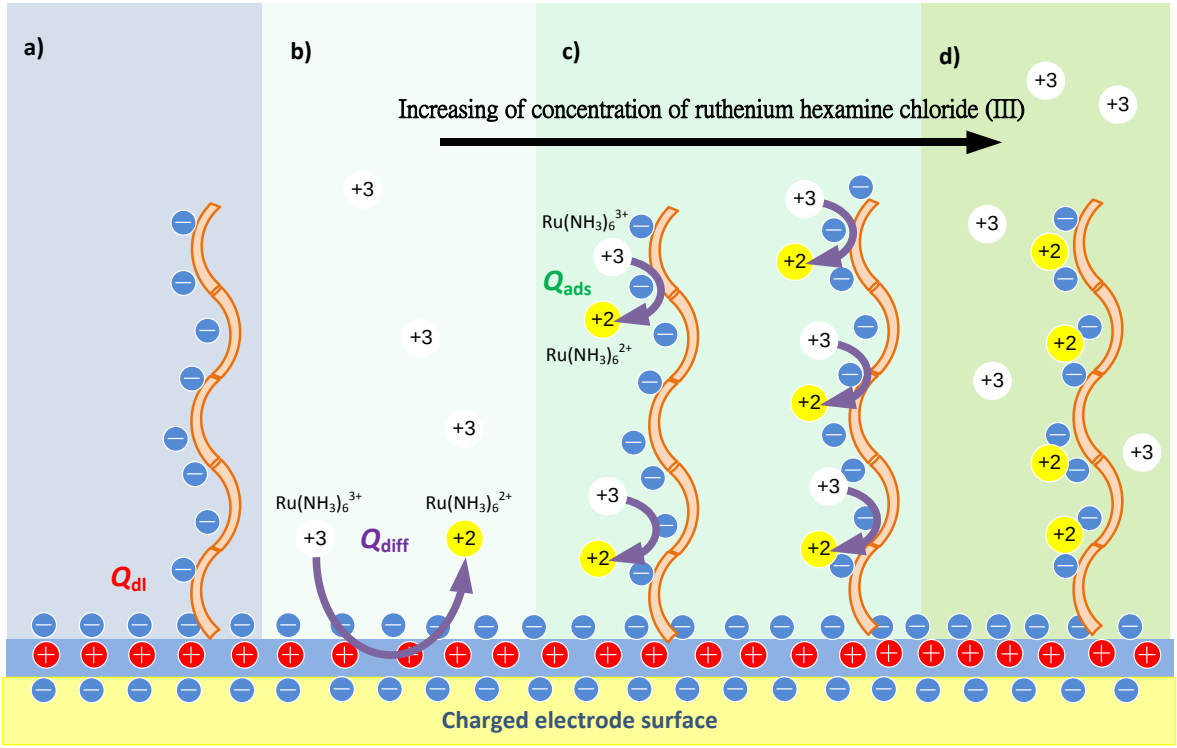

Figure 2.7 A Schematic of the charged surface modified with oligonucleotides in the absence and presence of the redox indicator. a) The charge comes merely from the electric double-layer in the absence of the redox indicators. The charge has two more components when the redox indicator is added into the electrolyte. b) The first charge reflects the diffusion of dissolved redox indicators toward the surface. c) The redox indicators adsorb electrostatically to the phosphate backbones. The measured charge is proportional to the concentration of redox indicator before reaching saturation. d) Saturation equilibrium is achieved with all the phosphate charges compensated by the reduced redox indicators.

where Γ_{DNA} is the probe surface density in molecules cm^{-2}, m is the number of bases in the probe DNA, z is the charge of the redox molecule, and N_A is Avogadro's number. The m value has to be corrected for the structure as the 5' end linker has six more phosphate moieties between the thiol anchors as shown in Figure 2.6 a). A typical charge vs. $t^{1/2}$ plot is shown in Figure 2.7. To derive the diffusion charge, Q_{diff}, a linear fitting is performed at the 0.2 to 0.5 s in $t^{1/2}$ where the linearity is good. The intercept of the fitting line at t=0 indicates the sum of Q_{ads} and Q_{dl}. Finally, Q_{ads} is obtained by subtracting the intercept with the charge of double-layer, Q_{dl}, measured from the absence of redox indicator.

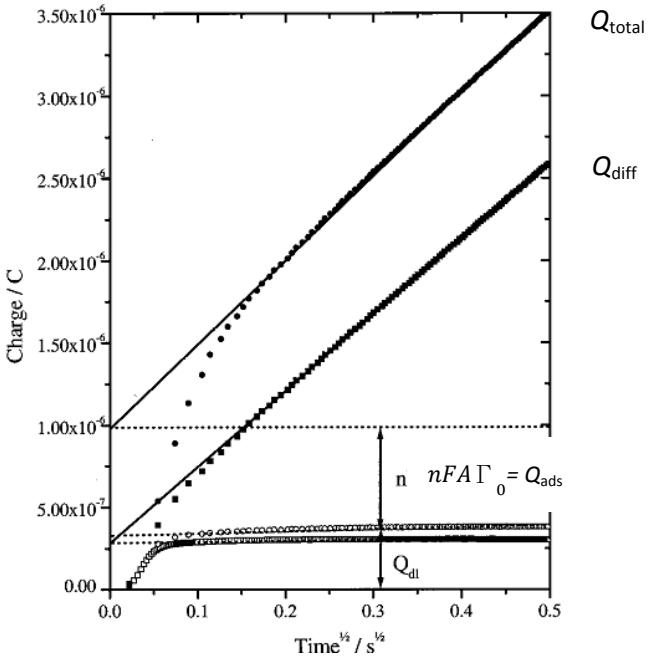

Figure 2.8 Chronocoulometry curve taken from Steel *et al.*[9] Chronocoulometric response curves for MCH (squares) and P1/MCH (circles, probe DNA passivated with mercaptohexanol) modified electrodes in the absence (open) and presence (closed) of 50 μM ruthenium hexamine. The total charge, Q_{total} is measured in the presence of redox indicators. The double-layer charge, Q_{dl}, is the integral of current in the absence of electroactive species. Based on equation (2.1), the adsorbent charge, Q_{ads}, may be derived from the intercept at t=0 of the linear fitting result from 0.2 to 0.5 in $t^{1/2}$ after subtracting the charge for the double-layer. (Reprinted with permission from Ref. [9]. Copyright© (1998) American Chemical Society.)

The step potentials are determined by cyclic voltammetry in Steel's work to ensure a complete reduction of ruthenium hexamine. A wider potential window is selected to perform the cyclic

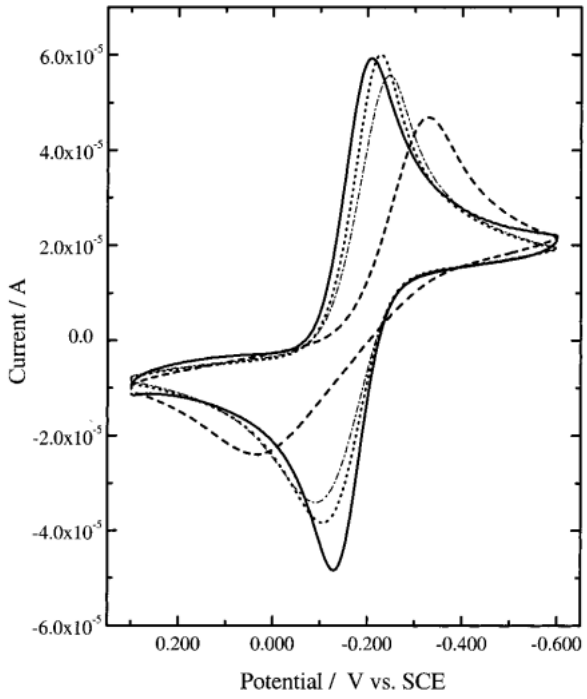

Figure 2.9 Voltammetric behavior of ruthenium hexaammine(3+ /2+) at DNA-modified electrodes. The data correspond to electrode modifications of MCE (solid line), MCH (dash line), P1/MCH (dot line),and oligonucleotide probe/MCH (dash - dot line). The concentration of ruthenium hexaammine was 1.8 mM in electrochemical buffer. The electrode area was 0.13 cm^2 , and the sweep rate was 100 mV/s. (Reprinted with permission from Ref. [9]. Copyright© (1998) American Chemical Society.)

voltammetry between 0.3 to -0.6 V at 100 mV s^{-1}. The cathodic peaks of the 1.8 mM ruthenium hexamine on the oligonucleotide-modified gold electrode appeared around -0.18 to -0.32 V and the anodic peaks at 0.4 to -0.12 V. -0.4 V are selected to provide a sufficiently negative potential to reduce all the ruthenium hexamine (+3) to (+2) as shown Figure 2.9. The anodic potential was set as 0.1 V to repel the electrostatically bound ions of ruthenium hexamine away from the probes in the low ionic strength electrolyte used (10 mM Tris base buffer (pH 7.4) with no sodium chloride addition).

A key step in Steel's method is the mercaptohexanol passivation which decreases the diffusion charge for the redox indicator reduction and the double layer charge on the bare Au surface. The SSV substrates used for the surface coverage measurement were passivated with 100 mM mercaptohexanol (Sigma-Aldrich) in the fume cupboard for 30 min after the oligonucleotide was immobilised. Mercaptohexanol forms a monolayer and lowers the interface capacitance. However mercaptohexanol treatment still allows ionic permeability, this reduces the potential perturbation of

double-layer and diffusive charge in the Cottrell equation, hence increases the reproducibility of measurements of absorbed charge.

The supporting electrolyte was purged with argon for 30 s to remove dissolved oxygen, then the electrolyte was covered by a continuous argon flow. The substrate was rinsed with 5 mM Tris buffer containing 10 mM NaCl (pH 7.4). 5 μM ruthenium hexamine chloride (Sigma-Aldrich) as the redox indicator was serially added into the 10 mM Tris buffer (pH 7.4). An extra 5 min deoxygenation was performed after each serial addition of redox indicator before the chronoamperometry measurement. The potential of the chronoamperometry steps to -0.4 V for 0.5 s after the conditioning potential at 0.1 V for 5 s. Finally the surface coverage of the immobilised oligonucleotide can be calculated from the measured charge based on equations (2.1) to (2.3).

2.3. Raman Measurement and Vibration Analysis

The Raman measurements were carried out on the Renishaw Raman System 2000 spectrometer (Renishaw, Gloucestershire, UK) with 1200 groove/mm grating and using a 632.8 nm Helium-Neon laser running at 50 mW, attenuated to produce 2.3 mW incident power on the specimen in 180° back scattering via a 50 × objective. The numerical aperture of the objective is 0.75. The grating was calibrated with a silicon wafer (111) at the peak of 520.6 cm^{-1}. Other conditions including the acquisition time or focusing parameter are given in the corresponding sections at the appropriate places. The Raman spectra were normalized in counts mW^{-1} s^{-1} unless otherwise indicated.

The Raman spectroelectrochemical cell used in this study, shown in Figure 2.10, was manufactured by Ventacon limited (Ventacon, Winchester, UK). The SSV chip was positioned in the centre sink adjacent to the homemade Ag/AgCl reference electrode. The Ag/AgCl reference electrode was made by anodising the 0.5 mm Ag wire in 1 M HCl for 30 min at 1 V vs. Pt wire and dried in the oven at 45 °C for 5 days.

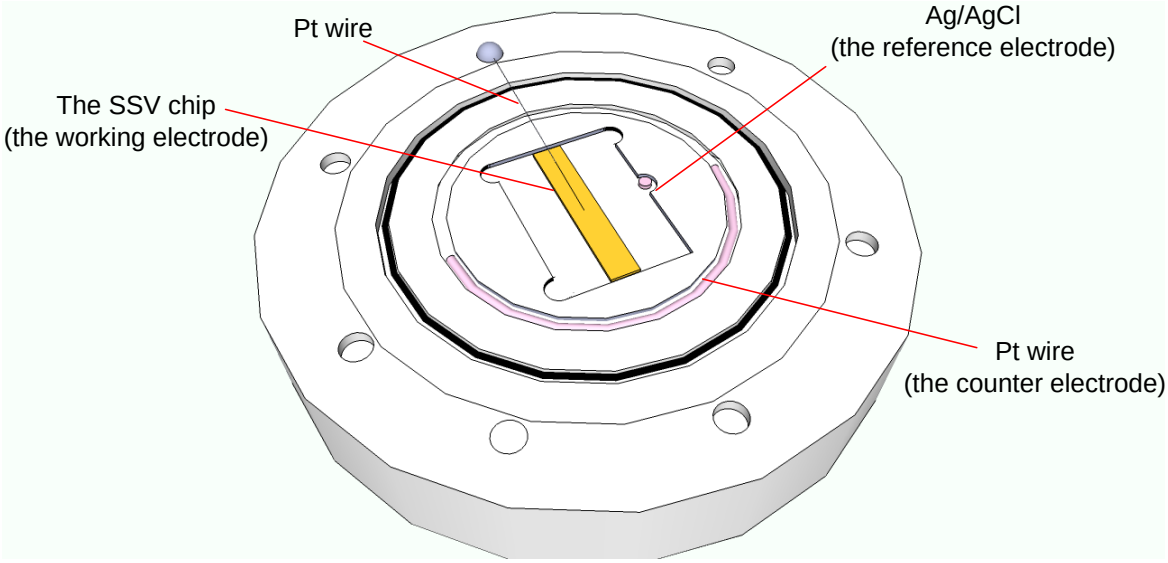

Figure 2.10 The Raman spectroelectrochemical cell (Ventacon Ltd, Winchester, UK) used in this study. The SSV chip was cut from the SSV substrate in ca. 2 × 12 mm and placed in the centre sink adjacent to the Ag/AgCl electrode. The semicircular Pt wire (2 mm) was used as the counter electrode while the Pt (0.5 mm) wire connected to the SSV chip as the working electrode. The volume of the cell is ca. 15 to 20 µL.

The Ag/AgCl electrode of the Raman spectroelectrochemical cell was further protected in a 1 % agarose gel containing saturated AgCl and KCl solution[15]. The reason to choose the saturated KCl as the surrounding electrolyte of Ag/AgCl electrode is to compare the conditions of reductive desorption of mercaptohexanol at significantly negative potential reported in the literature[16]. The gel cap worked as the miniaturized diaphragm to prevent mixing of the surrounding electrolyte (saturated KCl) of the Ag/AgCl electrode and the bulk supporting electrolyte used. This design provided a more stable potential control in Section 4.5.

Vibration analysis was performed by using the Gaussian 9. D01 (Gaussian Inc, Wallingford, USA)[17] on Iridis4, the supercomputing facility of the University of Southampton. The geometry optimisation of the molecules of interest has to be performed by the molecular orbital calculations to reach the minimum potential energy regarding the spacial ordinates. The same basis set, B3LYP, used in geometry optimization was also used for the vibration analysis. B3LYP (Becke three-parameter hybrid functional combined with Lee-Yang-Parr correlation functional) at 6-311++G(d,p) level contains polarisation functions on the C, N, O and S atoms[18,19]. The vibration modes of the molecule were then compared to the literature of the same molecule or similar molecules. Especially for the vibrational modes of the aromatic moiety, which is the core structure in the xanthene or cyanine dyes, can be compared with the Texas Red or Cy3 as a Raman label attached on the beacon probe. The Raman bands were assigned only for those the consistent results obtained from the calculation and the literature. For polyatomic molecules like Texas Red, each vibrational mode often contains more than one vibration, but the assignment indicates the major vibration which contributes the scattering intensity. Detailed commands of Gaussian can be referred to the user manual and the Ochterski's article [20,21].

2.4 References

(1) Abdelsalam, M. E.; Bartlett, P. N.; Baumberg, J. J.; Cintra, S.; Kelf, T. A.; Russell, A. E.*Electrochem. commun.* **2005**, *7*, 740–744.
(2) Dimitrov, A. S.; Nagayama, K.*Langmuir* **1996**, *12* (5), 1303–1311.
(3) Green, T. A.*Gold Bull.* **2007**, *40* (2), 105–114.
(4) Cintra, S.; Abdelsalam, M. E.; Bartlett, P. N.; Baumberg, J. J.; Kelf, T. A.; Sugawara, Y.; Russell, A. E.*Faraday Discuss.* **2006**, *132*, 191–199.
(5) Cole, R. M.; Baumberg, J. J.; DeGarcia Abajo, F. J.; Mahajan, S.; Abdelsalam, M.; Bartlett, P. N.*Nano Lett.* **2007**, *7*, 2094–2100.
(6) Lee, H.; Scherer, N. F.; Messersmith, P. B.*Proc. Natl. Acad. Sci. U. S. A.* **2006**, *103* (17), 12999–13003.
(7) Keighley, S. D.; Li, P.; Estrela, P.; Migliorato, P.*Biosens. Bioelectron.* **2008**, *23*, 1291–1297.
(8) Herne, T. M.; Tarlov, M. J.*J. Am. Chem. Soc.* **1997**, *119* (13), 8916–8920.
(9) Steel, A. B.; Herne, T. M.; Tarlov, M. J.*Anal. Chem.* **1998**, *70* (22), 4670–4677.
(10) Lipfert, J.; Doniach, S.; Das, R.; Herschlag, D.*Annu. Rev. Biochem.* **2014**, *83*, 813–841.
(11) McFail-Isom, L.; Sines, C. C.; Williams, L. D.*Curr. Opin. Struct. Biol.* **1999**, *9* (3), 298–304.
(12) Bard, A. J.; Faulkner, L. R.*Electrochemical methods : fundamentals and applications*, 2nd ed.; Wiley: New York, NY, 2001.
(13) Ho, P. S.; Frederick, C. A.; Saal, D.; Wang, A. H. J.; Rich, A.*J. Biomol. Struct. Dyn.* **1987**, *4* (4), 521–534.
(14) Grubb, M.; Wackerbarth, H.; Wengel, J.; Ulstrup, J.*Langmuir* **2007**, *23* (3), 1410–1413.
(15) Thomas, J. M.*J. Chem. Educ.* **1999**, *76* (1), 97.
(16) Widrig, C. A.; Chung, C.; Porter, M. D.*J. Electroanal. Chem. Interfacial Electrochem.* **1991**, *310* (1–2), 335–359.
(17) Frisch, M. J.; Trucks, G. W.; Schlegel, H. B.; Scuseria, G. E.; Robb, M. A.; Cheeseman, J. R.; Scalmani, G.; Barone, V.; Petersson, G. A.; Nakatsuji, H.; Li, X.; Caricato, M.; Marenich, A.; Bloino, J.; Janesko, B. G.; Gomperts, R.; Mennucci, B.; Hratchian, H. P.; Ort, J.V.; Fox, D. J.Gaussian, Inc.: Wallingford CT 2016.
(18) Wu, D.; Duan, S.; Ren, B.; Tian, Z.*J. Raman Spectrosc.* **2005**, *36* (6–7), 533–540.
(19) Wu, D. Y.; Hayashi, M.; Chang, C. H.; Liang, K. K.; Lin, S. H.*J. Chem. Phys.* **2003**, *118* (9), 4073–4085.
(20) *Gaussian 09 IOps Reference*, 2nd ed.; Caricato, M., Frisch, Æ ., Hiscocks, J., Frisch, M. J., Eds.; Gaussian, Inc.: Wallingford, CT, U.S.A.
(21) Ochterski, J. W.; Ph, D.Vibrational Analysis in Gaussian http://gaussian.com/vib/.

Chapter 3 Observation of the Beacon Probe on the Charged Au Surface

3.1 The Thermodynamics of the Beacon Probes

In the present work, a molecular beacon (MB) has been used for the first time to probe the fundamental changes of the oligonucleotide conformation under potential sweeping. A molecular beacon, shown in Figure 3.1, is a single-stranded oligonucleotide with partial pairing at the two terminals. Due to this self-complementary feature, the molecular beacon has a loop-stem structure in its folded state. The hybridization with the complementary target fragment at the loop region causes the beacon probe to unfold and reform as double stranded DNA, as shown in Figure 3.1. Using a molecular beacon has the advantage of flexible modification on its loop region and hence increases the specificity of DNA hybridization. When the receptor molecule which has absorption

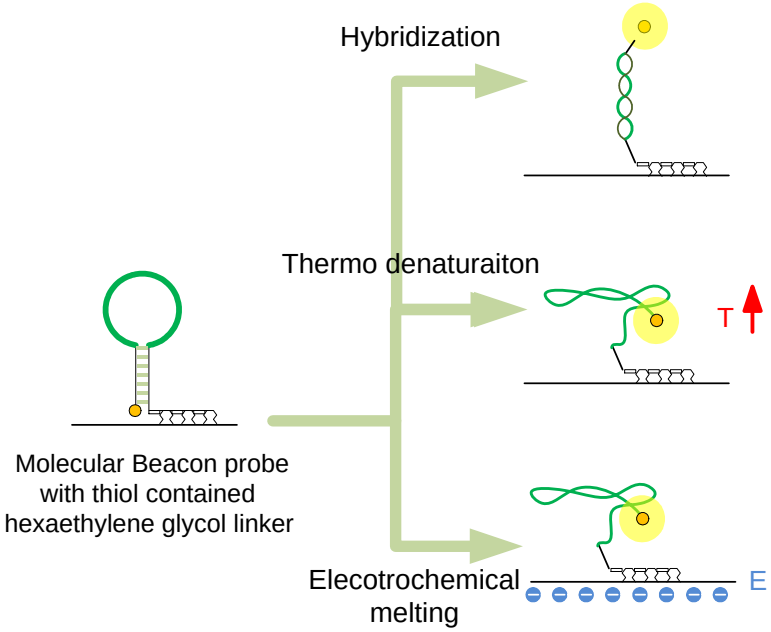

Figure 3.1 A schematic of a molecular beacon opening and folding in the distinct states. Hybridization with a complementary strand causes the beacon to unfold. The thermal denaturation occurs when the temperature is higher than its melting temperature. The negatively charged surface may induce the dissociation of the stem section of the immobilized beacon probe. The mushroom like conformation reflects the flexible and possible intermolecular pairing in the single stranded oligonucleotide.

spectrum partially overlapped to the emission spectrum of the donor molecule at the corresponding excitation, the distance between the two molecules determine that the overall fluorescence is quenched or emitted. The donor and acceptor molecules are used to be attached to the two ends of the beacon probe individually, the conformation change of beacon probe would results in an quenching of fluorescence (based on the Föster resonance energy transfer) in the folded state and re-emission in the open state. This 'off-on' characterisation makes the probe report a "beacon" like signal when hybridised to the complementary DNA strand, and thus in the open state. Hence the name "molecular beacon". Molecular beacon have received widespread application, not only being used in analytical assays like real-time PCR, but also in fundamental studies of the folding mechanics of oligonucleotides[44].

TH01 as a STR locus was used in this work given its moderate distribution of alleles from 3 to 14. The nomenclature of TH01 means: in the first intron of the human tyrosine hydroxylase gene. The chromosome position of TH01 is 11p15.5 which is located at the short arm of chromosome 11, 15.5 was numbered by the Geimsa staining method[1]. The tetranucleotide repeat motif of TH01 is AATG. Sometimes HUM- is included at the prefix to indicate the locus is from a human genome.

The pairing sequences of the TH01 5' flanking region were designed in the loop region. The stem part has 6 GC-rich and 1 AT pairing oligonucleotides on each end to form a stable loop-stem structure. The thermodynamic prediction of the secondary structure was done with the mfold program developed by Zuker *et al.*[2] The resultant structure is shown in Figure 3.2. The annotation numbers of

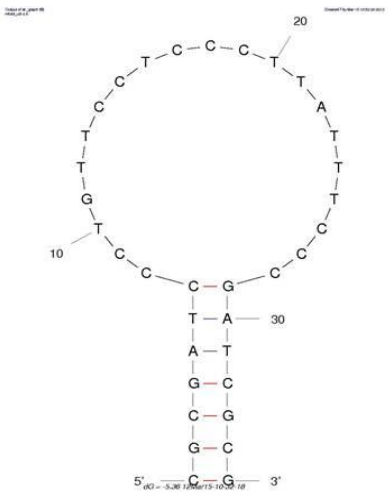

Figure 3.2 Secondary structure prediction result of the beacon probe based on mfold simulation[2] with the DNA sequences in Table 2.1 for the TH01 loci at the 20℃, 1M NaCl.

Table 3.1 Thermodynamic calculation results of free energy from structure at 20 ℃ with the DNA sequences in Table 2.1 for the TH01 loci in 1 M NaCl. The position of the nucleotide was labelled as the base and number at the subscript started from the 5' end of the oligonucleotide. The major structure of beacon probe is in bold font. The free energy was obtained from the mfold program reported by Zuker *et al.*[2]

Structural element	ΔG kcal mol^{-1}	Position Description
External loop	0.00	0 ss bases & 1 closing helices.
Stack	-2.63	External closing pair is C_1-G_{35}
Stack	-2.65	External closing pair is G_2-C_{34}
Stack	-2.63	External closing pair is C_3-G_{33}
Stack	-1.68	External closing pair is G_4-C_{32}
Stack	-1.23	External closing pair is A_5-T_{31}
Stack	-1.68	External closing pair is T_6-A_{30}
Helix	**-12.50**	**Stacking summation of the 7 base pairs**
Hairpin loop	**4.36**	**Closing pair is C_7-G_{29}**
Total	**-8.14**	**Summation of the Gibbs energy of the helix and hairpin loop.**

the base group in Table 3.1 represents the sequential number starting from the 5' end of the oligonucleotide. The total length comprises 35 oligonucleotides (35-mer) and the GC-rich region is on the 7-mer stem. The thermodynamics of the folded molecular beacon were calculated at 20 ℃ and 1 M ionic strength. The resultant ΔG = -8.14 kcal mol^{-1} and the melting temperature were calculated as 69.8 ℃.

The method used in the mfold program for dimers or single-stranded, folded monomers is based on a two-state model. The two states are the non-hybridized, 'random coil state' and the hybridized 'stem-loop state'. The free energy, enthalpy and entropy changes associated with the transition from 'hybridized at temperature *T*' to random coil are denoted by ΔG, ΔH, and ΔS. Both ΔG and ΔH are computed using published nearest neighbour coefficients[3]. For DNA, the mfold server uses the unified parameters of SantaLucia's work[3]. SantaLucia derived the unified nearest-neighbour

parameters from seven studies with the 108 oligonucleotide duplex. The result showed that six of the studies are actually in remarkable agreement with one another. For a beacon probe in its folded state, the Gibbs free energy at 37 ℃ is given as

$$\Delta G^{o}_{37} = \Delta G^{o}_{37\ \text{nearest-neighbor pairs}} + \Delta G^{o}_{37\ \text{initiation}} + \Delta G^{o}_{37\ \text{first mismatch}} + \Delta G^{o}_{37\ \text{symmetry}} \quad (3.1)$$

The first term in equation (3.1) is the energy of the nearest-neighbour pairs. The nearest-neighbour is defined as the adjacent Watson-Crick pairs of oligonucleotides which are made of 4 oligonucleotides. These stacking pairs are denoted as NN/NN where N is the oligonucleotide (it may be A, T, C or G), the left portion of the slash is expressed in 5' to 3' and the right is the paired dinucleotide in the opposite direction. In the case of Table 2.1, 5'-CGCGATC-3' is the stem sequence that forms the helix with Watson-Crick pairing shown in Figure 3.3. The 6 nearest-neighbour pairs are noted as CG/CG, GC/GC, CG/CG, GA/TC, AT/AT and TC/GA in Figure 3.3. The individual $\Delta G_{37}{}^{0}$ are shown in Table 3.2.

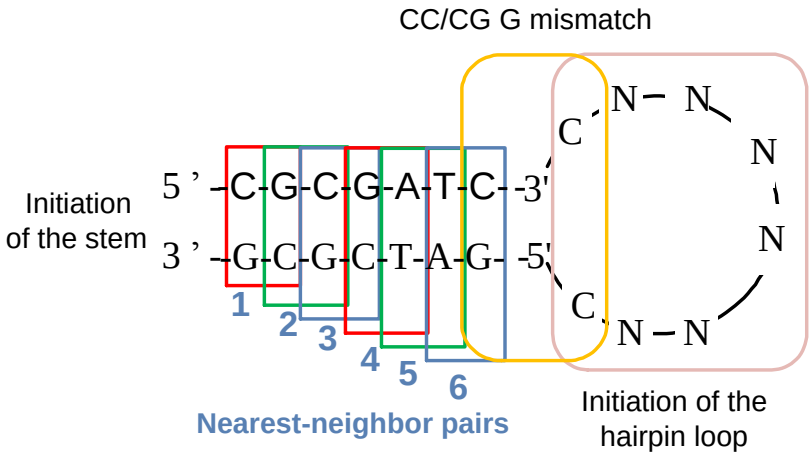

Figure 3.3 The thermodynamic elements for the hairpin probe. The elements contain nearest-neighbour pairs, initiation of the hairpin loop and the symmetry correction for self-complementary. The nearest-neighbour pairs are selected from the first Watson-Crick pairs at the start of the 5'strand, CG in this case, and the nearest-neighbour is GC (in the first red square on the left). CG/GC forms the first nearest-neighbour pair. The following 5 pairs can be selected by this rule. The extra initiation free energy is required to fold from both sides of the hairpin and the stem duplex. Finally, the energy increment of the C-C mismatch at the junction of the stem and the hairpin loop accounts for the nearest-neighbour pair CC/CG.

Table 3.2 Nearest-neighbor thermodynamic parameters for DNA Watson-Crick pairs in 1M NaCl at 37 ℃. Adapted from SantaLucia[3]. *The linear independent parameters of C-C mismatch formation in 1 M NaCl, pH 7 is adapted from Peyret *et al.*[4]

Propagation sequence		ΔH^0	ΔS^0	$\Delta G_{37}{}^0$
5'-3'/3'-5'	Equivalent 5'-3'/3'-5'	/ kcal/ mol	/enthalpy unit	/ kcal/ mol
AA/TT	TT/AA	-7.6	-21.3	-1.00
AT/TA		-7.2	-20.4	-0.88
TA/TA		-7.2	-21.3	-0.58
CA/GT	TG/AC	-8.5	-22.7	-1.45
GT/CA	AC/TG	-8.4	-22.4	-1.44
CT/GA	AG/TC	-7.8	-21.0	-1.28
GA/CT	TC/AG	-8.2	-22.2	-1.30
CG/GC	CG/GC	-10.6	-27.2	-2.17
GC/CG		-9.8	-24.4	-2.24
GG/CC		-8.0	-19.9	-1.84
Initiation		+0.2	-5.7	+1.96
C<u>C</u>/<u>C</u>G mismatch*		-1.5	-7.09	0.7

There are three other parameters then needed to be considered as depicted in Figure 3.3. The first is an initiation free energy[2], $\Delta G^{o}_{37\ \text{initiation}}$, this is required to account for the paired duplex. In the stem-loop conformation, one initiation is for the stem duplex side and the other one for the folded loop side. This is 1.96 kcal/ mol for each side at 37 ℃. The second parameter is the C-C mismatch at the junction between the stem and the hairpin. The energy increments of each nearest-neighbour pair shown in Table 3.2 are then calculated at 20 ℃ from the equation, $\Delta G = \Delta H - T\Delta S$. The difference for each of the stem elements is calculated as $T\ \Delta$S. Note the T is the absolute temperature (Kelvin) scale. The first nearest-neighbour pair, CG/CG, the ΔG^{o}_{37} calculated from Table 3.2 is -2.17 kcal/ mol. The $\Delta G^{o}_{20\ \text{nearest-neighbor pairs}}$ is given from $\Delta G^{o}_{37\ \text{nearest-neighbor pairs}} - T\Delta S$= -2.63 kcal/ mol which is consistent with the resultant Table 3.1. Similar mismatches in A-A, T-T, G-G have been studied extensively[4]. Here the mfold program adopts the resultant value of the energy increment in C<u>C</u>/<u>C</u>G mismatch as 0.7 kcal/ mol at 37 ℃ based on Peyret *et al.*[4] Finally, the corrections for the temperature at 20 ℃ give $\Delta G^{o}_{20\ \text{initiation}}$= 3.78 kcal/ mol and 0.59 kcal/ mol for $\Delta G^{o}_{20\ \text{first mismatch}}$.

The final parameter is the symmetry Gibbs free energy[5], $\Delta G_{\text{symmetry}}$, which accounts for the C_2 symmetry correction for the palindrome duplex, this is 0.43 kcal/ mol. In ordinary double-helical DNA, there is a pseudo C_2 axis, as depicted in Figure 3.4 a), since it applies to the phosphate backbones but not to the bases themselves. However, for DNA sequences containing a self-complementary strand, there is a true C_2 symmetry axis perpendicular to the helix axis as in Figure

3.4 b). The symmetry correction accounts for the decrease in order when a duplex with end-to-end symmetry is changed into two single strands that do not individually have end-to-end symmetry. Although all of the beacon probes have self-complementary ssDNA, not all of the sequences of stem duplex are palindromic. In the case of the beacon probe here, the symmetry correction is not necessary and as a result, no symmetry penalty is applied here.

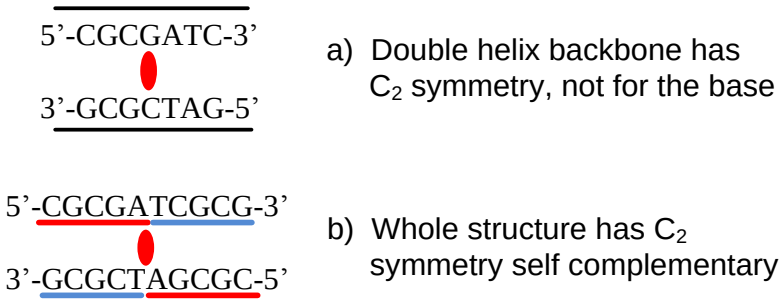

Figure 3.4 Symmetry and pseudosymmetry in DNA double helices. The base pairs and their attached backbone residues can be flipped by a 180° rotation around an axis through the plane of the bases and perpendicular to the helix axis (shown as a filled lens-shaped object). For a non-palindromic duplex in a), only the phosphate backbone has symmetry to the C_2 axis. By contrast, the palindrome duplex contains two identical parts toward the symmetry axis, in agreement with the C_2 symmetry.

The resultant ΔG^{o}_{20} for the beacon probe is the summation of the unified nearest-neighbour parameters as shown in equation (3.2).

$$\Delta G^{o}_{20} = \Delta G^{o}_{20\ \text{nearest-neighbor pairs}} + \Delta G^{o}_{20\ \text{initiation}} + \Delta G^{o}_{20\ \text{first mismatch}} + \Delta G^{o}_{20\ \text{symmetry}} \quad (3.2)$$

$$= [(-2.63) + (-2.65) + (-2.63) + (-1.68) + (-1.23) + (-1.68)]$$

$$+ \Delta G^{o}_{20\ \text{initiation}} + \Delta G^{o}_{20\ \text{first mismatch}} + \Delta G^{o}_{20\ \text{symmetry}}$$

$$= (-12.50) + (2 \times 1.89) + (0.59) + (0)$$

$$= (-12.50) + (4.36)$$

$$= -8.14 \text{ kcal/ mol}$$

The ΔG of the loop element is 4.36 kcal·mol^{-1} and the ΔG of the stem element is -12.50 kcal·mol^{-1}. Then the combined loop and stem helix structures produce the predicted summation of ΔG for the two elements giving ΔG=-8.14 kcal/ mol.

3.2 Surface Coverage of the Oligonucleotide on the Gold Electrode

Surface coverage represents the number of molecules adsorbed on per unit of the surface area. For the immobilized oligonucleotide, high surface coverage may reduce the hybridization efficiency to the target fragment due to the crowding effect. On the other hand, low surface coverage increases the hybridization efficiency but also reduce the overall signal. Consequently, choice of an appropriate surface coverage is a balance between the detection limit and the hybridization efficiency. The surface coverage of the immobilized oligonucleotides on Au electrode can be estimated by Steel's method as discussed in Section 2.2.2. Based on the charge measured from the chronoamperometry, the adsorption charge can be obtained by subtracting the double layer charge in the absence of redox mediator and the diffusion charge in the presence of redox mediator. The adsorption charge is then interpreted as proportional to the immobilized oligonucleotide coverage. In the case of the linear strand probes reported by Mahajan *et al.*[6], the surface density on average is 1.6×10^{12} molecules cm^{-2} from 1 μM single-stranded oligonucleotides as the immobilization solution. The corresponding average distance between the individual probes is 8.5 nm.

To estimate the distance between the individual probes, the packing form of the DNA probes has to be determined first. Based on the evaluations of the potential energy with molecular dynamics techniques, the hexagonal packing lattice showed the lowest potential energy in both ssDNA and dsDNA on the Au(111) surface[7–9]. Hexagonal close packing is chosen to estimate the distance between the probes. A unit cell of the hexagon is depicted in Figure 3.5 a). The dependence of the surface density (Γ_{DNA}) to the radius (R) of the hexagonal close packing is calculated in equation (3.3). The probes density (Γ_{DNA}) equals to per unit 1 cm^2 area occupied by the number of the area of the hexagon unit cell of a probe ($6R^2/\sqrt{3}$). The area of hexagon unit cell is composed of 6 triangles, and the area of each triangle is $R^2/\sqrt{3}$. Combination of the three relations gives the following equation

$$\Gamma_{DNA}=1/(6R^2/\sqrt{3}) \tag{3.3}$$

$$R=\sqrt{\frac{\sqrt{3}}{6\Gamma_{DNA}}} \tag{3.4}$$

The correlation plot is shown in Figure 3.5 c). The corresponding length of the DNA is further shown in Figure 3.5 d) and the 1.3 nm linker at the 5' end of beacon probe shown in Figure 2.6 a) is subtracted to show the relevance of the surface coverage.

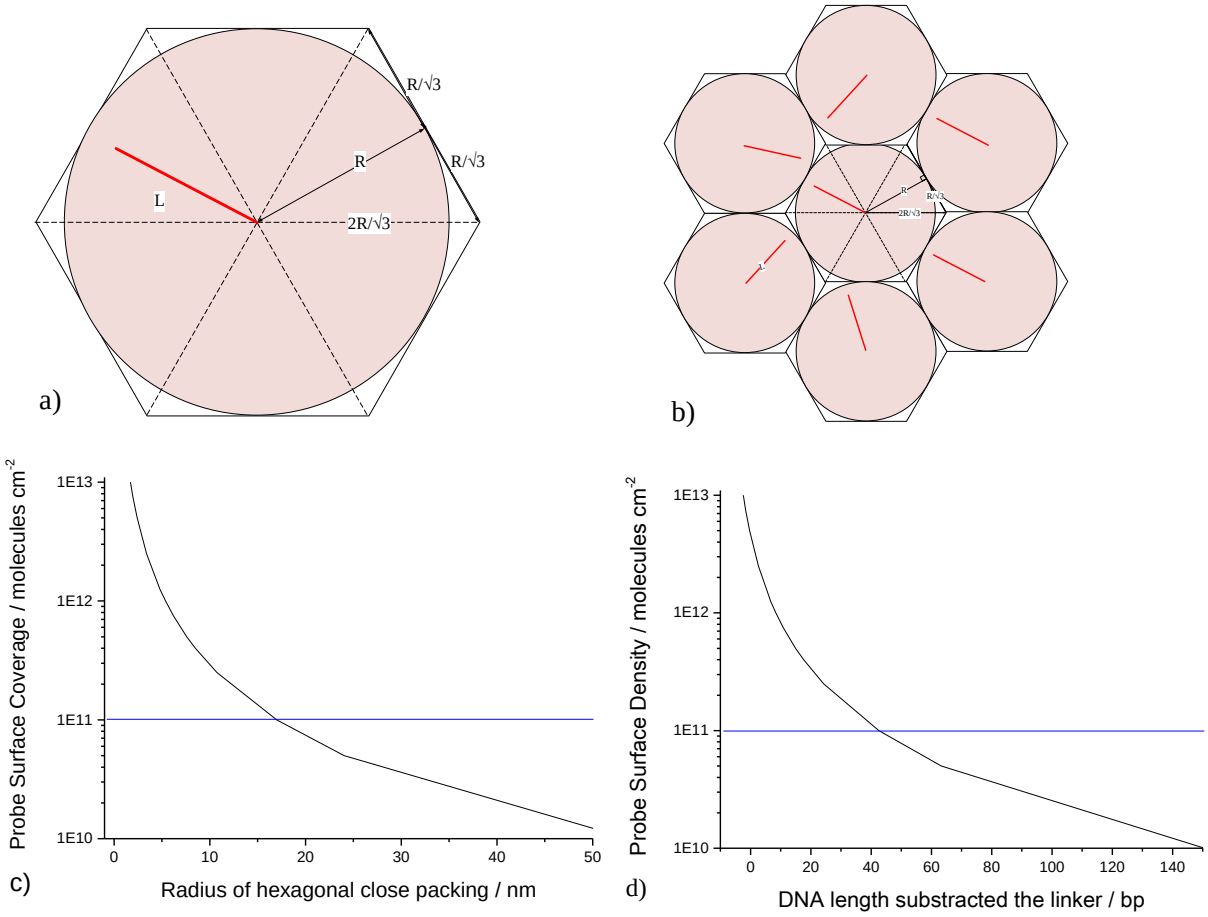

Figure 3.5 a) Schematic of the unit cell represents the immobilized probe (in red) and its gyration radius (L). The hexagon with its radius (R) is the occupied unit cell based on the assumed arrangement of probes at each vertex with hexagonal close packing. The area of the hexagon is calculated as $6 \times [2(R/\sqrt{3}) \times R \times 1/2] = 6R^2/\sqrt{3}$. b) The schematic shows the 7 probes with gyration radius (L) shorter than the radius (R) of the hexagonal close packing ensuring no steric crowding with each other. c) Calculated results of the correlation of probe surface density and radius of hexagononal close packing based on equation (3.4). d) The length of DNA probe minus the 2.5 nm linker and expressed in base pair (bp). The length of the linker is measured from Figure 2.5 b) using ChemBioOffice v.12. The distance is estimated between the oxygen atom attached to the C3 of 5' end of oligonucleotide to the oxygen atom attached to the phosphate moiety of the first di-thiol anchor. The line at 1×10^{11} molecules cm^{-1} denotes the detection limits of the Steel's method to measure the surface density.

To avoid the intramolecular interaction between the DNA probes strands, mercaptohexanol (MCH) was used to lower the density of the beacon probe by co-adsorption on the gold surface[10]. MCH also forms a self-assembly monolayer (SAM) which reduces the non-specific adsorption of DNA to the Au electrode surface[11].

The following experiment was carried out to compare the surface coverage of the immobilised Texas Red-labelled beacon probe with the backfilled passivation and co-adsorption of mercaptohexanol. The SSV substrates were fabricated as in Section 2.1 with the deposited thickness 480 nm for the 600 nm nanosphere template. For the case of backfilled passivation, the SSV chips were immersed in 1 μM Texas Red-labelled beacon probe solution containing 1 M NaCl, 10 mM Tris buffer (7.2) for 13 h. After the probe immobilisation, the SSV chips were immersed into 10 mM mercaptohexanol for 30 m in passivation. For the co-adsorption passivation, the SSV chips were immersed in 1 μM Texas Red-labelled beacon probe solution containing 1 M NaCl, 10 mM Tris buffer (7.2). 1 μM and 10 μM mercaptohexanol was added separately into the probe solution, for 13 h immobilization. After the preparation of the thiol backfilled or co-adsorbed Texas Red-labelled beacon probe substrates, the SSV chips were rinsed with copious amounts of 10 mM Tris buffer before the chronoamperometry. The detail of the chronoamperometry measurement have been described in Section 2.2.2.

The saturated surface density of the immobilized oligonucleotide is plotted in Figure 3.6. The surface density, 3.9×10^{11} molecules cm^{-2}, obtained in the 10 μM MHC co-adsorption case is about 6 times less than for 10 mM backfilled passivation and 3 time less than for 1 μM MHC co-adsorption. When compared to the immobilized linear probe reported by Mahajan[6] and Johnson[5] (1.6×10^{12} molecules cm^{-2}), 10 μM MHC co-adsorption still gives 4 times lower surface coverage. The average distance between the individual beacon probes for 10 μM MHC co-adsorption is 17 nm apart based on the model of hexagonal close packing.

However, Steel's method merely gives an average coverage value for of the interface and gives no information on the variations in the probe's distribution from place to place on the electrode. The recent work of Murphy *et al.*[12] indicated that non-specific adsorption of both ssDNA and dsDNA still occurs on Au surfaces which have been passivated by MHC. The distribution of both 5'-anchored 30 bp thiolated ssDNA and the corresponding dsDNA from the fluorescent images in Murphy's work of 3'-labeled dye on the target are heterogeneous in the specific region of intrest of 50 μm × 50 μm. They also observed similar heterogeneous surfaces were obtained with a range of [NaCl]= 10 - 1000 mM and [$MgCl_2$] = 0 - 500 mM. The result suggested the surface packing of

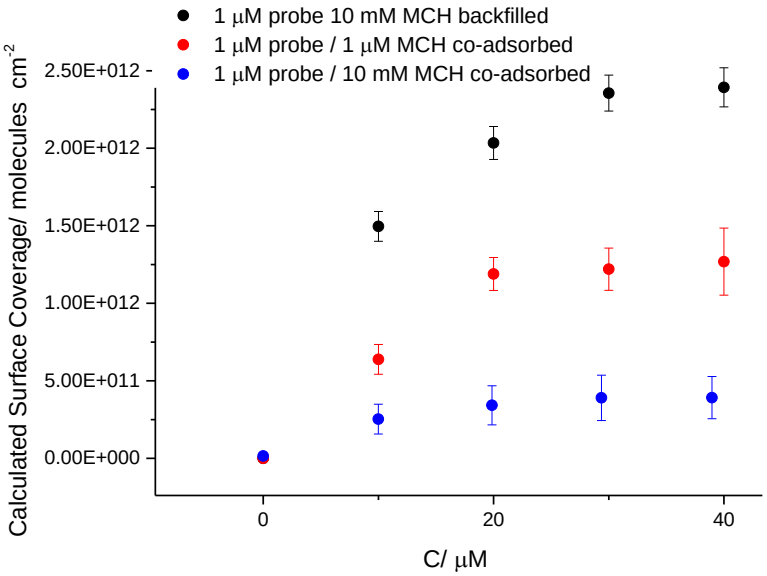

Figure 3.6 Surface density of the beacon probe for 1 μM and 10 mM mercaptohexanol co-adsorption and 10 mM backfilled passivation. The SSV chip was fabricated as decribed in Section 2.1. The SSV chips were immersed in 1 M NaCl, 10 mM Tris buffer containing 1 μM beacon probe for 24 h. In the case of the backfilled passivation, the 10 mM MHC was added into the buffer for 0.5 h after 24 h immobilization. In the co-adsorption case, the 1 μM and 10 mM MHC chip was added seperately into the immobilization buffer. The surface coverage was measured as described in Section 2.2.2. *C* represents the concentration of redox indicator, ruthenium hexamine (III) added serially into the 10 mM Tris buffer (pH 7.4) as the supporting electrolyte.

Table 3.1 Calculated surface density of the 1 μM beacon probe for mercaptohexanol modified by the co-adsorption or backfilled passivation at indicated concentration

Modification method	Concentration of mercaptohexanol	Calculated surface coverage of the beacon probe / molecules cm^{-2}
Backfilled adsorption	10 mM	2.4×10^{12}
Co-adsorption	1 μM	1.3×10^{12}
Co-adsorption	10 mM	3.9×10^{11}

the DNA is not arranged in an orderly manner. Other research reported by Lao *et al.*[52] used the electrochemical quartz crystal microbalance (EQCM) to analyse the mass change during the hybridization of non-thiolated and thiolated ssDNA while monitoring the change of the resonant frequency of the crystal oscillator. The DNA immobilization buffer was 10 mM Tris-HCl, 1 mM EDTA, 1.0 M NaCl. They also concluded that non-specific adsorption of ssDNA occurred on the mercaptohexanol passivated Au electrode. Although Murphy's work used a wider range of ionic

strength of the immobilization buffer than the Lao's work, both works concluded the oligonucleotides adsorb on the Au surface heterogeneously.

The hybridization of the target oligonucleotides onto the probes immobilized on the surface is widely described by the Langmuir isotherm[53,53b,54,55]. The adsorption behaviour of the target oligonucleotide has to meet three assumptions in the Langmuir model. First, the hybridization between the targets and probes is specific and has to achieve equilibrium. Secondly, the target is not self-complementary and does not form dimers with itself. Finally, there is no interaction between the probes, the in-plane separation between the probes is large compared to the range of their interactions. The former two requirements can be satisfied by selecting the sequences to achieve the specific binding and shielding the electrostatic interaction of the phosphate backbones by using high ionic strength. The third demand can be met by lowering the probe density. The equilibrium time for the target-probe hybridization generally requires more than 24 hr[56].

In the Langmuir model, the probe density in the equilibrium state is given by:

$$\Gamma = \Gamma_{\mathrm{p}} \frac{Kx}{1+Kx} \tag{3.5}$$

where Γ is the surface coverage of the targets, Γ_{p} is the surface coverage of the probes, K is the equilibrium constant and x is the concentration of the target in the bulk solution. Since the coverage is proportional to the signal intensity, the practical form of the signal of the target may be written as

$$I = I_p \frac{Kx}{1+Kx} + I_{\mathrm{background}} \tag{3.6}$$

where I_{p} is the saturation intensity above the background at infinite target concentration, K is the equilibrium constant of probe-target duplex formation, x is the concentration of target molecules and $I_{\mathrm{background}}$ is the background intensity. The equilibrium constant is defined by $K = \exp(-\Delta G/\mathbb{R}T)$, where ΔG denotes the free energy of the hybridization, $\mathbb{R}$ denotes the gas constant, and T denotes the temperature. In this model, when $Kx \gg 1$, namely, if the affinity of the probe is very strong, or the target concentration is high enough, the first term saturates as is constant, which implies that all probes bind to their target molecules.

In the case when a Watson-Crick pairing occurs in the beacon probe, an estimation of the equilibrium constant, *K,* can be derived from ΔG. ΔG for forming the duplex with the complementary strand of the loop sequence of the beacon probe is estimated at the hybridization temperature, 37 ℃. The target concentration is given as 1 μM in 1 M NaCl buffer. The resultant ΔG is -21.97 kcal/mol obtained from the united nearest-neighbor method[47]. The equilibrium constant, *K,* may be given as 3.49×10^{15} M^{-1}. The value of *Kx* is then calculated as 3.49×10^{9} which is >>1 and in agreement with the requirement that the signal intensity of the target is proportional to the surface coverage of the probes.

However, in many realistic situations, the requirements of the Langmuir model are not completely fulfilled. The first discrepancy is the non-specific adsorption of ssDNA on the mercaptohexanol-passivated Au substrates mentioned earlier. The second discrepancy is the self-hybridization of the folded beacon probe that is indirectly competitive with adsorption to the target. On the other hand, the lower surface density decreases the detectable signals simultaneously. Another issue is worthy of mention, due to the reproducibility of the double-layer charge, Steel's method[40] has a detection limit of 1×10^{11} molecules cm^{-2}. The value estimated in the case of 1 μM probe and 10 μM MHC co-adsorption is close to this detection limit. Both the measurable signals in SERS and the determination method of surface density have a limit at low surface density. Ideally, the binding of the target to the surface probe using the Langmuir model is a way to estimate the surface coverage, but those discrepancies mentioned above should also be considered if any influence affects the estimation of surface coverage.

Some improved models for the adsorption isotherm of the target-probe substrate has been presented. Most of these models still start from the Langmuir model as the fundamental basis and then modify the interfacial thermodynamic parameters[13,14]. The details of the various isotherm models are beyond the scope of this thesis. Here the Langmuir model is chosen to estimate the quantitative relation of target to probe in the perspective of the detection.

3.3 Electrochemical Melting of the Molecular Beacon

3.3.1 Melting by Linear Sweep Voltammetry and Cyclic Voltammetry

The linear sweep voltammetry began from -0.3 V then scanned to -1.2 V at 1 mV s^{-1}. Raman spectra were collected every 25 mV with a 15 s acquisition time. The potential change with time is plotted in Figure 3.8. Each sampling spot was exposed for 15 s during the 15 mV potential progression. For example, the first spectrum in Figure 3.8 b) was obtained from the 15 s exposure during the linear sweep in potential from -0.3 V to -0.315 V and is denoted -0.3 V in the following figures.

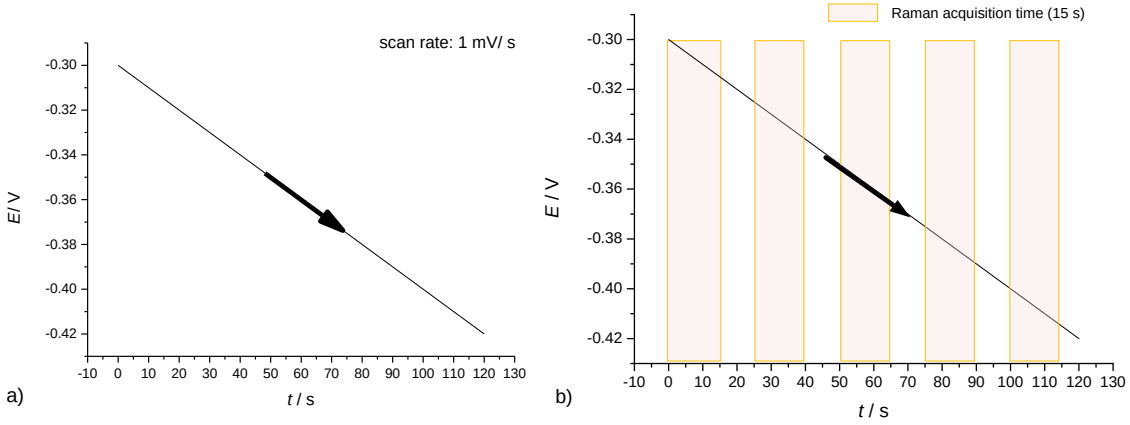

Figure 3.8 Example plots to demonstrate the acquisition Raman spectra during the potential scan. a) The potential vs. time plot for the linear sweep voltammetry at1 mV/s scan rate. The sweep started from -0.3 V and ended at -1.2 V. b) A selected plot to explaining the time window of the Raman spectra acquisitions. Each acquisition started from 25n mV (where n is an integer and starting from 0) and lasted for 15 s on the same place on the substrate before switching to a new spot to obtain the next spectrum to reduce the photobleaching effect. The arrow indicates the direction of potential sweeping.

Backfilled modification with mercaptohexanol after the beacon probes immobilization which results in high surface coverage of the beacon probe was compared the electrochemical SERS response with the co-adsorption of the beacon probe and thiol measured in Section 3.2. The result is shown in Figure 3.9. The conventional 2 steps modification which results in high surface density has more noise response as the cathodic potential scanning. The concentration of probe/

mercaptohexanol (1 µM/ 100 mM) of the 2 steps modification were referred to Mahajan's and John- son's works on the linear strand probes. However, the beacon probe immobilized by the same 2 steps backfilled method does not give a reproducible electrochemical SERS response. Contrast to backfilled modification with thiol, the co-adsorption with the probe and thiol gives a peak shape response and reproducible SERS intensity under the cathodic potential scanning. These results may be attributed to the variation of the surface coverage of the beacon probe. Although higher surface coverage of the beacon probe expresses stronger SERS intensity, due to shorter intramolecular distance, non-specific intermolecular interaction and steric crowding between the probes are both more evident, and this may reduce the consistency of the potential dependent conformation change.

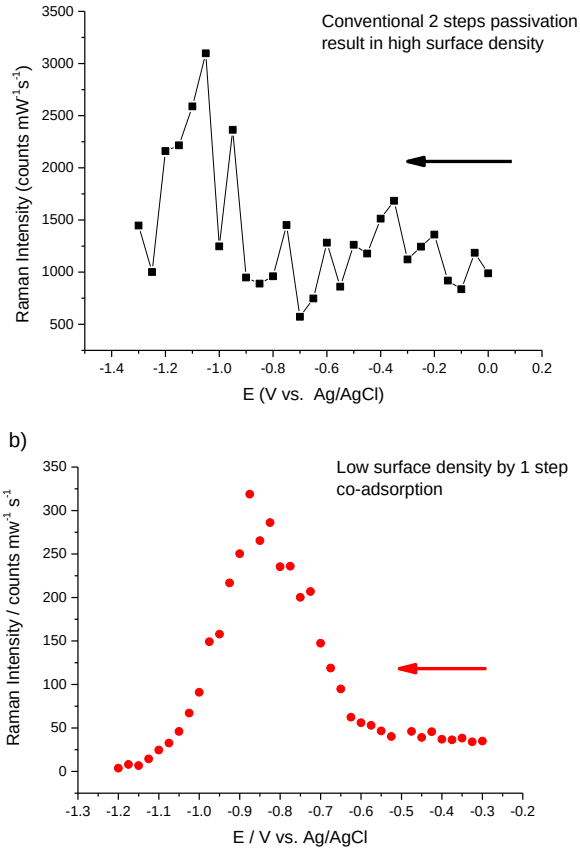

Figure 3.9 Electrochemical SER spectra of the 1504 cm^{-1} band of the Texas Red labelled beacon probe as the function of the sweep potential. a) The SSV substrate was modified by the conventional 2 steps method as 1 µM beacon probe with 3'-labelled Texas Red for 9 h and then passivated with 100 mM mercaptohexanol for 3h. b) The SSV substrate was modified by the co-adsorption one steps method as 1 µM beacon probe with 3'-labelled Texas Red and 10 mM mercaptohexanol for 9h. SSV substrates were fabricated at 480 nm deposition thickness on the 600 nm nanosphere template as described in Section 2.1. The arrow indicates the direction of potential sweeping.

Hence to reach the reproducible electrochemical SERS response, lower surface coverage of the beacon probe is necessary and can be manipulated by the co-adsorption with the probe and thiol.

The resultant Raman spectrum of the co-adsorption modification with the beacon probe and thiol shows the Raman bands at 1504 cm^{-1} and 1649 cm^{-1} are the most intense and observable bands of the Texas Red-labelled beacon probe as shown in Figure 3.10. The two bands are correlated to the C-C stretching (1504 cm^{-1}) and –NH deformation modes (1649 cm^{-1}) of the Texas Red respectively as reported by Mahajan *et al.*[13]. The rest of the Raman bands of Texas Red are relatively weak and it is harder to observe the potential dependence of their Raman intensity. The Raman intensity of the two bands of the Texas Red-labelled beacon probe initially increase from -0.4 to -0.9 V and eventually decrease to zero at -1.2 V as shown in Figure 3.10. No frequency shifts and no new band are observed indicating that the Texas Red remains intact during the potential sweep.

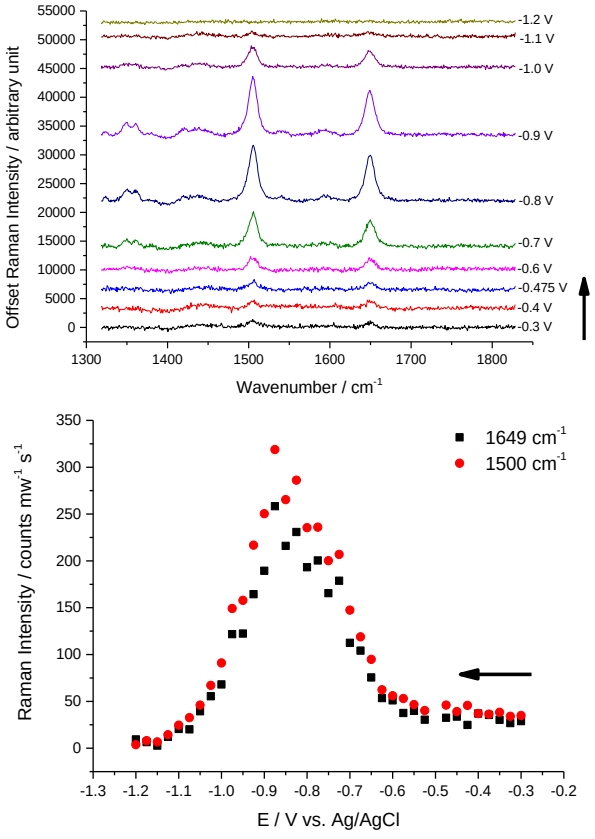

Figure 3.10 SER spectra a) and SERS intensity b) of the 1504 cm^{-1} and 1649 cm^{-1} bands as the function of the sweep potential. The SSV substrate was immersed in 0.1 µM beacon probe with 3'-labeled Texas Red, 10 mM mercaptohexanol and 1 M NaCl containing 10 mM Tris buffer pH 7.0 for 24 h. The substrate was then washed with the 1 M NaCl containing 10 mM Tris buffer pH 7.0. The Raman spectra were collected with 15 s exposure each 25 mV during a sweep potential from -0.3 V to -1.2 V at 1 mV s^{-1}. The fabrication of the substrates is described in Section 2.1. The arrow indicates the direction of potential sweeping.

For Texas Red attached on the 3' end of the beacon probe used herein, the representative bands at 1504 cm^{-1} and 1649 cm^{-1} are not obvious until around -0.7 V. A plausible explanation for this increase in the Raman intensity is that the polarizability of Texas Red re-oreients to result in a stronger Raman scattering along the surface normal between -0.3 to -0.7 V. The detailed orientation effect will be discussed in Section 4.2. Another explanation is that unwinding of the dsDNA is assumed to occur before the melting during the cathodic potential sweep and results in the increase and fluctuation of Raman intensity. The unwinding of the dsDNA describes the breaking of hydrogen bonds between the pairing bases of a localised region in duplex dsDNA and starts at the A+T rich regions15. Unwinding is observed at the beginning of a thermal melting process at slow heating rates (0.5-1 °C min^{-1}). However, there are other possible explanations for the decreasing intensity of the Texas Red including changes in orientation, decomposition, change in the distance, and the offset of charge transfer enhancement which will be discussed in Chapter 4. The renaturation experiment described in Section 3.3.2 gives further discussion to support the observation that the decreasing intensity of Texas Red Raman signals is may likely caused by the melting of the stem region of the beacon probe.

Assuming that when the duplex dsDNA of the hairpin loop beacon probe is melted, the conformation of the Texas Red-labelled beacon probe changes from a partial duplex into a random coil of ssDNA, and there will be an increase in the distance to the surface of the substrate. This will cause a decrease in the Raman intensity of the Texas Red label attached on the distal end of the beacon probe. This also increases the fluorescence if the excitation is close to the electronic transition. Ideally, the measurement of fluorescence should be measured under the fluorescence microscope mounted with the filters to filter out the wavelength minor than the emission. The fluorescence raises the background of the Raman spectra as well and hence reduces the intensity of Raman bands.

There are several features of Figure 3.11 b) which are noteworthy when comparing to the Raman response for the Texas Red label on a conventional and hybridized duplex dsDNA rather than a hairpin. First, the Raman intensity of the Texas Red-labelled beacon probe at -0.3 V is 10 times weaker than for the hybridized linear probe and the target strand. The 3 times lower surface density for the beacon probe can only give a partial explanation from the perspective of the surface concentration. The additional feature of 3.3 times may result from the orientation difference between the folded beacon probe and the linear strand duplex. There are extensive reports to support the fact that the 5'-thiolated probe and its target adopts an upright orientation of the duplex

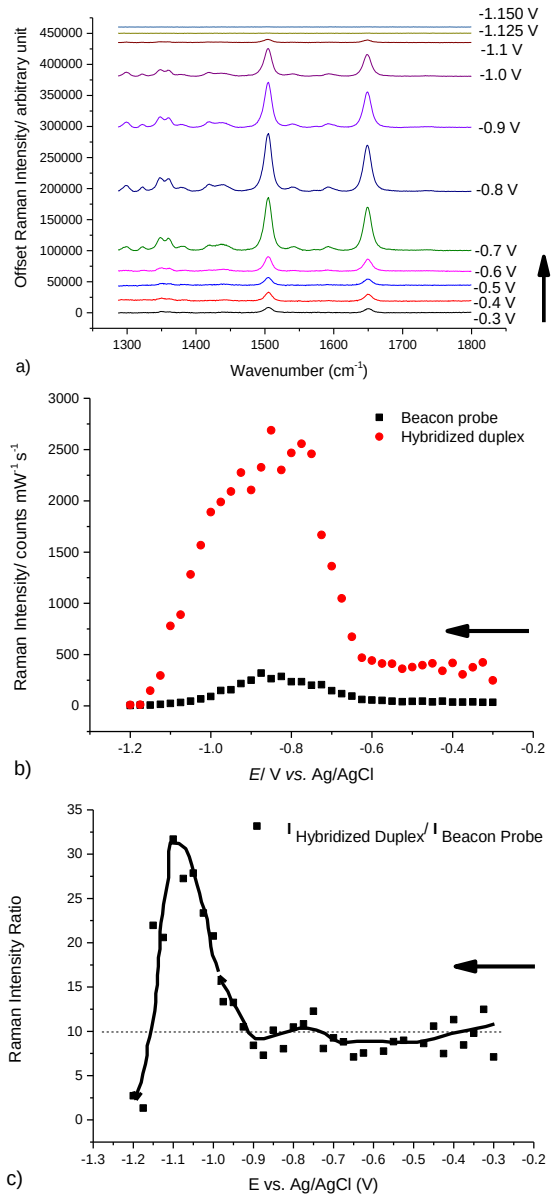

Figure 3.11 a) The 5'-thiolated 20 bp probes contained hydroethylene glycol spacer and dithiol structure as shown in Figure 2.2 a). The 22 bp sequence of the probe was 5'-AGGAAACACCAAAGATGATATT-3'. The SSV substrate was immersed in 1 μM probe overnight at room temperature and was then modified in 1 mM mercaptohexanol for 30 min. The SSV substrate was washed with 1 M NaCl containing Tris buffer pH7.0. Hybridization with the target which is 3'-labeled with Texas Red using the same NHS linker in Figure 2.2, was carried out in 1 M NaCl containing Tris buffer pH 7.0 for 3 h. The Raman spectra were obtained from every 25 mV using in 10 s acquisition time during the linear sweep voltammetry. The electrochemical buffer is the same with the washing buffer. Linear sweep potential at 1 mV s^{-1} started from -0.3 V to -1.2 V. b) Relative SERS intensity (counts mW^{-1} s^{-1}) for the Texas Red 1504 cm^{-1} band between the hybridized duplex and the beacon probe during the potential sweep. c) The Raman intensity ratio in Texas Red 1504 cm^{-1} is calculated as (intensity of the hybridized duplex/ intensity of the beacon probe) and plotted as a function of the potential. The arrow indicates the direction of potential sweeping.

dsDNA on the Au surface[28]. Hence the orientation of the beacon probe may be tilting from the surface base at the lower surface coverage and result in the lower intensity. The duplex DNA used for the comparison was composed of a 20 bp 5'-thiolated probe strand and its pairing strand has the 3' end labeled with Texas Red using the same linker structures shown in Figure 2.2. The detailed processing of the hybridized duplex is given in the legend of Figure 3.11. There was no mercaptohexanol present during the immobilization step or during the extra hybridization with its target. Figure 3.11 c) shows the intensity ratio of the labelled Texas Red for the hybridized duplex to the beacon probe. The average intensity ratio at -0.3 V to -0.9 V is around 10. The increase in the ratio as the potential is swept from -0.9 V to -1.2 V may be explained as the differential melting caused by the varied sequence composition between the beacon probe and the hybridized dsDNA. As explained by Johnson *et al.*[15], the longer 22 bp dsDNA results in a higher melting temperature which correlates to a more negative melting potential when compared with the 7 bp duplex in the beacon probe.

Second, the comparison of the signals at -0.3 V (as the signal "on" state) and -1.2 V (as the signal "off" state) are related to the corresponding beacon probe conformation and the detection distance. The difference of the two states is less than 25 counts mW^{-1} s^{-1} even in the best substrate condition as shown in Figure 3.12. It suggests that it is difficult to discriminate the "on- off" changes of the molecular beacon switch with respect to open circuit potential based on such a small change of Raman intensity. The original way to extract the electrochemical melting potential as a characteristic value from the electrochemical SERS curve may play a better role in discrimination of SNP when compared to the aspect of SERS "off and on" signals. Finally, assuming that the 5'-thiol-tethered dsDNA produces an upright orientation in the thiol-formed SAM, the distance between the reporter molecules and the surface may be estimated from the molecular simulation. At the surface density of the beacon probe, the distance of the Texas Red varied from 6.9 nm (folded state) to 17 nm (unfolded state). Although the effective distance of SERS enhancement was reported to be ca. 100 nm for SSV substrates[16], in the case of 3 times reduced surface coverage of the probe from that of linear strand duplex dsDNA, the Texas Red molecules only produce less than 25 counts mW^{-1} s^{-1} in the equilibrium state at -0.3 V. This relatively weak Raman intensity represents the immobilization at low surface coverage. When the beacon probe is hybridized to the target labelled with the corresponding reporter, the selection of the Raman active reporters needs to be considered if its Raman intentsity is sufficient to be observed in the future work. On the other hand, the variation of the single nucleotide on the target strand can be discriminated from the electrochemical SERS signals after the target hybridizing with the probe is more important from

the aspect of biosensing. If the lower intensity is caused by the orientation of the beacon probe, such as tilting at lower surface density, the choice of an alternative Raman label attached to the hybridized target may provide stronger Raman intensity as the linear duplex than the weaker intensity contributed by the Raman label of the beacon probe as seen in Figure 3.12 a) and b) which is supposed to have a more upright conformation.

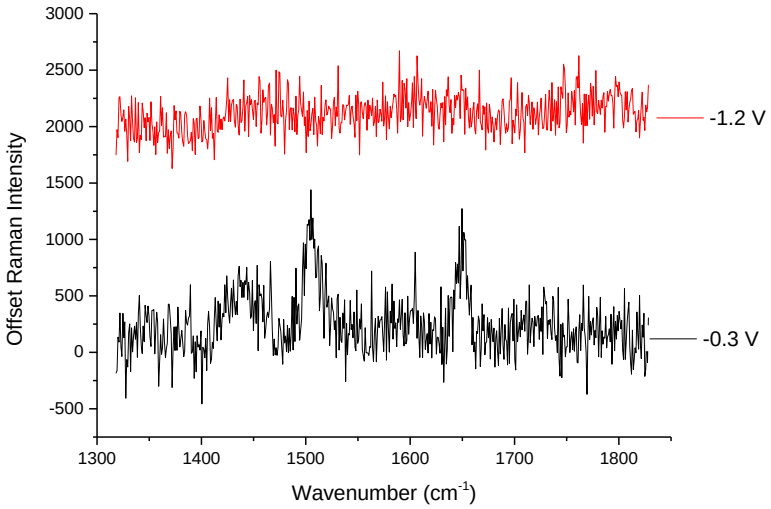

Figure 3.12 The comparison of the background substracted SERS spectra of Texas Red between the potential at the starting potential (-0.3 V) and the end potential (-1.2 V) selected from Figure 3.10 a). The two spectra were obtained in 15 second acquisition time and 2.8 mW laser power; the corresponding normalized intensity is 40.5 times lower signal/noise than the spectra shown in the bottom.

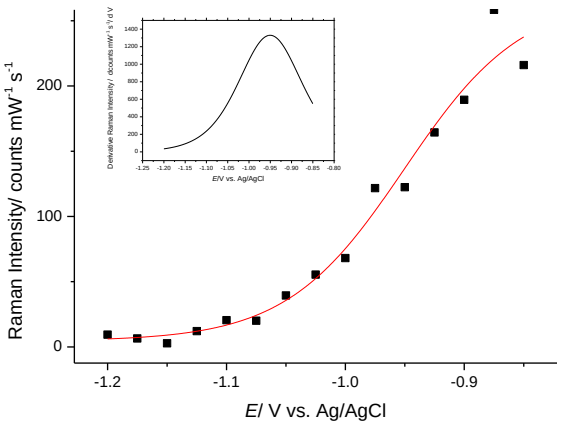

Figure 3.13 Change in SERS intensity of Texas Red 1500 cm^{-1} band with the potential. The scattered squares were selected over the potential range from -0.825 V to -1.2 V from Figure 3.10. The corresponding Raman intensity was fitted with a Boltzmann distribution to produce the sigmoidal curve. The inset plot is the first derivative of the Raman intensity with the potential. The peak reveals the midpoint of the Boltzmann distribution at -0.875 V.

Based on further evidence from the renaturation experiments in Section 3.3.2, the decrease in the Raman intensity between -0.9 V to -1.2 V is attributed to the melting process. The melting region around -0.9 V is shown in Figure 3.9, the melting transition has some scatter at -0.875 V and -0.95 V. This feature may imply in this case that the electrochemical melting is not an "all or none" process at 1 mV s^{-1} scan rate. This means that the decrease in SERS intensity of the Texas Red progresses steadily with the change of potential and does not occur in a continuous decrease at a particular threshold potential. However, this deviation does not affect the melting tendency of the beacon probe.

One plausible explanation for the hysteresis in the -0.3 to -0.9 V range is the range of transition orientations for the Raman label before the beacon probe melting, as shown in Figure 3.14. Unwinding is one of the transition conformations between the folded and unfolded states.

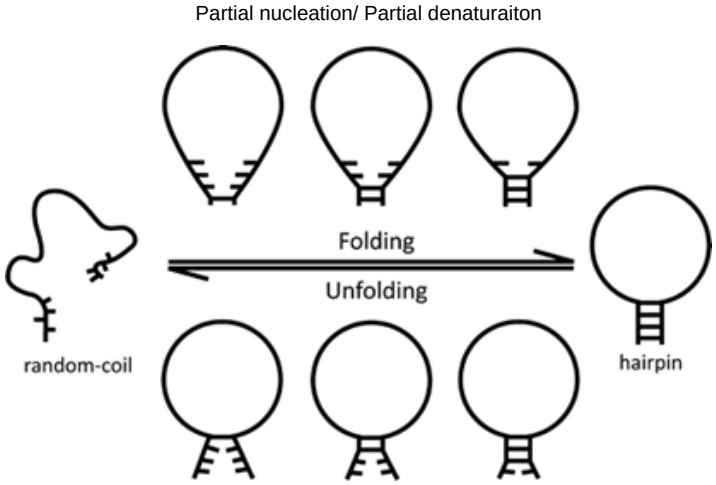

Figure 3.14 Multistate model for hairpin folding. The bulb-like transition states between the fully folded and fully unfolded (denaturation) express the varied nucleation extent. (Reprinted with permission from Ref.[17]. Copyright (2011) American Chemical Society.)

Narayanan *et al.*[18] found that hairpin probes possessed more than one transition conformation for hairpin probes which had 4-mers and 5-mers as the stem and 21-mers as the loop, as shown in Figure 3.14. The bulb-like transitions may propagate along the stem region, and the corresponding energy landscape is multiphase for the transition with one deep valley for the unfolded configuration as shown in Figure 3.15. However, progress among these transitions was normally on a millisecond or faster timescale based in their observations. However, Rant *et al.*[19] also reported a similar potential perturbation on a longer time scale of 10 s at a fixed potential. Their evidence was based on both experimental observation and simulation. Rant *et al.*[19] labeled the 3'-end of the probe with a fluorescent dye and the 5'-thiolated probe to perform the hybridization and then measure

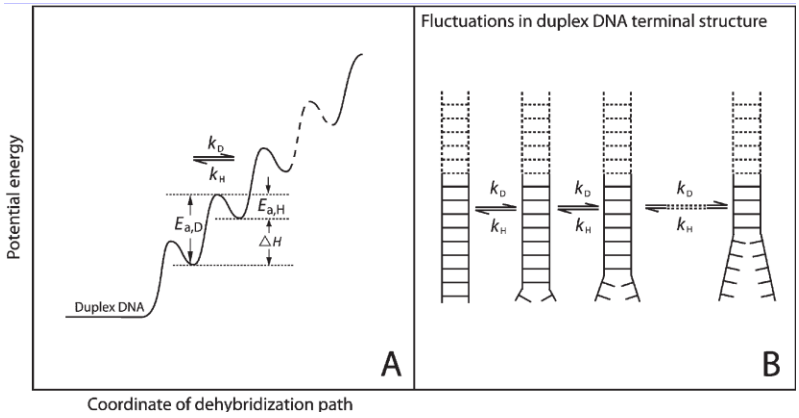

Figure 3.15 (A) Sketch of the energy profile along the denaturation path at a dsDNA terminal. Thermodynamic and dynamic parameters for one base-pair reaction are illustrated. The $E_{a,H}$ is the activation energy of the nucleation and the $E_{a,D}$ denote the free energy hybridization after the nucleation. (B) Scheme illustrating fluctuations in a duplex DNA terminal structure. The k_D and k_H are expressed the rate constant for the denaturation and hybridization respectively. (Reprinted with permission from Ref.[17]. Copyright (2011) American Chemical Society.)

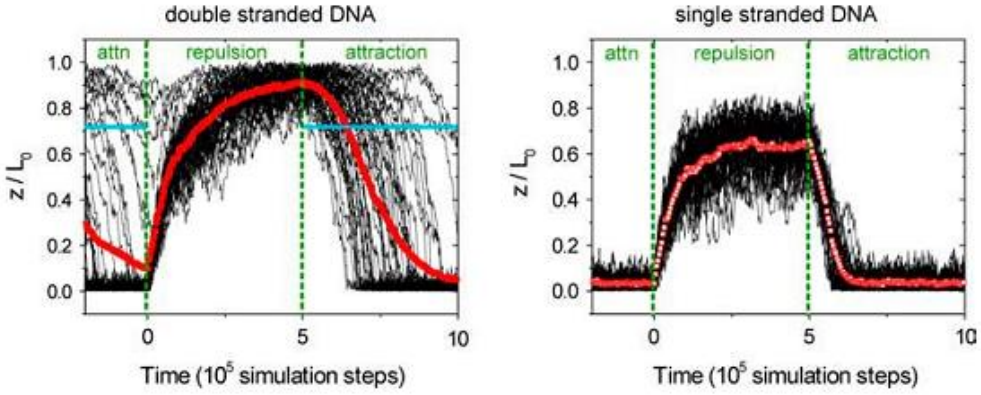

Figure 3.16 Adapted results from the simulations reported by Rant *et al*.[19] The distance of the DNA top end (z) as plotted for 50 simulation runs is normalized by the molecular contour length (L_0); thin black lines represent single molecule traces; red points denote averaged data. For dsDNA, the blue horizontal lines denote the 'point of capture' at which the electrostatic torque equals the thermal energy k_BT. (Reprinted with permission from Ref. [19]. Copyright (2006) Elsevier)

the dependence of the fluorescence on the applied potential at a Au surface; the fluorescence of the dye is quenched when approaching the surface and increases when away from the surface. The potential perturbation was seen in the fluorescence spectra at both 0.1 V and -0.2 V vs. Ag/AgCl. This implied that the potential perturbation may still exist on longer timescales up to 10 s which was supported by the simulation results from the Brownian dynamics as shown in Figure 3.16. The

explanation based on Rant *et al.*[19] is consistent with our results of the hysteresis in the -0.3 to -0.9 V is the range of transition orientations for the Raman label before the beacon probe melting.

To further discriminate the two transition states discussed above, the pre-melting state and the melting state, two separate cyclic voltammograms were conducted to compare the two potential regions.

The first CV began from -0.3 V, cycled to -0.9 V, and then reversed to -0.3 V. The second CV started from -0.9 V, scaned to -1.2 V, and then swept back to -0.9 V. The scan rate for was both 1 mV s^{-1}. The results shown in Figure 3.15 suggest that for the region from -0.3 to -0.9 V the change is reversible but for the potential range from -0.9 to -1.2 V that the change is irreversible on this time scale. Hysteresis is also prominent in the -0.3 to -0.9 V region. The two characteristic bands (1504 cm^{-1} and 1648 cm^{-1}) only varied in intensity and did not shift in the ratio of their intensity or in their frequencies. In addition no new peaks appear in the acquired wavenumber range. Consequently, we conclude that this result may due to the attached DNA strand and depends on the distance of the Texas Red label from the SSV surface. However, there is no reasonable explanation for the increasing SERS intensity of Texas Red in the -0.3 to -0.9 V region barely from the aspect of distance. A further detailed investigation hence was carried on in Chapter 4 on the intrinsic spectroelectrochemical properties of Texas Red.

The results shown in Figure 3.17 reveal distinct features of reversibility. Over the first potential region, -0.3 to -0.9 V, the SERS intensity increases with the cathodic scan and decreases with the anodic scan. This reversiblity suggests that the beacon probe may behave as a hinge at potentials positive of -0.9 V. In the second case, is the potential window from -0.9 to -1.2 V the signal does not recover on the return scan. This is consistent with the assumption of melting but the lack of the expected rehybridization on the return scan is significant to note. This irreversible melting is similar to that for thermally denatured dsDNA in some specific cases such as rapid chilling after thermal denaturation. Thermally denatured DNA renatures on slow cooling to ambient temperature but remains denatured on rapid chilling. The renaturation is a result of random motion and is a concentration-dependent process in an ideal duplex DNA which has no self-complementary sequences. The diffusion coefficient of 1 mM 24 nt nucleoside is estimated to be ca. 1×10^{-6} cm^2 s^{-1} reported by Lapham *et al.*[20]. On the nm scale, the mean time for a 24 nucleoside start to diffuse 1 nm is ~ 1×10^{-4} s, but the diffusion of the nucleotide has to be in the correct orientation with sufficient pairings to cause nucleation as shown in Figure 3.14. Only when the nucleus is stable enough to resist the thermal fluctuation from the environment, can the flanking bases pair to form

the duplex. As long as the nucleation occurs, the remaining segments in DNA renature rapidly. In electrochemical melting over the range -0.9 to -1.2 V the observed behavior implies that renaturation is not favoured during the return scan to -0.9 V. 0.1 V and -0.2 V (vs. Ag/AgCl) at 1 mV s^{-1}. This implies that the potential dependent conformation change of the oligonucleotide may still exist on a timescale longer than 10 s which was based on the simulation result from the

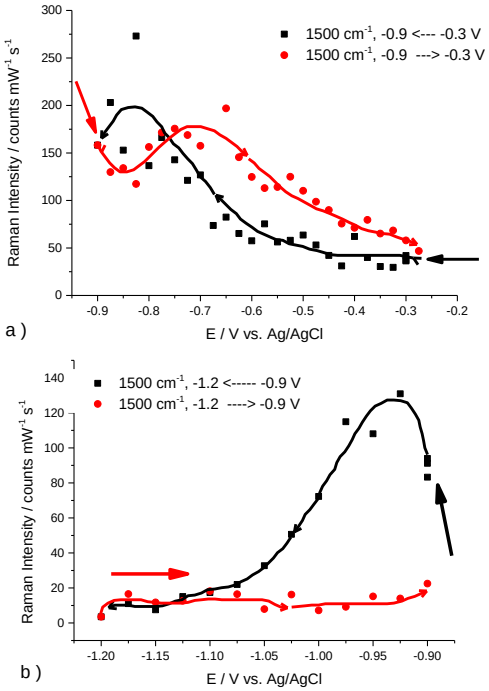

Figure 3.17 Change in intensity of Texas Red 1500 cm^{-1} of two individual cyclic voltammetry (CV). (a) The potential started from -0.3 V to -0.9 V and then swept back. (b) The potential began from -0.9 V to -1.2 V. and scanned back to -0.9 V. The both scan rate of the two CV were 1 mV/s. The SSV substrate was immersed in 0.1 µM beacon probe with 3'-labeled Texas Red , 10 mM mercaptohexanol and 1 M NaCl containing 10 mM Tris buffer pH 7.0 for 24 h. The substrate was then washed with the 1 M NaCl containing 10 mM Tris buffer pH 7.0. The Raman spectra were collected each 25 mV during the cyclic voltammetry in 15 s exposure time. The smoothened curve depicted the average tendency of the Raman intensity during the potential scanning.The arrow indicates the direction of potential sweeping.

Brownian dynamics as shown in Figure 3.16. Further renaturation experiments were carried out at longer timescale and are discussed in the next Section 3.3.2.

3.3.2 Renaturation after Electrochemical Melting

Renaturation experiments were carried out after a specified time for the electrochemically melted beacon probe on the same substrate. Details of the preparation of the SSV substrate are given in Chapter 2. The substrate was immersed in 0.1 μM beacon probe, 10 mM mercaptohexanol and 1 M NaCl, Tris buffer pH 7.2 overnight. Linear sweep voltammetry was conducted on the substrates first and then it was immersed in 10 mM mercaptohexanol and 1 M NaCl containing 10 mM Tris buffer (pH 7.2) at room temperature for a specified time until the next electrochemical SERS measurement. The Raman spectra were collected in 25 mV intervals using 15 s exposure under the same condition as used for the linear sweep voltammetry. The potential was scanned from -0.3 V to -1.2 V at 1 mV s^{-1}.

The results are shown in Figure 3.18. Reproducible renaturation is observed from the sequential monitoring. The decreased intensity over the 1 week interval may be attributed to differences in the sampling site between the two experiments.

Relatively weak, or no, recovered Raman signal was still observed on some substrates. This result may be caused by the lower surface density of the probe, weak nucleation of the beacon probe, or sampling bias on the substrate. Besides, the 10 mM mercaptohexanol added after the electrochemical SERS measurement may cause the thiol exchange reaction to the displacement of the thiol-gold binding sites with the passivated thiols. However, there are several factors need to be considered from the displacement exchange and has been reviewed by Love *et al.*[21]. The first is the exchange reaction generally does not yield homogeneous and uniform self-assembly monolayer (SAM). The exchange reaction usually takes place rapidly (hours) on the defects, grain boundaries and region of disorder rather than the dense region (days). The disulphide anchors moiety of the beacon probe reported by Shon *et al.*[22] and the longer alkyl chain length of the linker compared to the replaced mercaptohexanol[23] are both factors may reduce the exchange reactions. Again, these three factors decrease the renaturation efficiency. The observation of renaturation is further evidence that the probe remains on the surface after the scan to negative potential.

Combining the evidence including the SERS response as a function of potential for the different scanning experiments and even the different potential range, we now try to give an overview of the possible response of the beacon probe to the potential applied at the Au surface as shown in Figure

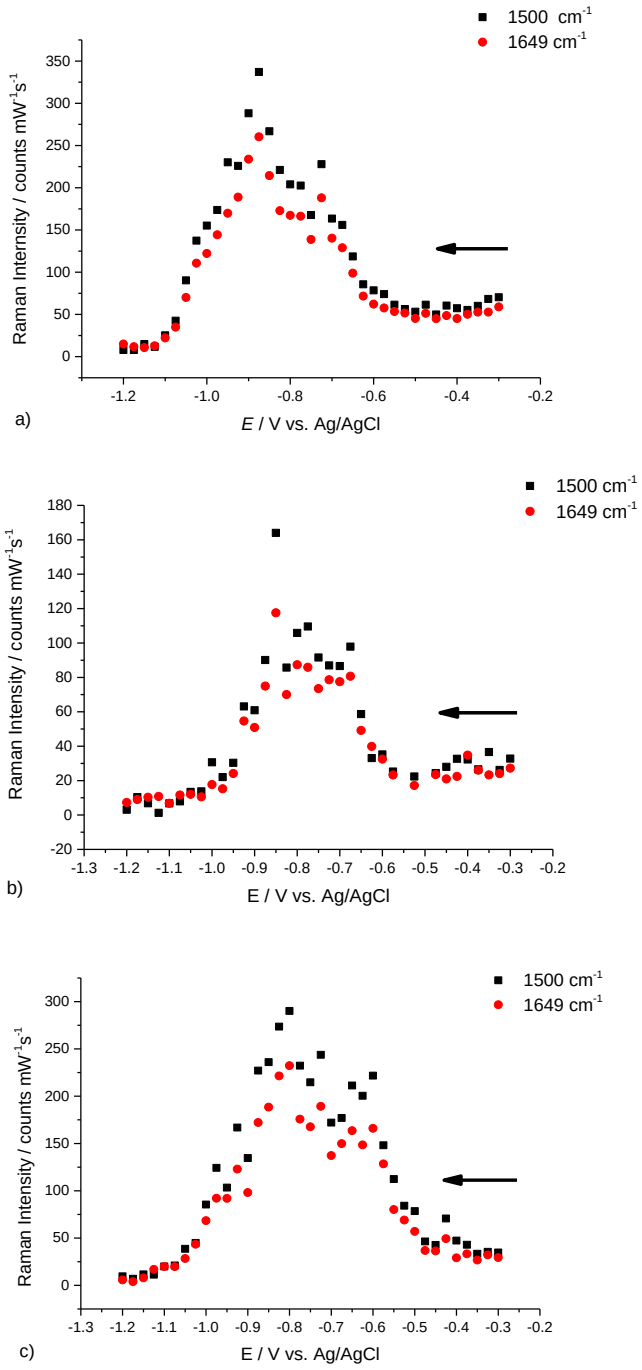

Figure 3.18 SERS intensity as a function of the linear sweep potential after various intervals. a) Original plot. b) 1st renaturation after one week. c) 2nd renaturation after one hour following b).The potential was from -0.3 to -1.2 V at 1 mV s^{-1}. The Raman spectra were collected every 25 mV using 15 s acquisition time. The SSV substrate was immersed in 10 mM mercaptohexanol and 1 M NaCl containing 10 mM Tris buffer pH 7.2 after each linear sweep measurement. The arrow indicates the direction of potential sweeping.

3.19. The surface density, reorientation of Raman label and the distance between the Raman label and the surface are the three major factors that contribute to the SERS intensity. First, the renaturation result excludes the possibility of desorption of the thiol-gold bonds and loss of the

beacon probe; the six thiol/Au bonds are strong enough to withstand the application of a significant negative potential (normally -1.2 V vs. Ag/ AgCl). Second, if the change of the SERS response is only caused by the change in orientation of the Texas Red, it is not realistic to conclude that there has no corresponding change in the probe that it is attached to. Third, if the change in SERS

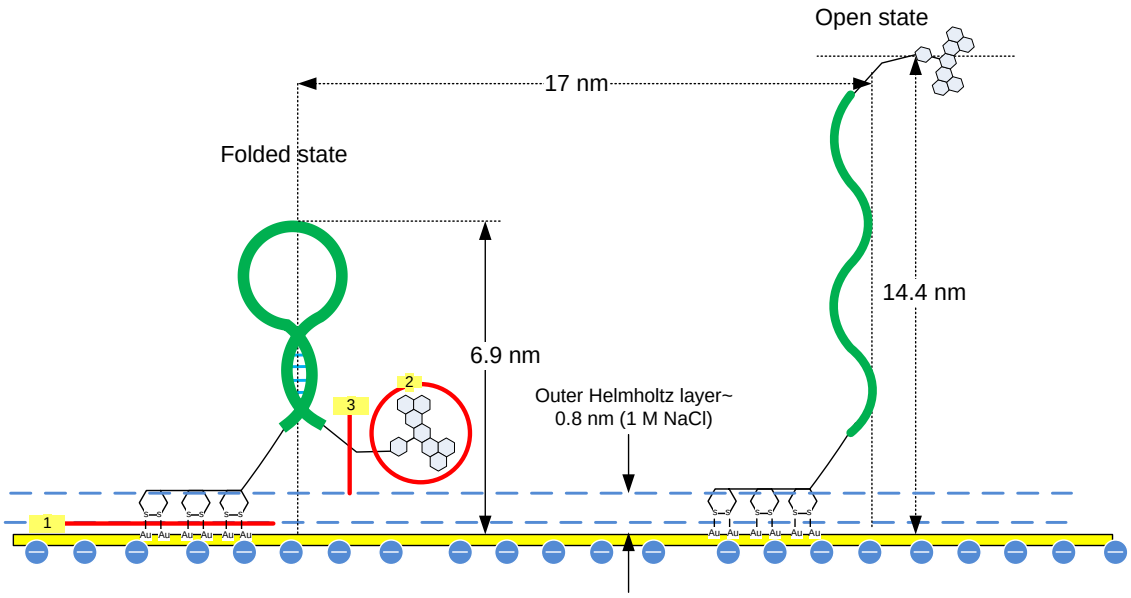

Figure 3.19 A schematic of the plausible mechanisms to explain the SERS of Texas Red change with the potential on the charged surface. There are several assumptions to explain the correlation between the SERS intensity and applied potential. 1) If the thiol-gold bonds were broken, the beacon probe would desorb away from the surface. 2) One assumption is the SERS response of Texas Red is merely related to the orientation of reporter itself; this is not realistic due to the covalent linker between the probe and the reporter. 3) If the linker between the reporter and the probe was broken, the observed SERS signal was caused by the adsorption and desorption of the reporter only. This assumption could not explain the result of regained SERS response in the renaturation experiment. Finally, the scale for the distance between the individual probes is determined in the surface coverage experiment in section 3.1. The length of the folded and unfolded state of the beacon probe was estimated by the Hyperchem (Hypercube, Inc. Gainsville, USA). Blue dash line denoted the Debye length[30] and the outer Helmholtz layer[32] which is resulted from the salinity of 1 M NaCl. Two ends of the probe is located in the effective distribution of inhomogeneous potential.

intensity for the Texas Red was caused by the linker between the probe and the Texas Red being broken, this could not explain why the SERS response of Texas Red could be repeatedly observed

in the fresh 1 M NaCl containing 10 mM Tris buffer which has no added Texas Red. The surface density of the beacon probe was measured in Section 3.2 giving an average of 3.9×10^{11} molecule cm^{-2} on the surface, the averge distance between the individual probes on the surface was then estimated as 17 nm assuming hexagonal close packing of the probes as shown in Figure 3.17.

After excluding the possibility mentioned above, our conclusion is that the orientation of the Raman label is related to the configuration of the probe through the covalent linker and may explain the potential dependent SER intensity. Although the orientation change will result in a change in the ratio of the out-of-plane stretching and in-plane stretching in aromatics, due to both of these two stretching bands of the Texas Red labelled beacon probe are too weak to be observed in the conditions investigated in this study. Hence the orientation change cannot be excluded entirely. The detailed discussion of the vibrational modes of the Texas Red would be discussed in Section 4.2.

We can then interpret the results of the voltammetry experiments from this perspective and further consider the configuration features of the beacon probe and its response to the applied potential which are consistent with our findings and are supported by the literature. In the potential range, -0.3 V< E < -0.7 V, the orientation of the Texas Red and the probe is not favorable to produce increasing Raman intensity at the lower surface density. When the potential is sweept in the range, -0.7 V< E< -0.9 V the orientation of the Texas Red changes to give stronger SERS, and the partial unwinding of the stem region may cause the fluctuation in the SERS intensity in this potential range. Due to the partial nucleation of the unwinding oligonucletide in this potential range, the renaturation is more rapid and reversible as can be observed in the cyclic voltammetry (Section 3.2.2). When the potential scans to -0.9 V< E <-1.2 V the beacon probe melts from the folded into the unfolded state and the distance between the Texas Red and the surface increases, this results in the disappearance of the SERS signals.

3.3.3 Electrochemical SERS response in Potential Step

Voltammetry

To gain further insight into for the intensity fluctuation, which is frequently observed in the potential range -0.7 V to -0.9 V for the beacon probe at lower surface density, fixed potential or potential step measurement were used to observe the behavior of the Raman label in the following experiments.

The substrate was prepared using the conditions described in Chapter 2. A constant potential of -0.9 V was held for 800 s to perform amperometry. Each SER spectrum was recored after an interval of 8.5 s and acquired for 15s. The results are shown in Figure 3.20. The scatter in the intensity of Texas Red signal implies a variation in the behavior on the surface even at fixed potential. The OCP of the initial state of the beacon probe was close to 0 V at the beginning of the experiment. The laser focusing was controlled by maintaining the microscope stage at the same height and position from the objective to the SSV substrate throughout all the measurements. On the other hand, the laser spot size shown on the ocular has larger variations on a roughen surface

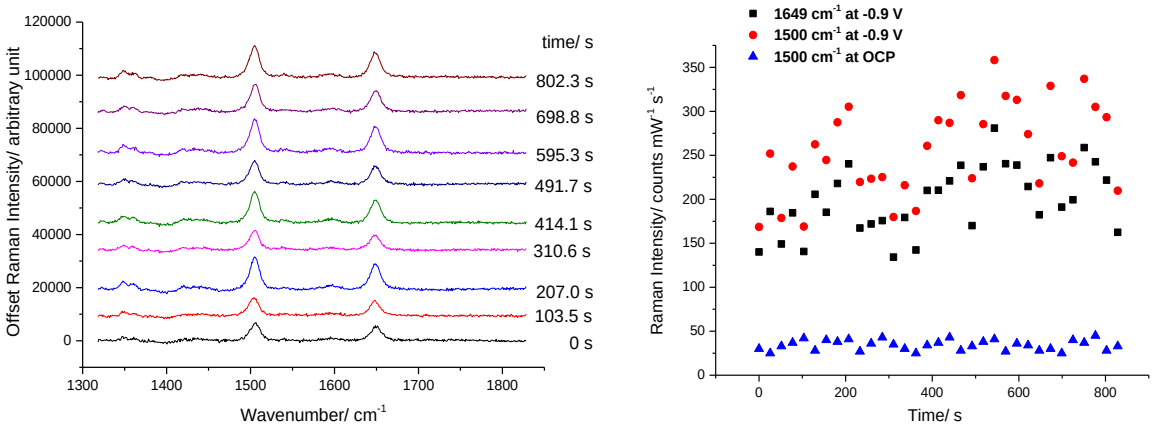

Figure 3.20 SERS intensity as a function of time during a fixed potential at -0.9 V. Left: Original Raman spectra. Right: The Raman intensity of 1504 and 1649 cm^{-1} band of the Texas Red-labelled beacon probe during the fixed potential, -0.9 V, holding for 800 s and at open circuit potential individually. Each SER spectra was recored after an interval of 8.5 s and acquired for 15s. Details of the preparation of the SSV substrate are given in Chapter 2. The substrate was immersed in 0.1 µM beacon probe, 10 mM mercaptohexanol and 1 M NaCl, Tris buffer pH 7.2 overnight. 1 M NaCl containing 10 mM Tris buffer pH 7.2 was the supporting electrolyte.

due to the diffraction coming out from the grating-like SSV surface. Hence the laser spot size focusing on the SSV substrate cannot be used directly to estimate the illumination area. Alternatively, the 5 μm diameter laser spot measured using the WIRE 3.2® (Renishaw, Gloucestershire) software from the flat region of evaporated Au film adjacent to the SSV deposit area. However, the size of the laser spot does not represent the actual beam diameter of the incident laser[24]. The radius of the diffraction limited laser spot size could be estimated by the value of (0.61 λ/ NA) where the λ is the incident wavelength and NA represents the numerical aperture[24]. In our case, the incident excitation is 633 nm, and the numerical aperture of the 50 × objective is 0.75 then the diameter of the diffraction limited laser spot is ca. 1063 nm as shown in Figure 3.21. The observed laser spot observed in the naked eye is the overall result of the diffraction of the laser beam irradiates on the substrate. The diffraction limited spot size gives the minimum of the perfect alignment of the laser, lenses and the stage. The diameter of the laser spot was estimated as 1.0 μm measured with the WIRE 3.2® (Renishaw, Gloucestershire) in the 'no defocusing' mode.

On the other hand, the micron-scaled laser spot size can be measured experimentally by the method of scanning knife-edge[25–29]. The laser beam is scanned perpendicularly and across a sharp edge of a uniform sample from the lateral side. The signal from the sample surface is measured as a function of displacement. In the backscattering Raman configuration used in this study, the silicon wafare can be used as the uniform sample. The edge of the silicon warfare chops the beam periodically while travelling at a known velocity in the xy plane. This results in a sigmoid shape response of the 520 cm^{-1} Raman band of silicon vs. the travelling displacement. As stated in an e-mail from Alex Keeler[30] (Chemistry, University of Southampton, UK), the laser spot size 4.0 ± 2.0 μm was obtained from the horizontal displacement between the maximum and minimum Raman intensity of 520 cm^{-1} Raman band of silicon. One of the reasons for the larger estimation of laser spot size by using the scanning knife-edge than the diffraction limitation calculation is limited by the displacement resolution controlled by the step-moving stage which is 2.0 μm in this study. Other reasons as Le Ru *et al.* indicated[29,31], the accuracy of the scanning knife-edge method decreases for small spots and is not suggested to used for beam width less than ~2 μm. This limitation is primarily due to lager divergence of the beam (that can therefore excite the sample from the side) and the quality of the cleaved edge.

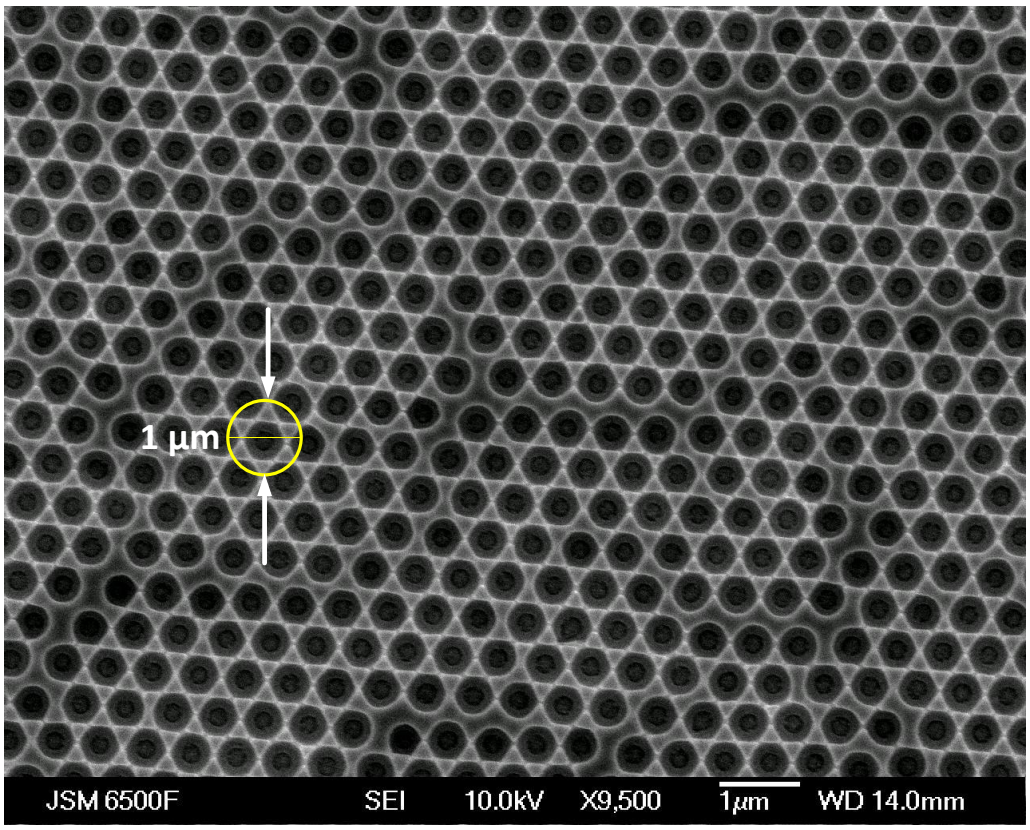

Figure 3.21 Laser spot size illustrated on the SEM image of SSV substrates. The diameter of the laser spot is 1.0 µm estimated by the diffraction limit in the non-defocusing mode controlled with the built-in WiRE® software (Renishaw, Gloucestershire). The thickness of the voids is 480 nm controlled by the deposition current in the chronoamperometry on the 600 nm nanosphere template. The circle represents the laser spot covers around 1.7 voids in average.

Assuming the focal spot is located between the bottom to the rim plane of the SSV substrate, the observation volume should cover the region with 1.3 µm in the z-axis and between 1 µm diameter in xy plane. Figure 3.21 shows on SEM image of the SSV surface. The laser spot covers the area of 2×10^{-8} cm^2 (around 1.7 voids). If the surface hybridization reaction follows the equilibrium model mentioned earlier, the probes should be able to bind the target with high affinity at the equilibrium state. The average number of molecules contained in a single void is 1.4×10^4 to 9.2×10^5 beacon probes, and the reporters attached contribute to the Raman signal in the equilibrium state. This might partially explain the variation of the variation between each electrochemical SERS measurements is due to the variation of SERS enhancement with an SSV unit cell. However, there still has Raman intensity fluctuation for a fixed position in open circuit potential shown in Figure 3.20. This fluctuation is consistent with the electrochemical SERS response of the bare Texas Red adsorbed SSV observed in Figure 4.1 and may be related to systematic bias between measurements.

On the other hand, the Raman intensity fluctuation may imply the potential dependent conformation change of beacon probe like unwinding, partially melted or renatured are occurring. However, the observation does not provide direct information to identify these possibilities. For more insight into the mechanism, it is useful to consider Rant's work and to compare with our result[19]. Rant *et al.*[19] chose a model of 24 monomer chain of elastically connected charged spherical beads with a radius characterized by the stretching and bending moduli, including full hydrodynamic interactions and the nonslip surface condition. The radius of the beads was 0.34 nm which corresponds to a single nucleotide. The effective linear charge density of the charged polymer is reduced by counterion condensation, leading to a renormalized charge of one electron per Bjerrum length as mentioned in Section 1.3. Since the Bjerrum length roughly corresponds to the bead diameter in the simulations, Rant and co-workers[19,32] took Manning condensation into account by assuming each bead to bear a charge of one electron, both for ss- and dsDNA. The salinity, 1 M NaCl, set the Debye length as κ^{-1} = 0.3 nm. The persistence length was 100 nm for dsDNA ad 0.68 nm for ssDNA. The surface potential was assumed to switch immediately from negative to positive bias and vice versa, neglecting the more complicated effects of finite double-layer charging time. Finally, the external potential bias was $\pm$ 0.125 V. The results are shown in Figure 3.16.

The results for the distance variation of the distal end for the ssDNA and dsDNA in Rant's work[19] and the SERS signal for the proximal end in our work are complementary to Rant' work[19] as shown in Figure 3.22. Since tethered probe acts as a hinge, the distal end and proximal end have an opposite displacement when the conformation of the duplex is tilting or rotating about the hinge. Even on the proximal end, the Texas Red is close to the electric field created by the double-layer, and the electrostatic interaction from the electric field has a major effect due to the charge on oligonucleotide phosphate backbone. Rant's explanation stated that the dsDNA was still repelled to some degree by the electric torque exerted on the lower segments by the negatively-charged surface. However there are several differences between Rant's work and our own. For example Rant used fluorescence rather than the SERS, the potential was -0.125 V rather than -0.7 V, the reporter was Cy3 rather than Texas Red and the hybridized target was with a linear probe rather than with a beacon probe. Most of these differences do not alter the overall oligonucleotide motion during the potential scan from a qualitative perspective. The environmental factors include the electrolyte, 1 M NaCl, and the lower surface density used to enable the free motion of the immobilized oligonucleotide which, as indicated by Rant *et al.*[19], are consistent with our discussion. The difference between the beacon probe and dsDNA deserves comment. The behaviour of the beacon

probe may be interpreted as the difference in motion between the ssDNA (loop region) in the region outside the double layer and the dsDNA (stem region) influenced by electrical field especially when the distance approaches the Debye length. The most distinct difference between

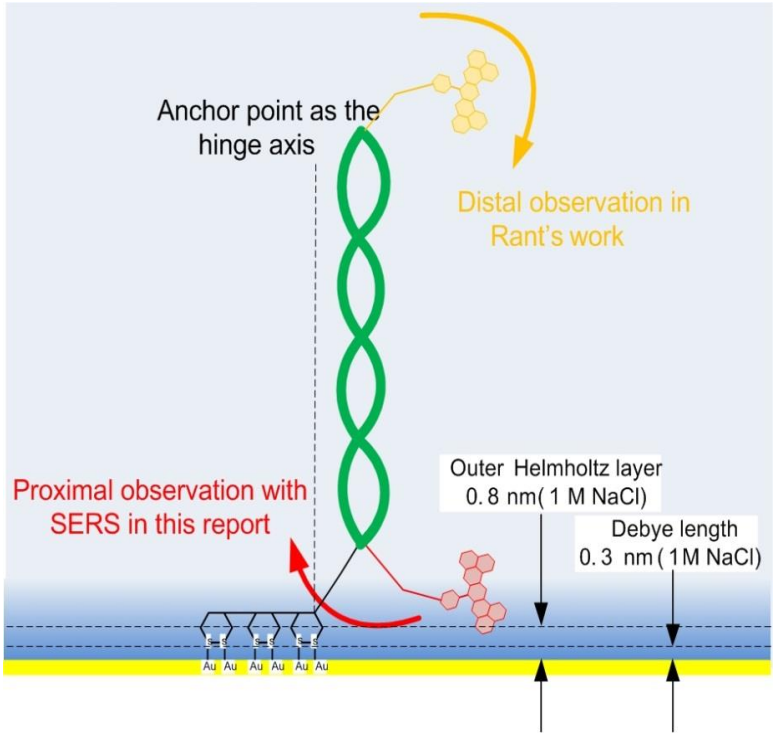

Figure 3.22 A schematic of the correlated motion between the distal end and the proximal end of the DNA. If the oscillating signals reflect the tilting and rotation movement of the duplex DNA, this movement should have a tethered point on the anchor, and both the distal and proximal ends have an opposite displacement from the surface as a result of the rigidity of the dsDNA. The Debye length[19] and the double-layer[33] denote the region where the electrostatic effects occurs as the short-distance effect from the surface.

the dsDNA and ssDNA in Figure 3.22 is that the relaxation time for the ssDNA was faster than that for the dsDNA due to the short persistence length when the potential was switched from -0.125 V to +0.125 V. The beacon probe may respond to an intermediate state between the dsDNA and ssDNA. The beacon probe is supposed to be more close to the dsDNA due to the Texas Red attached close to the stem end. Here, our SERS signals also record similar motions from the proximal end. This might be an explanation for the fluctuating response at fixed potential. The fluctuation may be minor in the proximal end from the torque perspective, as the distance to the proximal end is shorter than to the distal end. The fluctuating responses of the oligonucleotides at the negative potential surface are in agreement in both studies. However, from the averaging point of view, the potential dependent conformation change was simulated in 10^5 steps in Rant's work to

reach a smooth fluorescence signal transition, but the fluctuation observed in our experiments displays a higher noise during 800 s holding at -0.9 V.

To confirm if the fluctuation of the electrochemical SERS response is proportional to the applied potential, the following double potential step experiments were conducted with the same acquisition time of 15 s. The first potential step was to -0.9 V then a step to -0.3 V after 500 s, and hold at -0.3 V for the following 450 s. The preparation of the substrate and the immobilization details were described in Chapter 2. Each Raman spectrum was accumulated for 15 s exposure and had a 10 s interval to switch filter off and choose the next sampling spot on the substrate. Since the spectra were collected from different sites on the substrate, there is also the spatial variation to taking account in the SERS intensity. This spatial variation was compared with Mahajan[34], based on the same substrate the SERS signals are reproducible from place to place at a given film thickness with less than 10 to 30 % variation.

The resultant SERS signals for the two-step potentials are depicted in Figure 3.23. The resultant intensity changes for the two potential step experiments indicate that the potential perturbation of Texas Red both exists at -0.9 V and -0.3 V, but the coefficient of variation is larger at -0.9 V which support the assumption proportion relation between the fluctuation and the applied potential.

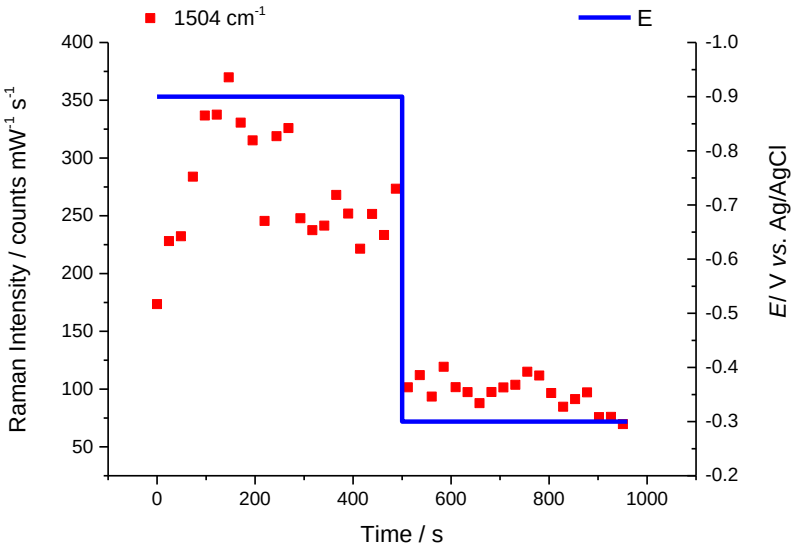

Figure 3.23 SERS (red scattered squares) intensity of the Texas Red 1504 cm^{-1} band during a potential step (blue line) from -0.9 V and -0.3 V. The SSV substrate was immersed in 0.1 µM beacon probe with 3'-labelled Texas Red, 10 mM mercaptohexanol and 1 M NaCl containing 10 mM Tris buffer pH 7.0 for 24 h. The substrate was then washed with the 1 M NaCl containing 10 mM Tris buffer pH 7.0. The Raman spectra were collected each 25 mV during the potential step in 15 s exposure time.

Finally, positive potentials has been reported to assist the hybridization of DNA on surface in Heller's work[35] and also observed in Rant's work[19], using an electrode array and hybridization of the target from solution to a probe immobilized is a larger on the surface. It is intresting to see if there is an enhanced effect of the potential on the beacon probe after electrochemical melting.

The potential multistep experiment was conducted on the same surface 40 min after it had been denatured at -1.2 V. The motivation for the design of the potential step was to observe the effect of potential on the recovery of the Texas Red signal. The details of the multi potential steps are shown in Table 3.3. The potential started from -0.9 V, which was the potential corresponding to the maximum intensity for Texas Red. Then the potential was changed to 0.1 V, then switched to -0.9 V again. The following potentials was stepped to 0.2 V, 0.3 V and 0.4 V separately with the interval potential fixed at 0.9 V. Every step was held for 100 s. The Raman spectra were measured using 15 s exposure time and at 8.5 s time intervals between each collection to switch the filter and select the next sampling spot in order to prevent possible photobleaching. Again, the preparation of the substrate and the immobilization details are described in Chapter 2.

The **i**ncreasing signal is assuming to correlate with the rehybridization of beacon probes in accord with our earlier results. The resultant plot, shown in Figure 3.24, shows that the change of Raman intensity a function of the potential. The results show no significant effect at the positive potential on the recovery of the Texas Red signal.

Table 3.3. Potential steps used the 8-step potential experiment. The chronoamperometry was performed in a conventional 3 electrode cell. All the electrochemical measurements were conducted in 1 M NaCl containing 10 mM Tris buffer (pH 7.2).

Step	1	2	3	4	5	6	7	8
Potential/ V vs.Ag/AgCl	-0.9	0.1	-0.9	0.2	-0.9	0.3	-0.9	0.4
Duration time / s	100	100	100	100	100	100	100	100

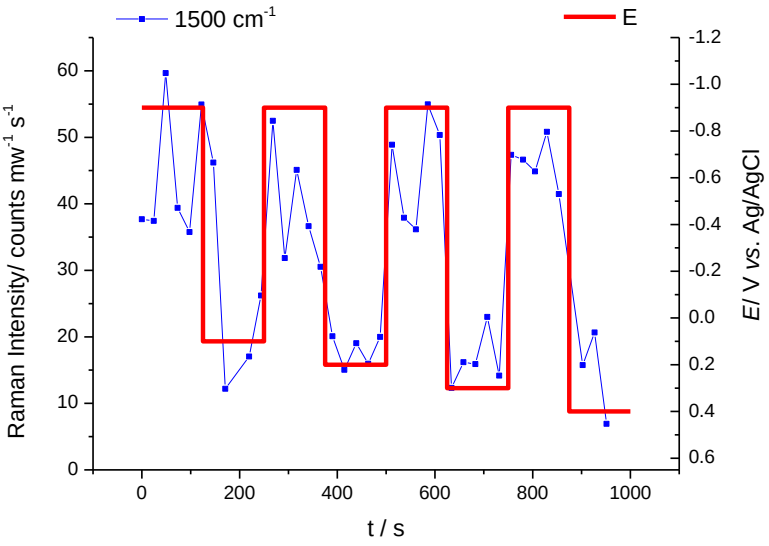

Figure 3.24 Changes in Raman intensity (blue-scattered line) for the Texas Red 1504 cm^{-1} band with the multi- potential steps (red line). Each step was held for 100 s, potential sequence, -0.9, 0.1, -0.9, 0.2, -0.9, 0.3, -0.9 and finally stop at 0.4 V.

The overall potential step voltammetry experiments performed in this section observed a potential dependent Raman intensity which has stronger at -0.8 to -0.9 V and weaker at -0.3 V. No signal recovery after tuning the potential step to the positive gradually from 0.1 to 0.4 V was observed. The potential dependent conformation change was initially chosen to explain the electrochemical SERS result, although the potential dependent Raman intensity is similar to the observation reported by Rant *et al*[19]. at fluorescence adsorption spectra. However, the potential dependent fluctuation and no recovery of SERS intensity of the supposed electrochemical melted (holding at -0.9 V) Texas Reed labelled beacon probe while the potential stepping to positive both cannot be explained from the averaging aspect and the potential-driven conformation change. On the other hand, both results suggest the assumptive potential driven conformation change of the oligonucleotide may not be the only mechanism to explain the electrochemical SERS behaviour of the beacon probe. There might be other mechanisms contribute to the resultant intensity as the diffusion layer effect cannot fully extend the beacon probe as well. Hence the intrinsic electrochemical SER spectra of the Raman label, Texas Red, would be investigated in the next Chapter.

3.4 References

(1) Butler, J. M.; Buel, E.; Crivellente, F.; McCord, B. R.*Electrophoresis* **2004**, *25*, 1397.
(2) Zuker, M.*Nucleic Acids Res.* **2003**, *31*, 3406.
(3) SantaLucia, J.*Proc. Natl. Acad. Sci. U. S. A.* **1998**, *95*, 1460.
(4) Peyret, N.; Seneviratne, P. A.; Allawi, H. T.; SantaLucia, J.*Biochemistry* **1999**, *38*, 3468.
(5) Allawi, H. T.; SantaLucia, J.*Biochemistry* **1998**, *37*, 2170.
(6) Mahajan, S.; Richardson, J.; Brown, T.; Bartlett, P. N.*J. Am. Chem. Soc.* **2008**, *130*, 15589.
(7) Vainrub, A.; Pettitt, B. M.*J. Phys. Chem. B* **2011**, *115*, 13300.
(8) Rant, U.*Bioanal. Rev.* **2012**, *4*, 97.
(9) Yao, D.; Kim, J.; Yu, F.; Nielsen, P. E.; Sinner, E.-K.; Knoll, W.*Biophys. J.* **2005**, *88*, 2745.
(10) Keighley, S. D.; Li, P.; Estrela, P.; Migliorato, P.*Biosens. Bioelectron.* **2008**, *23*, 1291.
(11) Herne, T. M.; Tarlov, M. J.*J. Am. Chem. Soc.* **1997**, *119*, 8916.
(12) Murphy, J. N.; Cheng, A. K. H.; Yu, H.-Z.; Bizzotto, D.*J. Am. Chem. Soc.* **2009**, *131*, 4042.
(13) Halperin, A.; Buhot, A.; Zhulina, E. B.*Langmuir* **2006**, *22*, 11290.
(14) Halperin, A.; Buhot, A. and; Zhulina, E. B.*J. Phys. Condens. Matter* **2006**, *18*, 463.
(15) Johnson, R. P.; Gao, R.; Brown, T.; Bartlett, P. N.*Bioelectrochemistry* **2012**, *85*, 7.
(16) Mahajan, S.; Cole, R. M.; Soares, B. F.; Pelfrey, S. H.; Russell, A. E.; Baumberg, J. J.; Bartlett, P. N.*J. Phys. Chem. C* **2009**, *113*, 9284.
(17) Yin, Y.; Zhao, X. S.*Acc. Chem. Res.* **2011**, *44*, 1172.
(18) Narayanan, R.; Zhu, L.; Velmurugu, Y.; Roca, J.; Kuznetsov, S.V.; Prehna, G.; Lapidus, L. J.; Ansari, A.*J. Am. Chem. Soc.* **2012**, *134*, 18952.
(19) Rant, U.; Arinaga, K.; Tornow, M.; Kim, Y. W.; Netz, R. R.; Fujita, S.; Yokoyama, N.; Abstreiter, G.*Biophys. J.* **2006**, *90*, 3666.
(20) Lapham, J.; Rife, J. P.; Moore, P. B.; Crothers, D. M.*J. Biomol. NMR* **1997**, *10*, 255.
(21) Love, J. C.; Estroff, L. A.; Kriebel, J. K.; Nuzzo, R. G.; Whitesides, G. M.*Chem. Rev.* **2005**, *105*, 1103.
(22) Shon, Y.; Colorado, R.; Williams, C. T.; Bain, C. D.; Lee, T. R.**2000**, 541.
(23) Laibinis, P. E.; Fox, M. A.; Folkers, J. P.; Whitesides, G. M.*Langmuir* **1991**, *7*, 3167.
(24) William M. Steen.*Laser Material Processing*; 3rd ed.; Speinger Verlag: London.
(25) Arnaud, J. A.; Hubbard, W. M.; Mandeville, G. D.; dela Clavière, B.; Franke, E. A.; Franke, J. M.*Appl. Opt.* **1971**, *10*, 2775.
(26) Suzaki, Y.; Tachibana, A.*Appl. Opt.* **1975**, *14*, 2809.
(27) Firester, A. H.; Heller, M. E.; Sheng, P.*Appl. Opt.* **1977**, *16*, 1971.
(28) Schneider, M. B.; Webb, W. W.*Appl. Opt.* **1981**, *20*, 1382.
(29) Hauer, P.; Grand, J.; Djorovic, A.; Willmott, G. R.; LeRu, E. C.*J. Phys. Chem. C* **2016**, *120*, 21104.
(30) Keeler, A. J., Chemistry, University of Southampton, Personal communication, 2018 March.
(31) LeRu, E. C.; Blackie, E. J.; Meyer, M.; Etchegoin, P. G.*J. Phys. Chem. C* **2007**, *111*, 13794.
(32) Kaiser, W.; Rant, U.*J. Am. Chem. Soc.* **2010**, *132*, 7935.
(33) Johnson, R. P.; Gale, N.; Richardson, J. A.; Brown, T.; Bartlett, P. N.*Chem. Sci.* **2013**, *4*, 1625.
(34) Mahajan, S.Engineering Substrates for SERS: Fundamentals and Applications, University of Southampton, 2008.
(35) Edman, C. F.; Raymond, D. E.; Wu, D. J.; Tu, E.; Sosnowski, R. G.; Butler, W. F.; Nerenberg, M.; Heller, M. J.*Nucleic Acids Res.* **1997**, *25*, 4907.

Chapter 4 Intrinsic Surface-enhanced Raman Spectroelectrochemistry of Texas Red

4.1 Intrinsic SER Spectrum and Adsorption of Texas Red on the Au Surface

An unsolved question in the SERS-melting is; why does the Raman intensity of Texas Red-labelled oligonucleotide increase as the potential becomes more negative from - 0.2 to - 0.8 V before then decreasing and ultimately falling to zero at potentials more negative than - 0.8 V? On the other hand, the Raman intensity of Cy5-labelled oligonucleotide has no such effect and maintains similar intensity until the intensity decrease starts at ca. -0.5 to -0.6 V[1]. Mahajan *et al.*[1] attributed this difference to the fact that the Cy5-labelled oligonucleotides had a 6 °C lower melting temperature than the Texas Red-labelled ones which was consistent with the 0.4 to 0.45 V less negative shift in the melting potential. They also discovered that region of falling intensity of Texas Red-labelled and Cy5 labelled oligonucleotides SERS signal can be used for the discrimination by hybridization and melting of the fully-complementary or single mutation target to the immobilised probe. However, the reason of the difference of potential dependent Raman intensity between the two SERS markers is not fully understood. To elucidate this question, a basic experiment was performed observing the Raman spectrum of Texas Red adsorbed on the Au electrode as a function of the potential.

The SSV chips were immersed into a 1 μM solution of Texas Red (sulforhodamine 101) (Sigma-Aldrich) dissolved in 10 mM Tris buffer (pH 7.2) containing 1 M NaCl for 16 h to ensure equilibrium adsorption. After the immersion step, the chips were rinsed with 10 mM Tris buffer (pH 7.2) containing 1 M NaCl for 10 s. The Raman spectroelectrochemical measurement was performed as described in Chapter 2 where the supporting electrolyte is the same as the rinsing buffer. Cyclic voltammetry was then started from -0.3 V (vs. Ag/AgCl) and reversed at two lower potential limits, -0.9 V and -1.2 V, to compare to the earlier dsDNA electrochemical melting experiments monitored by SERS. The results are shown in Figure 4.1.

Surprisingly, the response shown in Figure 4.1 is very similar to what described in Figure 3.13. However, there is no beacon probe attached on the Texas Red in the former case. This result strongly suggests that the increasing and decreasing Raman response during the potential perturbation is an intrinsic property of the Texas Red. However, the adsorption of Texas Red on the Au surface and the origin of its potential dependent Raman scattering is not clear. To clarify the possible mechanism behind this, we will analyse the electronic structure of Texas Red. Since the two N-heterocycle amines are well-understood in their behaviours by both Raman spectroscopy and electrochemistry, valuable information of their electronic structure can provide an explanation for the adsorption of Texas Red on Au electrodes.

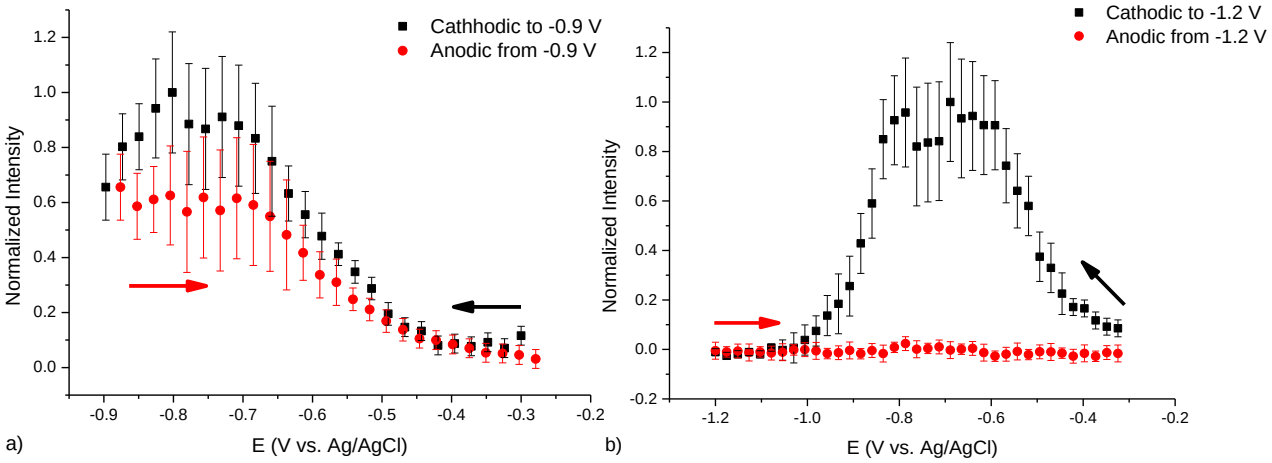

Figure 4.1 The Raman intensity at 1504 cm^{-1} plotted as a function of the potential. The SSV substrates were fabricated using 600 nm diameter polystyrene nanospheres as the template and Au-electroplating to 480 nm thickness. Surface-enhanced Raman spectrum acquired from the SSV chips after immersed into 1 µM Texas Red in 10 mM Tris buffer, pH 7.2 containing 1 M NaCl for 16 h. The SSV chips were rinsed with the 1 M NaCl solution containing 10 mM Tris buffer, pH 7.2 for 10 s. The cyclic voltammetry swept from -0.3 V (vs. Ag/AgCl) to -0.9 V a) and -1.2 V b) and back to -0.3 V individually using the same supporting electrolyte. The arrow indicates the direction of potential sweeping.

The geometry optimisation and the molecular orbital calculations for of Texas Red were performed using Gaussian software version 9. D01 (Gaussian Inc, Wallingford, USA) The detailed frequency analysis for Texas Red will be given in Section 4.2. The basis set used is B3LYP (Becke three-parameter hybrid functional combined with Lee-Yang-Parr correlation functional) at 6-311++G(d,p) level and contains polarisation functions on the C, N, O and S atoms. The structure used for geometry optimisation and the result are shown in Figure 4.2. a) and b). As we can see the Texas Red molecule can be divided into two major moieties. One is the xanthene plane (on the XY plane with respect to Cartesian coordinate) and the other is the 2,4-disulfonate phenyl ring next to the

xanthene plane. Two quinolizidine group, a decahydronaphthalene where one of the bridgehead carbons is replaced by nitrogen N(15), are fused to the lateral sides of the xanthene ring via C-(1)-C(2)-C(3). The other nitrogens, N(16), forms a bicyclic iminium cation linking C(10) with a double bond. Based on the geometry optimisation result, there is a chain of single bond-intercepted double bonds between the two nitrogen, N(16) and N(15), which indicates that π electrons can be delocalised along this conjugated chain and hence stabilise the orbital energy to shift the molecular transition into the visible and infrared region[2]. This resonance stabilisation results in the two nitrogens being indistinguishable in the molecule as shown in Figure 4.2 c) with the charge delocalised over the ring system. Thus in the case of a xanthene dye like Texas Red there is no static dipole moment parallel to the long axis of the molecule in either ground or excited state. This description is consistent with the calculated result shown in Figure 4.2 b) that the static dipole moment is along the direction perpendicular to the long

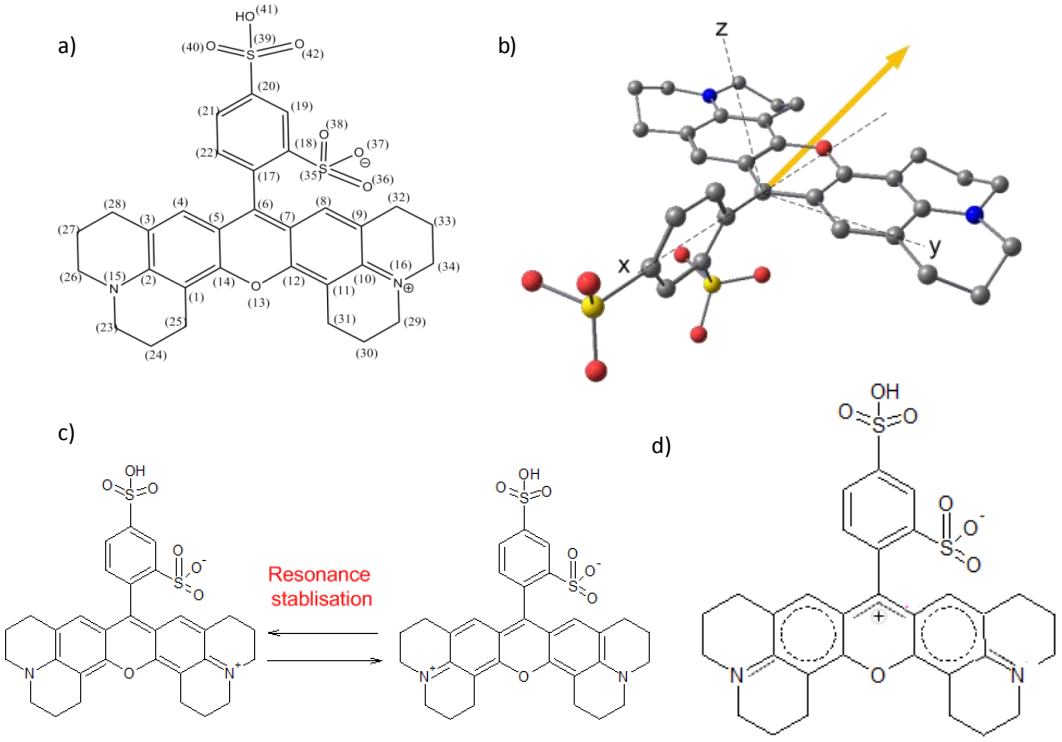

Figure 4.2. a) The original structure of Texas Red used for the quantum calculation. Atomic numbering is for the sake of clarity. b) Geometry optimization of Texas Red structure where the hydrogens are hiden to show the planarity of the xanthene moiety and phenyl sulfonate moiety. The arrow indicates the molecular dipole and the dashed lines are the Cartesian axes. c) The resonance stabilization along the conjugated bonds between the two Ns which are equivalent at the lateral sides of the xanthene plane. d) A schematic of the hybridization of the conjugated chain in the Texas Red is plotted as a dashed line. The positive charge is spread out over the conjugated region.

axis of the molecule. This resonance stabilisation also results in the electronic structure of the two N atoms being sp2 hybridized. On the other hand, the result of geometry optimisation shows the disulfonate phenyl ring is not purely perpendicular (83.3°) to the xanthene plane as was also reported by some authors for the xanthene dyes like rhodamine 6G[3,4]. This asymmetric structure hence reduces the symmetry of Texas Red. This asymmetric conformation has been indicated by Watanabe *et al.*[4] and Jensen *et al.*[3] in the case of the tilted phenyl ring relative to the xanthene plane in rhodamine 6G.

The orientation of Texas Red is expected to be with the xanthene plane parallel to the Au surface. However, the disulfonate phenyl ring is perpendicular to the xanthene plane and hence would tilt the xanthene plane partially up from the surface due to steric hindrance. This inference is well supported by the scanning tunnelling microscope (STM) images of xanthene dyes adsorbed Au electrodes reported by Su *et al.*[5] and Wang *et al.*[6] which presented the xanthene dyes eosin, rhodamine B, and fluorescein, all adsorbed on Au(111), with the orientation of xanthene plane parallel to the Au surface. Other evidence to support this comes from the Au- N, and Au-O bond stretching modes observed in the surface-enhanced Raman spectra. This will be discussed in more detail in Section 4.2 and 4.3.

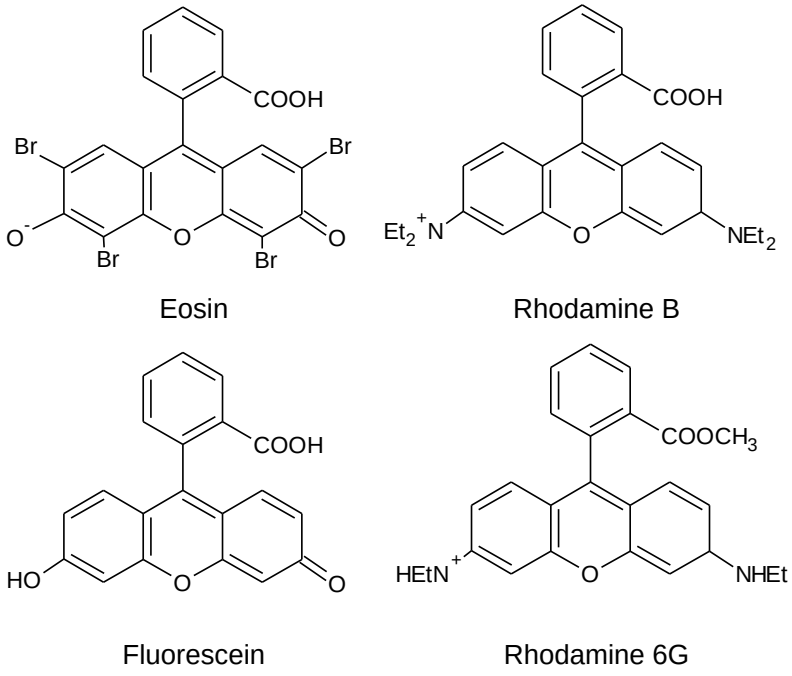

Figure 4.3 Molecular structures of xanthene dyes including eosin, rhodamine B and fluorescein studied by Su *et al.*[5] on Au(111) electrodes using STM and rhodamine 6G studied by Hildebrandt *et al.*[7,8] adsorbed on colloidal Ag. The rhodamine B and rhodamine 6G are the most similar models for the N atoms in Texas Red among the three dyes based on its conjugated structure.

From the Gaussian calculation, the highest occupied molecular orbital (HOMO) of Texas Red is localised on the sulfonate group on the phenyl ring next to the xanthene plane while the HOMO-1 orbital resides at the delocalised π electrons of the xanthene ring system (Figure 4.2 a)). The detailed discussion of the relation between the molecular transition and enhanced Raman intensity will be given in Section 4.7. Here we discuss the chemical interactions between the Texas Red and the Au electrodes that might originate from the delocalized π electrons in the N-C conjugated chain and the lone pairs on O based on the electronic structure. This chemisorption is similar to that for rhodamine 6G adsorbed on the Ag surface reported by Hildebrandt *et al.*[7,8]. The possible orientation of the long axis of Texas Red is parallel to the Au surface. We will discuss further the orientation of Texas Red during the potential perturbation in the next section.

4.2 Orientation and Vibrations of Texas Red on Au Electrodes during Potential Perturbation

Having discussed the adsorption of Texas Red on the Au surface, we now consider if the potential dependent Raman intensity of Texas Red can be attributed to orientation changes as the result of the change in potential. To answer this question, we need to extend the spectral range to collect more Raman bands which can provide characteristic information for determination of the orientation of the molecule. The following electrochemical SER spectra were acquired from the SSV surface, modified by adsorption for 1 μM Texas Red in 1 M NaCl containing 10 mM Tris buffer (pH 7.2) for 16 h to ensure equilibrium adsorption. The linear sweep voltammetry ranges from 0.2 V to -1.2 V (vs. Ag/AgCl) in 1 M NaCl containing 10 mM Tris buffer (pH 7.2). The scan rate was reduced to 0.34 mV s^{-1} to allow for the 55 s exposure time required for the collection of extended mode Raman spectrum from 120 to 1704 cm^{-1}. This region was selected because it covers most of the characteristic bands during the scan. The resultant spectra are shown in Figure 4.4.

Obviously, the Raman intensity of the 12 selected bands changes with the potential, *E,* and they reach their peak at -0.8 V (vs. Ag/AgCl) in the cathodic sweep from 0.2 to -1.2 V. No new bands occurred in the potential window when comparing the spectra between the initial (0.2 V) to the most intense (-0.8 V), which implies that the Texas Red remains intact as shown in Figure 4.4. b) and c). The 12 Raman bands were selected for the following vibration analysis and the band assignment. The enhanced ratio was normalised based on the initial intensity at 0.2 V of each selected band depicted in Figure 4.5 a) to l) to clarify the enhancement effect.

The potential dependent enhancement results in an approximately 10 fold increase in intensity across the potential range from 0.2 V to -1.2 V (vs. Ag/AgCl). From the enhanced Raman intensity observed between the 12 bands, the error bar of each band seems to be proportional to the enhanced Raman intensity as shown Figure 4.5. The selection of the anchor points in the Raman spectrum at 0.2 V to perform the baseline subtraction may contribute to the variation of the enhanced Raman intensity ratio. The relatively weak bands E, F and H also result in fluctuation in intensity in the potential window of 0.2 to ca. -0.4 V. However, overall the potential dependent Raman enhancement between the 12 bands was consistent with each other.

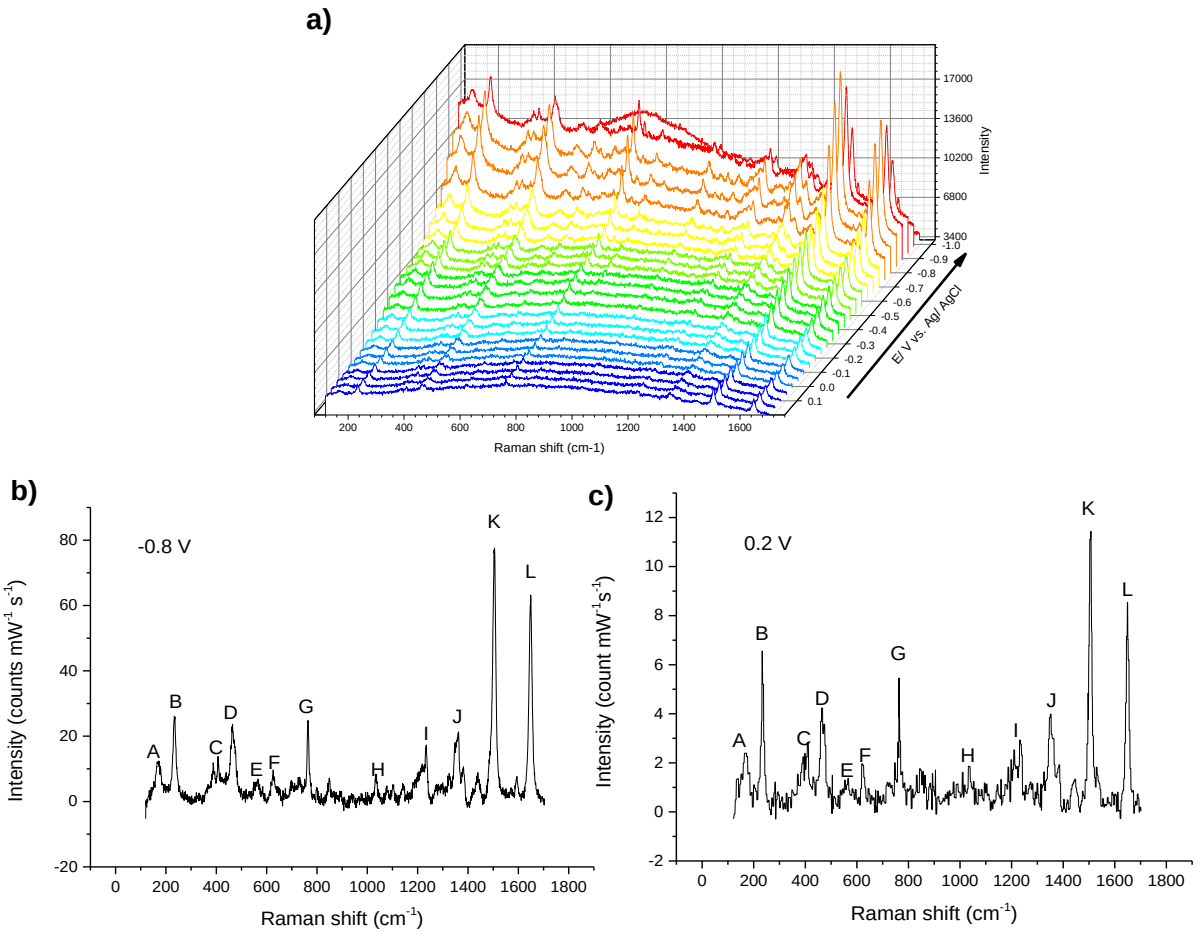

Figure 4.4 a) Extended mode Raman spectra under the potential perturbation from 0.2 V to -1.0 V (vs. Ag/AgCl) from 120 to 1704 cm^{-1} at 0.34 mV s^{-1}. The SSV substrate was modified by adsorbing a solute of 1 µM Texas Red, in 1 M NaCl containing 10 mM Tris buffer (pH 7.2) for 16 h. The substrates were then rinsed with 1 M NaCl containing 10 mM Tris buffer (pH 7.2) for 5 s before the electrochemical Raman measurement. Each Raman spectrum was acquired in 1 M NaCl containing 10 mM Tris buffer (pH 7.2) at 633 nm excitation (2.3 mW) during the potential sweep. The peak background around -1.0 V will be discussed in Section 4.5. The intense Raman spectra at -0.8 V (b) and 0.2 V (c) with the dominant 12 bands was labelled with capital letters. The potential dependent Raman-enhanced intensity ratio were obtained by dividing the Raman intensity of selected bands by the correspondent Raman intensity at 0.2 V. The enhanced Raman intensity ratios of each band are plotted as a function of the potential in Figure 4.5 a) to l) and listed in Table 4.1. The arrow indicates the direction of potential sweeping.

The symmetry of Texas Red, based on the geometry optimisation result in Section 4.1, was further assigned by the principles of the symmetry determination. Due to the absence of an appropriate axis and reflection plane to perform a symmetric operation, Texas Red is assigned to the C1 point group for which all the vibrational modes are Raman active and totally symmetric.

la-

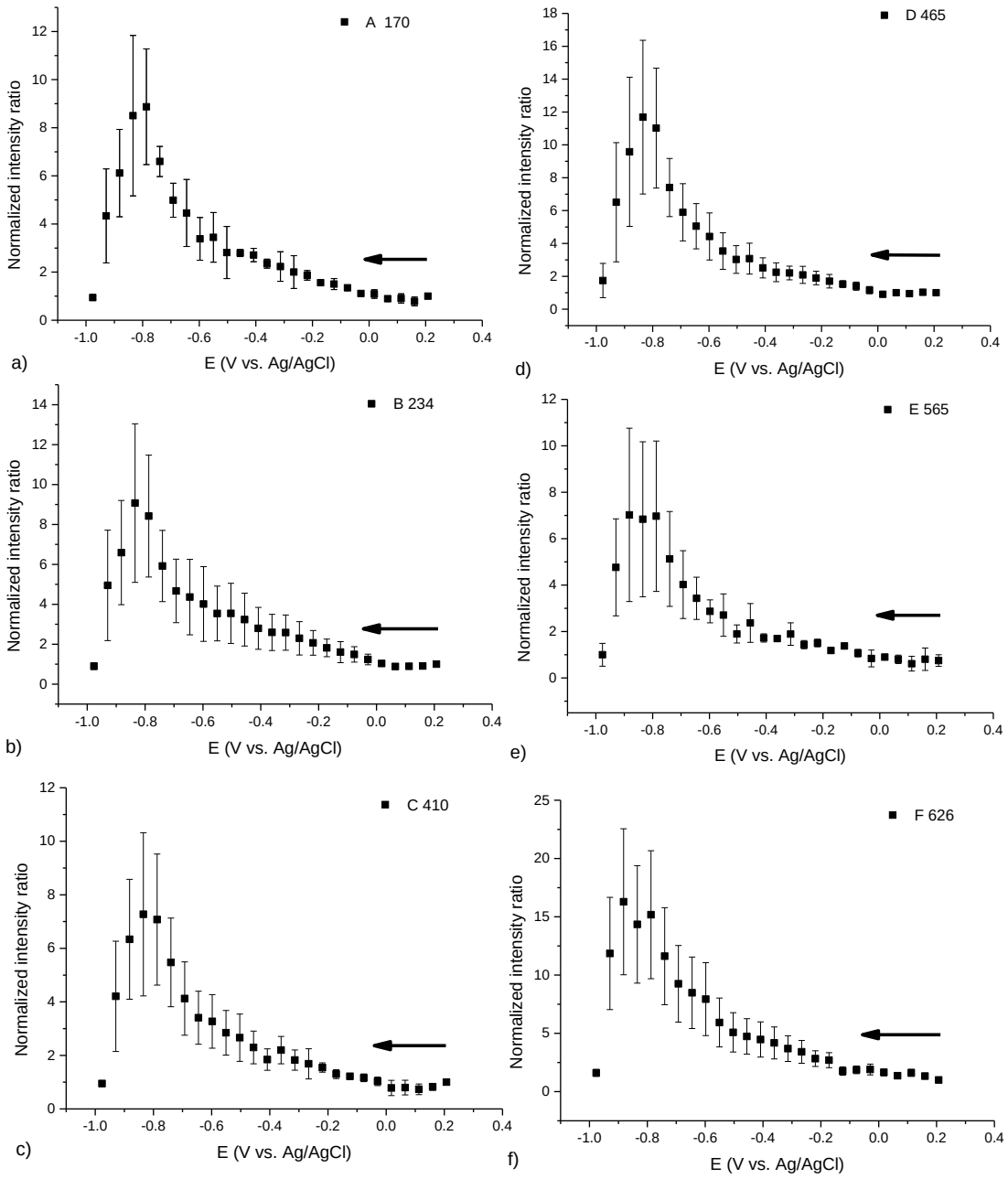

Figure 4.5 Raman intensity of the individual band A to F (a) to f)) selected from the Raman spectra of Texas Red from 120 to 1704 cm^{-1} as a function of the potential perturbation from 0.2 V to -1.0 V (vs. Ag/AgCl) at 0.34 mV s^{-1} in 1 M NaCl, 10 mM Tris buffer (pH 7.2). The SSV substrate was modified by adsorbing for a solute of 1 μM Texas Red, in 1 M NaCl containing 10 mM Tris buffer (pH 7.2) for 16 h and rinsed with 1 M NaCl, 10 mM Tris buffer (pH 7.2) for 5 s before the Raman measurement. Each Raman spectrum was measured in 55 s exposure at 2.3 mW 633 nm excitation. The arrow indicates the direction of potential sweeping.

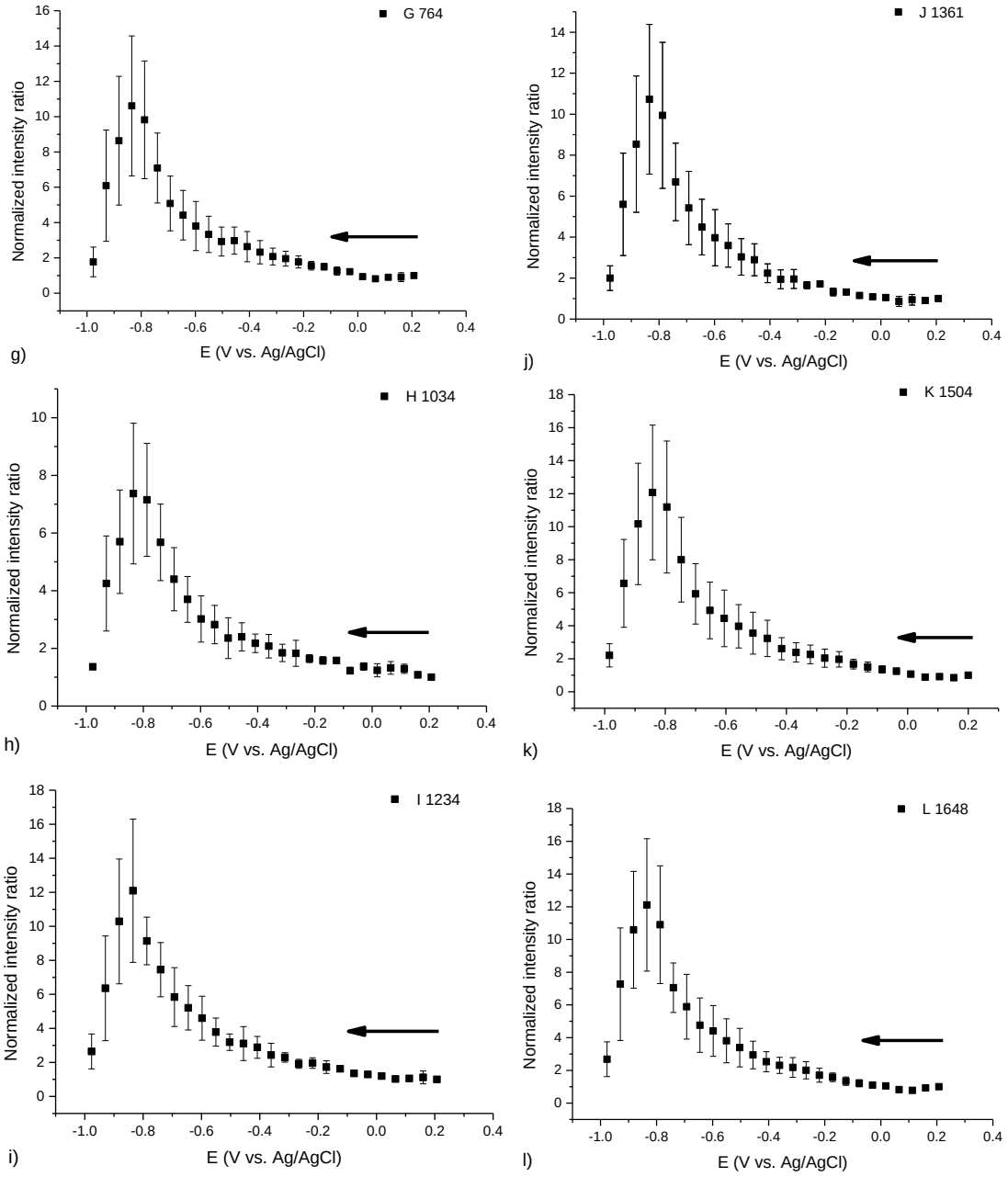

Figure 4.5 (continued) Raman intensity of the individual bands G to L (g) to l)) selected from the Raman spectra of Texas Red from 120 to 1704 cm^{-1} as a function of the potential perturbation from 0.2 V to -1.0 V (vs. Ag/AgCl) at 0.34 mV s^{-1} in 1 M NaCl, 10 mM Tris buffer (pH 7.2). The SSV substrate was modified by adsorbing for a solute of 1 μM Texas Red, in 1 M NaCl containing 10 mM Tris buffer (pH 7.2) for 16 h and rinsed with 1 M NaCl, 10 mM Tris buffer (pH 7.2) for 5 s before the Raman measurement. Each Raman spectrum was measured in 55 s exposure at 2.3 mW 633 nm excitation. The arrow indicates the direction of potential sweeping.

Table 4.1 The SERS band assignment based on the selected normal modes of Texas Red determined at the B3LYP/6-311++G(d,p) level and the literature[3,9–12]. The resolution of the Raman spectrometer is ca. 2 cm^{-1} in 1200 lines mm^{-1} grating density and 633 nm excitation.

Band label	Calculated Raman band		SERS band observed		Band assignment [3,9–12]
	Normal Mode No.	υ_{cal} (cm^{-1})	υ_{SERS}(cm^{-1})	Potential dependent enhanced ratio of peak intensity between 0.2 to -1.2 V	
A			170	8.8±2.4	Au-O stretching
B			234	9.0±3.0	Au-N stretching
C	41	384	410	7.2±2.4	Xanthene deformation
D	50	464	465	11.6±3.6	
E	61	584	565	6.8±3.2	C-C-C ring in-plane deformation
F	64	621	626	14.3±5.0	
G	74	753	764	10.6±3.3	C-H out-of-plane deformation
H	103	1031	1034	7.1±1.9	C-H in-plane deformation
I	130	1236	1234	12.0±4.2	C-O-C xanthene stretching
J	144	1363	1361	10.7±3.5	C-N/C-O stretching, C-H in-plane bending
K	168	1503	1504	12.0±4.0	Xanthene plane stretching
L	178	1650	1648	12.1±4.0	

The band assignment shown in Table 4.1 was based on the vibration analysis of the quantum calculation described in Section 4.1 at the level of B3LYP/6-311++G(d,p) and compared with the xanthene dyes from the literature[3,9–12]. The vibration patterns were visualised by the atomic displacements as shown in Figure 4.6. The atomic displacement of selected normal modes is larger for the hydrogen of lower atomic weight and smaller for the heavy atom like carbon, nitrogen and sulphur. The calculated scattering frequencies was scaled by the scaled quantum mechanics force field (SQMF) procedure used to analyse vibrational bands of all fundamentals[13,14]. The SQMF was a selective scaling factor used in vibration analysis. The calculated scattering frequency in Gaussian based on the harmonic oscillator model was obtained from the conversion of the elastic potential energy of reduced mass into the vibration energy. However, this model does not consider the anharmonicity of the molecular vibrations which cause the energy gaps between the adjacent energy levels to be unequal as the vibrational quantum number increases[15]. These deviations in the energy gaps also reflect on the Raman shift calculated for the harmonic oscillator and hence there have to be modified by the scaled quantum mechanics force field. For simpler molecules, a uniform scaling factor may provide satisfactory calculation when compared to the experimental result. However, in the case of larger molecules, Pulay *et al.*[16] have developed a selective scaling factor

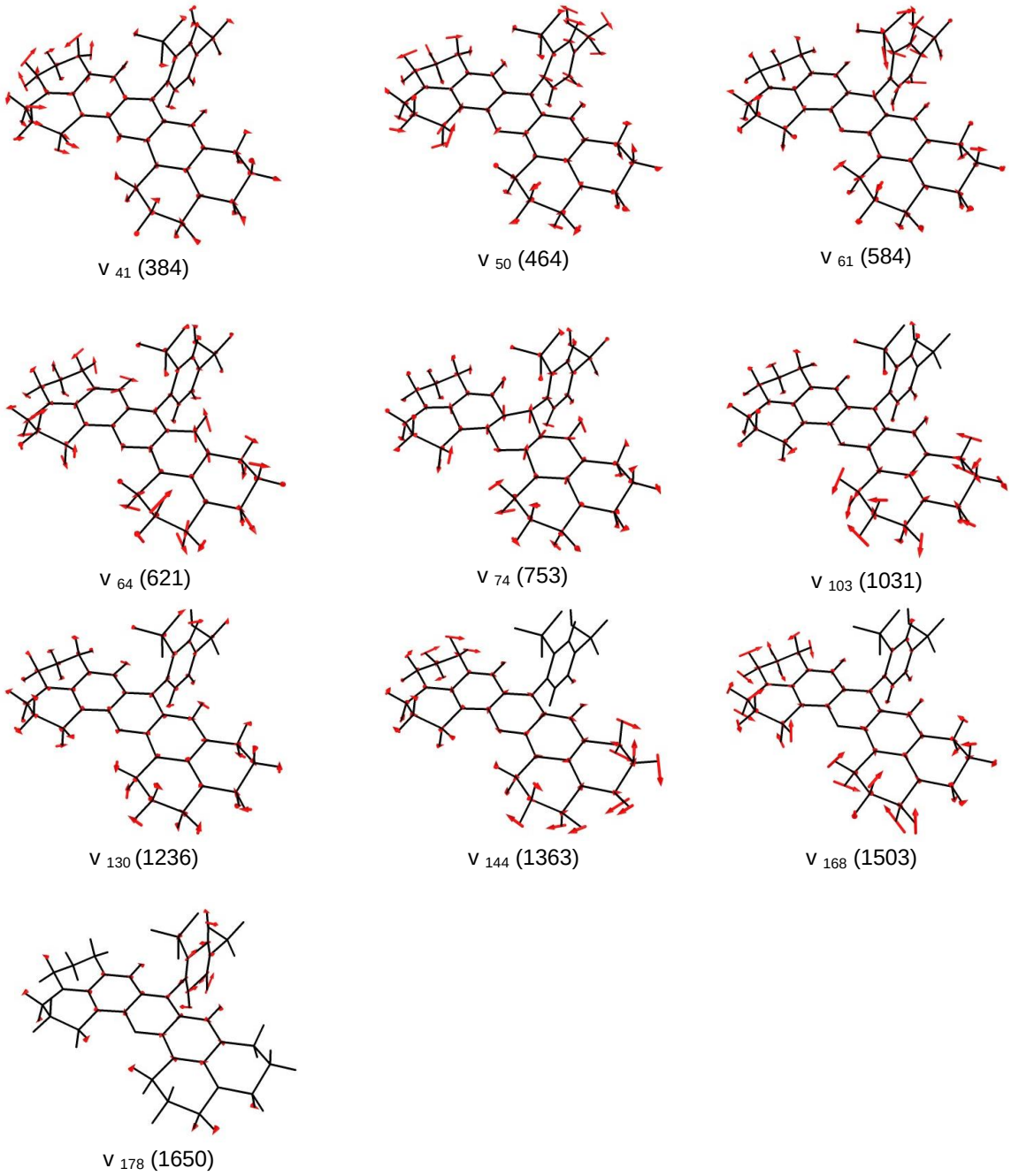

Figure 4.6. Vibrational patterns of the normal mode of Texas Red. The scaled quantum mechanics force field (SQMF) procedure was used to analyse vibrational bands of all fundamentals[13,14]. Mode numbers and calculated frequencies scaled by two factors, 0.992 at the frequencies below 1584 cm^{-1} and 1.01 for above 1584 cm^{-1}. See the text for the details of scaled quantum mechanics force field (SQMF).

based on the scaled quantum mechanics force field (SQMF) to prove better agreement. Here the calculated frequencies were scaled by two factors, 0.992 for the frequencies below 1584 cm^{-1} and 1.01 for frequencies above 1584 cm^{-1}. This scaling reduced the frequency deviation between the calculated and experimental observed frequency to approximately 15-20 cm^{-1}, an acceptable range as described by Krishnakumar *et al.*[14] On the other hand, the resultant normal modes have good agreement to the vibration assignments in the literature for xanthene dyes[3,9–12].

The orientation effects of molecules in surface-enhanced Raman scattering were demonstrated experimentally and theoretically by Moskovits and coworkers[17,18]. They examined the surface enhanced Raman spectra of heteroaromatic compounds including quinolone and pyridine. At low coverage and saturated coverage they found differences in the intensity of the in-plane and out-of-plane vibrations which they interpreted as the result of reorientation. Moskovits and coworkers[17] have discussed the surface selection rules for SERS. Two mechanisms contribute to the orientation dependence of Raman intensity. The first mechanism is the symmetry reduction due to the formation of the molecule-metal complex. The second mechanism is the field gradient mechanism. The symmetry reduction takes account of the fact that the higher symmetry of the molecule may be reduced as a result of being adsorbed on the metal surface to form a molecule-metal complex. In the case of strongly adsorbed molecules, the symmetry reduction can be critical in the surface-enhanced spectra. On the other hand, the field gradient mechanism arises because the electromagnetic enhancement will be lower when the distance of the molecule increases from the metal surface. Moskovits and his colleagues concluded the field gradient mechanism is the major factor in the case of molecular orientation. If we denote the surface normal as the Z_S direction the excitation irradiates around of the red of the surface plasmon frequency of an SERS-active substrate. The molecular polarizability α can be divided into three components along the surface normal Z_S. Since the electromagnetic field of light which contributes to the major scatterings enhancement is most intense in the surface normal Z_S, therefore the α_{zz} is more intense than α_{zx} and α_{zy} [17]. The totally symmetric modes, which are often most intense, will vary their polarizability component, α_{zz}, during the re-orientation process. Consequently the resultant change in the relative intensity can be probed in this way. They further suggested that the C-H stretching modes (in-plane deformation) of planar aromatic molecules can used as an indicator of orientation[18]. For example, if the planar aromatic molecules is adsorbed on the metal surface in a perpendicular orientation to the surface normal, the C-H in-plane deformation modes are expected to be more intense than the C-H out-of-plane vibrations. Additionally, since the surface selection rule recognised by Moskovits and his colleague was studied on the planar metallic surface which misses out the orientation effect

because of the interaction of the field normal to the surface with the polarizability tensors of the molecule. Le Ru and Etchegoin[19] discussed the recent studies on the more realistic substrates containing hot spots. For the SSV substrate, Cole *et al.*[20] have concluded that the analytic solutions for the electromagnetic problems are not yet possible. The detailed EM approximation of the Raman tensor related to the molecular orientation is beyond the scope of this thesis. Here we will discuss the Moscovits' surface selection rule which has been proved to explain the molecular orientation by several groups[13,21–24] mainly based on colloidal SERS substrates.

We, therefore, compare the potential dependent intensity of the Raman bands at 764 cm^{-1} and 1034 cm^{-1} which are assigned to the C-H out-of-plane deformation and C-H in-plane deformation respectively. The C-H out-of-plane deformation is the vibration moving along the Z_m-axis with the respect to the xanthene plane while the C-H in-plane deformation means the vibration is moving in the X_mY_m plane of the xanthene plane. Since to the two vibrations are perpendicular to each other, their polarizability component α_{zz} would change during the re-orientation process in the opposite way[13]. However, the result shown in Figure 4.6 clearly shows that the potential dependent Raman intensity for the two vibrations in the selected potential window were approximately synchronised to their peak enhancement at ca. -0.8 V. This data is different to the potential dependent re-orientation case of 1-butyl-3-methylimidazolium cations (BMI) [13] and phthalazine [17,25], in the literature. The α_{zz} polarizability components should have an approximately linear increase if the

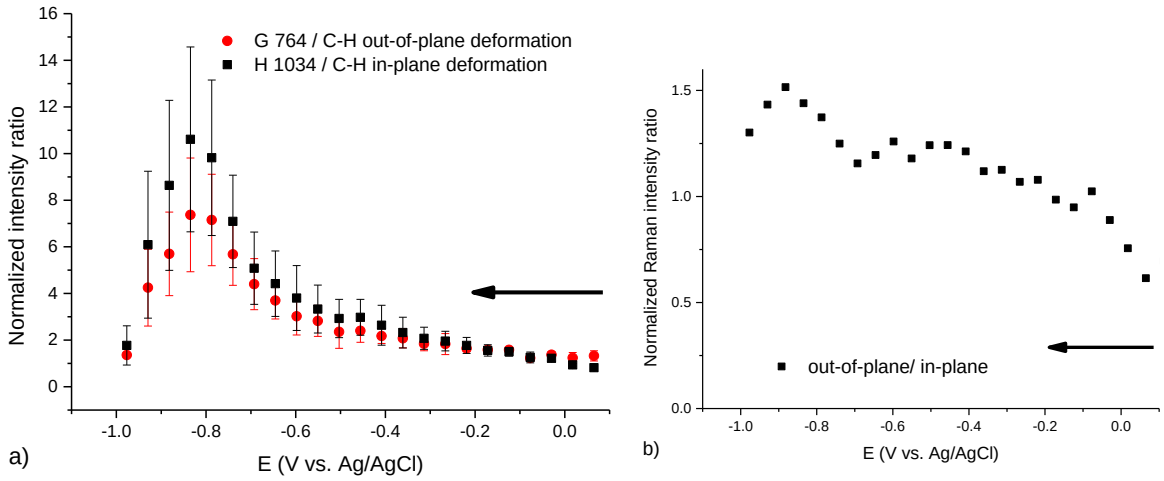

Figure 4.6 a) Potential dependent intensity of the Raman bands at 764.4 cm^{-1} and 1034.4 cm^{-1} which represent the out-of-plane deformation and in-plane deformation respectively in the cathodic sweep from 0.2 to -1.2 V at 0.34 mV s^{-1} in 1 M NaCl, 10 mM Tris buffer pH 7.2. b) the Normalized intensity ration calculated by dividing the Raman intensity of the out-of-plane band (764 cm^{-1}) by the in-plane band (1034.4 cm^{-1}). The arrow indicates the direction of potential sweeping.

aromatic plane was tilted from flat to perpendicular orientation during the potential change while the other polarizability component α_{zx} and α_{zy} did not. Our SERS data, interpreted by the surface selection rule, do not support the re-orientation of Texas Red adsorbed on the Au SSV substrates over the selected potential window. Based on the Raman intensity ratio of C-H out-of-plane/C-H in-plane shown in Figure 4.6 b), one can note the ratio between the 2 vibrational modes is clearly changing with potential. Therefore a change in orientation is occurring. The aromatic plane of Texas Red tends to move from the laying-down toward perpendicular (to the surface) from 0.1 to -1.0 V. Although the potential dependent orientation seems not completely correlate to the corresponding Raman response, we could not rule out that change in orientation is not contributing to the potential dependent intensity. On the other hand, the potential dependent orientation change does not fully explain the intensity changes in some regions including 0.1 to -0.3 V and also -0.8 to -1.0 V where the Raman intensity stays unchanged and decreases respectively. Consequently, the potential dependent Raman enhancement of Texas Red may partially attribute to the re-orientation under the potential perturbation, but this also suggests there is still another factor(s) which contribute to the overall potential dependent Raman enhancement.

4.3 Potential-tuning Effect of Distance Dependence of Surface Plasmon Resonance

Serveral recent studies[26,27] have shown that surface plasmon resonance can be tuned by appling an external electric field on the substrate in solution. This tuning results in a shift in the chracteristic wavelength of LSPR and may enhance/decrease the electromagnetic mechanism at a given excitation wavelength. Overall this results in a change in the scattering cross section and leads to an intensity change for surface-enhanced Raman scattering. We will discuss the effect, and the possible influence in our system, in detail in this Section.

Jeanmaire and Van Duyne in their siginificant work[28] in 1977 first suggested that the potential dependent electric double layer might have an effect on the resultant surface–enhanced Raman intensity. This electric double layer, caused by the external potential, results in perturbation to the dipole moment induced at the proximity of the interface and hence affects the photon-electron coupling of plasmons. Recent works by Byers *et al.*[26] and Brown *et al.*[27] demonstrated that an external electric field applied to a plasmonic substrate affects the chracteristic frequency of surface plasmon resonance.

In the work of Byers *et al.*[26], the surface plasmon was measured for 50 nm Au nanoparticles deposited on indium tin oxide (ITO) to provide a transparent conducting surface to allow the variation of the potential. A condenser lens was used to collect the reflectence spectrum which represents the surface plasmon absorption. An 8 meV blueshift of the surface plasmon frequency was observed in 25-50% of the 50 nm Au nanoparticles at -0.8 V (vs. Ag) relative to 0.4 V in 100 mM NaCl. The wavelength shift of the chracteristic suface plasmon resonance was equal to ca. 10 nm on switching from 0.4 V to -0.8 V (vs. Ag). A similar blueshift in the LSPR have been reported by other authors for negatively charged gold nanorods [29,30] .

As explained in Section 1.2 , a shift in the wavelength of the local surface plasmon resonance (LSPR) can affect the enhancement factor in SERS. A correlation between wavelength of LSPR and the SERS enhancement factor was studied by Van Duyne's group[31]. They indicated that the maximum enhancement takes place when the featured LSPR wavelength falls midway between the exitation raidation and the Stoke's shift of the Raman band based on the nanosphere lithography substrates. However, the correlation between LSPR and SERS intensity in the spherical segement voids (SSV) substrates is more complicated. Cole *et al.*[20] used the boundary element method (BEM)

to model the electric field and the resultant angle-dependent plasmon mode. Mahajan *et al.*[32] followed the electrical field distribution of the surface plasmons of the SSV surface calculated using the result of Cole *et al.*[20] and interpreted the SERS intensity change with the plasmon modes at different deposition thickness at specific angle. The most relevant plasmon modes near the 633 nm excitation is the $1P_+$ (green) and $1P_-$ (black) modes as shown in Figure 4. The $1P_+$ mode possesses a field distribution aligned across the cavity, with charge nodes located within the rim, and a field distribution in the plane of the rim. This mode provides a strong field enhancement directly at the metal rim as well as a significant field enhancement at the center of the cavity opening[20]. The $1P_-$ mode also has a strong field component at the metal rim, but the void mode and rim contributions have field components aligned in antiphase; in this case, the void field component is forced deeper into the void[20]. The distribution of the plasmon modes is also affected by the interface dielectric as shown in Figure 4. 7 a). When the reflectance spectra were measured in water (n = 1.3) a significant redshift can be observed and they also indicated that a factor of 3 may be accounted for by the increased refractive index of water (n = 1.3) which reduces the electric field, reducing the SERS by n^4. On the other hand, the SERS intensity was plotted as a blue dot where the dot diameter represents the SERS intensity for the probe molecule, benzenthiol. One can note that the thickness distibution of intense SERS signal became narrower when the dielecctric changes

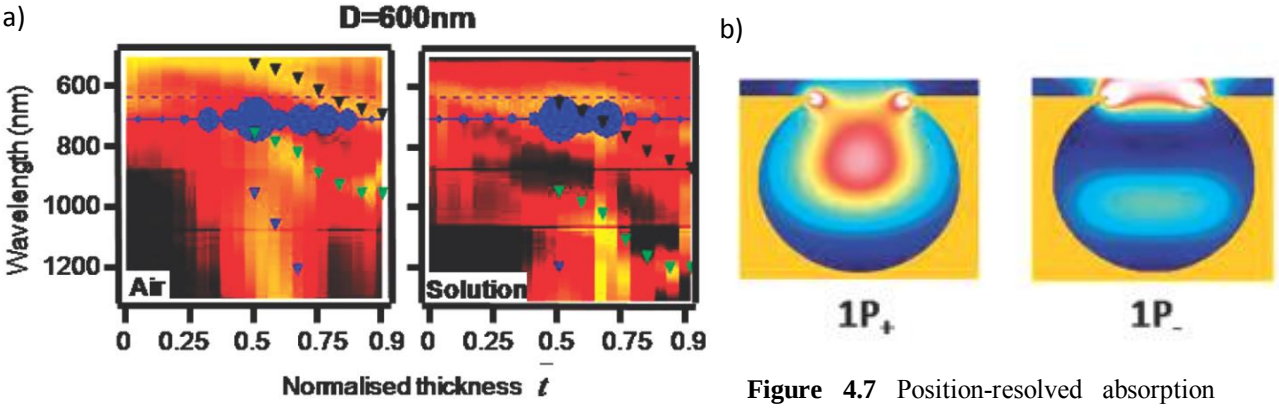

Figure 4.7 Position-resolved absorption maps with the SERS intensity overlaid for SSV substrates fabricated with sphere diameters D = 600 nm, recorded in air and water shown in a). The blue spot size corresponds to the background corrected peak intensity of the 1571 cm^{-1} band of benzenethiol The dashed blue line indicates the 633 nm laser input. The plasmon modes indicated by triangles are as follows: (blue) low energy mode, (green) $1P_+$, (black) $1P_-$, (gray) 1D. The plotted plasmon mode energies are extracted in air and scaled for the solution refractive index. b) Fields of identified modes. The maximum *E*-field enhancement for the $1P_+$ mode is 60 while for the $1P_-$ mode it is about 3 times weaker. Adpted from Ref. [32]. Copyright © (2009) of American Chemical Society.

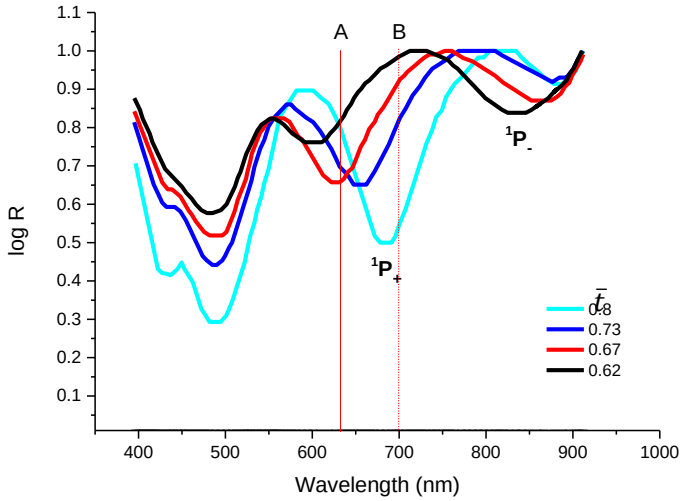

Figure 4.8 Adapted from Cintra *et al.*[33]. The reflectance spectrum of the SSV substrate for varied deposition thickness. $\bar{t}$ represents the ratio of the deposited film thickness to the nanosphere diameter (600 nm). Line A is the excitation radiation (633 nm). Line B is the selected Stoke's shift Raman band for Texas Red 1504 cm^{-1}. (Reproduced from Ref. [33]. with permission, Copyright© (2006) of the Royal Society of Chemistry.)

from air to water. The local intense SERS signals for different deposition thickness are scattered at ca. $\bar{t}$ = 0.25 to 0.8, a wider range in the air dielectric, but reduced to a narrower thickness range ($\bar{t}$ = 0.5 and 0.73) when the substrate was immersed in water due to the higher reflection index. Another feature is the maximum SERS intensity is the approximate match to the corresponding plasmon mode for $^1P_+$ (green) in the case of air and $^1P_-$ (black) in water. Mahajan *et al.*[32] further explained that the SERS enhancement doesnot necessarily correlate to absorption by plasmons but has a complicated dependence on both the geometry of the SSV surface and the plasmon field profile. A balance is expected between more radiative modes which have better out-coupling of the inelastically scattered plasmons, compared to more localized modes which have larger plasmon field confinement at the metal-molecule interface. Mahajan *et al.'s* experiments reveal that absorption is indeed by far the greatest contribution to extinction by these structures, and indeed we see good correlation with SERS in Figure 4.7. While quantitative comparison of the enhancement due to different modes at the same position on a sample is complicated by the different efficiencies of the three very different Raman spectrometers employed in their study, they find that similar SERS enhancements are found for each plasmon type (except for delocalized plasmons which show little SERS enhancement). This is broadly confirmed by their simulations which track the optical field averaged around the metal surface and the input and output plasmon coupling. Hence,

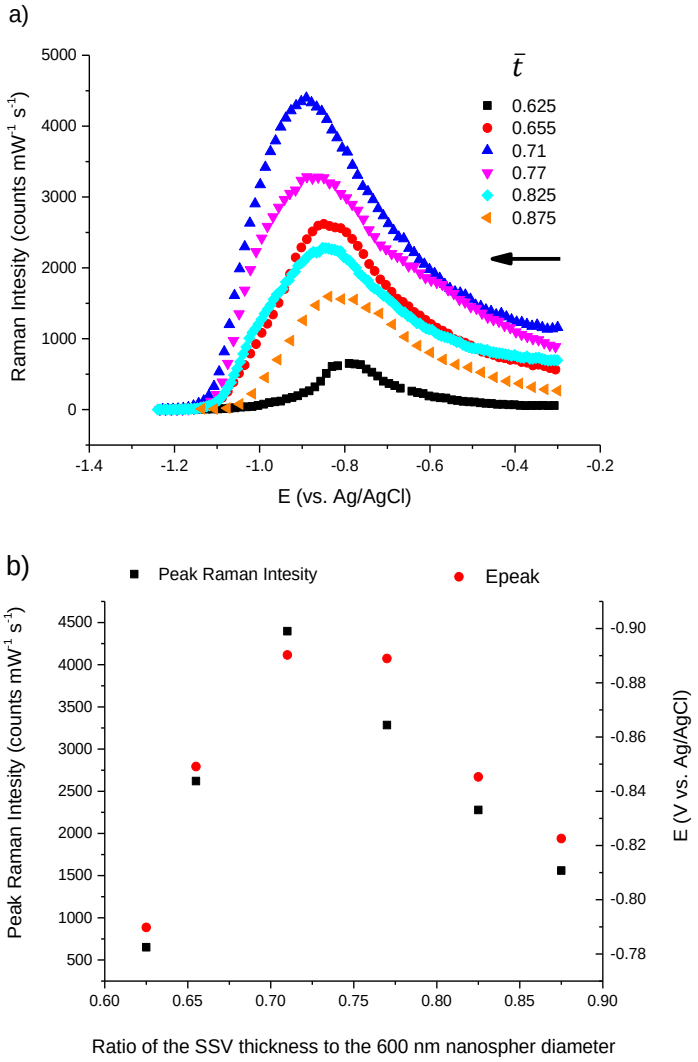

Figure 4.9 The Raman intensity of Texas Red (1504 cm^{-1} band) plotted for the potential sweep from -0.3 to -1.25 V at 1 mV s^{-1} in 1 M NaCl, 10 mM Tris buffer (pH 7.2). Laser power was 2.3 mW for 633 nm excitation. The SSV substrates were fabricated as described in Section 2.1 with varied deposition thicknesses, $\bar{t}$, from 0.625 to 0.875. Each substrate was immersed in 1 µM Texas Red solution containing 1 M NaCl and 10 mM Tris buffer (pH 7.2) for 16 h to ensure equilibrium adsorption. The SSV substrates were rinsed with 1 M NaCl and 10 mM Tris buffer (pH 7.2) for 5 s before the Raman measurement. a) The potential dependent Raman intensity b) The left axis denotes the correlation of the maximum Raman intensity under the potential perturbation as a function of the deposit thickness. The right axis depicts the potential at the maximum Raman intensity also related to the deposit thickness. Note the scale of the right axis was set at the range of -0.78 V to -0.9 V to show the plasmon-dependent potential shift. The arrow indicates the direction of potential sweeping.

for the SSV substrates, all the localized plasmon resonances are effective in providing efficient SERS[32].

The reflectance spectrum studied by Cintra *et al.*[33] gave another perspective of the reflectance spectrum in Figure 4.8. The $1P_+$ mode and $1P_-$ mode was shown as an dip in the 600-700 nm and 850-900 nm range respectively. As the deposition thickness, $\bar{t}$ (the ratio $\bar{t}$ of the deposited thickeness to the diameter of the nanosphere) increases from 0.62 to 0.8, a redshift is shown for both $1P_+$ and $1P_-$ modes. Line A is the 633 nm excitation and Line B the Stoke's shift for the Raman band at 1504 cm^{-1} (equal to 699.3 nm) of Texas Red. Based on Mahajan *et al.*'s work[32] on the correlation between the thickness, the plasmon modes and the SERS enhancement, we chose the deposition thickness from 0.62 to 0.87 for the following experiment as the corresponding surface plasmon spectra are in close proximity to the excitation and scattering wavelengths.

If one assumes that a negatively charged potential dependent blueshift occurrs on the SSV substrate, the blueshift of ca. 10 nm of the potential-shifted reflectance spectrum of LSPR would result in a change (increase or decrease) on the corresponding SERS enhancement. To test this assumption between the potential dependent LSPR shift and the resultant Raman intensity, 5 different thicknesses ranging from $\bar{t}$=0.625 to 0.875 of the SSV substrate were immersed in 1 μM Texas Red, 1 M NaCl containing 10 mM Tris buffer (pH 7.2) for 16 h. The SSV substrates were then rinsed with 1 M NaCl containing 10 mM Tris buffer (pH 7.2) for 5 s. The following Raman spectra were aquired at 1 mV s^{-1} from -0.3 to -1.25 V (vs. Ag/AgCl) in 1 M NaCl containing 10 mM Tris buffer (pH 7.2). The resultant plots are shown in Figure 4.9. By comparing with Cintra's work, $\bar{t}$ =0.625 to 0.875 were selected for the deposit thickness to cover more than 100 nm range of the LSPR relflectance spectrum. In the absence of applied potential, the local mxaimum of SERS intensity is located at the $\bar{t}$ =0.71 substrate and is ca. 10 times stronger than the SERS intensity of the $\bar{t}$ = 0.625 substrate. This 10 fold increase in SERS intensty between the two thickness is consistent with their SERS intensity at -0.3 V. The overall SERS intensity for the variant thicknesses changes with the potential *E*. The largest enhancement in the absence and presence of external potential is at about $\bar{t}$ = 0.71 which is consistent with the simple model in the Figure 4.8 for the reflectance spectra. Second, in all cases the intensity increases as the potential scans negatively toward their peak SERS intensity.

If the increase in Raman signal on scanning from -0.3 to -0.8 V (vs. Ag/AgCl) were due to a potential dependent blueshift in the LSPR for the $^1P_+$ then we should expect an increase in enhancement for the thicker film (ex. $\bar{t}$ =0.8) but a decrease for the thinner films (ex. $\bar{t}$ =0.62). Clearly this is not the case.

The other interesting result observed in Figure 4.9 is the maximum shift to more negative potential as the enhancement gets bigger. The possible explanation is not known at this moment and we focus on the potential *E* dependence increase of SERS intensity.

4.4 Irreversible Loss of the Potential Dependent Raman Intensity of Texas Red

The reversibility with potential cycling of the molecular Raman intensity at a charged SERS-active electrode is of interest to many researchers both in respect of the fundamentals and in sensor applications. Molecular Raman scattering gains intensity enhancement from localized surface plasmon resonance based on the interactions between the electric field of the radiation and free electron oscillation of the metal nanostructures especially at high curvature sites (also referred to as hot spots). A change in geometry of these nanostructures, for example at the scale of 10 nm, can cause a 10-fold change in the Raman enhancement in the case of the increased distance between the two tips of the pairs of Au nano-triangles in bowtie strucutres[34]. However, this subtle change of the nanostructure geometry may take place at a charged surface and result in the irreversible loss of Raman intensity. Several authors had reported this phenomenon for various SERS-active substrates including nanoparticles and metal films deposited on nanospheres[35,36]. The observation of mophological changes and the simultaneous collection of the Raman spectra is difficult, nevertheless some authors speculated that this irreversible loss is due to the deformation of the nanostructure at high cathodic potentials[37,38]. Connecting change of nanostructure geometry with the spectra is very difficult because subtle changes at the 10 nm scale may result in drastic variations in Raman enhancement. An ideal measurement of nanoscale at 10 nm resolution combined with a Raman sampling spot at an equivalent 10 nm scale on a charged substrates may be able to give direct experimental evidence but, to the best of our knowledge, such *in situ* observation has never been reported. Van Dyune and coworkers[36] used an alternative method to compare the roughness of Ag electrodes fabricated by depositing an Ag film over nanosphere (MFON) before and after one potential cycle from -0.7 to -1.2 V (vs. Ag/AgCl). According to AFM observation, the electrode RMS (root mean square) roughness was reduced from 30 to 50 nm to approximately 20 nm. A corresponding decrease of 30% in Raman intensity of the 1008 cm^{-1} pyridine band was attributed to this loss of roughness as shown in Figure 4.16. Conversely, the other Ag electrode fabricated by roughening using oxidation/reduction cycling, lost more than 80 % of the Raman intensity for the same band for adsorbed pyridine. Moreover, Abdelsalem *et al.*[38] used the sphere segment void (SSV) Au electrode surface and observed the SERS of adsorbed pyridine, the SERS signal reduces dramatically at potentials below -1.2 V (vs. SCE) and when the electrode was returned to more positive potentials the pyridine signals did not return to the same intensity.

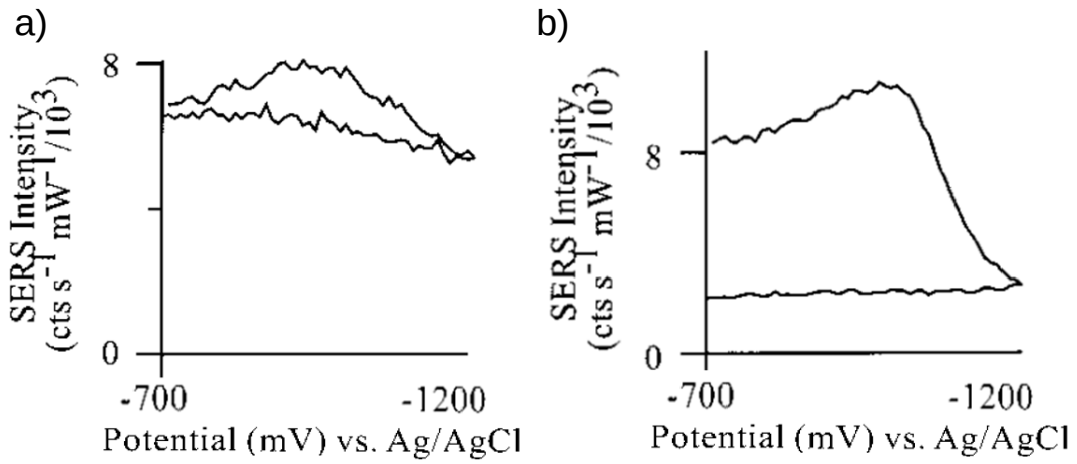

Figure 4.10 SERS detected during cyclic voltammetry. SERS intensity of the 1008 cm^{-1} band of pyridine as a function of potential. (a) Ag film over nanosphere electrode and (b) *in situ* Ag electrode fabricated by oxidation/ reduction cycling (25 mC cm^{-2}). Laser excitation was 4 mW at 632.8 nm, 0.1 s dwell time, 50 mM pyridine in 0.1 mM KCl (Reproduced with permission from Ref.[36] , Copyright© (2002) American Chemical Society)

Abdelsalem *et al.*[38] attribute this to the formation of hydrogen in the pores at -1.6 V since when the electrode was thoroughly wetted by a fresh solution of pyridine the SERS signal returned to its original intensity demonstrating that this substrate does not suffer an irreversible loss of SER activity under these conditions. These studies indicated the irreversible loss of surface-enhanced Raman intensity may be avoided in some cases for well-fabricated substrate, but a generally accepted substrate that can guarantee no loss of Raman intensity on cycling the potential to significant negative values is still not available currently. On the other hand, hydrogen evolution may also result in the lower Raman intensity which will be discussed in Section 4.5.

In addition, adsorbate desorption also reduces the surface enhanced Raman intensity, and the desorption depends on the type of adsorbate-metal interaction (chemisorption or physisorption), as well as intramolecular interactions (the lateral interaction between the adsorbate molecules)[39] and the solubility of the adsorbate[40]. To discriminate the loss of Raman intensity caused by adsorbate desorption, measurement of differential capacitance can provide the capacitance variation during the onset of adsorption/desorption, however the capacitance may also change because of surface area changes.

The following two experiments were performed individually to investigate the role of desorption and irreversible loss of Raman intensity for Texas Red under the potential perturbation. The sphere

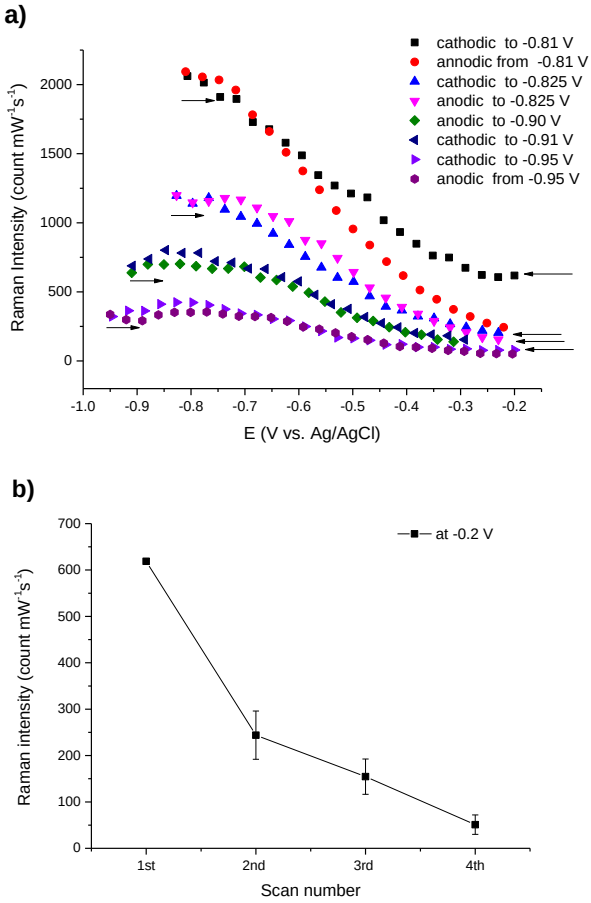

Figure 4.11 a) The 1504 cm^{-1} band of Texas Red as a function of the cycling potential. Surface-enhanced Raman spectrum acquired from the SSV electrodes after immersed into the solution containing 1 μM Texas Red in 10 mM Tris base, pH 13 and 1 M NaCl for 16 h. The supporting electrolyte in the Raman spectroelectrochemical measurement is 0.1 M KOH, in 10 mM Tris base, pH 13 and 1 M NaCl. The potential was swept 4 times from -0.2 V to the 4 increasingly cathodic limits, -0.81, -0.825, -0.91 and -0.95 V at 1 mV s^{-1}. Raman spectra were acquired during every 25 mV interval for 10 s exposure in the static mode of 1180 to 1704 cm^{-1}. b) The Raman intensity at -0.2 V before entering each potential cycle were plotted as a function of scan number. The arrow indicates the direction of potential sweeping.

void substrate was immersed in a solution containing 1 μM Texas Red, 0.1 M KOH, 1M NaCl 10 mM Tris base (pH 13) for 16 h. The potential was swept 4 times from -0.2 V to the 4 increasingly shifted cathodic limits, -0.81 , -0.825, -0.91 and -0.95 V at 1 mV s^{-1} in the electrolyte containing 0.1 M KOH, 1M NaCl and 10 mM Tris base (pH 13). Raman spectra were aquired at 25 mV intervals for 10 s exposure in the static mode between 1180 and 1704 cm^{-1}. The intense Raman band of Texas Red at 1504 cm^{-1} was selected to reflect the potential dependence shown in Figure 4-17 a). The Raman intensity at -0.2 V before entering each potential cycle was plotted to represent the intact Raman intensity before the potential dependent enhancement in Figure 4-17 b). The

reason for performing this measurement in alkaline solution (pH 13) to eliminate the interference of hydrogen evolution which will be discussed in Section 4.5.

There are two things to notice. First, a reversible change in Raman intensity for the same potential cycle is clear in the 4 potential cycles with progressively cathodic limits. Second, there is a progressive decrease in Raman intensity in Figure 4-17 a) with each potential cycle to successively more cathodic potentials. To see whether the Raman intensity loss could be correlated to the extent of Texas Red desorption, capacitance measurements where performed using electrochemical impedance.

The capacitance was determined by impedance measurements assuming a simple series equivalent circuit as shown in Figure 4.12. When a neutral molecule adsorbs on the metal electrode, the molecule replaces the adsorption site that was originally occupied by electrolyte ions and solvent molecules and reduces the ability to store charge at the interface. Hence, the adsorbed molecule reduces the double layer capacitance. The frequency of the sinusoial potential modulation was varied by 6 to 7 orders of magnitude (normally from 10^{-1} to 10^{6} Hz) and the amplitude was normally less than 10 mV.

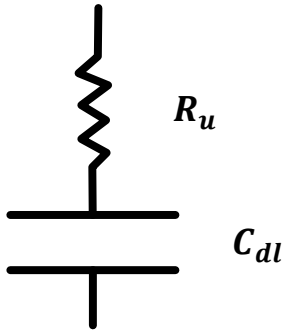

Figure 4.12 The equivalent circuit represents the uncompensated resistance of the electrolyte and the series electric double layer capacitance.

The impedance measurements in this study were performed using an Autolab PGSTAT 302 (Metrohm, Switzerland) at a 2 mm Au disc electrode (ALS, Japan), the Au electrode was polished sequentially with finer aluminum oxide powders (Buehler, USA 1, 0.3 and 0.05 μm) and rinsed with deionized water for 10 s, and sonicated for 5 min between each polishing. Before the measurements electrochemical polishing was undertaken using cyclic voltammetry between -0.1 and 1.6 V (vs. SCE) at 0.1 V s^{-1} for 60 cycles to obtain a reproducible Au reduction peak centred at 0.9 V in 0.5 M sulphuric acid. The surface area was then determined by dividing the Au oxide

reduction peak area of the voltammetric curve by the scan rate and the Au reduction charge suggested by Trasatti *et al.*[41] as 390 μC cm^{-2}. After the cleaning step, the Au electrode was immersed into the solution of 0.1 M KOH, 1M NaCl 10 mM Tris base (pH 13) for 16 h and rinsed with the same supporting electrolyte before the measurement. The supporting electrolyte was agitated with argon for 30 min to remove the dissolved oxygen.

The uncompensated resistance measured in this Section (4.4) was recorded at the open circuit potential (ca. 0.14 V vs. SCE) at 10^{-1} to 10^{5} Hz with the amplitude of the sinusoidal perturbation of 10 mV (peak to peak). The solution composition was the same as used in the Raman measurement in Figure 4.11. (0.1 M KOH, in 1 M NaCl and 10 mM Tris base, pH 13). The resultant uncompensated resistance, 27.2 Ohm, was obtained from the intercept of the real component (Z') of the impedance in the Nyquist plot as shown in Figure 4-13 a.

In the folowing experiment, the capacitance was derived at a fixed frequency in order to observe the

variation of capacitance for a bare Au electrode and for electrodes with Texas Red adsorbed as a

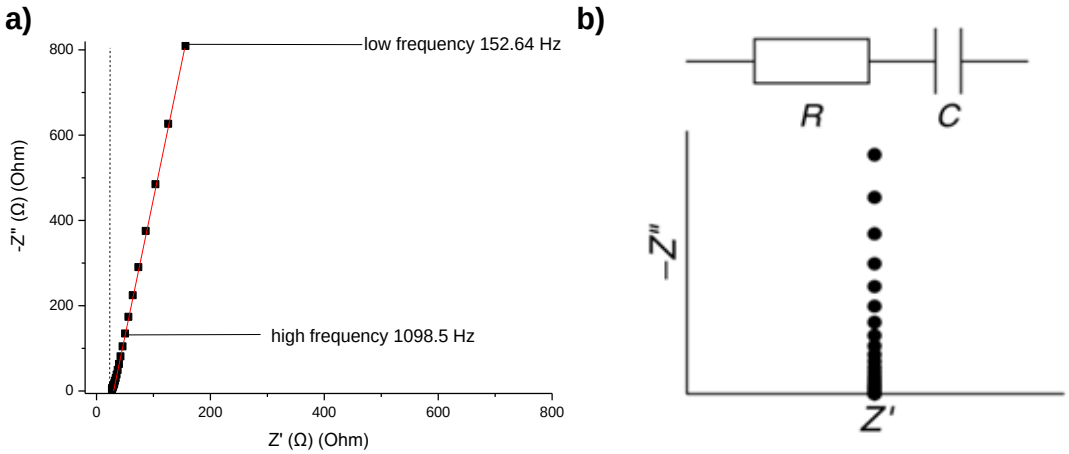

Figure 4.13 a) The Nyquist plot for Texas Red adsorbed at a Au electrode. b) Bode phase angle plot of the Texas Red adsorbed at a Au electrode. The dashed line in both a) and b) indicates the ideal circuit of a resistor and a capacitor in series. The Au electrodes were immersed in 1 μM Texas Red solution containing 1 M NaCl and 10 mM Tris base, pH 13 for 16 h then rinsed with same soltuion in the absence of Texas Red for 5 s. The impedance measurements were conducted at the open circuit potential (ca. 0.14 V) and 10^{-1} to 10^{5} Hz with the amplitude of the sinusoidal perturbation of 10 mV (peak to peak). The composition of the supporting electrolyte was the same electrolyte as used in the Raman measurement in Figure 4.11 , 0.1 M KOH, in 1 M NaCl and 10 mM Tris base, pH 13. b) Reprinted with permission from Ref. [42]. Copyright © 2003 Wiley.

function of the potential. The capacitance can be deduced from the equivalent circuit as shown in Figure 4-12 [42]. Since the currents flowing through both the resistor and capacitor are the same the total potential is equal to the sum of the potentials dropped across the resistor and capacitor

$$V(t) = I(t)R - \frac{\mathrm{j}\, I(t)}{\omega C} \qquad (4.1)$$

where V is the externally applied potential; I the response current; R the uncompensated resistance; j the imaginary unit; ω the frequency of the potential perturbation in rad s^{-1}, and C the double layer capacitance. Since the uncompensated resistance is independent of the potential perurbation, the capacitance could be obtained from equation (4.1). As seen from Figure 4.13, the given frequency (251.2 Hz) which has the maximum phase angle is closest to the R_s-C_{dl} equalvalent circuit and hence is chosen to measure the double layer capacitance, the differential capacitance can then be calculated to explore the surface charge distribution during the potential scan.

The impedance was first measured in potential steps from -0.2 V to -0.95 V (vs. SCE) for the bare Au electrode. The perturbation amplitude was 10 mV peak to peak at 251.2 Hz, corresponding to the maximum phase angle obtained from Figure 4.13 b). 0.1 M KOH solution containing 1 M NaCl and 10 mM Tris base, pH 13 was chosen as the supporting electrolyte. The pre-treatment and Texas Red immobilization protocol on the 2 mm Au electrodes (ALS, Japan) were the same as those described in Section 4.2 unless otherwise indicated.

After confirming that the electrolyte resistance remained constant at ca. 27.16 (±0.5) Ohm in the selected potential window, the capacitance was derived from the measured impedance over a potential range from -0.2 V to the 4 progressively shifted cathodic potential limits at -0.8, -0.85, -0.9 and -0.95 V in 25 mV steps.

The results are shown in Figure 4-14. The bare Au has a larger capacitance (16.8 to 20.1 µF cm^{-2}) and the Texas Red coated Au electrode has a lower capacitance (9.6 to 14.1 µF cm^{-2}) for the 4 potential scans to progressively more cathodic limits from -0.8 to -0.95 V. Since the reorientation of Texas Red on sweeping (0.2 to -1.3 V) as described in Section 4.2 is not evident based on the relative Raman intensity of the in-plane and out-of-plane vibration modes, the lowering capacitance is supposed to be unrelated to the molecular reorientation of Texas Red.

To conclude, the partial desorption of Texas Red (onset at -0.4 V) might contribute to the reduction of Raman intensity during the potential sweep and the results show this reduction onset before the Raman peak intensity at -0.8 V. Hence the potential dependent Raman enhancement could not be

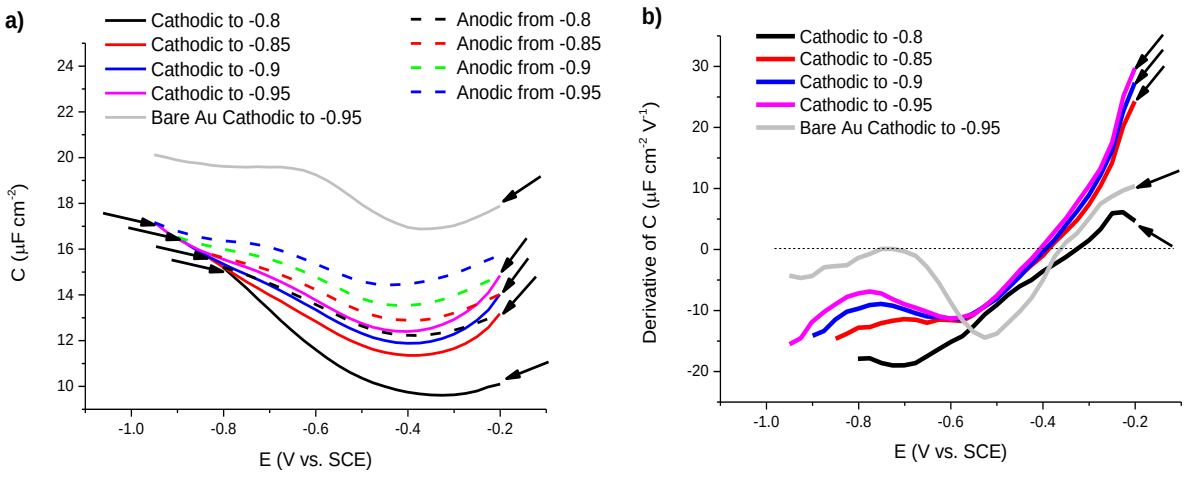

Figure 4.14 a) Differential capacitance measured as a funciton of the potential on the bare Au electrode and the Texas Red adsorbed Au electrode. The preparation of the Au 2 mm disc electrodes was as described in Figure 4.13. The potential of the Texas Red adsobed Au electrode was scanned from -0.2 V to successively more negetive potential limits, -0.8, -0.85, -0.9 and -0.95 V in 25 mV steps and back to -0.2 V. The impedance measurements were performed with a peak to peak amplitude of 10 mV and frequency of 251.17 Hz. b) The first derivative of the capacitance on the cathodic scans in a). Dash line of zero in b) was denoted to probe local extremes from a). Arrows indicate the scan directions.

related to the desorption of Texas Red, or irreversible loss, or geometrical deformation of the SSV nanostructure. Basically the results show lower capacitance for Texas Red coated Au on cycling this capacitance increase systematically consistent with desorption of Texas Red at negative potentials so that the capacitance approach the value for the bare Au electrode.

We have systematically examined the factors that can account for the potential dependent Raman enhancement for Texas Red adsorbed on Au electrodes from the perspective of the orientation, localized surface plasmon resonance, and desorption. None of these factors can explain the potential dependent Raman enhancement with a peak intensity at ca. -0.8 V and the reversible Raman intensity change over the same potential cycle as shown in Figure 4-1. Obviously, there is some other factor(s) involved. We will discuss these in the next Section 4.5.

4.5 Hydrogen Evolution and the Electrochemical-SERS Response in Alkaline Electrolyte

In Section 4.2, we discussed the SER spectra for Texas Red from 120 to 1700 cm^{-1}, the region which contains most of the characteristic bands of Texas Red, under electrochemical potential control from 0.2 to -1.2 V (vs. Ag/AgCl). The intensity of Raman bands grows as a function of the potential from 0.2 to -0.8 V, and then decreases rapidly from -0.8 to -1.0 V as shown in Figure 4.16. In the potential region from -0.9 to -1.2 V, the decreasing Raman intensity of Texas Red is accompanied by a growing baseline as shown in Figure 4.16. The growing baseline was noted between ca. 200 to 1000 cm^{-1} at -0.9 to -1.0 V and then eventually widened toward the high wavenumber side to the most intense band of 1504 cm^{-1}. Since the onset potential of the growing Raman baseline overlaps with that of the decreasing Raman bands one cannot know if these two characteristic responses have the same origin simply based on the experimental result shown in Figure 4.16. In addition gas bubbles appear to form with of the growing baseline at ca. -0.9 V. The size of the bubbles roughly increased and sporadically merged with the adjacent bubbles during the progress of the cathodic potential scan. The bubbles consequently cover 30 to 80 % of the surface substrate at -1.2 V. The characteristics above suggested the growth of the baseline and the formation of bubbles on the substrate surface may both be the result of hydrogen evolution during the cathodic scan process. The presence of bubbles might further reduce the SERS intensity cathodic of -1.0 V.

To understand if the growing baseline of the Raman spectra was caused by hydrogen bubbles, we measured the Raman spectra of Texas Red during the cathodic potential sweep to compare to the corresponding spectra in neutral solution.

Two SSV chips were cut from the same SSV substrate and immersed in 1 μM Texas Red solution containing 1 M NaCl, 10 mM Tris buffer (pH 7.2) for 16 h. The pH of the electrolyte 1 M NaCl, 10 mM Tris buffer (pH7.2) was changed to pH 13 by adding 0.1 M KOH to the supporting electrolyte for the Raman spectra acquisition. The spectra shown in Figure 4.16 a) exhibit the same vibration features as the neutral solution between 200 and 1700 cm^{-1} shown in Figure 4.4 of Section 4.2. There are no new bands and no measurable frequency shifts in the spectra between the two pH values.

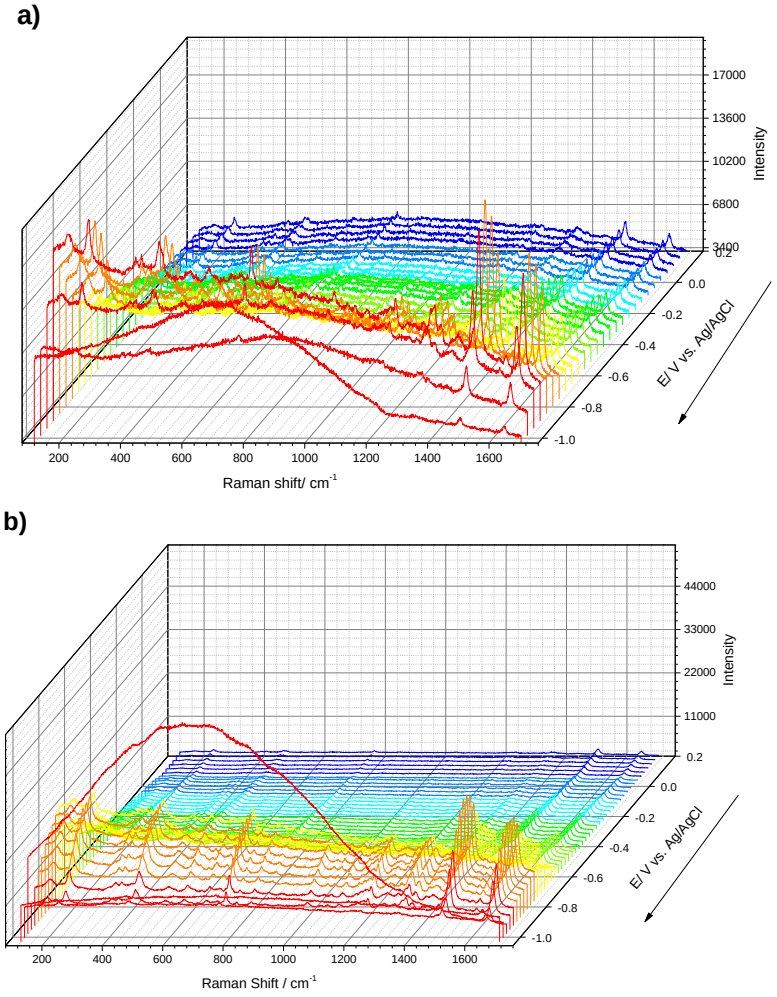

Figure 4.16 Examples of the growing baseline in the successively recorded Raman spectra for Texas Red adsorbed on a Au electrode. Extended mode Raman spectra recorded during potential cycling from 0.2 V to -1.0 V (vs. Ag/AgCl) at 0.34 mV s^{-1}. Each Raman spectrum was acquired in 1 M NaCl containing 10 mM Tris buffer (pH 7.2) at 633 nm excitation (2.3 mW) during the potential sweep. a) Raman spectra viewed from the negative potential (-1.0 V) side of Figure 4.4. b) Another example of the growing baseline with the broaden bandwidth toward the high wavenumber side at 1504 cm^{-1} at -0.975 V. The arrow indicates the direction of potential sweeping.

The detailed band assignment of the Raman bands and the variation between the potential dependent Raman enhancements is given in Table 4.3. The potential dependent Raman enhancement in the alkaline solution appears to be about to ½ to ¼ of that in neutral solution. However, although this comparison was made between two substrates with the same deposition

Table 4.5 The assignments of the Texas Red Raman bands obeserved in the 0.1 M KOH, 1 M NaCl and 10 mM Tris base (pH 13.0) as the supporting electrolyte and compared with the result in 1 M NaCl and 10 mM Tris base (pH 7.2) as the supporting electrolyte.

	υ (cm^{-1})	Potential dependent enhanced ratio of Raman intensity		Band assignment [3,9–12]
		pH 7.2	pH 13	
A	170	8.8±2.4	1.8±1.2	Au-O stretching
B	234	9.0±3.0	1.6±0.8	Au-N stretching
C	410	7.2±2.4	1.7±0.6	Xanthene deformation
D	465	11.6±3.6	2.3±1.3	
E	565	6.8±3.2	2.3±0.8	C-C-C ring in-plane deformation
F	626	14.3±5.0	2.3±1.5	
G	764	10.6±3.3	2.4±1.1	C-H out-of-plane deformation
H	1034	7.1±1.9	2.0±1.1	C-H in-plane deformation
I	1234	12.0±4.2	2.5±1.3	C-O-C xanthene stretching
J	1360	10.7±3.5	2.1±1.2	C-N/C-O stretching, C-H in-plane bending
K	1504	12.0±4.0	2.2±1.3	Xanthene plane stretching
L	1648	12.1±4.0	2.4±1.3	

thickness ($\bar{t}$ = 0.77), there may be some variation in nanosphere packing between the two substrates that results in a variation in the normalized intensity ratio.

The spectra shown in Figure 4.17 are noted for the sloping baseline at -0.2 V, which increases in intensity with the potential cathodic scan to -0.8 V, and then decrease to become flat in both wavenumber and intensity scales at -1.2 V. Clearly the SER spectra acquired in the alkaline solution do not have the growing baseline observed in the neutral solution. The characteristic Raman bands of Texas Red are plotted individually in Figures 4.24 and 4.19. These bands have similar potential dependence and lower normalized intensity ratio (the Raman intensity divided by the intensity of the corresponding band at the initial potential, -0.2 V). The difference in the Raman intensity decrease from -0.8 to -1.2 V measured in the neutral and alkaline solution is not obvious but becomes critical to determine the potential of the complete disappearance of the Raman intensity. In the case of the SER spectra in neutral solution, the presumed hydrogen evolution raises the Raman baseline and hence eventually masks the Raman bands. This results in the Raman intensity disappearing at ca. -1.0 V which is 0.2 V positive of the value measured in the alkaline solution. On the other hand, the gas bubbles and the growth in baseline in the Raman spectra were both no longer observed in alkaline solution at -0.9 to -1.2 V. These results suggest that the evolution of hydrogen was delayed and hence the masking of the Raman bands was removed to show a slower decrease of Raman intensity.

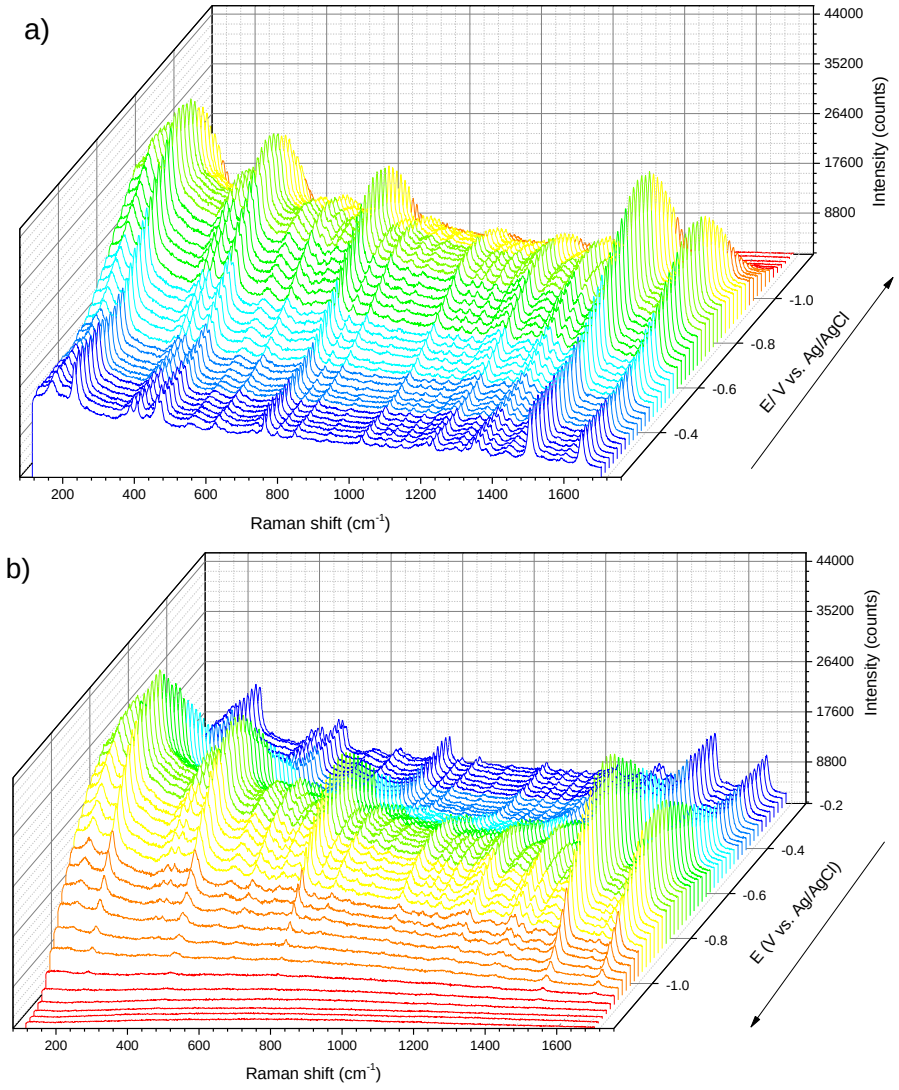

Figure 4.17 Successive SER spectra recorded during the linear sweep voltammetry for Texas Red adsorbed on the Au SSV electrode in alkaline solution (0.1 M KOH, 1 M NaCl, 10 mM Tris base (pH 13.0). The potential was swept from -0.2 to -1.2 V at 0.34 mV s^{-1}. The SSV chips were immersed in the 1 µM Texas Red solution containing 1 M NaCl, 10 mM Tris buffer (pH 7.2) for 16 h and rinsed with 0.1 M KOH solution containing 1 M NaCl, 10 mM Tris solution for 5 s before the Raman measurement. Each Raman spectrum was measured in 55 s exposure at 2.3 mW 633 nm excitation. a) Viewing from the -0.2 V side toward -1.2 V. b) Viewing from the -1.2 V side toward -0.2 V. The arrows indicate the potential scanning direction. The arrow indicates the direction of potential sweeping.

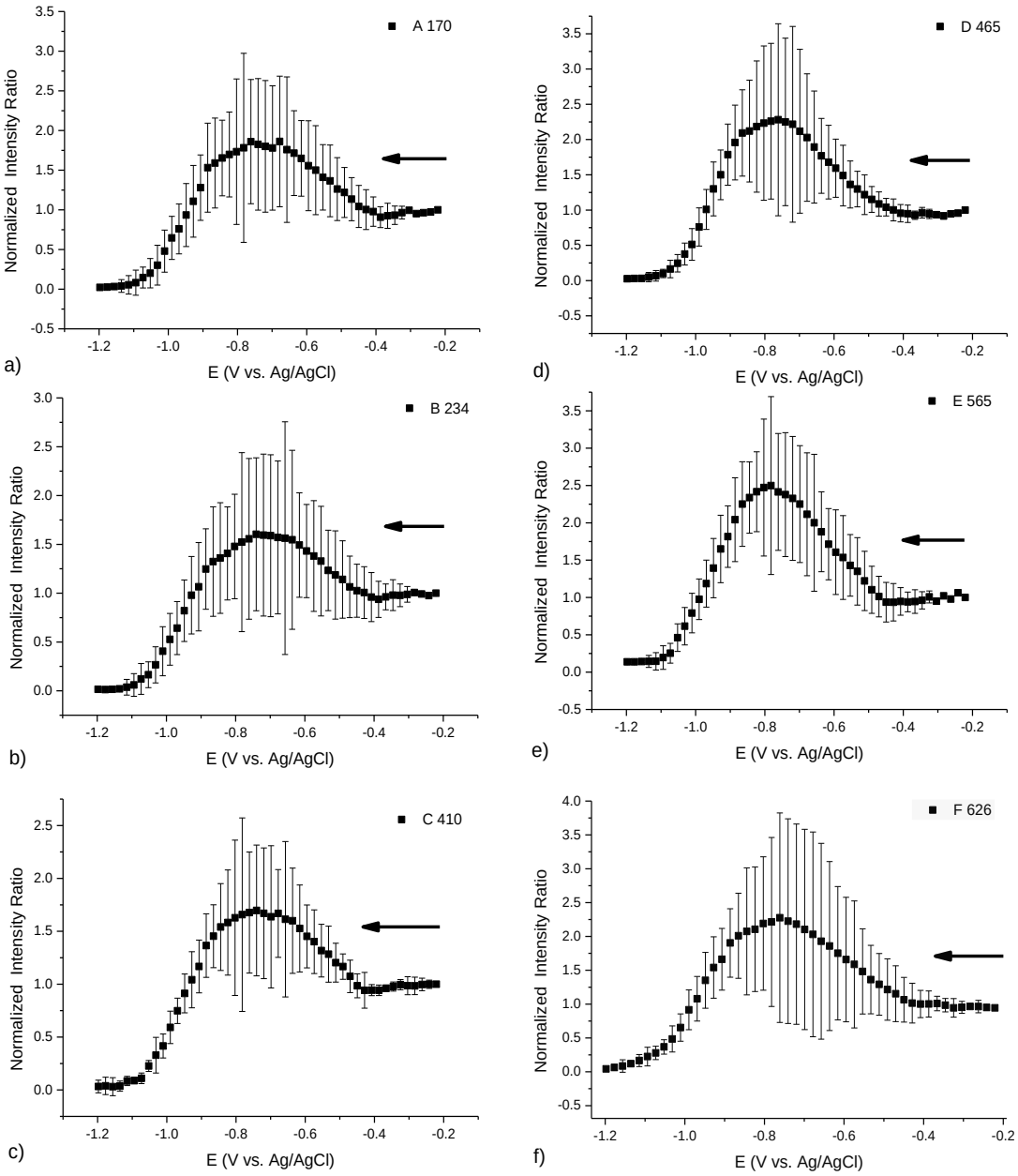

Figure 4.24 Raman intensity of the individual bands A to F (a) to (f) selected from the Raman spectra of Texas Red between 120 to 1704 cm^{-1} as a function of the potential from 0.2 V to -1.0 V (vs. Ag/AgCl) scan at 0.34 mV s^{-1} in 0.1 M KOH solution containing 1 M NaCl, 10 mM Tris buffer (pH 7.2). The SSV substrate was modified by adsorption from a solution of 1 μM Texas Red, in 1 M NaCl containing 10 mM Tris buffer (pH 7.2) for 16 h and then rinsed with 0.1 M KOH solution containing 1 M NaCl, 10 mM Tris solution for 5 s before the Raman measurement. Each Raman spectrum was measured using 55 s exposure at 2.3 mW, 633 nm excitation. The arrow indicates the direction of potential sweeping.

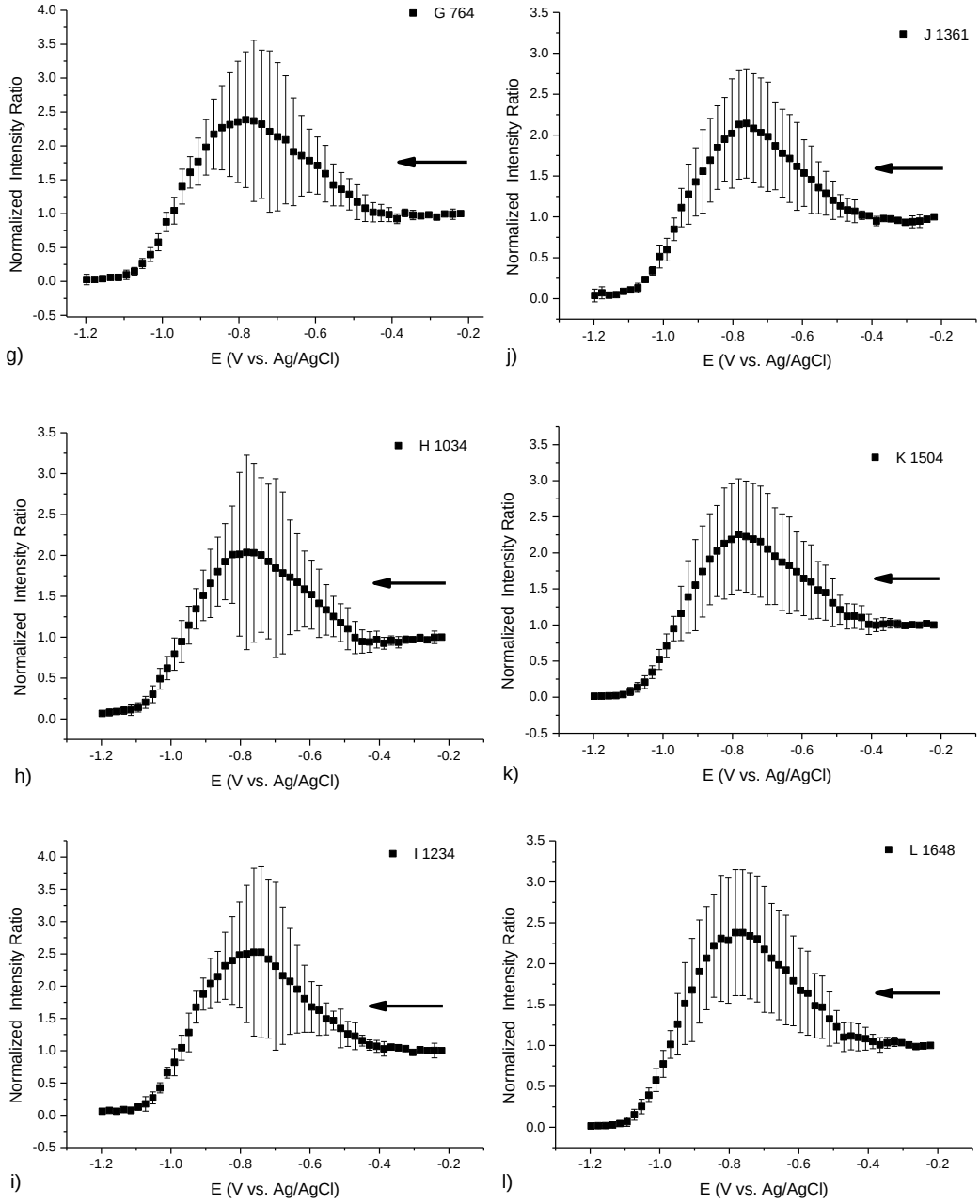

Figure 4.25 Raman intensity of the individual bands G to L (g) to (l) selected from the Raman spectra of Texas Red between 120 to 1704 cm^{-1} as a function of the potential 0.2 V to -1.0 V (vs. Ag/AgCl) scan rate 0.34 mV s^{-1} in 0.1 M KOH solution containing 1 M NaCl, 10 mM Tris buffer (pH 7.2). The SSV substrate was modified by adsorption from a solution of 1 μM Texas Red, in 1 M NaCl containing 10 mM Tris buffer (pH 7.2) for 16 h and rinsed with 0.1 M KOH solution containing 1 M NaCl, 10 mM Tris solution for 5 s before the Raman measurement. Each Raman spectrum was measured for 55 s exposure at 2.3 mW, 633 nm excitation. The arrow indicates the direction of potential sweeping.

To identify any particular differences between the spectra acquired in neutral and alkaline solution, the spectra were normalized to the intensity of the Au-O band at 170 cm^{-1}. This band was chosen since the Au-O vibration is assumed to be independent of the Texas Red. The Raman difference spectrum was calculated by subtraction of the two normalised spectra of adsorbed Texas Red. The main difference, Figure 4.26 b), is that the 4 bands labelled I to L are more intense in the alkaline solution. These bands are related to the xanthene stretching modes containing the band J, the

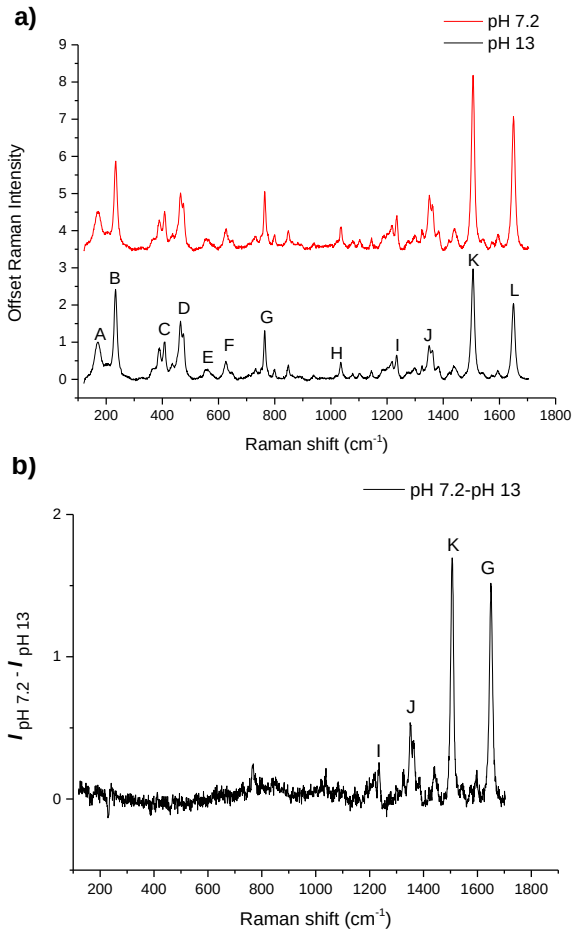

Figure 4.26 a) Raman spectra acquired in neutral (pH 7.2) and alkaline (pH 13) solution for Texas Red adsorbed on Au SSV substrate. Conditions as in Figure 4.25. b) The difference Raman spectrum calculated by substraction the Raman spectrum measured in the alkaline electrolyte from the Raman spectrum measured in the neutral electrolyte. The two spectra were normalized by the 170 cm^{-1} band of Au-O stretching before the subtraction.

vibrations of C-N/C-O stretching, and the C-H in-plane bending also reside on the xanthene moiety (Table 4.5). This result suggests that the Raman intensities of the 4 vibrational modes were lower in alkaline electrolyte. However the reason for this is not clear currently. From the pH aspect, Texas Red is reported to be insensitive to pH, compared to the other rhodamine dyes such as fluorescein,

when labelled on a nucleic acid[43], from measurements of the fluorescence decay spectra. Hence this difference may arise if there is a slight difference in the enhancement with Raman shift in the two cases. This could also result because band A was chosen to normalize all the bands and hence the variation shows up at the other end of the spectra. Another possible change is in the refractive index of the solution which can lead to a slight shift in the position of the plasmon resonance, and hence change the SERS enhancement.

4.6 Evaluation of the Stark Effect for Texas Red Adsorbed on Au Electrodes

Another possible explanation for the potential dependent change in Raman enhancement of Texas Red adsorbed on the SSV Au electrode is the electronic Stark effect which results in a frequency shift in the molecular electronic absorption transition. The electronic Stark effect describes the shift in the electronic levels caused by the electric field and hence the change in position and intensity which are mainly due to the change of dipole moment under the electric field. The effect depends on the difference in dipole moment between the ground state and the excited state $S_0 \neq S_1$. The change in the position of the electronic bands will be reflected in the energy gap between the highest occupied molecular orbital (HOMO), and lowest unoccupied molecular orbital (LUMO) and hence shifts the molecular transition frequency. The change of energy gap can either be higher, which results in a blueshift, or lower, which results in a redshift in the electronic absorption spectrum. The blueshift (or redshift) of the electronic absorption spectrum may approach (or move away from) the excitation wavelength used in the Raman measurement and finally results in an enhanced (or weakened) resonance transition. In our case for the adsorbed Texas Red, this enhanced molecular resonance transition would result in increased surface enhanced resonance Raman scattering (SERRS).

One question may be raised "would the electronic Stark effect co-exist with the vibrational Stark effect?" This question may be answered from equation (4.2) in which the second term of the polarizability is related to the corresponding vibrational modes and may not be observable in the case when the electric field is lower than 10^7 V cm^{-1}. Another reason was discussedd by Bublitz[44] who indicated that the vibrational Stark effect was often observed for small molecules. The larger the probe molecule, the more complicated the vibrational modes involved. To isolate the potential dependent virbrational modes from multi-component vibrations becomes more difficult and hence reduces the chance of observing the vibrational Stark effect.

An example of electrochromism can be found in Pope *et al.*[45] who used a modified hemicyanine with a thiol anchor, the modification of 3-mercpto-1-propane and 12-mercapto-1-dodecane was co-adsorbed on the Au surface as shown in Figure 4.28. The frequency shift can be estimated as

$$h\Delta\upsilon = -\Delta\mu\Delta E\cos\theta - \frac{1}{2}\Delta\alpha_{ge}\Delta E^2\cos\theta \qquad (4.2)$$

where h is Plank's constant, $\Delta\upsilon$ is the shift of the energy of the peak between the two electric fields, $\Delta\mu$ is the total change in dipole moment between the ground and excited states of the dye, ΔE is the

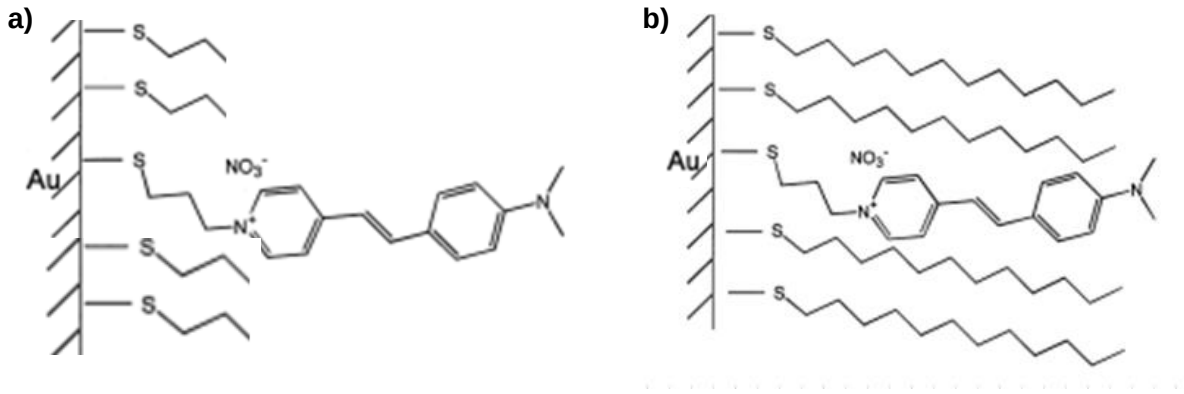

Figure 4.27 Modified schemes from the Ref. [45]. Hemicyanine nitrate was co-adsorbed with a) 3-mercapto-1-propane SAM and b) 12-mercapto-1-dodecane SAM on the Au electrode individually.

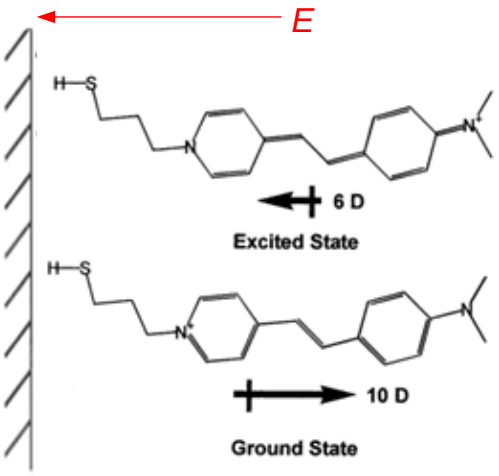

Figure 4.28 Scheme modified from Ref. [45]. The arrows with the crossed lines indicate the dipole moments of hemicyanine at its ground state (lower) and the excited state (upper). The electric field (*E)* direction of the electrode is shown in an arrow normal to the electrode surface. Note there might be an angle between the electric field and the dipole moment which depends on the tilting orientation of hemicyanine in the alkanethiol SAM.

change of magnitude of the electric filed between any two potentials, θ is the angle between the vectors, and $\Delta\alpha_{ge}$ is the change in the polarizability between the ground state and excited state. The second term on the right hand side of equation (4.4) contains the polarizability arising from the change of dipole moment and is usually negligible for electric field magnitudes below ca. 10^7 V cm^{-1}. Due to the electric field of the electrode and potential range used in this work the electroc field is ca. 10^4 to 10^5 V cm^{-1} as estimated by Kaiser *et al.*[46] and hence may be ignored herein.

To evaluate the role of the electronic Stark effect in the potential dependent Raman enhancement, one needs to obtain the dipole moment of Texas Red in the ground and excited states. The excited state was calculated based on the ground state for Texas Red calculated in Section 4.2 at B3LYP/6-311++G(d,p) level and then adopting the configuration interaction approach in Gaussian. The configuration interaction approach models excited states as combinations of single electron substitutions out of the ground state function obtained by the Hartree-Fock self-consistent-field procedure[47]. The method is thus named Configuration Interaction-Singles (CIS) which is a primary qualitative method to model the excited states of molecules[48]. The change of electric field estimated by Pope *et al.*[45] based on 12-mercapto-1-dodecane is ca. 3 x 10^5 V cm^{-1} V^{-1} and 3-mercapto-1-propane as 4 x 10^4 V cm^{-1} V^{-1}. In the case of 3-mercapto-1-propane passivation, the modified hemi-cyanine is not embedded inside the passivation layer, Pope and his colleagues used two experiments to exclude interference from re-orientation of the pendant hemicyanine moiety. In the first the orientation was monitoring by *ex-situ* reflection-absorption Fourier transform infrared spectroscopy (RA-FTIR). This did not show any evident bias between the relative band intensities of two nonparallel vibrational modes. The second is that the Stark effect is weakly dependent on the small θ angle between the transition dipole moment at potentials close to the potential of zero charges (-0.4 V) measured in their study. We will use the two values for the change in magnitude of the electric field for 3-mercapto-1-propane and 12-mercapto-1-propane as a range to estimate the effect for adsorbed Texas Red on the Au electrode.

The resultant dipole moments of the ground state and excited state are shown in Figure 4.29 for a Texas Red molecule adsorbed on the Au(111) atomic plane. Based on the Au-N stretching mode observed, the fact that no re-orientation was observed from the SER spectra in Section 4.2, and the STM image of xanthene dye reported by Su *et al.*[5], the Texas Red is assumed to have a face-on orientation as shown in Figure 4.29. The electric field E was assumed to be normal to the surface at the negatively charged Au. Therefore the vector of the transition dipole moment is at ca. 118° and the value can be used to give an estimation of the frequency shift in the molecular transition for Texas Red at 595 nm. The resultant frequency shift is small (-1.5 × 10^{-9} THz) which is less than 10^{-5} nm based on a change in the magnitude of the electric field of 3 x 10^5 V cm^{-1} V^{-1} but corresponding to a redshift which implies the possibility that an electronic Stark effect may be involved in the potential dependent Raman enhancement. If the effect is of the order of 10^{-5} nm, this effect will be too small to be significant. Hence, a further investigation of measuring the reflectance specrum of the Texas Red adsorbed SSV Au electrode is neccessary to compare with the results of the calculation.

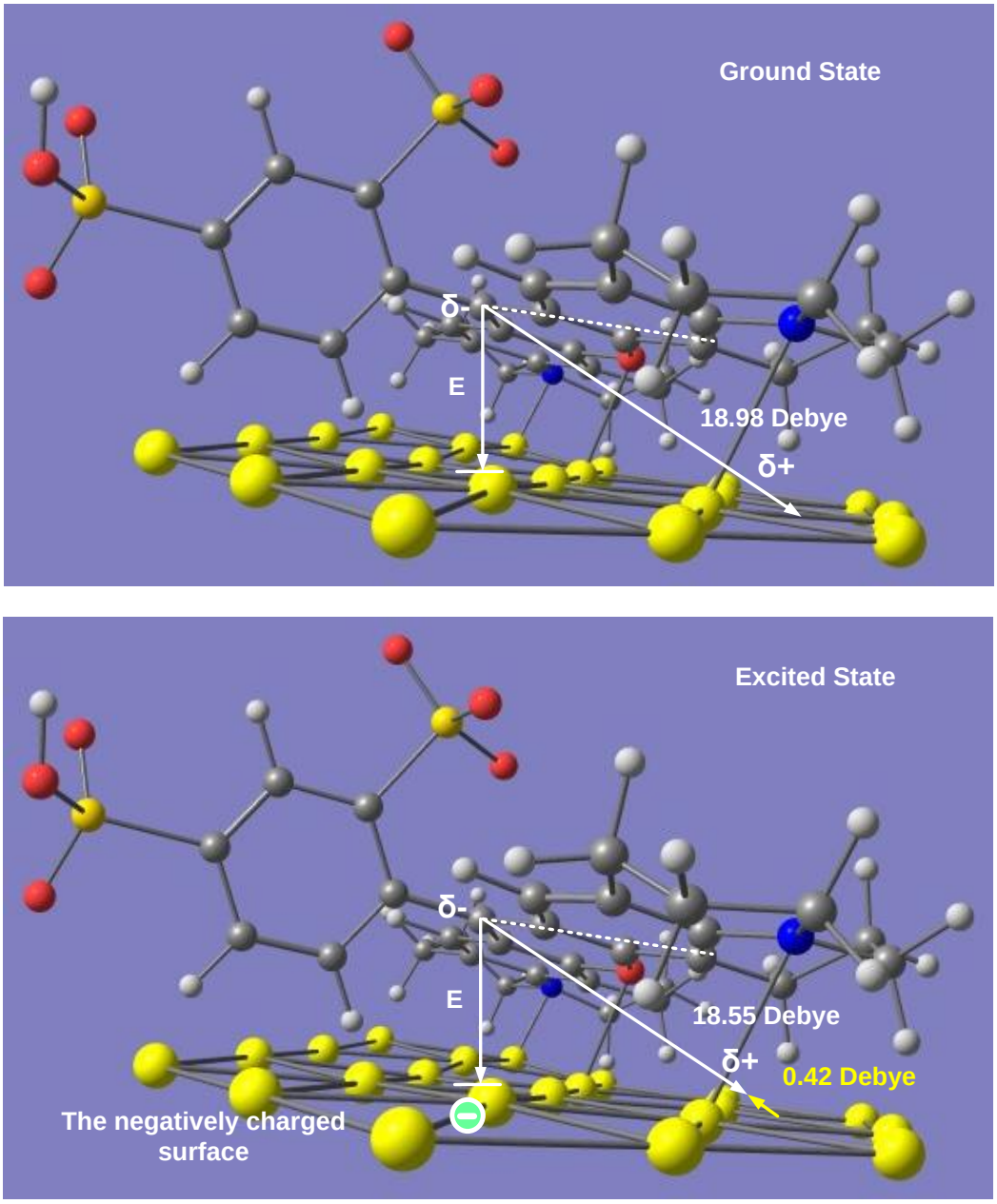

Figure 4.29 Scheme The calculated dipole moments of the ground state and excited state of Texas Red at B3LYP/6-311++G(d,p) and CIS level individually by Gaussian software version 9. D01 (Gaussian Inc, Wallingford, USA).δ- and δ+ represents the vector of the dipole moment. E stands for the vector of electric field which is assumed to be normal to a negatively charged Au surface.

4.7 Excitation Wavelength Dependence of Texas Red SERS

As discussed in Sections 4.1 to 4.5, Texas Red adsorbed on the Au SSV electrode exhibits a significant potential dependent Raman enhancement with a peak in Raman intensity at -0.8 to -0.9 V (vs. Ag/AgCl) which cannot be explained by the potential-tuning of the localized surface plasmon resonance (LSPR). The tuning of the LSPR by changing the deposit thickness of the SSV surfaces (in Section 4.3) has an effect on the potential dependent Raman intensity, but the LSPR lacks a connection between the expected blueshift of the cathodic potential sweep and the potential dependent Raman enhancement. In addition, the assumed desorption of Texas Red that occurs between -0.4 to -0.8 V (vs. SCE) cannot cause the potential dependent Raman signal to go up in the same potential region. From the literature, we find that this potential dependent Raman enhancement might be explained by the chemical enhancement mechanism which is highly dependent on the electronic structure of the adsorbate and the position of the Fermi level of the metal electrode. In other words, the chemical enhancement can be tuned by either the excitation wavelength or the electrochemical potential. To investigate the possible effect of the chemical enhancement, we used the same thickness SSV substrate ($\bar{t}$ = 0.825), where the $\bar{t}$ represents the ratio of the deposited thickness to the 600 nm template nanosphere diameter. This thickness gives a comparable Raman enhancement for excitation at 633 and 785 nm as reported by Mahajan *et al.*[32] The SSV substrates were immersed in 1 μM Texas Red solution containing 1 M NaCl and 10 mM Tris buffer (pH 7.2) for 16 h. The SSV surfaces were separated from the same substrate to minimise the bias of the surface packing of nanospheres between the substrates. The supporting electrolyte for the Raman spectroelectrochemical measurements was 1 M NaCl, 10 mM Tris buffer (pH 7.2) with no Texas Red added.

Raman measurements were made using 2 separate Raman spectrometers; a Renishaw Raman 2000 system spectrometer equipped with 633 nm excitation HeNe laser as described in Section 2.3, and a Renishaw Raman inVia spectrometer with 1200 groove/mm grating and using a 785 nm 100 mW diode laser, attenuated to produce 4.02 mW incident power by the WiRE 3.4 software on the specimen in 180° backscattering via a 50 × objective, the numerical aperture of the objective is 0.75.

The spectra recorded during the potential sweep from -0.3 to -1.2 V (vs. Ag/AgCl) at 1 mV s^{-1} using the two spectrometers are shown in Figure 4.30. The responses of the adsorbed Texas Red at

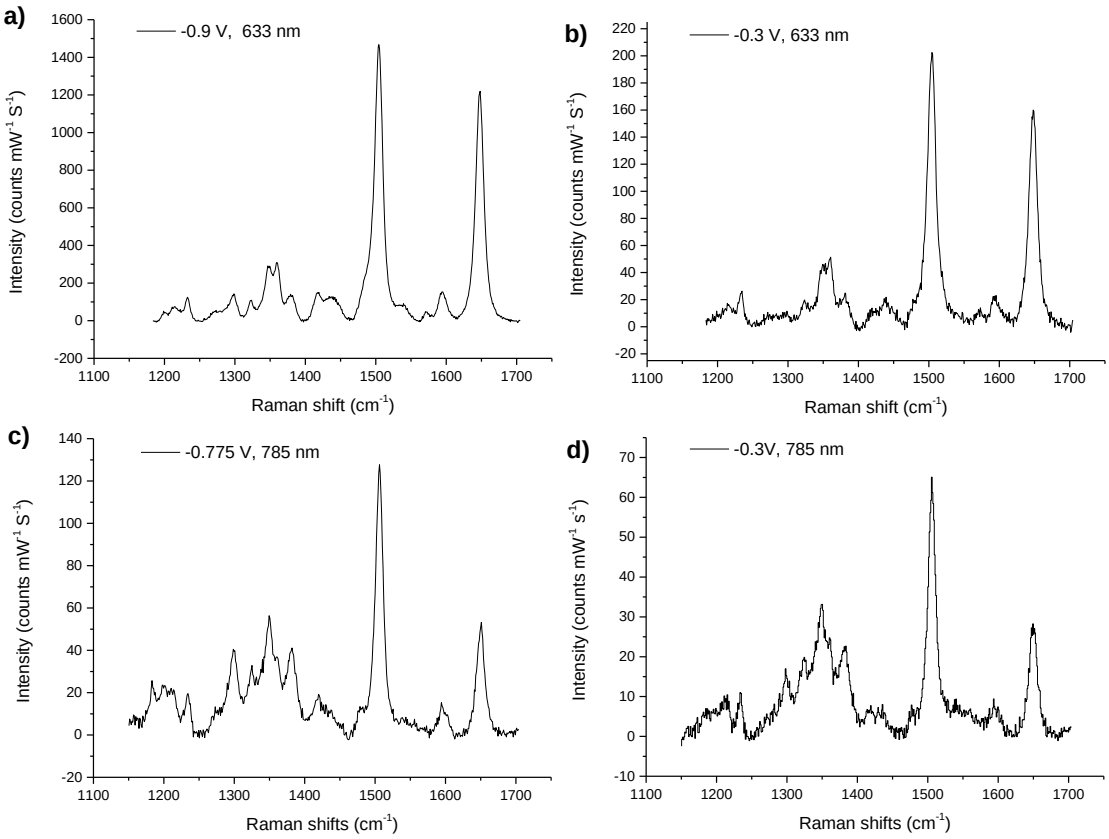

Figure 4.30 Background-subtracted SERS detected during the linear sweep voltammetry at 633 nm (a), b)) and 785 nm (c), d)). a) c) shows the peak Raman intensity at the corresponding potential while b) d) is the initial Raman spectrum at -0.3 V. The SSV chips were immersed in 1 μM Texas Red solution containing 1 M NaCl and 10 mM Tris buffer (pH 7.2) for 16 h. The chips were separated from the same substrate to minimise the bias of the surface packing of nanospheres. The supporting electrolyte was 1 M NaCl and 10 mM Tris buffer (pH 7.2) in the absence of Texas Red during the Raman spectroelectrochemical measurement.

633 nm excitation exhibits more intense Raman intensity than that of 785 nm. We will discuss the distinct spectra for 633 nm and 785 nm excitation first, and then go back to discuss the potential dependent Raman enhancement. Notably, the spectra for both 633 nm and 785 nm excitation exhibit the same vibrational bands but with different relative intensities to the most intense band at 1504 cm^{-1}. This variation in band intensity, caused by the choice of excitation wavelength, has also been observed for rhodamine 6G by Jensen *et al.*[3] in respect of resonance Raman scattering. The resonance Raman enhancement is achieved when using an excitation wavelength that is in resonance with an electronic transition of the molecule. Those vibrational modes that are coupled to this electronic transition will be resonantly enhanced and their Raman bands will appear much stronger relative to those bands of vibrational modes not coupled to the electronic transition. Con-

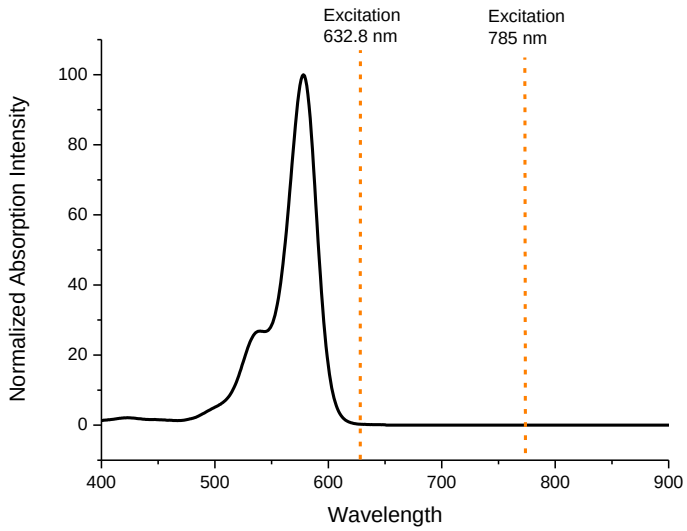

Figure 4.31 The adsorption electronic spectrum of Texas Red (dissolved in methanol) from the Fluorescence SpectraViewer (Thermo Fisher Scientific Inc., Waltham, USA). The electronic transition has a peak at 595 nm . Two excitation lines (633 nm and 785 nm) are indicated. Note the position of the electronic transition would be shifted in different solvents and also by absorption on gold. Ideally the electronic spectrum should be measured from the Texas Red labelled beacon probe in the electrolyte of interest to approximate the materials used in the electrochemical SERS measurement.

sequently, Raman spectra obtained from one molecule can appear different depending upon whether the laser excitation is in resonance with an electronic transition of the molecule or not[49]. Based on the work of Jensen *et al.*[3], the electronic transition for Texas Red peaks at 595 nm; much closer to the excitation at 633 nm as compared to 785 nm, Figure 4.25. Consequently, the 633 nm and 785 nm excitation can be regarded as a pre-resonance and an off-resonance excitation respectively. From the calculation in Section 4.1 (Figure 4.3) the HOMO of Texas Red is located around the xanthene ring. Hence resonance should result in greater enhancement in those modes, especially those at 1504 and 1649 cm^{-1}, for 633 nm excitation while the band corresponding to the in-plane ring bending (1360 cm^{-1}) is less enhanced by the pre-resonant 633 nm excitation.[3] For the most intense band at 1504 cm^{-1}, the effect of potential on the Raman enhancement is much greater for excitation at 633 as compared to 785 nm excitation as shown in Figure 4.32. Obviously, the change of the potential dependent Raman response is more dependent on the choice of wavelength between 633 nm and 785 nm as shown in Figure 4.31. The other associated phenomenon is that the most intense Raman band (1504 cm^{-1}) for the pre-resonance excitation (633 nm) is more enhanced than that for off-resonance (785 nm) as shown in Figure 4.30. Both results suggest that the effect of the potential on the Raman enhancement is highly dependent on the excitation wavelength. For the SSV surfaces, the Raman enhancement for benzenethiol was comparable for both 633 nm and 785 nm excitation according to Mahajan's work[32]. As discussed in Section 4.3, although the

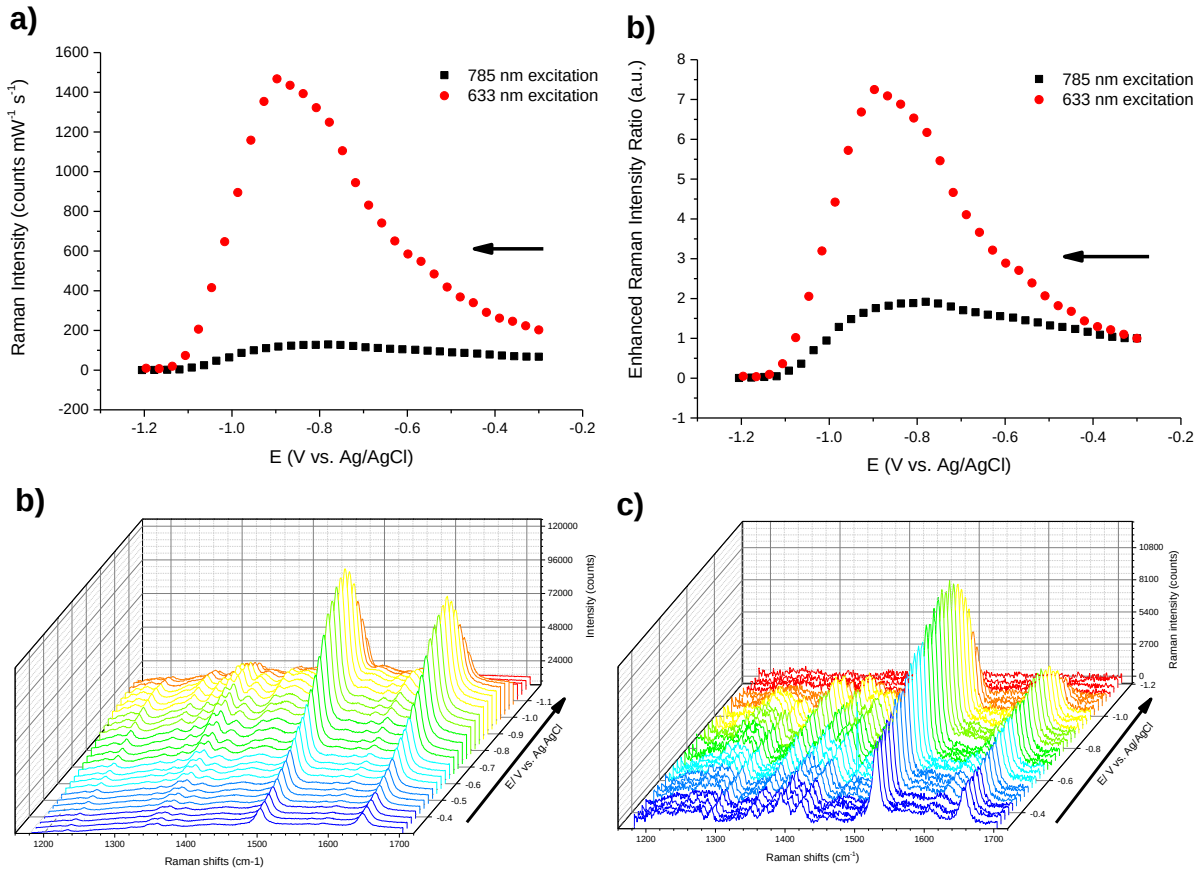

Figure 4.32 SERS recorded during linear sweep voltammetry. a) Comparison of the potential dependent Raman intensity for the 1504 cm^{-1} Texas Red band obtained with the two excitations (633 nm and 785 nm). b) Normalized Raman intensity ratio for the 1504 cm^{-1} Texas Red band obtained by dividing the Raman intensity by the initial Raman intensity at -0.3 V (vs. Ag/AgCl). c) and d) are the raw spectra recording during the potential sweep at 1 mV s^{-1}. The SSV surfaces were immersed in 1 µM Texas Red solution containing 1 M NaCl and 10 mM Tris buffer (pH 7.2) for 16 h. The SSV surfaces were separated from the same substrate to minimise the bias of the surface packing of nanospheres between the substrate. The supporting electrolyte was 1 M NaCl and 10 mM Tris buffer (pH 7.2) in the absence of Texas Red during the Raman spectroelectrochemical measurement. The arrow indicates the direction of potential sweeping.

electromagnetic enhancement of the local surface plasmonic resonance has a correlation to the excitation wavelength of the plasmon modes and the blueshift caused by the cathodic potential sweep, the potential dependent Raman enhancement at -0.3 to ca. -0.8 V cannot be attributed to a purely plasmonic effect. From the respect of CT enhancement, which requires the appropriate energy level alignment of the molecular resonance of the adsorbate, the excitation wavelength and the potential position suggests that the potential dependence in the Raman enhancement in the case

of Texas Red adsorbed on the SSV electrode might be correlated with the chemical enhancement. It is important to point out that the chemical enhancement discussed above (Section 4.7) does not exclude the existence of effects from electromagnetic enhancement (or plasmon effect) and molecular orentation which can contribute to the potential dependent Raman enhancement. Here we are trying to identify the most critical factor to explain the overall potential dependent Raman enhancement for Texas Red adsorbed on the Au SSV electrode. As indicated at the beginning of this Section, for the chemical enhancement the Fermi level (electrochemical potential) of the electrode can be tuned into an intermediate state to couple with the resonant state of the adsorbate and this results in an enhanced Raman scattering.

Unlike electromagnetic enhancement, chemical enhancement is not a universal effect in SERS, because it requires particular resonance conditions. These conditions for chemical enhancement include the appropriate electronic structure of the adsorbate, in addition the appropriate excitation wavelength and the correct position of the electrochemical potential are required in respect of the energy to collectively contribute the enhancement. To clarify the chemical enhancement effect, we will explain the model for chemical enhancement for pyridine adsorbed on coinage metals and then evaluate how the relevant factors for chemical enhancement contribute to the case of Texas Red adsorbed on Au SSV electrodes.

The characteristic potential dependent SERS scattering for pyridine was observed first by Fleischmann *et al.*[50] and later extensively studied by Jeanmaire and Van Duyne[28] in 1977. In their experiment, pyridine was chosen as the adsorbate on the SERS-active Ag electrode in 0.1 M KCl electrolyte. The response of the SERS bands was divided into two groups as shown in Figure 4.33. Bands a (1006 cm^{-1}, υ_1), b (1035 cm^{-1}, υ_{12}) and c (3056 cm^{-1}, υ_{7b}), from the first group which can be measured in the potential range 0 to -1.0 V (vs. SCE). The second group contains bands d (623 cm^{-1}, υ_{6a}), e (1215 cm^{-1}, υ_{9a}) and f (1594 cm^{-1}, υ_{8a}) whose intensity is weak at 0.0 V then grows stronger as the potential approaches -0.85 V. They ascribed the potential dependence of the Raman intensity to changes in the surface coverage and the electric field effect of the double layer. However, these two factors were not supported by latter studies. For the surface coverage, Hamelin *et al.*[51] reported that pyridine desorption from the Ag electrode begins at -1.0 V and is complete at -1.4 V (vs. SCE) based on differential capacitance measurements which indicated surface coverage changes at potentials positive than -1.0 V were not observable. Hence, the potential dependent Raman enhancement peak at -0.6 and -0.8 V cannot be explained by a change in the surface

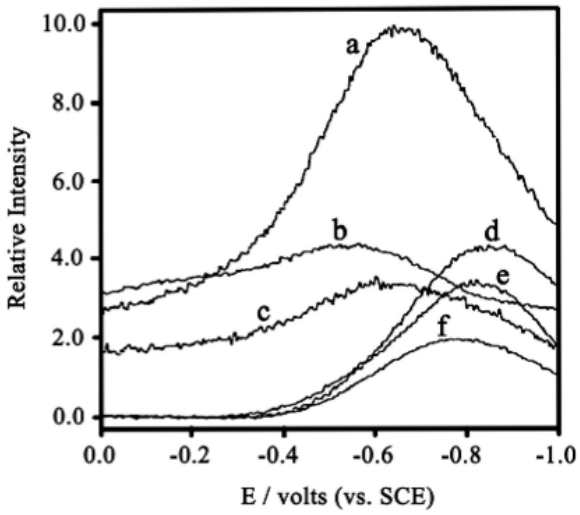

Figure 4.33 Adapted from Ref. [28]. Raman intensity dependence for adsorbed pyridine as a function of electrode potential. (a) 1006 cm^{-1}, (b) 1035 cm^{-1}, (c) 3056 cm^{-1}, (d) 1215 cm^{-1}, (e) 1594 cm^{-1}, (f) 623 cm^{-1}. The electrode surface was anodized under standard conditions. A relatively large spectrometer bandpass (20 cm^{-1}) was used to minimize the error in intensity measurement due to the effect of frequency band changes with electrode potential. Laser excitation wavelength 514.5 nm (2.41 eV). The electrode potential was scanned at a rate of 1.024 V s^{-1} beginning at 0.0 V vs. SCE. Each curve was signal averaged over ten potential scans. (Reprinted with permission from Ref. [28], Copyright© (1977) Elesvier)

coverage. The second factor suggested by Jeanmaire and Van Duyne, the double layer effect on LSPR, has been discussed in Section 4.3. The blueshift of LSPR caused by the cathodic scan can only tune the Raman enhancement in one direction, either increase or decrease, and hence cannot explain the peak shape of potential dependent Raman intensity, increasing at -0.3 to -0.8 V and then decreasing at -0.8 to -1.0 V, observed in the electrochemical SER spectra of Texas Red adsorbed on Au SSV electrodes. Such an increase in the SERS intensity with increasing cathodic potential has been previously observed for pyridine and pyrazine adsorbed on an Au(210) electrode by Brolo *et al.*[52] They also demonstrated that the increased intensity was not caused by a change in coverage or orientation of pyridine over the potential range -0.7 to +0.4 V (vs. SCE) and thus concluded that no single relationship could be found between SERS intensities and surface coverage for surface concentrations close to one monolayer. However, they did not consider the experimental result in respect of charge transfer. This also showed the limitation of the interpretation of the potential dependent Raman enhancement solely from the coverage aspect in the case of pyridine adsorbed on the Ag electrode.

Subsequent researchers investigated this characteristic potential dependent response of the SERS bands for adsorbed pyridine by examining the chemical bonding between the pyridine and the SERS-active metal surfaces. Tian's group[21,55] gave a most plausible explanation by adopting pyridine-metal models which contain Ag_4, Au_4 and Pt_5 clusters to carry out density funtional theory (DFT) calculations for the electron orbitals and binding interaction effects. They found the binding interaction between pyridine and metal has an ascending order Py–Ag_4<Py–Au_4< Py–Pt_5 which results in the band (υ_{12}) having a descending intensity in the order Py–Ag_4>Py–Au_4> Py–Pt_5. In contrast, the intensity of bands (υ_{6a}), (υ_{9a}) and (υ_{8a}) were strengthened by binding interactions. The occurrence of potential dependent bands (υ_{1}), (υ_{6a}), (υ_{9a}) and (υ_{8a}), was due to simultaneous charge-transition from the Fermi level of the Ag electrode to two unoccupied excited states $3b_1$ and $2a_2$ (with a small band gap of 0.5 eV) of the pyridine molecule. Here $3b_1$ and $2a_2$ are the assignments of the excited orbitals, the first digit is the number of the orbital level above the highest unoccupied molecular orbital (HOMO) of corresponding symmetry (a or b), the second letter and its subscript are the symmetry class of the structure of the orbital, a stands for the rotation axis and b for the symmetry plane.

Finally, the enhanced intensity of the potential dependent band is proportional to an electron-phonon coupling parameter, the Huang-Rhys factor S, that measures the enhancement of totally symmetric vibrations and scales roughly as $\Delta^2/2$, where Δ is the magnitude of displacement of the excited state potential surface along the Raman active normal coordinate. This correlation of the vibration energy was converted from the potential energy of a harmonic vibration $U = \frac{1}{2} k \Delta^2$, where the k is the force constant[56]. The displacement Δ is shown in Figure 4.36

Tian's group[54] concluded that the chemical enhancement comprises two processes: (1) the chemical binding induced enhancement; and (2) the charge transfer (CT) enhancement. The chemical binding depends on the molecular structure and the coinage metal involved in the process and is a relatively short-range effect compared to the charge transfer mechanism.[54] Moreover, the charge transfer mechanism is less sensitive to surface adsorption as compared to the chemical binding effect and hence can be observed at a relatively longer distance. Hence, for a weakly adsorbed molecule the CT enhancement may be more prominent than the chemical binding enhancement.

Jeanmaire and Van Duyne[28] also noticed that molecules with charge-transfer enhancement in Raman intensity usually had unsaturated nitrogen atoms in the molecular structure and have binding via the lone pair electrons with the coinage metal surface which may contribute to chemical enahancement. This speculation on the characteristic of molecular structure was later

supported by Lombardi and Birke[57], who measured the electrochemical SERS response to develop the theory for the charge transfer mechanism.

Although the chemical enhancement is weaker, when compared to the electromagnetic enhancement, it has been the subject of much debate over the years[19]. On the subject of electrochemical SERS, the plasmon-enhanced electromagnetic field could not solely explain the potential dependent Raman intensity which only happens under certain conditions such as the dependence on the adsorbate[54]. The topic of chemical enhancement latter attracted several groups to explore the factors affecting the chemical enhancement. In addition to Tian's group, the CT enhancement was first suggested by Gersten, Lombardi and Birke[58] approximately at the same time as several other researchers[59,60]. Lombardi and Birke[61] later described the CT enhancement in 1986. They modeled the CT enhancement as being driven by both the incident photon and the tuning of the position of the Fermi level of the metal electrode to result in an intermediate state that can couple with the excited state or ground state to produce a resonant like Raman enhancement. Resonance Raman scattering, which involve an excited electronic state of the molecule, was introduced into the CT model to explain the potential dependent Raman enhancement. We will discuss the basic theory of resonance Raman scattering first and then explain how Lombardi and Birke[61,62] extended this idea to relate the charge transfer mechanism into the resonance Raman model. The normal Raman scattering as shown in Figure 4.34 describes three scattering processes,

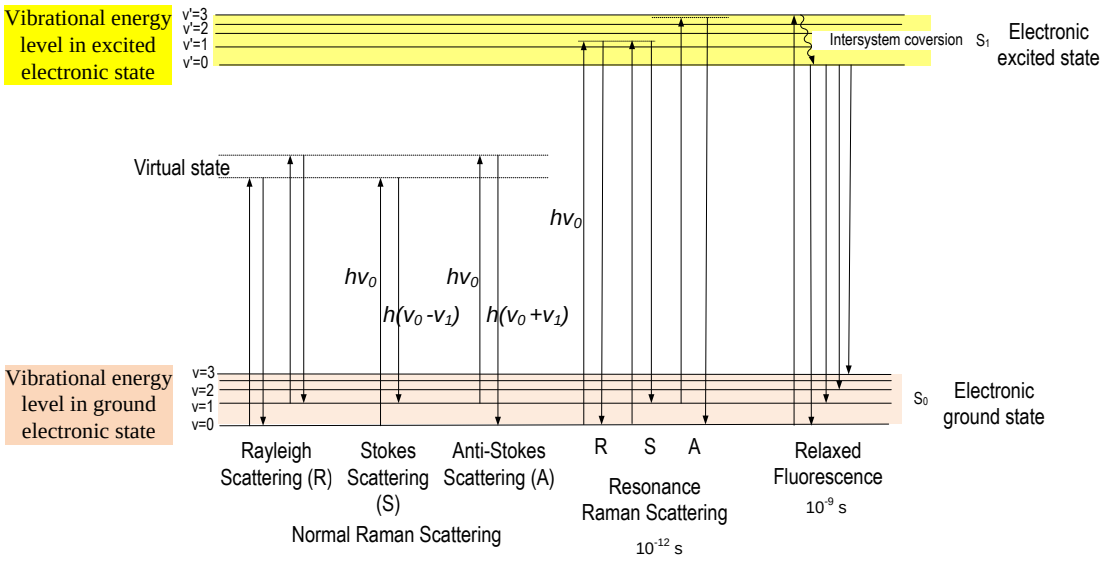

Figure 4.34 Energy diagram depicting the process of the excitation light (hv_0) and the scatterings ($hv_0 \pm v_1$). Each electronic state can be subdivided into several vibrational states. In the case of the resonance Raman scattering and fluorescence, the excitation is significantly high to enable the electron transition from the ground state to an excited state.

elastic (Rayleigh) and inelastic (Stokes) scatterings when the excitation energy (hv_0) is too low to promote the electron from the ground state into the excited state. The electric filed of the incident light absorbed by the molecule polarizes the molecule and induces a dipole. This absorbed energy radiates in the form of the scattered photon from the molecule. The photons might exchange, or not exchange energy with vibrations in the molecule. The resultant energy shift is recorded by the spectrometer and called the Raman shift. When the excitation energy is sufficiently high for the electron to be excited into an excited state, resonance Raman scattering and fluorescence occur. Although the resonant Raman process is more rapid (ca. 10^{-12} s) than fluorescence (ca. 10^{-9} s), one can hardly discriminate the two phenomena without using time-resolved techniques for example, Kerr gate [63].

The process of resonance Raman scattering contains the perturbation not only in nuclear vibrations, as in normal Raman, but also the energy transition between the excited electronic state and the electronic ground state. Based on the review of Clark *et al.*[64] , the wave functions of the valence electrons and that of the atomic nuclei can be separated by using the adiabatic Born-Oppenheimer (ABO) approximation. The ABO approximation assumes that the nuclei are "frozen" with respect to the electrons, and that the electron transition is essentially rapid compared to the motion of the atomic nuclei. Consequently the electronic states part in the ABO approximation is defined for fixed nuclear positions and hence is an eigenfunction of a total molecular Hamilton, which contains the electron-nuclear and nuclear-nuclear potential energies (based on the electrostatic attraction and repulsion), but locks the nuclear kinetic energy terms. Therefore, the vibronic states can be resolved as the products of pure vibrational states with pure electronic states.

The validity of the ABO approximation depends on the separability of the electronic and nuclear vibrational motions which is related to the ratio of the electronic to the nuclear mass. In the case of electronic states that have a large energy gap compared with a vibrational quantum, the ABO approximation gives a good energy correlation between the excited electronic states and nuclear vibrations based on the fixed positions of the nuclei. However, in the case of near degenerate levels of different vibronic modes which have very close energy gaps, and where the separability of the electronic and nuclear vibrational motions is low, a breakdown in the Born-Oppenheimer approximation may occur. This case may be introduced in the scattering formalism by the expansion of the exact molecular eigenstates using the ABO as a basis.

Albrecht[65] used the ABO approximation to substitute into the polarisability expression in the Kramers-Heisenberg-Dirac (KHD) equation (4.3), and invoked the Taylor expansion to describe

the weak dependence of nuclear coordinate on electronic states. Finally, complete integration over the electronic coordinates of resonance Raman scattering in the matrix elements can be described by the A, B and C terms in equation (4.7). Equation (4.3) will be introduced first, and then we will discuss how the ABO approximation can be applied to equation (4.3). The transition polarizability for resonance Raman scattering can be expressed by the Kramers-Heisenberg-Dirac (KHD) equation:

$$(\alpha_{\rho\sigma})_{i\to f} = \frac{1}{\hbar}\sum_{k}\left[\frac{\langle i|\mu_\rho|k\rangle\langle k|\mu_\sigma|f\rangle}{v_{ik} - v_0 + \mathrm{i}\Gamma_n} + \frac{\langle i|\mu_\sigma|k\rangle\langle k|\mu_\rho|f\rangle}{v_{kf} + v_0 + \mathrm{i}\Gamma_n}\right] \qquad (4.3)$$

The subscripts i, f and k represent initial, intermediate, and final vibronic states (Figure 4.35), respectively, and the sum is over all related states. Note the states $|i\rangle$ and $|f\rangle$ are typically vibrational ground states for before and after the resonance as shown in Figure 4.35, and the sum

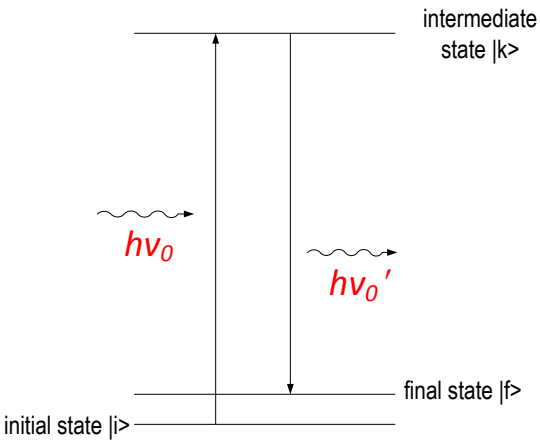

Figure 4.35 Energy diagram of KHD equation in the case of resonant Raman scattering where |i> is the initial state, |k> the intermediate state and |f> the final state. Typically |i> and |f> are located in the different vibrational level in the ground state while the |k> resides in the vibrational level in the excited state. The hv_0 and hv_0' reflect the two-photon process in Raman scattering as incident and emitted light at its corresponding frequency.

over k, in principle, runs over all vibrational sub-levels of all excitation states and excludes the initial state $|i\rangle$ and final state $|f\rangle$. μ_ρ and μ_σ are the components of the dipole moment operator where the subscripts ρ and σ denote the appropriate Cartesian components of the polarizability tensor in the molecule frame.

The numerator of each term in the KHD equation is related to the intensity of the transitions i to k and k to f, through the transition dipole moments, where, for example, $\langle i|\mu_\rho|k\rangle$ is the component of the transition dipole moment along the ρ direction, connecting states i and k. Γ_k is the damping factor or natural half-width of the state $|k\rangle$. i is the imaginary unit to multiply with Γ_k as the

damping term which is proposed by Dirac to prevent the original expression without this damping term from becoming infinite in the case of resonance scattering. When the frequency of incident radiation approaches, and becomes equal to, that of the molecular transition v_0=v_{ik} the first term in the square bracket in equation (4.3) may give a large increase of scattering intensity and the numerator is the Γ_k equal to the half-width of the excited state. The second term in the square bracket in equation (4.3) is non-resonant and produces a slowly varying background contribution which is usually negligible compared to the first term in the resonant condition. However, in the case of normal Raman scattering where v_{ik}>> v_0>> v_{if}, both terms should be taken into account.

The detailed derivation steps from the KHD equation to the Albretcht's equations can be found in the review of Clark *et al.*[64]. Albrecht[65] substituted the product of wave functions at ABO states into the polarizability expression of equation (4.3), then the integration over the electronic coordinates in the matrix elements, M, can be completed to represent the magnitude of the electronic transition moment and is still parametrically dependent on the equilibrium coordinate, Q through the electronic states.

Since the dependence of the matrix element in a dipole moment transition, M, is supposed to be a weak function of the internuclear coordinates, Q, it is described by a rapidly converging Taylor series expanded near the equilibrium nuclear coordinate, Q_0. To simplify the presentation here we consider only one normal mode coordinate $\mathrm{Q}_a$of the a^{th} normal mode of the appropriate symmetry and important in this expansion as

$$\mathrm{M}_{ik}^{\rho}(\mathrm{Q}) = \mathrm{M}_{ik}^{\rho}(Q_0) + (\frac{\partial \mathrm{M}_{ik}^{\rho}}{\partial \mathrm{Q}_a})_{Q_0}\mathrm{Q}_a + \cdots \qquad (4.4)$$

The transition moment M no longer only depends on the equilibrium nuclear coordinate, Q_0. In the second term on the right, a new dependence established on the nonzero second term indicates that the transition moment can be coupled with the first term on the right at the perturbed nuclear coordinate, Q_a . This is the core concept of vibronic coupling. The nuclear position is no longer purely "frozen" to the electronic transition as assumed in ABO approximation in this case. This new intermediate state is defined with "m" in the subscript to indicate the transitions between the ground and excited states.

The first-order partial derivative of the matrix element in equation (4.4) is referred to as the Herzberg-Teller term and can be written

$$\left(\frac{\partial \mathrm{M}_{ik}^{\rho}}{\partial \mathrm{Q}_a}\right)_{Q_0} = \sum_m M_{mi}^{\rho}(Q_0) h_{km} \tag{4.5}$$

where

$$h_{km}(Q) = \frac{1}{\hbar} \frac{< \mathrm{k}| \frac{\partial \mathrm{H}}{\partial \mathrm{Q}_a} |\mathrm{m} >}{\omega_{km}} \tag{4.6}$$

and $h_{km}(Q)$ is the coordinate operator to mix two electronic states including the intermediate state, |i>, and the new intermediate states, |m>. Note this coordinate operator h differs from the Plank constant $\hbar$. This electronic state mixing distorts both the upper and lower states that are mixed, giving extra intensity to the weaker one thereby creating a strong resonance Raman enhancement as shown in Figure 4.36 c) and d).

Albrecht[65] further substituted the two terms of the Taylor expansion in equation (4.4) into the KHD equation (4.3) and the resultant transition polarizability can, therefore, be expressed as

$$(\alpha_{\rho\sigma})_{i\to f} = A + B + C \tag{4.7}$$

where

$$A = \sum_{k\neq i}\sum_{k}\left[\frac{M_{ki}^{\sigma}(Q_0) M_{ki}^{\rho}(Q_0)}{\hbar(\omega_{ki} - \omega) + \mathrm{i}\Gamma_k} + \frac{M_{ki}^{\rho}(Q_0) M_{ki}^{\sigma}(Q_0)}{\hbar(\omega_{ki} + \omega) + \mathrm{i}\Gamma_k}\right] \langle i|\mathrm{k}\rangle\langle k|\mathrm{f}\rangle \tag{4.8}$$

$$\begin{aligned} B = \sum_{k\neq i}\sum_{k}\sum_{m\neq k}\Bigg[&\frac{M_{ik}^{\sigma} h_{km} M_{mi}^{\rho}}{\hbar(\omega_{ki} - \omega) + \mathrm{i}\Gamma_k} + \frac{M_{ik}^{\rho} h_{km} M_{ki}^{\sigma}}{\hbar(\omega_{ki} + \omega) + \mathrm{i}\Gamma_k}\Bigg] \frac{\langle i|k\rangle\langle k|Q_a|f\rangle}{\hbar\omega_{mk}} \\ &+ \left[\frac{M_{im}^{\sigma} h_{mk} M_{ki}^{\rho}}{\hbar(\omega_{ki} - \omega) + \mathrm{i}\Gamma_k} + \frac{M_{im}^{\rho} h_{mk} M_{ki}^{\sigma}}{\hbar(\omega_{ki} + \omega) + \mathrm{i}\Gamma_k}\right] \frac{\langle i|Q_a|f\rangle\langle k|f\rangle}{\hbar\omega_{mk}} \end{aligned} \tag{4.9}$$

$$\begin{aligned} C = \sum_{k\neq i}\sum_{k}\sum_{m\neq i}\Bigg[&\frac{h_{im} M_{mk}^{\sigma} M_{ki}^{\rho}}{\hbar(\omega_{ki} - \omega) + \mathrm{i}\Gamma_k} + \frac{h_{im} M_{mk}^{\rho} M_{ki}^{\sigma}}{\hbar(\omega_{ki} + \omega) + \mathrm{i}\Gamma_k}\Bigg] \frac{\langle i|k\rangle\langle k|Q_a|f\rangle}{\hbar\omega_{im}} \\ &+ \left[\frac{M_{im}^{\sigma} h_{mk} M_{ki}^{\rho}}{\hbar(\omega_{ki} - \omega) + \mathrm{i}\Gamma_k} + \frac{M_{im}^{\rho} h_{mk} M_{ki}^{\sigma}}{\hbar(\omega_{ki} + \omega) + \mathrm{i}\Gamma_k}\right] \frac{\langle i|Q_a|f\rangle\langle k|f\rangle}{\hbar\omega_{im}} \end{aligned} \tag{4.10}$$

The *A*-term represents a Franck-Condon contribution and the B and C-terms Herzberg-Teller contributions. Only totally symmetric modes are enhanced by the *A*-term. However, the *B*-term and *C*-term can enhance both totally symmetric and non-totally symmetric vibrations. When the Fermi level of the metal lies between the excited and the ground states of the adsorbed molecules, the *B*-

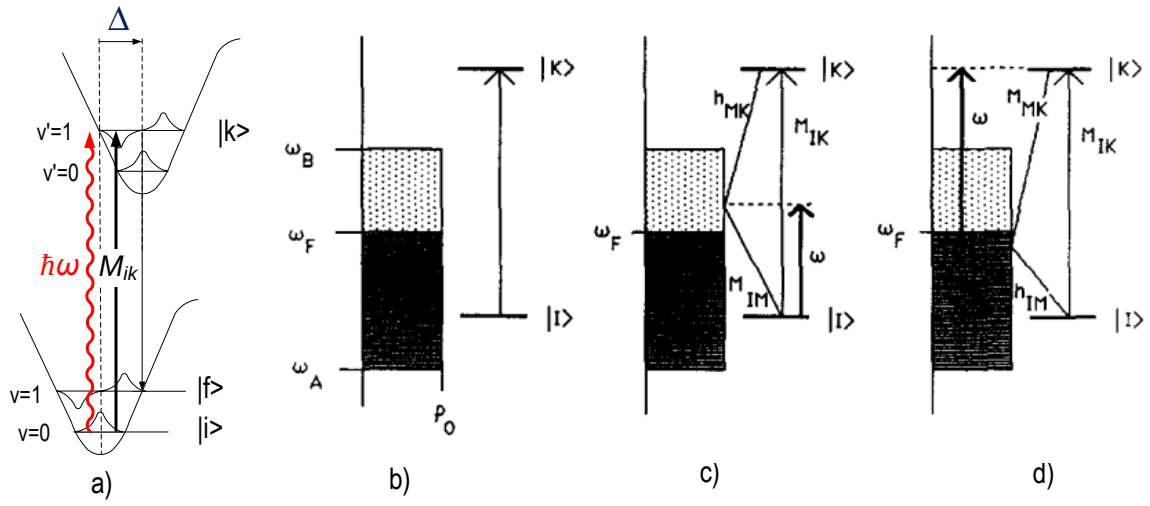

Figure 4.36 a) Modified from Ref. [56]. A schematic to explain the Albrecht equation of resonance Raman polarizability. M_{ik} are the electronic transition moments between the states |i> and |k>. h_{mk} the Herzberg-Teller coupling parameter between the states |m> and |k>. |i> represent the lowest occupied molecular orbital (ground state), |m> is the excited charge-transfer state; |k> reflects the excited state. Δ represents the nuclear displacement between the ground state and the excited state. b) to d) reprinted from Ref. [61]. b) Energy level scheme for molecule-metal system. The (discrete) molecular levels are |i> and |k>, between which a transition is assumed to be allowed. The (continuous) metal levels of the conduction band of the metal are shown on the left. The conduction band ranges between ω_A and ω_B . The filled levels range up to ω_F' the Fermi level, and are depicted by lines, while the unfilled levels are depicted by dots. c) The scheme for molecule-to-metal charge transfer transitions between the ground molecular state and unfilled levels of the metal. The transition borrows intensity from the allowed transition by means of vibronic coupling between metal levels and the excited molecular level through the matrix element h_{MK}. d) The scheme for metal-to-molecule charge transfer transitions between filled levels of the metal and the excited molecular state. The transition borrows intensity from the allowed transition by means of vibronic coupling between metal levels and the ground molecular state through the matrix element h_{IM}. (Reprinted with permission from Ref. [61]. Copyright 1986 American Physics Institute)

term and *C*-terms cannot be ignored. Due to this symmetry-dependent enhancement mechanism for a molecule which adsorbs on the SERS-active surface, with its orbital energy levels lying across the Fermi level, the resultant enhanced intensity would have a different response on potential. The red terms indicate the absorbed radiation related energy.

Note the first terms in each angular bracket in equations (4.8) to (4.10) are the resonant terms which contribute the dominant intensity in the appropriate conditions. The *A*-term does not differ from the KHD equation, the critical parameter in the numerator of matrix elements, the zero-order term of the Taylor series (4.4), $\mathrm{M}_{ik}^{\rho}(Q_0)$, contributes the *A*-term in equation (4.7) which still obeys the ABO assumption. However, the first-order term, $(\frac{\partial \mathrm{M}_{ik}^{\rho}}{\partial \mathrm{Q}_a})_{Q_0}\mathrm{Q}_a$, represents the non-zero dependence of the transition moment on the nuclei coordinate, which is breakdown of ABO approximation and results in *B* and *C*-terms in equation (4.7). The physical meanings of the *B* and *C*-term are two fold. First, a vibronic coupling (a change of nuclear coordinates occurs upon electronic transition) and the nuclei are no longer purely "frozen". Second, due to the shifted displacement of nuclei positions, the electron transition can gain observable intensity from the electronically forbidden, but vibronically allowed, transition, if the electronic transition moment depends strongly on the nuclear coordinate, or if the transition can borrow intensity from the electronically allowed transition. The electronically forbidden cases mean that the excitation wavelength ($h\omega$) is less than the molecular transition gap ($h\omega_{ki}$) or the product of transition moment is not totally symmetric. An electronic transition must be allowed since the direct product of any irreducible representation with itself must always include the totally symmetric representation (and hence the electronic transition moment can be non-zero). These vibronic coupling conditions in *B* and *C*-terms result in an extra "vibronic state" in which the vibration levels were coupling into the electronic excited state using the coordinate operator *h* as shown in Figure 4.36.

Lombardi and Birke[61] followed Albrecht's conclusion and further realized that when the Fermi level of the SERS-active electrode is close to the energy gap of the adsorbate, tuning the position of the Fermi level can collaboratively promote the valence electron at the HOMO excited by low energy radiation (less than the resonance wavelength) into the intermediate state as shown in Figure 4. 37.

This photon-induced coupling with the excited state, tuned by the electrochemical potential, results in resonance-like Raman enhancement which has been experimentally observed in the literature. The reported adsorbates include p-aminothiophenol[66], rhodamine 6G[67], crystal violet[68], Malachite Green[68], Rose Bengal[68], the azo dye 4-(dimethylamino) azobenzene-4'-sulfonyl aspartate (DABS)[69], and the ruthenium-based dye N719[70]. The potential dependent Raman enhancement observed for these adsorbates have similar features in the molecular structure as observed by Jeanmaire and Van

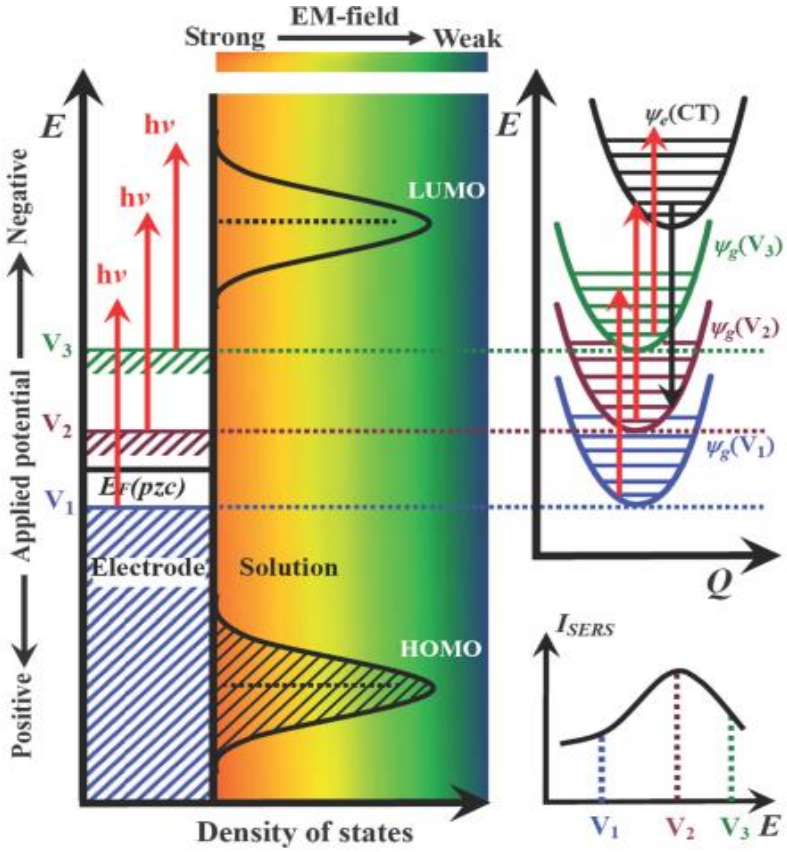

Figure 4.37 Schematic diagrams of the photon-driven charge transfer from a metal electrode to an adsorbed molecule in the EC-SERS system. Left: the conceptual model of the energy levels changed with the electrode potential in the CT process. Right: the relevant energy states involved in the electronic levels and the vibrational levels in the CT process. Right bottom: the corresponding SERS intensity-potential profile. V_i denotes the applied potential. Reprinted from Ref. [54] with permission, Copyright© (2008) of the Royal Society of Chemistry.

Duyne[28]. These features include the adsorbates either have atoms with lone pairs (S or N) that can contribution of the chemical binding with the metal or possess a conjugated chain of π-electrons to involve in the (donating or accepting) charge transfer state. Based on the CT model, only when the electrochemical potential matches the corresponding energy level of the excited electronic state of the molecule can the resonant-like enhancement be observed.

After reviewing the charge-transfer mechanism described by Lombardi *et al.*[62], we further calculated the molecular orbital energy distribution for Texas Red at the B3LYP/6-311++G(d,p) level and the work function of the polycrystalline Au electrode to examine the consistency between the experimental results and the CT theory. The Fermi level for the Au electrode can be converted into the physical scale using the equation reported by Trassatti where $E_{abs} = E_{SHE} + 4.44$ (eV). E_{abs}

represents the absolute potential and E_{SHE} is the standard hydrogen electrode. The physical scale is the negative value of the absolute potential scale. The pseudo-reference Ag/AgCl electrode used in our experiments can be converted to the saturated calomel electrode scale and results in -0.012 V vs. SCE in 1 M NaCl 10 mM Tris buffer, pH7.2. The correlation energy diagram between the molecular orbitals and the electrochemical potential scale is shown in Figure 4.38.

Although the results for Texas Red used from the calculation refer to the vacuum state without the solvation and metal interactions included, the energy levels still provide crucial information in order to discuss the CT mechanism. First of all, the 632.8 nm HeNe excitation is not close enough to the natural electronic transition in Texas Red to enable direct resonance Raman scattering. The natural electronic transition for Texas Red is estimated from the major absorption peak to be at 595

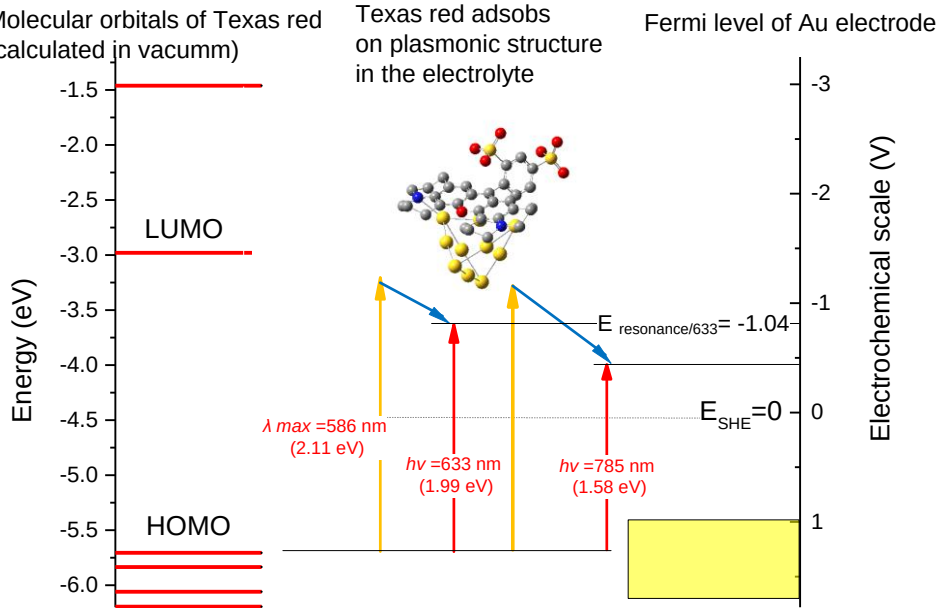

Figure 4.38 Energy level diagram showing the correlation of molecular orbitals and the Fermi level of the Au electrode. The work function was estimated to be 5.4 eV for clean polycrystalline Au based on Wan *et al.*[71] The energy gap between the LUMO and HOMO was estimated from the maximum absorption at 595 nm in Figure 4.31. The resonant potential of peak Raman intensity of the 1504 cm^{-1} is obtained at -1.04 eV converted from the Trassatti's equation[72] and the experimental result shown at -0.85 V (vs. Ag/AgCl) in Figure 4.32. The 633 nm and 785 nm excitation were converted into the physical scale. The blue arrows indicate the molecule to metal charge transfer resonance into the unfilled Au electrode level as decribed in this Section 4.7.

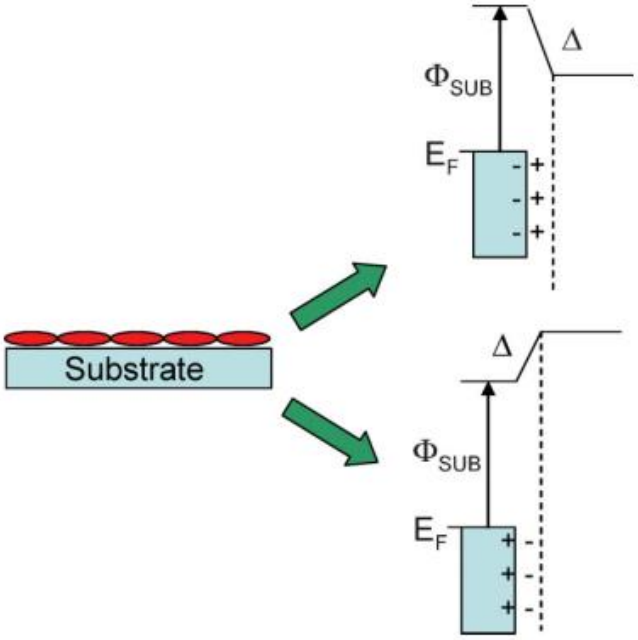

Figure 4.39 Schematic picture of a charge-transfer-induced interface dipole (Δ) created by chemisorption of a molecular monolayer that shift the work function Φ_{SUB} down (electronic charge transferred to the substrate, top right) or shifts the work function Φ_{SUB} up (electronic charge transferred from the substrate, bottom right). (Reprinted with permission from Ref. [73] Copyright© 2009 of John Wiley & Sons)

nm from Figure 4.31. The electronic absorption spectrum of Texas Red indicates that the adsorption of Texas Red decreases dramatically when the wavelength of the incident light is longer than 610 nm. Hence, the *A*-term in the Albrecht equation is less obvious for the Raman intensity in this case. Second, the resonant potential of the peak in Raman intensity obtained from the experimental results in the beginning of this Section 4.7 is ca. -1.04 eV (-0.85 vs. Ag/AgCl) and is located in the unfilled levels of the Au electrode. Combining these conditions, the potential dependent Raman enhancement of Texas Red adsorbed on the Au electrode meets the requirement to be attributed as a molecule-to-metal charge transfer resonance.

Third, the LUMO+1 orbital of Texas Red is located at higher energy (1.5 eV) than the LUMO orbital. This large energy gap between LUMO and LUMO+1 reduces the chance to invoke the second enhancement of the Raman intensity onset at a much more negative potential to the first one that peaks at ca. -0.8 V. The Texas Red might desorb before the supposed potential of the second enhancement in the Raman intensity. This large energy gap in the frontier LUMO orbitals of Texas Red is different from the case of pyridine on the Ag electrode at discussed earlier in the beginning of this Section 4.7, where the small energy gap between the excited states (LUMO and LUMO+1) may allow a second potential dependent Raman enhancement. Following the attribution of the

molecule-to-metal CT model shown in Figure 4.36, the molecule-to-metal CT will result in a positive potential shift of the peak Raman intensity in the case of long wavelength excitation such as 785 nm excitation. However, this positive potential shift of the peak Raman intensity as shown in Figure 4.38 is not obvious while the enhancement intensity ratio clearly decreases. To explore this descrepency and more details on the CT enhancement, the literature and this study indicate that the work function of the organic adsorbates and the metal are both of importance as the solid fundamental information to prove or disprove the CT model. As the review of Braun *et al.*[73], the energy level alignments of the organic/metal interface are complicated especially in the chemisorption case. They described two effects on the shift of the vacuum level in the chemisorption of organic molecules on metal electrodes. In the first effect, shown in Figure 4.39 the charge transfer will induce an interface dipole which either shifts the work function down (electronic charge transfer from molecule to metal) or up (electronic charge transfer from metal to molecule). The two effects are consistent with the CT model while the extra shift of the energy level of the vacuum level needs to be considered. The work function is also affected by the surface curvature, supporting solvent, adsorbates, residual impurities, and crystal face[74]. Each factor might cause the bias when one tries to discuss the CT enhancement. However, these factors are beyond the scope of this study and the extensive research on the work function of the metal is left for future work.

Conclusions

In this Chapter the potential-dependent Raman enhancement for Texas Red adsorbed on the SSV Au electrode has been investigated considering the effects of adsorption/desorption, re-orientation, potential-tuning plasmon resonance, interference of hydrogen evolution and the accompanied potential dependent baseline growth. Based on the experimental results, we conclude that the excitation wavelength, electrode potential and the electronic structure of Texas Red are the most critical factors in the potential dependent Raman enhancement and that it is related to the chemical enhancement. The higher energy gap of Texas Red to LUMO+1 reduces the chance of exciting a second group of Raman bands to exhibit a potential dependent enhancement as seen for pyridine. This conclusion does not exclude the contribution of plasmonic enhancement but only describes the most significant factors in the potential dependent Raman enhancement in the case of the adsorbed Texas Red. The plasmonic enhancement still makes a significant contribution to the overall SERS enhancement and can tune the potential dependent enhancement based on the corresponding LSPR

as discussed in Section 4.3. As in the unified view described by Lombardi *et al.*[62], the SERS enhancement is a collective contribution between the plasmonic resonance (LSPR), molecular resonance and the charge transfer resonance, each of which makes a contribution to a varied extent that depends on the excitation wavelength, electrode potential and the adsorbed molecule. We will compare the behaviour of the potential dependent Raman enhancement in the case of adsorbed Texas Red to the Texas Red-labelled beacon probe, and discuss how they result in the next Chapter.

4.8 References

(1) Mahajan, S.; Richardson, J.; Brown, T.; Bartlett, P. N.*J. Am. Chem. Soc.* **2008**, *130*, 15589.
(2) Drexhage, K. H.In *Topics in Applied Physics*; Springer, 1973; pp. 144–193.
(3) Jensen, L.; Schatz, G. C.*J. Phys. Chem. A. Lett* **2006**, *110*, 5973.
(4) Watanabe, H.; Hayazawa, N.; Inouye, Y.; Kawata, S.; Spectroscopy, T. R.*J. Phys. Chem. B* **2005**, *109*, 5012.
(5) Su, G. J.; Yin, S. X.; Wan, L. J.; Zhao, J. C.; Bai, C. L.*Surf. Sci.* **2004**, *551*, 204.
(6) Wang, D.; Wan, L. J.; Wang, C.; Bai, C. L.*J. Phys. Chem. B* **2002**, *106*, 4223.
(7) Hildebrandt, P.; Stockburger, M.*J. Phys. Chem.* **1984**, *88*, 5935.
(8) Hildebrandt, P.; Keller, S.; Hoffmann, A.; Vanhecke, F.; Schrader, B.*J. Raman Spectrosc.* **1993**, *24*, 791.
(9) Chowdhury, J.; Pal, P.; Ghosh, M.; Misra, T. N.*J. Colloid Interface Sci.* **2001**, *235*, 317.
(10) Vosgröne, T.; Meixner, A. J.*J. Lumin.* **2004**, *107*, 13.
(11) Vosgröne, T.; Meixner, A. J.*ChemPhysChem* **2005**, *6*, 154.
(12) Li, J. F.; Huang, Y. F.; Ding, Y.; Yang, Z. L.; Li, S. B.; Zhou, X. S.; Fan, F. R.; Zhang, W.; Zhou, Z. Y.; Wu, D. Y.; Ren, B.; Wang, Z. L.; Tian, Z. Q.*Nature* **2010**, *464*, 392.
(13) Zhang, M.; Yu, L. J.; Huang, Y. F.; Yan, J. W.; Liu, G. K.; Wu, D. Y.; Tian, Z. Q.; Mao, B. W.*Chem. Commun.* **2014**, *50*, 14740.
(14) Krishnakumar, V.; Keresztury, G.; Sundius, T.; Ramasamy, R.*J. Mol. Struct.* **2004**, *702*, 9.
(15) Larkin, P.*Infrared and Raman Spectroscopy: Principles and Spectral Interpretation*; Elsevier: Amsterdam, The Netherlands, 2011.
(16) Márquez, M. J.; Márquez, M. B.; Cataldo, P. G.; Brandán, S. A.*Open J. Synth. Theory Appl.* **2015**, *4*, 1.
(17) Moskovits, M.; Suh, J. S.*J. Phys. Chem.* **1984**, *88*, 5526.
(18) Suh, J.S., Moskovits, M.*J. Phys. Chem.* **1988**, 6327.
(19) LeRu, E. C.; Etchegoin, P. G.*Principles of Surface-Enhanced Raman Spectroscopy and related plasmonic effects*; Elsevier: Amsterdam, The Netherlands, 2008.
(20) Cole, R. M.; Baumberg, J. J.; DeGarcia Abajo, F. J.; Mahajan, S.; Abdelsalam, M.; Bartlett, P. N.*Nano Lett.* **2007**, *7*, 2094.
(21) Gao, X.; Davies, J. P.; Weaver, M. J.*J. Phys. Chem.* **1990**, *94*, 6858.
(22) Pagannone, M.; Fornari, B.; Mattei, G.*Spectrochim. Acta.* **1987**, *43*, 621.
(23) Xue, G.; Ma, M.; Zhang, J.; Lu, Y.; Carron, K. T.*J. Colloid Interface Sci.* **1992**, *150*, 1.
(24) Macdonald, I. D. G.; Smith, W. E.*Langmuir* **1996**, *12*, 706.
(25) Takahashi, M.; Furukawa, H.; Fujita, M.; Ito, M.*J. Phys. Chem.* **1987**, *91*, 5940.
(26) Byers, C. P.; Hoener, B. S.; Chang, W. S.; Yorulmaz, M.; Link, S.; Landes, C. F.*J. Phys. Chem. B* **2014**, *118*, 14047.
(27) Brown, A. M.; Sheldon, M. T.; Atwater, H. A.*ACS Photonics* **2015**, *2*, 459.
(28) Jeanmaire, D. L.; VanDuyne, R. P.*J. Electroanal. Chem.* **1977**, *84*, 1.
(29) Novo, C.; Funston, A. M.; Gooding, A. K.; Mulvaney, P.*J. Am. Chem. Soc.* **2009**, *131*, 14664.
(30) Dondapati, S. K.; Ludemann, M.; Müller, R.; Schwieger, S.; Schwemer, A.; Händel, B.; Kwiatkowski, D.; Djiango, M.; Runge, E.; Klar, T. A.*Nano Lett.* **2012**, *12*, 1247.
(31) Haynes, C. L.; VanDuyne, R. P.*J. Phys. Chem. B* **2003**, *107*, 7426.
(32) Mahajan, S.; Cole, R. M.; Soares, B. F.; Pelfrey, S. H.; Russell, A. E.; Baumberg, J. J.; Bartlett, P. N.*J. Phys. Chem. C* **2009**, *113*, 9284.
(33) Cintra, S.; Abdelsalam, M. E.; Bartlett, P. N.; Baumberg, J. J.; Kelf, T. A.; Sugawara, Y.; Russell, A. E.*Faraday Discuss.* **2006**, *132*, 191.
(34) Hatab, N. A.; Hsueh, C.-H.; Gaddis, A. L.; Retterer, S. T.; Li, J.-H.; Eres, G.; Zhang, Z.; Gu, B.*Nano Lett.* **2010**, *10*, 4952.
(35) Owen, J. F.; Chen, T. T.; Chang, R. K.; Laube, B. L.*Surf. Sci.* **1983**, *131*, 195.
(36) Dick, L. A.; McFarland, A. D.; Haynes, C. L.; VanDuyne, R. P.*J. Phys. Chem. B* **2002**, *106*, 853.
(37) Abdelsalam, M.; Bartlett, P. N.; Russell, A. E.; Baumberg, J. J.; Calvo, E. J.; Tognalli, N. G.; Fainstein, A.*Langmuir* **2008**, *24*, 7018.

(38) Abdelsalam, M. E.; Bartlett, P. N.; Baumberg, J. J.; Cintra, S.; Kelf, T. A.; Russell, A. E.*Electrochem. commun.* **2005**, *7*, 740.
(39) Ulman, A.; Scaringe, R. P.*Langmuir* **1992**, 894.
(40) Satjapipat, M.; Sanedrin, R.; Zhou, F.*Langmuir* **2001**, *17*, 7637.
(41) Trasatti, S.; Petrii, O. A.*Pure Appl. Chem.* **1991**, *63*, 711.
(42) Krause, S.In *Encyclopedia of Electrochemistry, Volume 3*; John Wiley & Sons: New York, NY, 2003; pp. 196–229.
(43) Unruh, J. R.; Gokulrangan, G.; Wilson, G. S.; Johnson, C. K.*Photochem. Photobiol.* **2007**, *81*, 682.
(44) Bublitz, G. U.; Boxer, S. G.*Annu. Rev. Phys. Chem.* **1997**, *48*, 213.
(45) Pope, J. M.; Buttry, D. A.*J. Electroanal. Chem.* **2001**, *498*, 75.
(46) Kaiser, W.; Rant, U.*J. Am. Chem. Soc.* **2010**, *132*, 7935.
(47) Dreuw, A.; Head-Gordon, M.*Chem. Rev.* **2005**, *105*, 4009.
(48) Foresman, J. B.; Frisch, A. E.*Exploring chemistry with electronic structure methods: a guide to using Gaussian.*; 2nd ed.; Gaussian Inc.: Pittsburgh, PA, USA, 1996.
(49) Tuschel, D.*Spectroscopy* **2016**, *31*, 14.
(50) Fleischmann.M.; Hendra, P. J.; McQuilla.A.J.*Chem. Phys. Lett.* **1974**, *26*, 163.
(51) Hamelin, A.; Morin, S.; Richer, J.; Lipkowski, J.*J. Electroanal. Chem.* **1989**, *272*, 241.
(52) Brolo, A. G.; Irish, D. E.; Lipkowski, J.*J. Phys. Chem. B* **1997**, *101*, 3906.
(53) Wu, D. Y.; Hayashi, M.; Chang, C. H.; Liang, K. K.; Lin, S. H.*J. Chem. Phys.* **2003**, *118*, 4073.
(54) Wu, D. Y.; Li, J. F.; Ren, B.; Tian, Z. Q.*Chem. Soc. Rev.* **2008**, *37*, 1025.
(55) Wu, D. Y.; Hayashi, M.; Lin, S. H.; Tian, Z. Q.*Spectrochim. Acta - Part A Mol. Biomol. Spectrosc.* **2004**, *60*, 137.
(56) Asher, S. A.*Annu. Rev. Phys. Chem.* **1988**, *39*, 537.
(57) Lombardi, J. R.; Birke, R. L.; Sanchez, L. A.; Bernard, I.; Sun, S. C.*Chem. Phys. Lett.* **1984**, *104*, 240.
(58) Gersten, J. I.; Birke, R. L.; Lombardi, J. R.*Phys. Rev. Lett.* **1979**, *43*, 147.
(59) Burstein, E.; Chen, Y. J.; Chen, C. Y.; Lundquist, S.; Tosatti, E.*Solid State Commun.* **1979**, *29*, 567.
(60) Persson, B. N. J.*Chem. Phys. Lett.* **1981**, *82*, 561.
(61) Lombardi, J. R.; Birke, R. L.; Lu, T.; Xu, J.*J. Chem. Phys.* **1986**, *84*, 4174.
(62) Lombardi, J. R.; Birke, R. L.*Acc. Chem. Res.* **2009**, *42*, 734.
(63) Smith, E.*Modern Raman Spectroscopy*; Wiley: New York, NY, 2005.
(64) Clark, R. J. H.; Steward, B.In *Structure and Bonding, Inorganic chemistry and spectroscopy*; Springer Berlin: Heidelberg, 1979; pp. 1–80.
(65) Albrecht, A. C.*J. Chem. Phys.* **1961**, *34*, 1476.
(66) Osawa, M.; Matsuda, N.; Yoshii, K.; Uchida, I.*J. Phys. Chem.* **1994**, *98*, 12702.
(67) Grochala, W.; Kudelski, A.; Bukowska, J.*J. Raman Spectrosc.* **1998**, *29*, 681.
(68) Kudelski, a.*Chem. Phys. Lett.* **1996**, *253*, 246.
(69) Siiman, O.; Smith, R.; Blatchford, C.; Kerker, M.*Langmuir* **1985**, *1*, 90.
(70) Qiu, Z.; Zhang, M.; Wu, D. Y.; Ding, S. Y.; Zuo, Q. Q.; Huang, Y. F.; Shen, W.; Lin, X. D.; Tian, Z. Q.; Mao, B. W.*ChemPhysChem* **2013**, *14*, 2217.
(71) Wan, A.; Hwang, J.; Amy, F.; Kahn, A.*Org. Electron. physics, Mater. Appl.* **2005**, *6*, 47.
(72) Trassatti.*J. Electroanal. Chem. Interfacial Electrochem.* **1986**, *209*, 417.
(73) Braun, S.; Salaneck, W. R.; Fahlman, M.*Adv. Mater.* **2009**, *21*, 1450.
(74) Hwang, J.; Wan, A.; Kahn, A.*Mater. Sci. Eng. R Reports* **2009**, *64*, 1.

Chapter 5 Effect of Potential on the Raman Response of Texas Red-labelled Beacon Probe

5.1 Wavelength Dependence of Texas Red-labelled Beacon Probes

The surface enhanced Raman spectroelectrochemistry of Texas Red (TR) was discussed in Chapter 4. We now go back to compare the behaviour of the Texas Red-labelled beacon probe under the same conditions at the SSV electrode. Based on our conclusions from Chapter 4, we interpret the potential dependent Raman enhancement for the Texas Red in terms of the photon-induced charge transfer (CT) resonance; the excitation plays a critical role in enhancing the Raman intensity of Texas Red in the specific electrode potential range. However, the CT model basically can only apply when the molecule (Texas Red) direct contacts the Au surface. It may not work if there is any distance or another molecule in the way.

First, we compare the Raman response for the TR-labelled beacon probe and for adsorbed TR at the same substrate with 633 and 785 nm excitation. The Au SSV substrates were fabricated as described in Section 2.1 using a 600 nm diameter template with a depostion thickness of 525 nm. This substrate shows Raman enhancement for both 633 and 785 nm excitation as discussed in Section 4.6. The SSV substrates were modified with a 1 μM TR-labelled beacon probe solution containing 1 μM mercaptohexanol in 0.5 M NaCl, 10 mM Tris buffer (pH 7.2) for 16 h. The other SSV substrates, cut from the same original template sample, were immersed in a 1 μM TR solution containing 1 M NaCl, 10 mM Tris buffer (pH 7.2) for 16 h. The Raman measurements using 633 nm excitation were carried out as described in Section 2.3 . The potential was scanned from -0.3 to -1.2 V at 1 $mV\,s^{-1}$.

The results are shown in Figure 5.1. It is clear that the Texas Red-labelled beacon probe has a weaker spectrum when compared to the Texas Red adsorbed electrode because the coverage of the Texas Red-labelled beacon probe is less, but there is a small enhanced Raman response that peaks at -0.8 V. The normalized Raman intensity ratio of the 1504 cm^{-1} band of TR and TR-labelled beacon probe is ca. 1.5 to 7 fold increased. The reason for the shift in the peak potential for the maximum Raman enhancement from -0.85 to -0.78 V is not obvious currently and may be attributed to the charge-transfer-induced dipole created by chemisorption mentioned at the end of

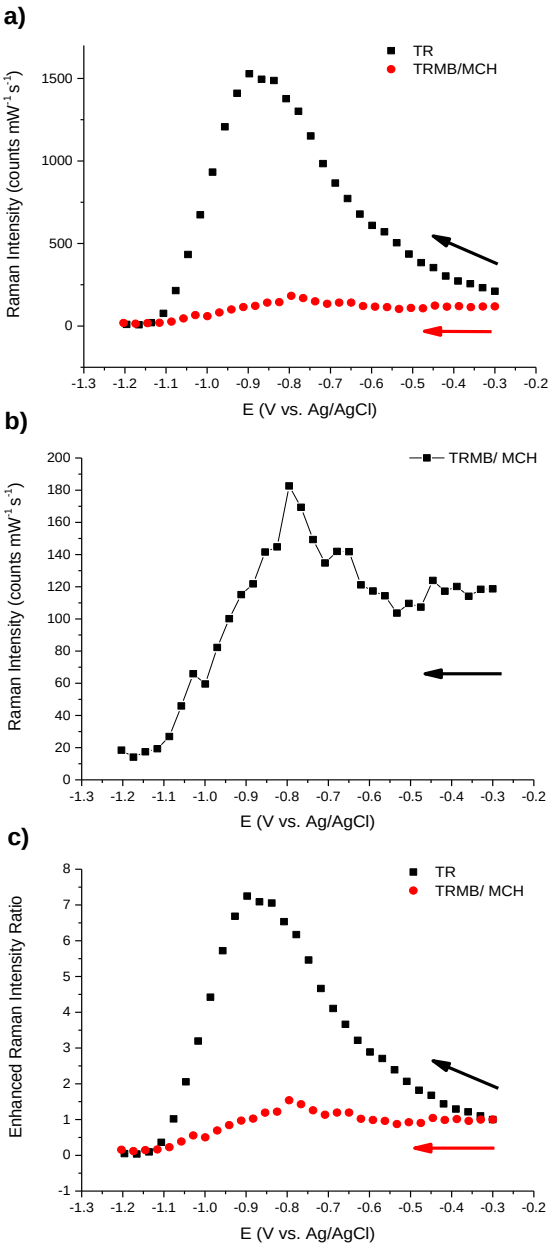

Figure 5.1 a) SERS intensity of the 1504 cm^{-1} band recorded during linear sweep voltammetry for adsorbed Texas Red (TR) and Texas Red–labelled beacon probe (TRMB)/ mercaptohexanol (MCH) adsorbed on SSV Au electrodes individually. The SSV substrates were fabricated as described in Section 2.1. Texas Red was adsorbed on the SSV electrode by immersion in a 1μM Texas Red solution containing 1 μM mercaptohexanol in 1M NaCl and 10 mM Tris buffer (pH 7.2) for 16 h. The Texas Red-labelled beacon probe was adsorbed from a 1 μM solution of TR labelled solution containing 1 μM mercaptohexanol in 0.5 M NaCl, 10 mM Tris buffer (pH 7.2) for 16 h. The potential was swept from -0.3 to -1.2 V at 1 mV s^{-1}. The Raman spectra were acquired using 25 s exposure during the 25 mV potential cathodic sweep. b) The Raman intensity of the 1504 cm^{-1} band for TRMB/ MCH during potential sweep. c) The enhanced Raman intensity ratios the 1504 cm^{-1} band for TR and TRMB/ MCH were normalized by the initial Raman intensity at -0.3 V. The arrow indicates the direction of potential sweeping.

Chapter 4. The other difference between the adsorbed TR and the TR-labelled beacon probe is the onset potential of the Raman enhancement. The potential dependent Raman intensity of the 1504 cm^{-1} band for the Texas Red-labelled beacon probe starts to increase from ca. -0.5 V while for the adsorbed Texas Red, the potential onset is earlier at -0.3 V. A possible reason for this difference may be the presence of the adsorbed mercaptohexanol preventing adsorption of the Texas Red of the TR-lablelled probe during the potential sweep from -0.3 to -0.5 V. By preventing the adsorption of the TR of the beacon probe the mercaptohexanol will block CT enhancement over this potential range. When the potential is swept cathodic of -0.5 V, the partial desorption of mercaptohexanol could remove the blocking layer and allow direct adsorption of the TR label at the surface and hence the charge transfer enhancement can then make a contribution to Raman enhancement. We explore this hypothesis in Section 5.2.

A second experiment was carried out to further compare the Raman response of the Texas Red-labelled beacon probe at the mercaptohexanol passivated electrode using 633 and 785 nm excitation. The SSV substrates were prepared and modified in the same way as described above.

For the measurement at 785 nm a Renishaw Raman inVia spectrometer with 1200 groove/mm grating and a 785 nm diode laser running at 100 mW, attenuated to produce 4.02 mW (adjusted with the WiRE 3.4 software and measured using the laser power meter) on the specimen, in 180° backscattering via a 50 × objective was used. The numerical aperture of the objective was 0.75.

The result, shown in Figure 5.2, is compared with the result discussed in Section 4.6 for the excitation wavelength dependence of the SERS of adsorbed Texas Red. The Texas Red-labelled beacon probe exhibits a similar potential dependent Raman enhancement as for the adsorbed Texas Red except that the effect is weaker in both overall intensity and in the magnitude of the effect of the potential on the Raman intensity. A more detailed difference between the 633 and 785 nm spectra of the Texas Red-labelled beacon probe is that the enhancement ratio was decreased from 2.1 to 1.5 on average, accompanied by a positive potential shift of the maximum Raman intensity. Obviously we note that the difference between the enhanced Raman intensity ratio between the Texas Red (1.9) and Texas Red-labelled beacon probe (1.5) was similar for 785 nm as compared to that for 633 nm excitation found in the earlier experiment. Again the positive potential shift of the maximum Raman intensity is more evident in the case of the Texas Red-labelled beacon probe where it shifts from -0.83 V for 633 nm to -0.65 V for 785 nm excitation even though the onset potential of the potential dependent Raman enhancement for the Texas Red-labelled beacon probe with both 633 and 785 nm excitation is around -0.5 V. The suggested explanation for the onset

potential of the potential depedent Raman enhancement at -0.5 V in terms of the onset of partial desorption of mercaptohexanol is consistent with this change. The reason for the positive potential shift in the maximum Raman intensity of the adsorbate is still not known. A possible explanation

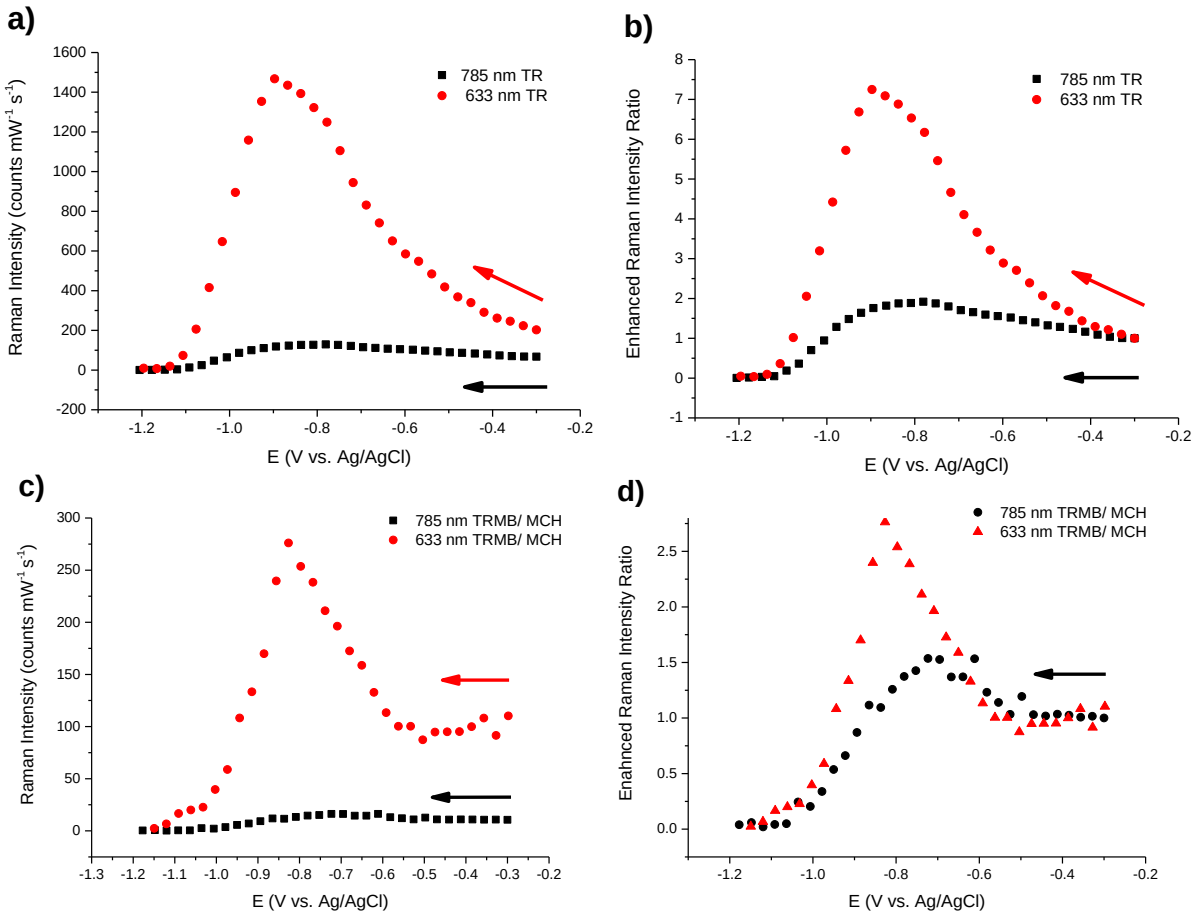

Figure 5.2 Comparison of the SERS intensity of 1504 cm^{-1} band during linear sweep voltammetry for adsorbed Texas Red (TR) (a) and b) adapted from Figure 4.20) and the Texas Red-labelled beacon probe in c) and d). The SSV substrates in a) and b) were immersed in 1 µM Texas Red solution containing 1 M NaCl and 10 mM Tris buffer (pH 7.2) for 16 h. The supporting electrolyte for the spectroelectrochemical scan was 1 M NaCl and 10 mM Tris buffer (pH 7.2) with no Texas Red presence in solution. The other SSV substrates in c) and d) were modified with the Texas Red-labelled beacon probe (TRMB) from a solution containing 1 µM probe, 1 µM mercaptohexanol (MHC), 0.5 M NaCl, 10 mM Tris buffer (pH 7.2) for 16 h. The potential was swept from -0.3 to -1.2 V at 1 mV s-1. The Raman spectra were acquired for 25 s exposure during the 25 mV potential cathodic sweep. The SSV substrates for a) and c) were not the same. The enhanced Raman intensity ratios shown in b) and d) were obtained by normalizing the Raman intensity to the initial Raman intensity at -0.3 V. The arrow indicates the direction of potential sweeping.

can be obtained from the review of Braun *et al.*[1], an adsorbate induced shift in the work function of the electrode in terms of the energy level may further affect the relative position of the CT resonance. Because the Texas Red-labelled beacon probe and mercptohexanol are two different adsorbates on the SSV Au electrode rather than just Texas Red, there may be a further shift of the work function of the electrode from the Texas Red adsorbed electrode that then affects the resultant CT enhancement as mentioned in Section 4.6[1].

To further investigate the excitation wavelength dependence of the potential dependent Raman intensity we used a different Raman label, Cy3 (1,1',3,3,3',3'-hexamethylindodicarbocyanine dye). This label was attached to the same beacon probe by ATDBio (Southampton, UK). The structure is

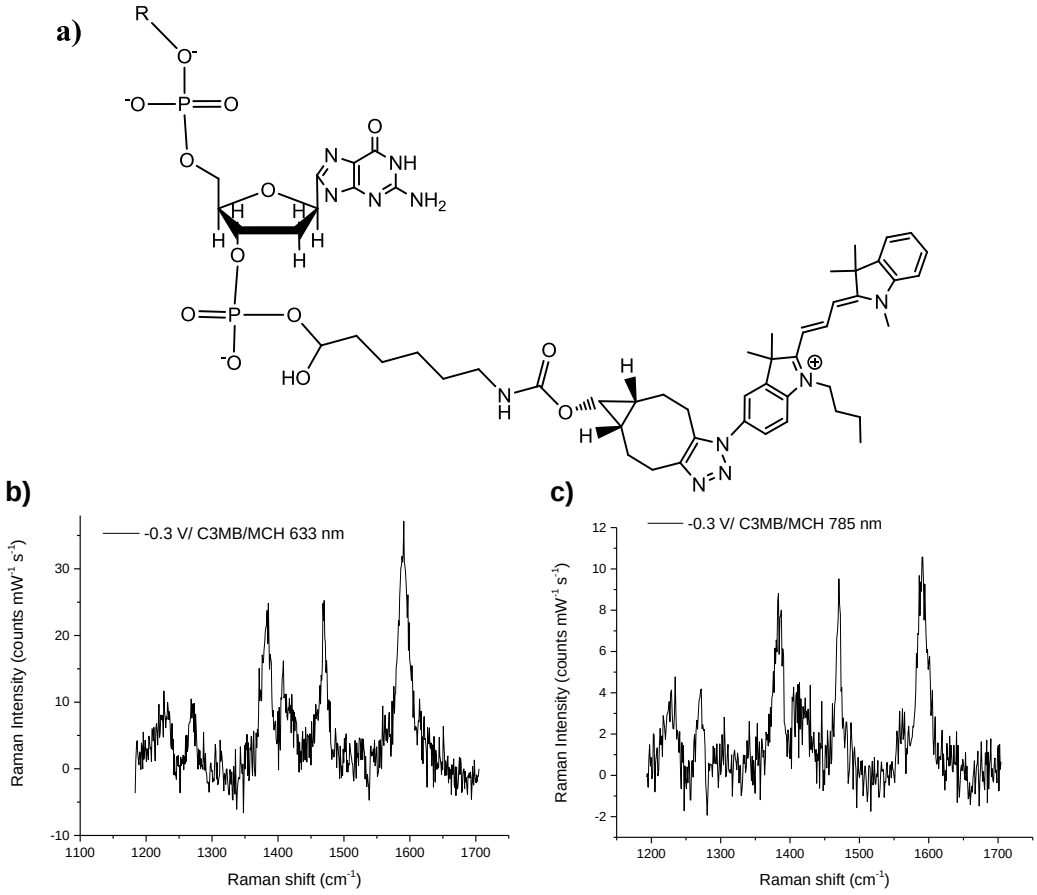

Figure 5.3 a) The structure of Cy3 (trimethine cyanine dye) coupled to the bicyclo[6.1.0]nonyne (BCN) moiety by the click chemistry (the copper-catalysed 1,3-dipolar cycloaddition) between the alkyne-modified cyanine dye and the azide modified oligonucleotide. The bicyclo[6.1.0]nonyne (BCN) was linked to the 3' phosphate by the reduction of the primary C7 amine with NHS ester. R represents the linked oligonucleotide at the 5' position. The Raman spectrum of Cy3-labelled beacon probe at -0.3 V (vs. Ag/AgCl). The SSV chips were fabricated as described in Section 2.1 with a deposit thickness of 575 nm to support SERS enhancement at both 633 b) and 785 nm c). The band assignments were listed in Table 5.1.

Table 5.1 Raman bands of Cy3-labelled beacon probe assignments based on Sato *et al.*[2]

υ (cm^{-1})	Sato *et al.*[2] υ (cm^{-1})	Band assignment
1233	1233	Ph=C stretching
1268	1267	Carbocyanine stretching
1385	1380	C-C stretching, C-N stretching of quinolone ring
1408	1403	Carbocyanine ring stretching (C=N)
1469	1467	CH asymmetric deformation and Carbocyanine ring stretching
1590	1594	Carbocyanine ring stretching (C=N)

shown in Figure 5.3. The SSV surfaces from the same substrate were modified with the Cy3-labelled beacon probe (C3MB) from a solution containing 1 µM probe, 1 µM mercaptohexanol (MHC), 0.5 M NaCl, 10 mM Tris buffer (pH 7.2) for 16 h. The SSV surfaces were rinsed with copious amounts of 1 M NaCl, 10 mM Tris buffer (pH 7.2) before the Raman measurements. The supporting electrolyte used to record the SERS was the same as that used for the Texas Red-labelled beacon probe. The Raman spectrum of the Cy3-labelled beacon probe at -0.3 V is shown in Figure 5.3 b) for 633 nm excitation and c) for 785 nm excitation. The Raman band assignments for Cy3 are listed in Table 5.1. There is no significant difference between the two excitation wavelengths for the Cy3-labelled beacon probe/mercaptohexanol interface, in contrast to the behaviour of the Texas Red-labelled beacon probe/mercaptohexanol. This can be understood from the absorption spectra of the electronic transition of Cy3 which has a λ_{max} at 544 nm, relatively far away (Figure 5.4) from both 633 and 785 nm, and so can be regarded as off-resonant with both

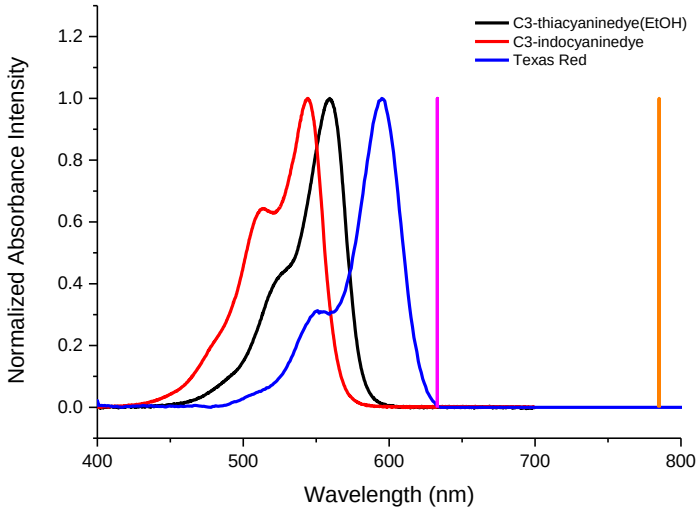

Figure 5.4 Absorbance spectra of Cy3 and 3,3'-diethylthiacarbocyanine iodide (from the PhotoChemCAD developed Lindsey and coworkers[3]). The absorbance spectrum of Texas Red is found from the Fluorescence SpectraViewer (Thermo Fisher Scientific Inc., Waltham, USA). The absorbance spectra are normalized to compare the position of λ_{max} with the excitation lines at 633 and 785 nm.

lasers. Before we discuss the potential dependent Raman intensity of the Cy3-labelled beacon probe, we should comment that we were not able to compare this to behaviour of the bare Cy3 dye adsorbed on the Au electrodes, due to the the low solubility of Cy3 in aqueous solution. The majority of commericially available Cy3 dyes are attached to functional groups such as thionyl chloride or N-hydroxysuccinimidyl ester (NHS ester) as reactants for conjugation to biomolecules. We therefore choose 3,3‘-diehtylthiacarbocyanine iodide as an alternative model molecule to observe the Raman response for adsorbed dye during potential cycling. 3,3‘-diethylthiacarbocyanine has better solubility than Cy3 and has a similar structure except that two sulphur atoms substitute on the individual indole ring while the Cy3 has dimethyl carbons attched on the indole ring (Figure 5.5). Because the S atom will interact with the Au, this may not be a good model for Cy3. In addition, the electronic transition for 3,3‘-diethylthiacarbocyanine has a maximum at 558 nm, between that for the Cy3 (544 nm) and Texas Red (586 nm) (Figure 5.4). The

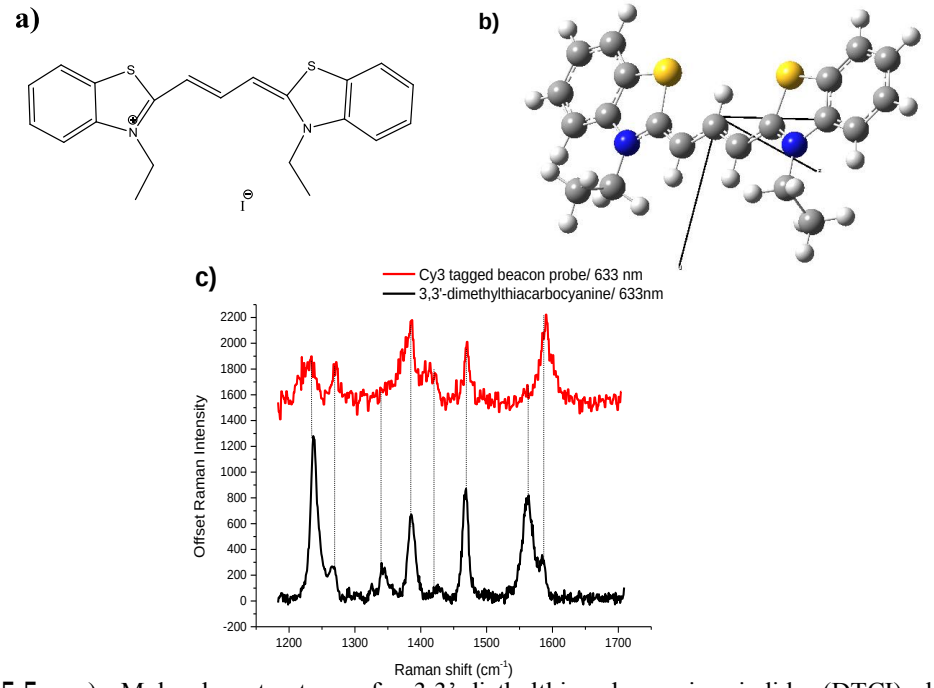

Figure 5.5 a). Molecular structure of 3,3’-diethylthiacarbocyanine iodide (DTCI). b) Geometry optimization result of DTC at B3LYP/6-311++G(d,p) level. c) SERS spectra of the Cy3-labelled beacon probe (red) and the 3,3’-diethylthicarbocyanine (black) where the dash lines indicate the corresponding Raman bands in between. For the Cy3-labelled beacon probe, the SSV substrate was modified in a solution of 1 µM Cy3-labelled beacon probe, 1 µM mercaptohexanol, 0.5 M NaCl and 10 mM Tris buffer (pH 7.2) for 16 h. The other SSV surface was immersed into a 1 µM DTCI solution containing 1 M NaCl and 10 mM Tris buffer (pH 7.2) for 16 h. Both surfaces were rinsed with copious amounts of 1 M NaCl, 10 mM Tris buffer (pH 7.2) before the Raman measurement in the same rinsing buffer. The Raman exposure time is 25 s at 633 nm excitation with 2.3 mW power.

variation of Raman spectra between Cy3 and DTCI has been reported by Sato *et al.*[2] and the band assignments for DTCI are listed in Table 5.2. When one compares the 6 intense bands of Cy3 (assigned in Table 5.1) and the 8 intense bands of DTCI (assigned in Table 5.2), over the range 1200 to 1700 cm^{-1}, one can note that DTCI contains all of the 6 vibrational modes in Cy3 and has varied relative intensities. The 2 extra bands at 1385 and 1564 cm^{-1} for DTCI represent the ring stretching (C=N) and C-C stretching in the middle conjugated chain as reported by Iwata *et al.*[4].

The following Raman measurements for DTCI adsorbed on the SSV Au electrode were carried out in the identical way to the experiments for Texas Red described in Section 4.2 except that the Texas Red (1 μM) was replaced by DTCI (1 μM). Two excitation wavelengths, 633 and 785 nm are compared in Figure 5.6. No frequency shifts were seen but new bands (labeled as *) were found at 408, 543, 709 and 1025 cm^{-1}. These less intense bands are consistent with the bands in the Raman spectra of polystyrene in the literature[5–8]. We attribute these bands to polystyrene impurity on the substrate from the template. The relative intensity of the common bands varied between the 2 excitation wavelengths which is consistent with the Raman spectra of DTCI in the literature[4,9,10] Most of the ring vibration modes (J, L, N, O bands) were more intense at 633 cm^{-1} except for the I band; this might be explained, as in Section 4.6, by the coupling of these vibrational modes to the electronic transition so that their Raman bands appear much stronger relative to those bands for vibrational modes not coupled to the electronic transition. Consequently, Raman spectra obtained from one molecule can appear different depending upon whether the laser excitation is in resonance with an electronic transition of the molecule or not[11]. The vibration modes calculated as decribed in Section 4.2 corresponding to the band assignments in Figure 5.6 are shown in Figure 5.7. The vibrational modes are in aggrement with the band assignments.

The potential dependent Raman enhancement for DTCI recorded with 633 nm excitation was acquired on two separate SSV chips cut from the same substrate over two wavenumber ranges, the first, from 200 to 1200 cm^{-1}, is shown in Figures 5.8 a), b) and c) and the second, from 1200 to 1700 cm^{-1} is shown in Figures 5.8 d), e) and f). These results indicate clearly, even for off-resonance excitation (633 nm compared to the electronic transition of DTCI at 558 nm), that the potential dependent Raman enhancement still occurs and is similar to the response of Texas Red discussed in Section 4.2.

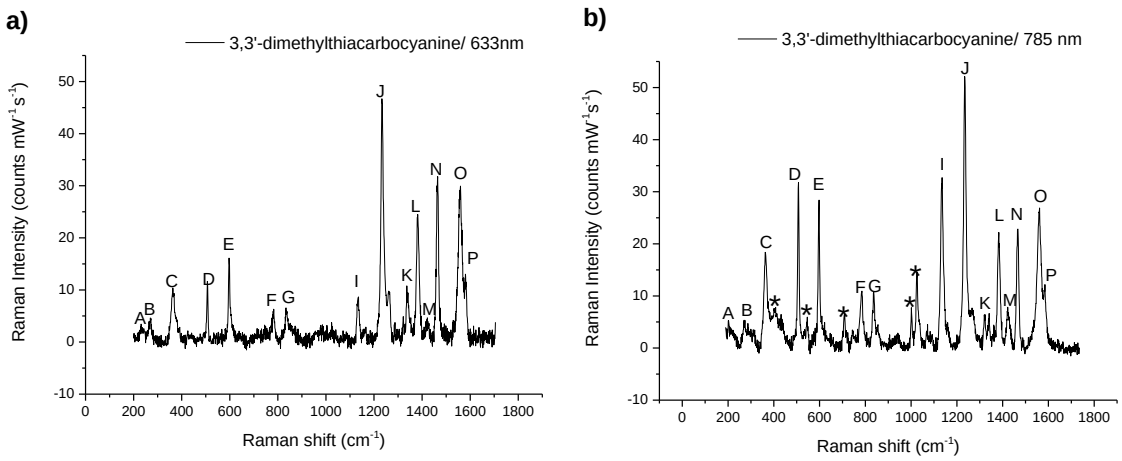

Figure 5.6 SER spectra of 3,3'-diethylthiacarbocyanine iodide (DTCI) recorded with 633 a) and 785 nm b) excitation. The SSV substrates were immersed in 1 μM DTCI solution containing 1M NaCl, 10 mM Tris buffer (pH 7.2) for 16 h. They were then rinsed with 1 M NaCl, 10 mM Tris buffer (pH 7.2) and the Raman spectra were measured in the same rinsing solution at open circuit potential. The intense Raman bands are labelled with capital letters and assigned in Table 5.2.

Table 5.2 Raman band assignments for 3,3'-diethylthiacarbocyanine (DTCI) based on the literature[2,4,12,13] and the vibration analysis (*) calculated at B3LYP/6-311++G(d,p) level, detailed vibrational patterns as shown in Figure 5.7.

	Experimental results υ (cm^{-1})	633 nm	785 nm	DFT calculation υ (cm^{-1})	Band assignment
A	231	w#	w	224	C-H out-of-plane bending*
B	269	w	m#	269	C-H out-of-plane bending*
C	363	m	m	367	Ring breathing*, Chain stretching*
D	510	m	st#	512	C-S-C Ring vibrations[4]
E	603	st	st	604	Chain stretching[4]
F	782	w	w	785	Ring vibrations[4]
G	834	w	w	843	C-H out-of-plane bending[4]
I	1135	w	st	1125	Ring vibrations[4]
J	1228	st	st	1221	Ring stretching[4]
K	1336	m	w	1331	CH_3 deformation[4]
L	1381	m	st	1375	Ring stretching (C=N)[4]
M	1423	w	w	1424	C-H in-plane bending[4]
N	1460	st	st	1459	Ring vibration[4]
O	1560	st	st	1552	C-C stretching in the middle conjugated chain[4]
P	1576	st	st	1587	Ring vibrations[4]

#w represents weak Raman intensity. m for moderate and st for strong.

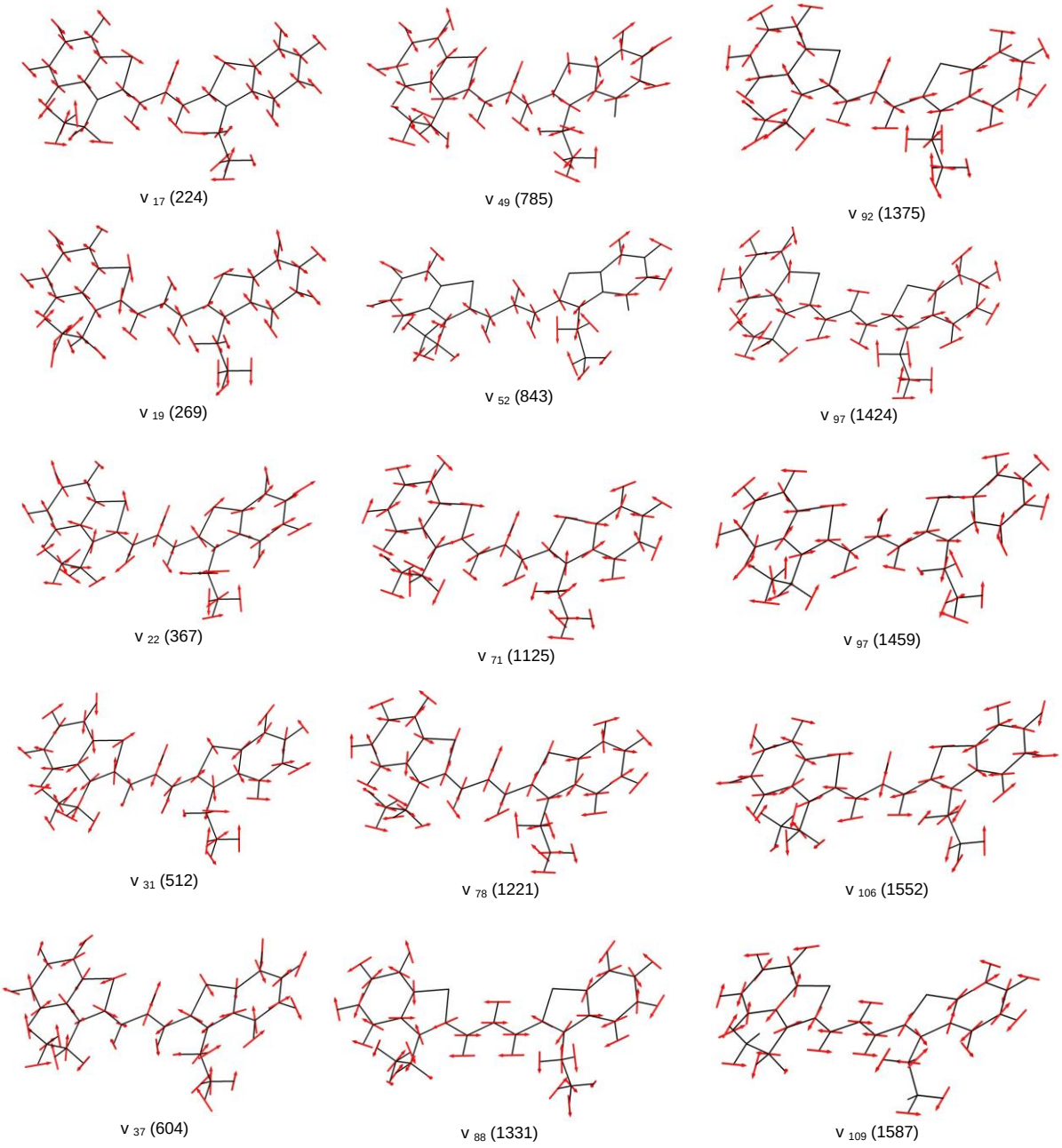

Figure 5.7 Vibrational modes for 3,3'-diethylthiacyanine (DTC) calculated at B3LYP/6-311++G (d,p) level. A scale factor of 0.978 was used for the Raman bands higher than 1100 cm^{-1} and 1 for those below 1100 cm^{-1}. The arrow lengths in each cae are not considered the relative displacement distance between atoms but only show the vibrational direction.

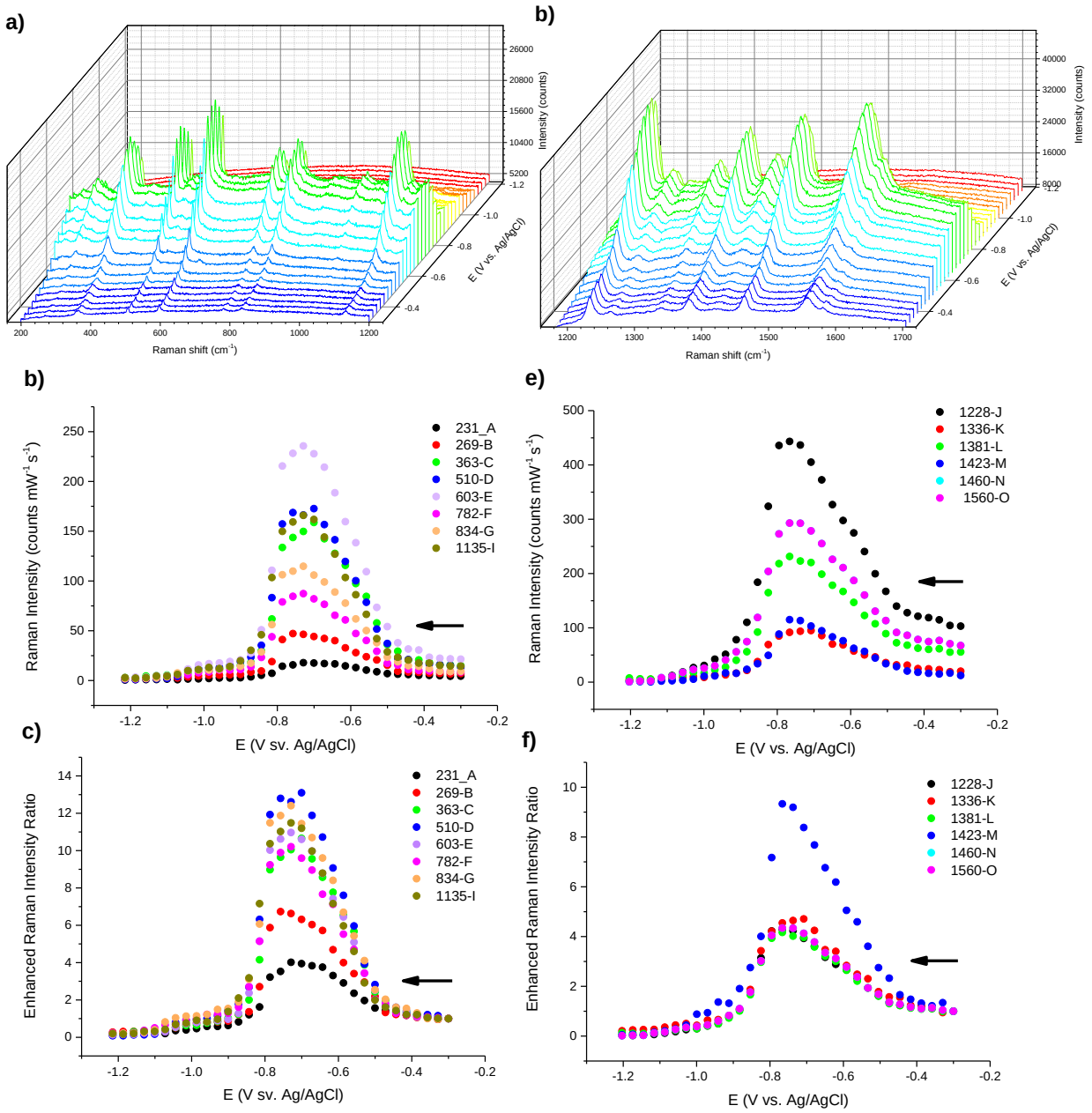

Figure 5.8 SER spectra of 3,3'-diethylthiacarbocyanine iodide (DTCI) for excitation at 633 nm in two wavenumber ranges a) 200-1200 cm^{-1}. b) 1183-1700 cm^{-1} The two SSV substrates were cut from the same SSV substrate deposit thickness 575 nm and immersed the 1 µM DTCI solution containing 1 M NaCl, 10 mM Tris buffer (pH 7.2) for 16 h. The SSV chips were rinsed copiously with 1 M NaCl, 10 mM Tris buffer (pH 7.2) and the Raman spectra were measured in the same rinsing solution over the two wavenumber range. The intense Raman bands are labelled with the capital letters and assigned in Table 5.2. The Raman intensity as a function of potential are shown in c) and d) while the enhanced Raman intensity ratio shown in e) and f) are normalized by dividing the Raman intensity by the corresponding Raman intensiy at -0.3 V. Note the 1460 cm^{-1} band is overlapped with the 1560 cm^{-1} band in d) and f). The arrow indicates the direction of potential sweeping.

No new bands are assigned to the DTCI and no obvious frequency shifts are observed. However, the normalized intensity ratio may grow larger when the enhanced Raman intensity is divided by the small initial Raman intensity as in the case of band M (1423 cm^{-1}). The shoulder adjacent to band M also increases to become a better resolved peak as the potential scans negative to -0.6 V.

Another characteristic of the potential dependent Raman enhancement is that the peak intensities increase abruptly from -0.5 V on the cathodic scan when compared to the result for Texas Red. The Raman intensity peaks at ca. -0.7 V and then drops rapidly at ca.-0.9 V. This results in a narrower potential width for the Raman response than that of Texas Red.

An analysis of possible reorientation of the dye was carried out by comparing the relative intensity of the C-H in-plane bending mode (1423 cm^{-1}) and the C-H out-of-plane bending mode (834 cm^{-1}) as shown in Figure 5.9. There is no obvious change in the relative intensity between the two modes, hence we can exclude re-orientation as the explanation for the increase of the potential dependent Raman intensity. The potential dependent Raman enhancement is clearly seen over the 200-1200 and 1200-1700 cm^{-1} range. The enhanced Raman intensity ratios reach up to 3 to 13 times and cannot be ignored. The normalized intensity ration obtained from the Raman intensity ratio of Raman intensity of C-H out-of-plane (834 cm^{-1}) / the C-H in-plane (1423 cm^{-1}) also shows less correlation between the change of the orientation and the potential dependent Raman enhancement in Figure 5.9 b).

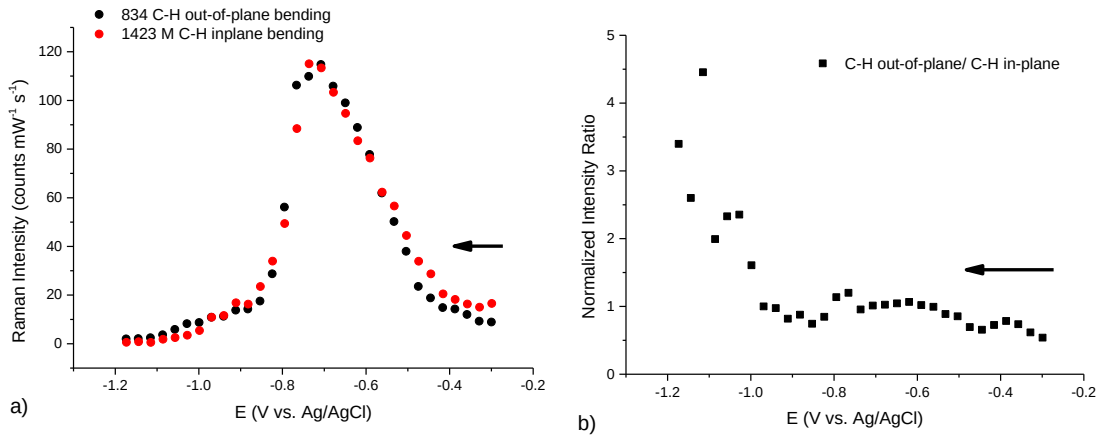

Figure 5.9 a) Potential dependent Raman enhancements for the 3-3'-diethylthiacarbocyanine iodide (DTCI) 834 cm^{-1} and 1423 cm^{-1} bands corresponding to the C-H out-of-plane bending mode and the C-H in-plane bending mode recorded with 633 nm excitation. The Raman intensities of 834 and 1423 cm^{-1} band were selected from Figure 5.8. b) Normalized intensity ratio calculated from the Raman intensity of C-H out-of-plane (834 cm^{-1}) / the C-H in-plane (1423 cm^{-1}). The arrow indicates the direction of potential sweeping.

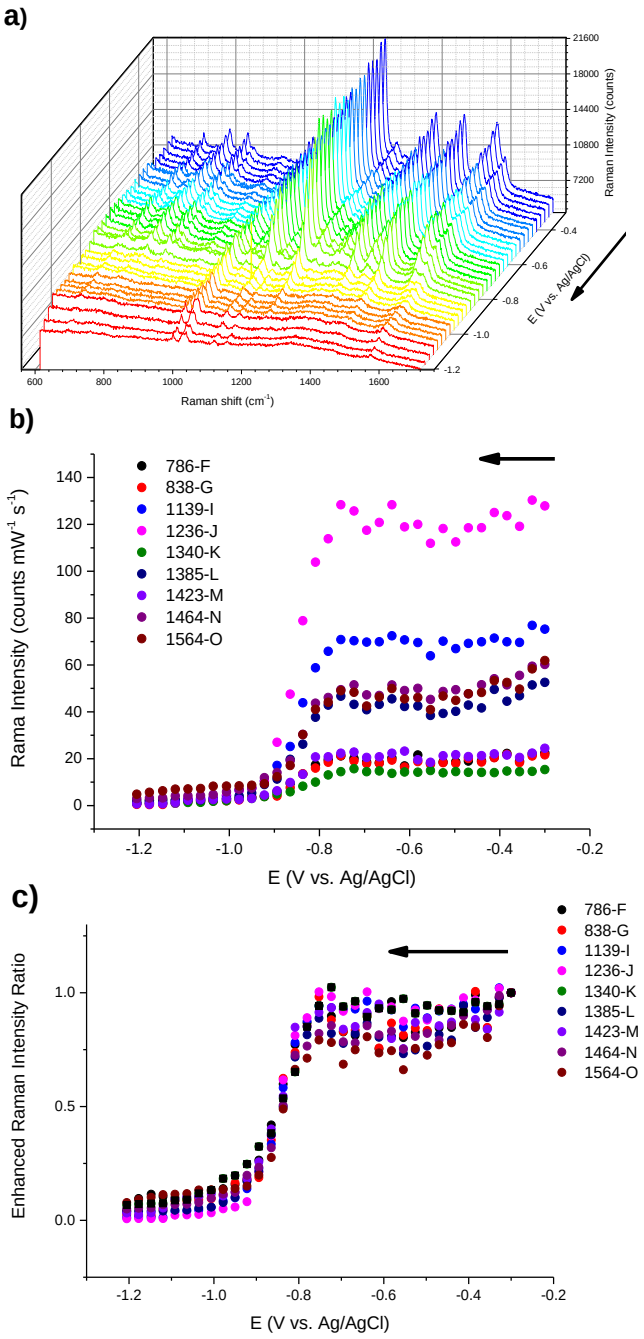

Figure 5.10 Potential dependent Raman intensity for DTCI adsorbed on the SSV Au electrode recorded using 785 nm excitation. The SSV substrate was fabricated as described in Section 2.1 with a deposit thickness of 575 nm. The SSV chip was cut from the same substrate as used for the 633 nm excitation measurements in Figure 5.7. The SSV chip was immersed in 1 µM DTCI solution containing 1 M NaCl and 10 mM Tris buffer (pH 7.2) for 16 h. The SSV chip was than rinsed with copious amounts of 1 M NaCl and 10 mM Tris buffer (pH 7.2) and the Raman spectra were acquired in the same supporting electrolyte. The potential was swept from -0.3 to -1.2 V at 1 mV s^{-1}. The raw Raman spectra a) were background-subtracted and then plotted in b) as a function of applied potential. The enhanced Raman intensity ratios were normalized by the initial Raman intensity of the corresponding band at -0.3 V. The arrow indicates the direction of potential sweeping.

In addition, the potential-dependence of the SERS background follows the potential dependence of the Raman bands which is consistent with the result for Texas Red in Section 4.6. SERS using 785 nm excitation was recorded over the range 614 to 1704 cm^{-1} on the SSV chips from the same substrate used for the 633 nm excitation. The results for the potential dependent Raman intensity shown in Figure 5.10 have no significant increase in the Raman intensity with the cathodic potential sweep. The potential dependence in Figure 5.10 is very different from all the results so far.

From the results, one can note that the potential dependent Raman enhancement for adsorbed DTCI has a wider effective range between the excitation wavelength (λ_0) and the absorption spectrum maximum (λ_{max}); the difference ($\lambda_{max} - \lambda_0$) is much larger than that for Texas Red. The excitation at 633 nm is far away from the DTCI absorption maximum at ca. 594 nm (Figure 5.4). To explore the possible Stark effect induced resonance Raman scatterings, the transition dipole moment of the DTCI was evaluated. The further calculation was carried out by using the same DFT method as described in Section 4.7. The electric field strength was assumed to be the same as in Section 4.7 and the literature therein. The orientation of adsorbed 3,3'-diethyltricarbocyanine (DTTCI) on the Au surface has been studied by Dietz *et al.*[14] using polarized angle-dependent UV-vis spectroscopy and density functional theory. DTTCI has 5 methine groups as compared to DTCI which has 3 methines between the two nitrogen atoms. Dietz *et al.*[14] proposed the orientation of DTTCI/Au as shown in Figure 4.10 a) with the long axis of DTTCI parallel to the surface and the rings head-on. This DTTCI/Au orientation is not the orientation expected for Au-S interactions. However, the S atom in the DTTCI is a thioether rather than a thiol or disulphide which form stronger Au-S bond via deprotonation. There are many studies that indicate that the C-S-C bond of a thioether does not break on at Au surface[15–17]. For example a dialkyl thioether/Au does not form an upright alkyl chain but adsorbs with the alkyl chains lying on the Au surface via van der Waals interactions. For a cyclic thioether like DTCI and DTTCI the van der Waals force are expected to decrease further due to the short alkyl chain length in contact with the Au surface[15–17]. The calculated dipole moment in the ground and excited states for the DTCI/Au interface are shown in Figure 4.10 b) and c). The final adsorption shift that results from the change of the dipole moments is ca. -5.8×10^{-10} THz (less than 10^{-5} nm) based on a change in the magnitude of the electric field of 3×10^5 V cm^{-1} V^{-1}. This is insignificant and would be hardly measurable. There is also no report of electrochromism (electronic Stark effect) for the DTCI/Au interface to result in the potential dependent SERRS effect, to our best knowledge. Although we do not have an estimation of the energy level alignment of the LUMO and HOMO for DTCI/Au at this moment, based on the potential dependent Raman enhancement of DTCI, the intermediate molecule

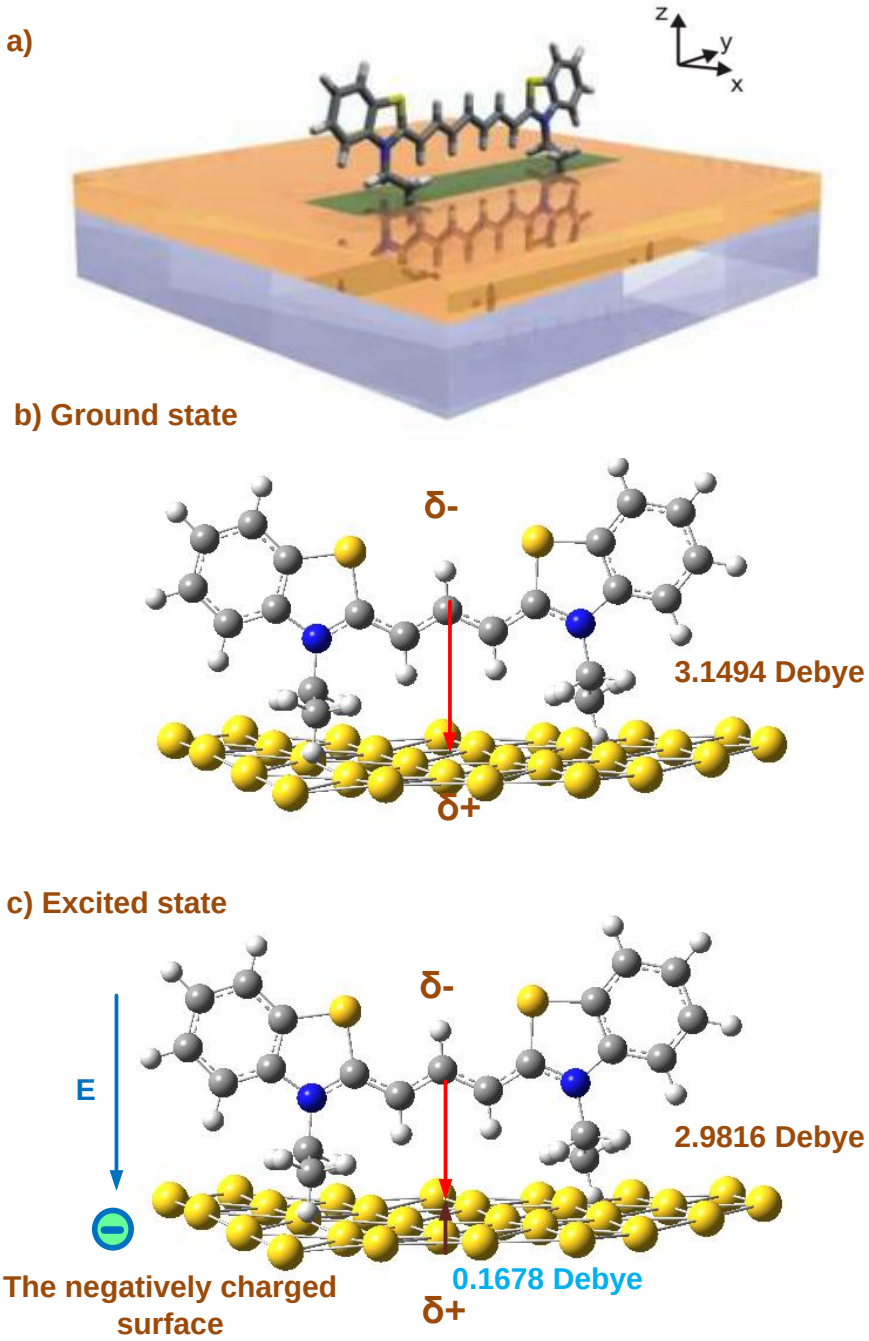

Figure 5.11 a) The orientation 3,3'-diethylthiatricarbocyanine adsorbed on the Au surface proposed by Dietz *et al.*[14] with the long axis parallel to the surface and rings head-on. The calculated dipole moments of the ground b) state and excited c) state of 3,3'-diethylthiacarbocyanine iodide (DTCI) at B3LYP/6-311++G(d,p) and CIS level individually by Gaussian software version 9. D01 (Gaussian Inc, Wallingford, USA). δ- and δ+ represents the vector of the dipole moment. *E* stands for the vector of electric field which is assumed to be normal to a negatively charged Au surface.

has an electronic transition (559 nm) between Cy3 (544 nm) and Texas Red (586 nm), we tentatively infer that the effect of the potential dependent Raman enhancement would be weaker in the case of Cy3 for both 633 and 785 nm excitation. In addition, based on the results we obtained for the Texas Red-labelled beacon probe, a further weakened potential-dependence of the Raman enhancement can be expected due to the direct adsorption of the later being blocked by the passivating thiol layers.

When we examine the Stark effect, which contains the electronic and vibrational Stark effects, the electronic Stark effect describes the potential-tuning of the electronic transition between the ground and excited states of the adsorbate. The vibrational Stark effect correlates the potential-tuning shift of the energy gap between the vibrational energy level of the ground and excited states for the adsorbate. The energy gap associated with any electronic transition is much larger than that for normal vibrational levels, as shown in Figure 4.22, and consequently any electronic transition must encompass some associated vibration levels. Hence the electronic Stark effect triggered by the electric field will be accompanied by a vibrational Stark effect. This phenomenon has the same origin as the difference in the intensity of different vibration modes between normal Raman scattering and resonance Raman scattering as discussed in Section 4.6.

The critical chracteristics of the Stark effect in Raman scattering that discriminates it from the CT enhancement is that the frequency shift in proportional to the potential. Based on the review of Bartlett *et al.*[18], in electrochemical SERS there can be a significant dependence, up to 100 $cm^{-1}\ V^{-1}$ or more, of the band frequencies on the electrode potential for adsorbates and molecules close to the electrode surface. This is referred to as the Stark effect or Stark tuning and can have contributions from the effect of the potential on metal – adsorbate bonding as well as from the purely electrostatic effect of the field at the electrode surface on the vibrational force constant . In the example shown in Figure 5.13, Tian and co-workers[19] measured the UV-SERS on a Rh electrode modified with SCN^{-} using 325 nm excitation. There is an obvious frequency shift over the potential range 0.4 to -1.2 V with a linear tuning rate of ca. 73 $cm^{-1}\ V^{-1}$. Similar observations of the frequency shifts with potential were also reported by Harris and co-workers[20] in the case of the nitrile stretching mode acquired from a series of monolayers composed of alkanethiols ($HS(CH_2)_xCH_3$, where $6 \leq x \leq 10$) and mercaptododecanenitrile ($HS(CH_2)_{11}CN$). One sould note that the two Stark tuning rates can be explained in terms of the distance of the vibrational chemophore from the electrode surface. Obviously, the Stark tuning rate decreases as

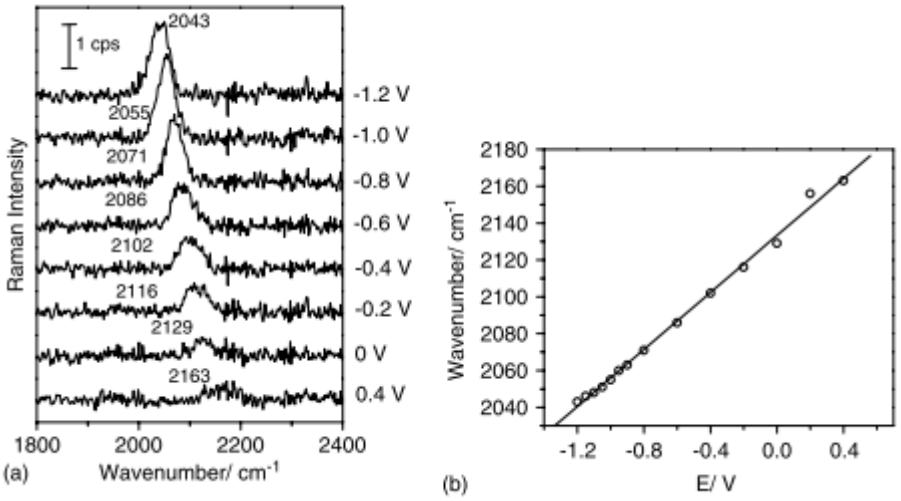

Figure 5.13 (a) UV–SER spectra of SCN adsorbed on a roughened Rh electrode in 0.1 M $NaClO_4$, 0.01 M NaSCN at different potentials. Excitation, 325 nm; acquisition time, 200 s. (b) Plot of the wavenumbers of ν_{CN} with the electrode potential extracted from (a). (Reprinted with permission from Ref.[19] Copyright© 2005 Wiley & Sons.)

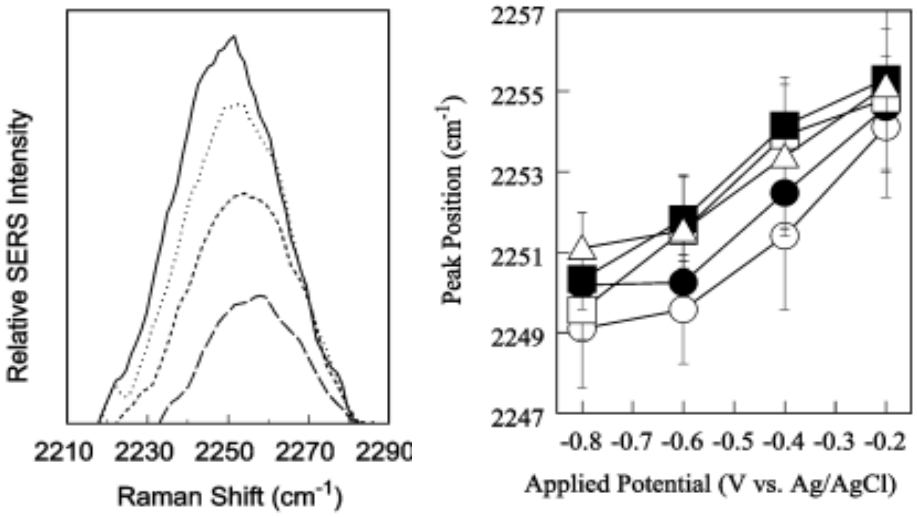

Figure 5.14 Left panel: nitrile stretching region of SERS spectra: C_{11} /C_{11}CN SAM as a function of applied potential in 10 mM $NaClO_4$. Right panel: Peak position of the nitrile stretching mode due for allmixed-monolayer types in 10 mM $NaClO_4$: - $S(CH_2)_6$ CH_3 /-$S(CH_2)_{11}$-CN (○), - $S(CH_2)_7CH_3$/ - $S(CH_2)_{11}$CN (●), - $S(CH_2)_8$ CH_3 / - $S(CH_2)_{11}$ -CN (□), - $S(CH_2)_9CH_3$/ - $S(CH_2)_{11}$CN (■), - $S(CH_2)_{10}CH_3$/ - $S(CH_2)_{11}$-CN (Δ). (Reprinted with permission from Ref.[20]. Copyright© 2003 American Chemical Society.)

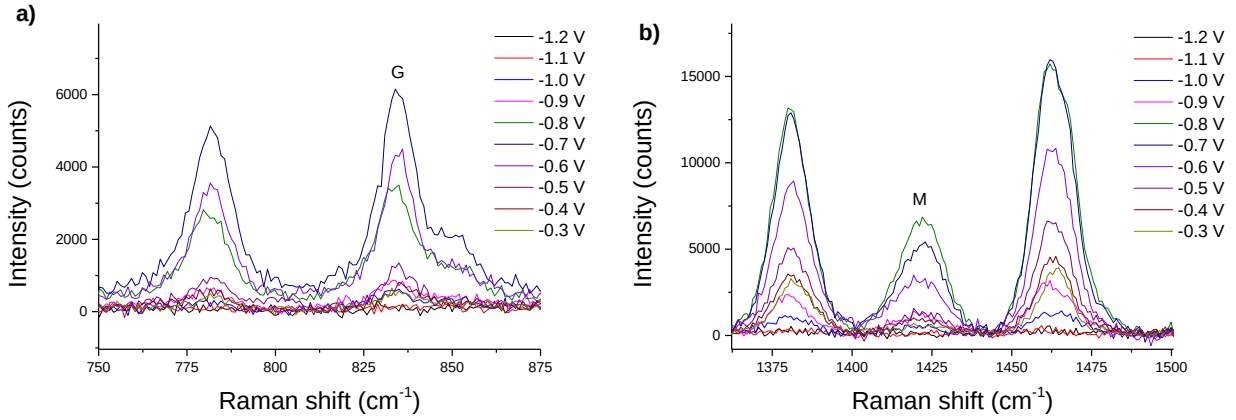

Figure 5.15 SER spectrum of DCTI adsorbed on the Au SSV electrode from Figure 5.8 substrated from the background. The G (834 cm^{-1}) in a) and M (1423 cm^{-1}) in b) band represent the C-H out-of–plane bending and C-H in-plane bending respectively. The overlapped spectra in the two wavenumber ranges show the frequency and relative intensity change during the potential sweep from -0.3 to -1.2 V (vs. Ag/Ag/Cl).

the the CN group goes from close (73 cm^{-1} V^{-1}) to the distal position in the SAM (ca 10 cm^{-1} V^{-1}). When we go back to compare this potential-tuning shift and change in the relative intensity in the case of DTCI, the frequency shift (2-5 cm^{-1}) is not significant and lack of linearity with the potential over the potential range -0.3 to -1.2 V is likely attributed to the digitization errors. The case for Texas Red is similar and the frequency shift (2-7 cm^{-1}) is small (data not shown). The adsorbed Texas Red and DCTI are assumed to directly contact the electrode surface where the electric field is much larger and hence the frequency proportional shift with the potential is expected to be resolved using the Raman spectrometer of 4 cm^{-1} resolution during the ca. 1 V potential tuning in this study. On the other hand, because the Stark tuning affects those vibration modes in the direction parallel to the electric field, we selected band G (834 cm^{-1}) and band M (1423 cm^{-1}) which represent the C-H out-of-plane bending and C-H in-plane bending respectively as shown in Figure 5.15. These two modes are normal to each other; hence the C-H in-plane bending, based on the orientation of adsorbed DCTTI from Dietz *et al.*[14], is parallel to the electric field direction and should be more evidently affected during the potential sweep. However none of them exhibits a significant potential dependent frequency shift. Based on these results, the electronic Stark effect and the resultant resonance Raman scattering are not likely to explain the potential dependent Raman intensity of DCTI and Texas Red discussed in Section 4.6.

After discussing the potential dependent Raman intensity for DTCI, we can now go back to the experiments with the Cy3-labelled beacon probe. As before, the Cy3-labelled beacon probe was

immobilised on the SSV substrates from a 1 μM solution of the probe in 1 μM mercaptohexanol, 0.5 M NaCl and 10 mM Tris buffer (pH 7.2) for 16 h. The chips were rinsed with copious amounts of 1 M NaCl and 10 mM Tris buffer (pH 7.2) and the Raman spectra were obtained in the same supporting electrolyte using 633 nm and 785 nm excitation. The potential was scanned from -0.3 to -1.2 V at 1 mV s^{-1}.

We note that the Raman intensity for the Cy3-labelled beacon probe is ca. 3.45 times stronger at 633 nm than at 785 nm as shown in Figure 5.16. To compensate for this difference in intensity, the Raman spectra were normalized by the initial Raman intensity at -0.3 V. The potential dependent Raman intensity for the Cy3-labelled beacon probe exhibits a similar pattern for both laser wavelengths unlike that for the Texas Red-labelled beacon probe (Figure 5.11) has peak shape enhancement in 633 nm excitation. Since the laser power and exposure time between the two excitations have been normalized in terms of counts mW^{-1} s^{-1}, there still exists the difference of the spectral efficiency between the two spectrometers which contains the CCD pixel size, slit width, excitation wavelength[21]. Nevertheless, even this difference exists, the potential dependent Raman intensity between the two excitations can still be discussed when the Raman intensities were normalized to the initial intensity at -0.3 V. The Raman intensity of the Cy3-labelled beacon probe at both excitations (633 nm and 785 nm) does not have an increase from -0.5 V, and conversely, decreases from -0.5 V to -1.2 V. There is no clear peak in the potential dependent Raman intensity of the Cy3-labelled beacon probe with either excitation. The nomalised Cy3-labelled beacon probe shows a very similar response with respect of the normalized Raman intensity ratio and is different from that for the Texas Red-labelled beacon probe. This result suggest that the potenital dependent Raman intensity of the labelled beacon probe is label dependent and that the Raman label has an intrinsic intensity response under the potential perturbation. It suggest that it is related to the SERRS effect and is seen when there is a resonance or pre-resonance contribution. The increase in SERS intensity with potential is associated with the pre-resonance SERRS and only significant with the excitation wavelength for the laser is close to λ_{max} for the dye.

Due to the lack of the electrochemical SERS data for adsorbed Cy3/Au, we cannot exclude the possibility that the potential dependent Raman intensity of the Cy3-labelled beacon probe may result from the electronic Stark effect, but the proportional frequency shift with the potential sweep is not observed at the Cy3-labelled beacon probe/Au interface. Hence the detailed mechanism to explain the potential dependent Raman intensity of the Cy3-labelled beacon probe remains uncertained. Clearly the different Raman labels exhibit different dependence on the potential,

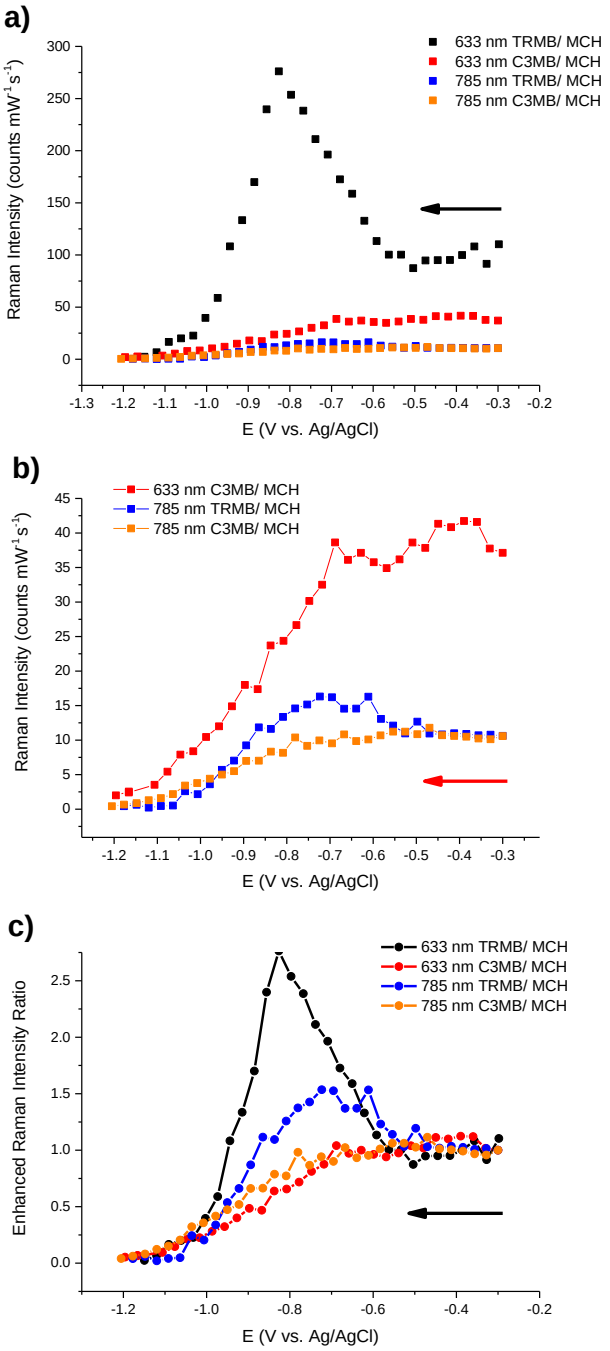

Figure 5.16 The SSV substrates were fabricated as described in Section 2.1 and immersed into 1 µM beacon probe solution containing 1 µM mercaptohexanol (MCH), 0.5 M NaCl and 10 mM Tris buffer (pH 7.2) for 16 h. The SSV chips were then rinsed with copious amounts of 1 M NaCl, 10 mM Tris buffer (pH 7.2) before the Raman measurement. The potential was scanned from -0.3 to -1.2 V at 1 mV $s^{-1.}$ a) Comparison of the potential dependent Raman intensity of Texas Red-labelled (TRMB) (1504 cm^{-1} band) and Cy3-labelled beacon probe(C3MB) (1385 cm^{-1} band) backfilled with mercaptohexanol for 633 and 785 nm excitation. b) A close-up view of a) at the intensity range 0-45 counts mW^{-1} s^{-1}. c) The enhanced Raman intensity ratio normalised by the corresponding Raman intensity at -0.3 V. The arrow indicates the direction of potential sweeping.

excitation wavelength and the realted electronic absorption spectrum. In the case of the Texas Red-labelled probe, the potential dependent Raman enhancement might be attibuted to the CT enhancement which strongly depends on the excitation, the electronic transition (which is adsorbate specific) and also on the electrochemical potential (Fermi level) of the electrode.

Charge transfer resonance can only occur when an adsorbed molecule has an appropriate position of the energy gap between its LUMO and HOMO, the excitation is close to but less than the molecular resonance, and tuning of the potential (Fermi level) of electrode allows the photon to couple with the electron at the ground or excited electronic state into the charge transfer resonance. This charge transfer resonance is different from the electronic Stark effect (electrochromism) driven by the large change in dipole moment between ground and excited states which results in a shift of the electronic transition. Since the Stark effect could not explain the absence of the co-existing vibrational Stark effefct which is characterized by frequency shifts proportional to the electric potential in the cases of the Texas Red and DCTI, the potential dependent Raman enhancement of the two molecules cannot be attributed to the Stark effect.

5.2 The Effects of the Self-Assembly Monolayer to the Texas Red-labelled Beacon Probe on the Charged Au Electrodes

As we saw in Section 5.1, the Texas Red-labelled beacon probe exhibits an increasing Raman intensity at -0.5 V while the adsorbed Texas Red has a more smooth increase between -0.3 to -0.8 V. It appears that the presence of the mercaptohexanol monolayer probably delays the onset of the potential dependent Raman intensity increase. To explore this, the SSV substrates were fabricated as described in Section 2.1 with a deposit thickness of 480 nm using a 600 nm nanosphere template. The SSV surfaces from the same substrate were then modified using a 1 μM Texas Red beacon probe solution containing 0.5 M NaCl, 10 mM Tris buffer (pH 7.2) for 18 h. The following immersion of mercaptohexanol is carried out in different exposure time and this experimental design assumes that the surface coverage of each surface on the same substrate is similar. The mercaptohexanol adsorption process can be monitored by comparing the potential dependent Raman response of the Texas Red label. Hence, the 1 μM mercaptohexanol was added into the solution for 1, 2, 6 and 18 h to compare the potential dependent Raman intensity of the bare Texas red labelled beacon probe in the absence of mercaptohexanol. The modified SSV substrates were rinsed with a copious amounts of rinsing solution and the Raman spectra recorded in the electrolyte containing the same composition of 1 M NaCl, 10 mM Tris buffer (pH 7.2). The Raman spectra were acquired using the 633 nm laser, 2.3 mW laser power in the static mode from 1180 to 1704 cm^{-1} using 25 s exposure time during each 25 mV potential cathodic sweep. The potential was scanned from 0.2 to -1.2 V at 1 mV s^{-1}.

The result are shown in Figure 5.11. There are interesting difference in the absence and presence of the mercaptohexanol monolayer. First of all, the Texas Red-labeled beacon probe on the bare gold electrode shows the potential dependent Raman signal peaked at ca. -0.8 V in the absence of mercaptohexanol. Also, an evident decreasing in the Raman intensity onset from 0.2 to -0.2 V is seen in the short-term (1 and 2 h) mercaptohexanol exposure case. The reason for the decreasing Raman intensity of Texas Red-labelled beacon probe with the cathodic potential sweep is not clear at this moment. It might be as suggested by the Jambrec *et al.*[23], due to restructuring of cations/ anions in the electric double layer in the vicinity of the potential of zero chrage. Since there is no decrease Raman intensity of adsorbed Texas Red observed between 0.2 to -0.2 V as observeed in Section 4.2, the decreasing Raman intensity of Texas Red-labelled beacon probe with the cathodic

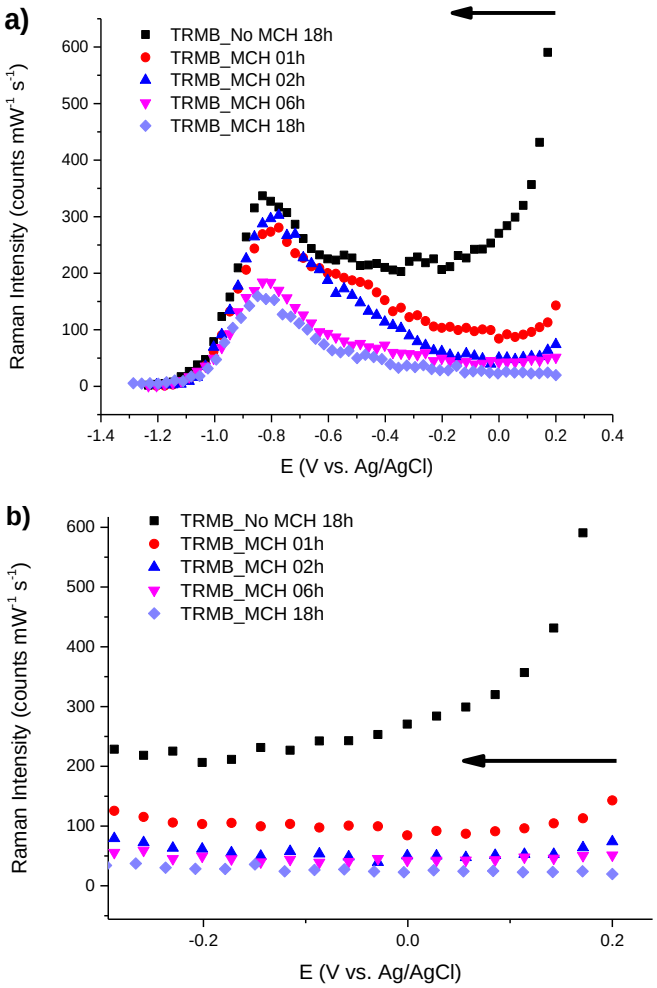

Figure 5.11 a) Intensity of 1504 cm^{-1} Texas Red band plotted as a function of potential. b) A close up view of the potential dependent Raman enhancement for Texas Red-labelled beacon probe from a) at the 0.2 to -0.2 V. The SSV substrates were fabricated as described in Section 2.1 with a deposit thickness of 480 nm using the 600 nm nanosphere template. The SSV chips from the same substrate were then modified in 1 µM Texas Red-labelled beacon probe (TRMB) solution containing 0.5 M NaCl. 10 mM Tris buffer (pH 7.2) for 18 h. The 1 µM mercaptohexanol (MCH) was added into the immersing solution and left for 1, 2, 6 and 18 h to compare the difference to the potential dependent Raman intensity. Raman spectra were recorded in 1 M NaCl, 10 mM Tris buffer (pH 7.2) using 633 nm laser, 2.3 mW in static mode from 1180 to 1704 cm^{-1} using 25 s exposure time during each 25 mV potential cathodic sweeping. The potential was scanned from 0.2 to -1.2 V at 1 mV s^{-1}. The arrow indicates the direction of potential sweeping.

potential scan is more plausiblely attributed to a change in the beacon probe conformation rather than the intrinsic Texas Red response..

Due to the immobilisation at intermediate ionic concentration used herein (0.5 M NaCl) in the absence of mercaptohexanol, the beacon probe is supposed to take a partially laying-on conformation via non-specific adsorption on the Au. The single-stranded oligonucleotide at the loop region is more sensitive to the potential perturbation due to the shorter persistence length and would be attracted to the Au surface at positive potential as reported by Kaiser *et al.*[24] and Tymoczko *et al.*[25] but was eventually repelled from the surface where more anions accumulated during the cathodic potential scan[26,27]. This process strongly depends on the ion packing and the transient accumulation of the cations and anions in the vicinity of the potential of zero charge as proposed by Jambrec *et al.*[23] and could explain our experimental results. Hence, the backfilled mercaptohexanol results in an insulating layer that causes the Raman intensity reduce as the SAM formed.

The Raman intensity fluctuation is larger for the short-term (1 and 2 h) mercaptohexanol exposure than in the relatively long-term (6 and 18 h) counterparts. The reason for the differenc of the intensity fluctuation can be explained by the packing process of the mercaptohexanol as described by Love *et al.*[28] and by Schwartz[29]. The thiol (-SH) group of the alkanethiol first adheres to the Au surface randomly is a lying-down chain conformation, then gradually packs up with the adjacent thiol maximising the lateral van der Waals interaction btween the alkane side chains. Finally the packed alkanethiol achieves a self-assemblely monolayer (SAM) after 18 h as shown in Figure 5.12 a). As Widrig *et al.*[30] and Munakata *et al.*[31] showed, the thiol underwent reductive desorption at more negative potentials from ca. -0.6 V, where the onset potential is proportional to the alkyl chain length of the thiol. The packed alkane thiol monolayer does not behave as a purely ionic insulator before the corresponding desorption[32–34]. Boubour *et al.*[32], measured the impedance at negative potenital for alkane thiol $CH_3(CH_2)_n$ S/Au (n = 7 - 15) SAMs from 0.4 to -0.5 V in the 50 mM K_2HPO_4 (pH 7.0) without any redox species in solution. They observed a drop in the phase angle from 90° at a frequency lower than 100 Hz with cathodic potential steps from -0.2 V which implied that the interface was no longer a pure capacitor. However, the corresponding capacitance did not change before the reported desorption potential. To explain these impedance results, they introduced a parallel RC circuit into the original equivalent circuit model to represent defects in the monolayer. They concluded that at a critical potential (V_c) potential before thiol desorption surface defects are induced in SAM structure. For $CH_3(CH_2)_7$ S/Au this critical potential was V_c ca. -0.15 V (vs.Ag/AgCl). Similar defects formed in thiol SAMs before desorption were also observed using AFM by Kolb and coworkers[35]. In addition to these potential dependent defects, there are intrinsic defects in SAMs possibly formed at surface impurities, gold step edges, SAM crystal edges,

vacancy islands[36], and Au grain boundaries as shown in Figure 5.12 b). Defects at SAM crystal edges is the defects of the SAM formed on of the boundries of different crystalline faces. A vacancy island is one kind of surface imperfections which represents several atoms are missing from the normally occupied lattice site. All of these may cause packing defects on polycrystalline Au surfaces.

We speculate that this fluctuation of potential dependent Raman intensity might be mainly due to the increase in defects during the cathodic potential scan especially after only short term exposure to mercaptohexanol. When the packing density of the mercaptohexanol is increased at longer exposure time, this flunctuation of potential dependent Raman intensity reduced simutaneously as shown in the long-term (24 h) modification case.

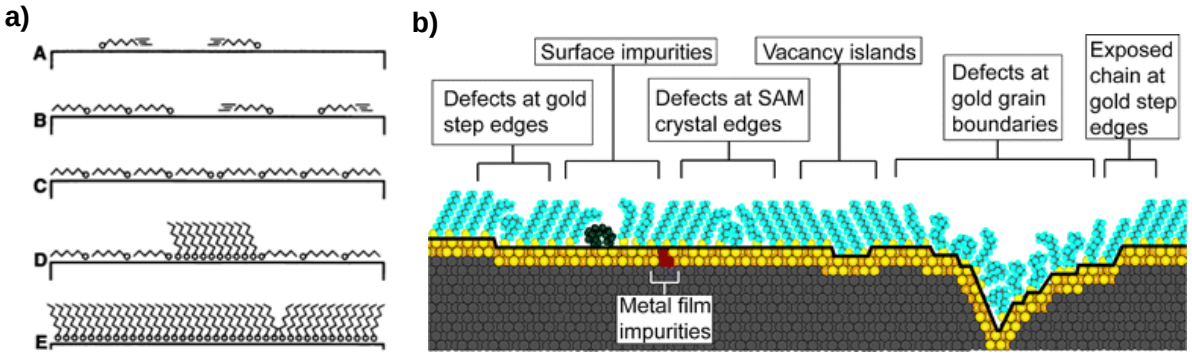

Figure 5.12 a) Adapted from Poirier *et al.*[37] to demonstrate the assembly process of thiol packing on single crystalline Au (111). A. The thiol adsorbs on the Au surface in a lying down conformation. B. to C. The lying down conformation of thiol accumulates on the surface. D. The lateral alkane side chains pack together to form a tilting upright conformation via the van der Waals interaction of the alkane chain sides. E. The saturated packing state of the thiol with partial defects between the clustered packing. (Reprinted with permission from Ref.[37]. Copyright© (1996) The American Association for the Advancement of Science.) b) Adapted from Love *et al.*[28] to illustrate some of the intrinsic and extrinsic defects found in SAMs formed on polycrystalline substrates. The dark line at the metal – sulfur interface is a visual guide for the reader and indicates the changing topography of the substrate itself. (Reprinted with permission from Ref. [28]. Copyright© (2005) American Chemical Society.)

In light of the discussion above, the thiol assembly backfilling process seems to have two effects on the Texas Red-labelled beacon probe. First, good packing of the mercaptohexanol results in substitution of the majority binding sites of the Texas Red and the base moieties of beacon probe

adsorbed to the Au surface. The second effect is the insulating character which reduces electron and ion exchange between the bulk electrolyte and the Au interface. Both effects might reduce the potential dependent Raman enhancement of the Texas Red label. To investigate the relative significance of these two possible effects on the Raman intensity for the beacon probe, we further compared the passivation of ω-hydroxyl alkanethiols with varied alkyl chain length in Sections 5.2.1 and 5.2.2. For the perspective of the effect of distance on SERS enhancement, we will review the literature and present a comparison of monolayers formed of varied length alkanethiols on the Texas Red-labelled beacon probe at the open circuit potential first in Section 5.2.1 and there is the presence of the potential scan in Section 5.2.2.

5.2.1 Distance Dependence of Surface-enhanced Raman Intensity of Texas Red and Texas Red-labelled Beacon Probe

As discussed in Section 1.2 and in the result reported in Section 5.1, the distance between the molecule and the metal surface is one of the factors that affects the surface-enhanced Raman intensity. Based on the electromagnetic enhancement, the Raman intensity is proportional to the r^{-10} where r is the distance between the molecular and the metal surface for nanoparticles with a diameter less than 10 nm according to Dieringer *et al.*[38]. Rcently, Masango *et al.*[39] used atomic layer deposition on Ag film over nanoparticle substrates to carry out a high-resolution distance dependence study of SERS intensity. They modified the former distance dependence by adding an additional term

$$I_{SERS} = C_1(1 + \frac{r}{a_1})^{-10} + C_2(1 + \frac{r}{a_2})^{-10} \qquad (5.1)$$

where the first and second term on the right represent the short and long range distance dependence. The parameters a_1 and a_2 are the short-range and long-range radii of curvature of the Ag over nanosphere (AgFON) features, respectively, and C_1 and C_2 are constants that account for the relative contributions of the two terms.

Ray and co-workers reported a SERS ruler system to measure the distance-dependent Raman signal by using hybridised double-stranded DNA[40]. The single-stranded DNA was first synthesised with Rhodamine 6G labelled at the 5' terminal and thiol at the 3' end to anchor to Au nanoparticles with 30 nm and 8 nm diameters. The complementary strand of the oligonucleotide was then hybridised to the labelled strand. The length of the duplex ranged from 2 to 57 mer. The decay of SERS signal was explained as due to the distance-dependence in a scale of sub-20 nm on 30 nm diameter nanoparticles based on Gersten and Nitzan's estimation [41]. Their result also supports the idea that the distance dependence of the SERS intensity is also affected by the metal structure and plasmons.

Most studies of plasmon distribution use numerical methods to obtain approximate solutions of Maxwell's equations based a unit cell of the nanostructure. Since the energy distribution for LSPR depends strongly on the substrate geometry, as the geometry of the plasmonic structure becomes more complicated and larger, more factors need to be taken into account, including nonlocal dielectric effects, nonlocal optical effects, extraneous surface charges, and higher multipolar responses, as discussed in several publications[41–46] reviewed by Ray *et al.*[47].

Analytic solutions of Maxwell's equations for truncated voids in the SSV substrate are not yet possible; Cole *et al.*[48] evaluated the plasmon modes of SSV structures by using boundary element methods (BEM). Their calculation indicated that the localised plasmons of the SSV structures were mainly focused on the opening of the truncated voids and slightly lowered and trapped in the cavity for the 480 nm deposit thickness. Based on the BEM calculation, Mahajan *et al.*[49] indicated a long-range distance dependence of LSPR up to 100 nm in the case of the SSV substrate, but no subsequent experimental data or theoretical equation for the relevant SERS intensity is available at this moment.

After reviewing the literature on the distance dependence of the SERS intensity, we designed the following experiment to examine the extent of the distance effect on the Raman intensity for Texas Red and Texas Red-labelled beacon probe. The SSV surfaces were separated from the same substrate deposit thickness, 480 nm, using 600 nm nanosphere templates. The SSV surfaces were immersed in 1 µM Texas Red-labeled beacon probe solution containing 0.5 M NaCl, 10 mM Tris buffer (pH 7.2) for 16 h followed by treatment with hydroxyl-terminated alkanethiols with alkane lengths of C2, C4, C6 and C9 for 24 h to ensure equilibrium coverage. The Raman spectra shown in Figure 5.12 were acquired at the open circuit potential. Texas Red was used as the standard for the intrinsic Raman intensity of the 1504 cm^{-1} band. The remaining Texas Red Raman bands other than 1504 and 1649 cm^{-1}, were relatively weak in the case of the Texas Red-labelled beacon probe and hence were not appropriate as an indicator to study the distance dependence of the SERS intensity.

The estimated distance of 2.83 Å for the adsorption of Texas Red on the Au surface is based on the orientation from STM data reported by Su *et al.*[50], and the Au-N stretching mode (170.3 cm^{-1}) and bond length refered from Wu *et al.*[51] as shown in Figure 5.14. The thickness of the passivated ω-hydroxyl alkanethiols was based on the measurement results reported by Porter *et al.*[52] using ellipsometry.

The converted distance dependence of the Raman intensity of the 1504 cm^{-1} Texas Red band is shown in Figure 5.15. For the respect of the distance tuned by the ω-hydroxylalkanethiol between the Texas Red label and the Au surface, the Raman intensity of the 1504 cm^{-1} Texas Red band dropped to ca. 60%, 40% and 30% for passivation with $HOCH_3(CH_2)_nS/Au$, n = 1,3,5 respectively. This decrease of Raman intensity for the Texas Red-labelled beacon probe might be explained as the probe was lifted up by the ω-hydroxyl terminated alkanethiols in the case of the backfilled

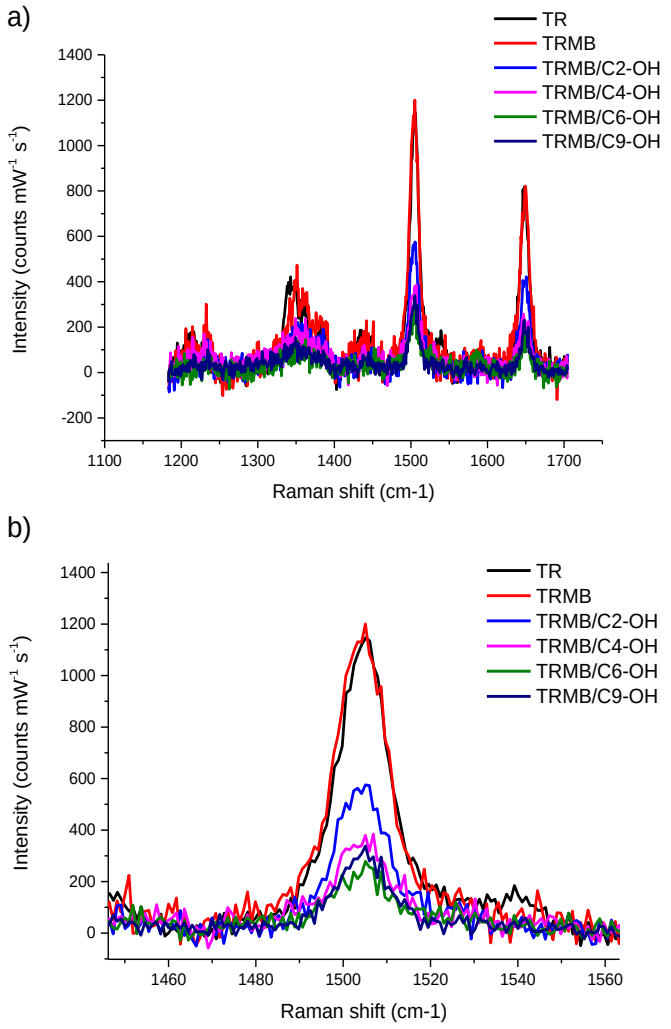

Figure 5.13 a) Raman spectra of the Texas Red-labelled beacon probe (TRMB) modified surfaces exposed to ω-hydroxylalkanethiol, $HO(CH2)_nSH$. n=2, 4, 6, 9 respectively for 24 h. The SSV surfaces were separated from the same substrate deposit, thickness 480 nm, made using 600 nm nanosphere templates. The SSV surfaces were immersed in 1 µM Texas Red-labeled beacon probe solution containing 0.5 M NaCl, 10 mM Tris buffer (pH 7.2) for 16 h followed by treatment with 1 µM hydroxyl-terminated alkanethiols with alkane lengths of C2, C4, C6 and C9 for 24 h to ensure equilibrium coverage. Another modification of the SSV surface was immersed in 1 µM Texas Red to subsititute the 1 µM Texas Red-labeled beacon probe in the same solution composition. b) The close up view of a) for the Raman band at 1504 cm^{-1} for the Texas Red adsorbed to the SSV surface and the SSV surfaces modified with Texas Red-labelled beacon probe to mercaptoalkanols exposure for 24 h.

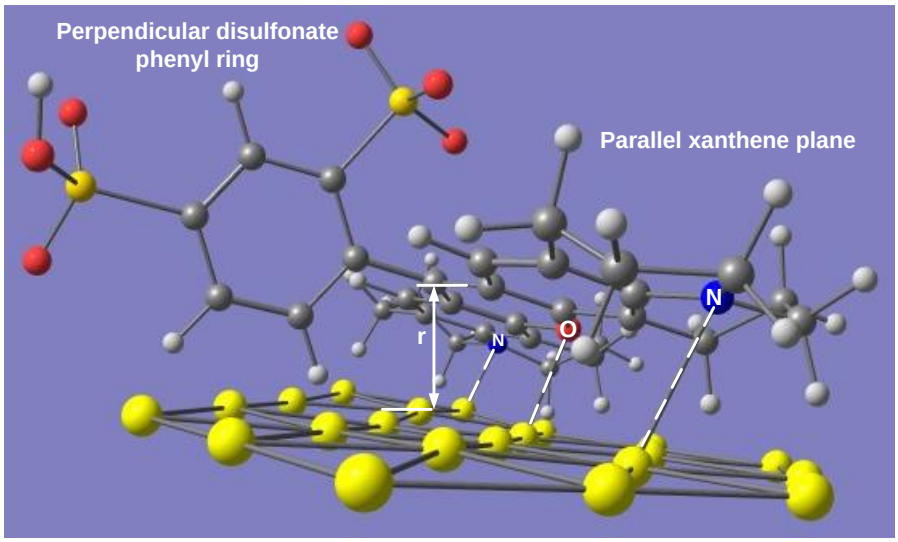

Figure 5.14 Schematic of the adsorption of Texas Red on the Au surface. The geometry optimisation of Texas Red was calculated at the B3LYP/6-311++G (d, p) level. The Au plane was assembled as a hexagonal close-packed shown with a Au-Au bond (2.88 Å) based on Wu *et al.*[53] The Au-N and Au-O bonding were assigned to Raman bands at 170 cm^{-1} and 233 cm^{-1} individually of the surface-enhanced Raman spectrum of Texas Red on the Au surface in Section 4.3. The hinge carbon that links the disulfonate phenyl ring and the xanthene plane and also the closest atom to the mass centre of Texas Red, was used for the distance estimation between the Texas Red to the Au surface and is 2.83 Å

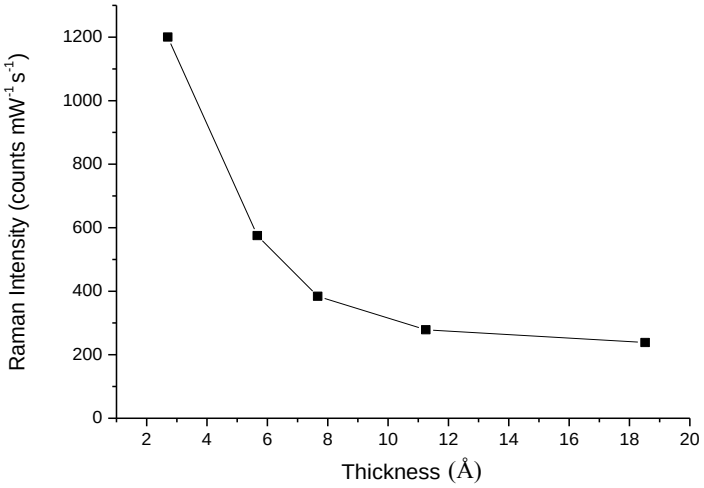

Figure 5.15 The distance dependence of the Raman intensity tuned by modification with ω-hydroxylalkanethiols for the Texas Red-labelled beacon probe (TRMB) immobilised at the Au SSV surface. C2, C4, C6 and C9 represent the 2-mercaptoethanol, 4-mercaptobutanol, 6-mercaptohexanol and 9-mercaptoundanol respectively. Texas Red (TR) adsorbed directly to bare Au serves as a standard control. The distance estimation of Texas Red adsorbed on the Au surface was based on the STM image reported by Su *et al.*[50] and the Au-N bond length as 2.83 Å. The thickness of passivation thiols obtained from the Porter *el al.*[52]

preparations at varied alkyl chain length. Details of the packing effect of thiol monolayer will be discussed in Section 5.2.2.

The Texas Red-labelled beacon probe was immobilized first and then backfilled with ω-hydroxyl terminated alkanethiol on the SSV surfaces; it is assumed that after 18 h exposure the Texas Red beacon probe should reach its equilibrium coverage. The coverage of the beacon probe should therefore be similar before the subsequent formation of the thiol SAM. The other uncertainty related to the orientation of Texas Red label may change (increase or decrease) the Raman intensity of Texas Red during the increase of the alkyl chain length in the SAM backfilling. However, we do not have experimental evidence to prove this assumption currently. Change the thickness of the mercaptoalkanols can have other effects on the system including local field, double layer capacitance and local dielectric. Some further observations on the different preparation of ω-hydroxyl terminated alkanethiol SAMs and the interpretation of the orientation of the Texas Red label were discussed in Section 5.2.2.

If we relate the potential dependent enhanced intensity to the distance dependence as shown in Figure 5.15, the increase of Raman intensity would be interpreted as the shorter distance between the molecules to the surface under potential sweeping. From the aspect of the molecule-metal interaction, if the molecule were immobilized on the surface by a shortened Au-N bond, the geometry of Texas Red would have to distort especially on the moiety of the disulfonate phenyl ring. Consequently, this would result in a change in molecular orientation. However, we do not observe this distortion based on the Raman spectra acquired under potential sweep. Therefore we conclude that the orientation change of adsorbed Texas Red cannot relate to the potential dependent Raman intensity discussed in Section 4.2. Hence it is hard to attribute the increase of potential-dependence of the Raman intensity of Texas Red to the distance dependence.

The Raman spectra of Texas Red and the labelled beacon probe adsorbed on the SSV substrates were acquired under open circuit conditions in this Subsection (5.2.1). In the next Section 5.2.2, we apply external potential on the same adsorbates (Texas Red and the labelled beacon probe) to observe the potential dependent Raman intensity and discuss how much contribution can be related to the distance dependence.

5.2.2 Potential dependent Raman Enhancement of Texas Red and Texas Red-labelled Beacon Probe in the Presence of Varied Chain Length ω-hydroxyl alkanethiols

In this subsection, we further compare the Raman response of the adsorbed Texas Red and the Texas Red-labelled beacon probe at electrodes modified with various hydroxyl-terminated alkanethiols as a function of potential. The SSV substrates were fabricated as in Section 2.1, and the deposit thickness was 480 nm using a 600 nm nanosphere template. The SSV substrates were separated from the same substrate to minimise the packing bias of the nanospheres. The SSV substrates were immersed in 1 μM Texas Red-labelled beacon probe solution containing 0.5 M NaCl, 10 mM Tris buffer (pH 7.2) for 18 h. The SSV substrates were selected to be modified with ω-hydroxylalkanethiol $HOCH_2(CH_2)_nSH$ with varied alkane length (n = 1,3,5,8) individually for 6 h. The Raman spectra were acquired using 633 nm excitation (2.3 mW) in static mode in 1180 to 1704 cm^{-1} using 25 s exposure during the 25 mV potential sweep. The potential was scanned from 0.2 to -1.2 V at 1 mV s^{-1}.

The result shown in Figure 5.16 indicate that the self assembly effect of the monolayer on the potential dependent Raman response of the Texas Red-labelled beacon probe is not smooth and may not be real on the backfilled with 2-mercaptoethanol and 4-mercapto-1-butanol with 6 h exposure. However when this fluctuation in Raman intensity for Texas Red label is compared to the longer (24 h) exposure as shown in Figure 5.18, the fluctuation seems to grow into a clearer peak and hence might be explained as correlating the packing density of the hydroxyl-terminated alkanethiol as the films with shorter alkane chains are less compact after 6 h exposure as compared to the mercaptohexanol and 9-mercapto-1-nonanol. However, for the case of 9-mercapto-1-nonanol passivation, the two contributions observed at the beginning of Section 5.2 are no longer be able to explain the results in Figure 5.18 by the complete substitution effect and ionic insulating. A further increase of peak Raman intensity and shift of the potential of peak Raman intensity took place for 9-mercpto-1-nonanol.

In contrast to the case of 9-mercpto-1-nonanol shown in Figure 5.16, the blocking of the potential dependent Raman enhancement and reductive desorption cannot completely explain the increase of peak Raman intensity. To discuss the effect of mercaptoalkanol on the immobilised beacon probe,

we consider the two possible SAM states in the localised region around the Texas Red label as shown in Figure 5.17.

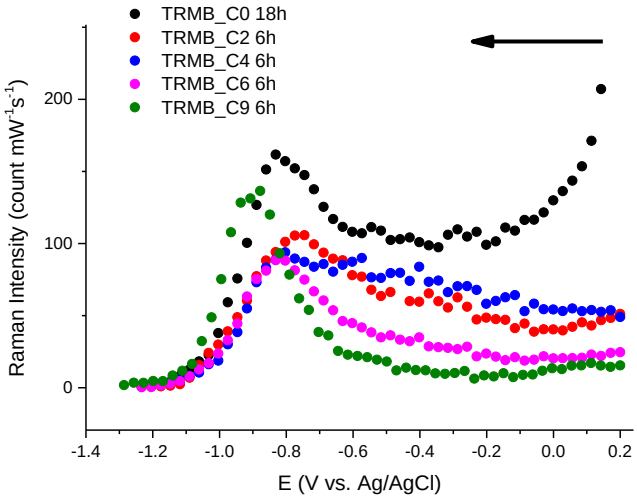

Figure 5.16 The potential dependent Raman response for Texas Red-labelled beacon probe (TRMB) at electrodes with the various ω-hydroxyl alkanethiols. The SSV substrates were fabricated as in Section 2.1, and the deposit thickness was 480 nm using a 600 nm nanosphere template. The SSV substrates were separated from the same substrate to minimise the nanosphere packing bias. The SSV surfaces were immersed in 1 μM Texas Red-labelled beacon probe solution containing 0.5 M NaCl, 10 mM Tris buffer (pH 7.2) for 18 h. The SSV surfaces were then selected to be passivated with 1 μM ω-hydroxylalkanethiol $HOCH_2(CH_2)_nSH$ with varied alkane lengths (n = 1,3,5,8) individually for 6 h. The Raman spectra were acquired using 633 nm excitation (2.3 mW) in static mode for 1180 to 1704 cm^{-1} using 25 s exposure during the 25 mV potential sweep. The potential was scanned from 0.2 to -1.2 V at 1 mV s^{-1}. The arrow indicates the direction of potential sweeping.

These two states of SAM collectively contribute to the overall effect on the Raman intensity. The contributions of the complete substitution packing and the surface impurity-like defect to the resultant Raman intensity may be different by choosing different praparation methods of SAM. The SAM prapartation procedures include backfilling mercaptoalkanol after the beacon probe immobilization or co-adsorption the mercaptoalkanol with the beacon probe. Both sates has been reported by Josephs *et al.*[27,54] using atomic force microcope (AFM) for DNA/ mercaptohexanol adsorbed on the Au(111) surfaces. We will discuss the two modifications methods in the following experimental results.

The fundamentals of alkanethiol self assembly have been reviewed by Schwartz[29] and the effects of packing disorder and defects in alkanethiol films have been extensively studied in the

literature[28,55,56]. The SAM packing around the Texas Red label can be regarded as a surface impurity as shown in Figure 5.12 b). The packing of the thiols adjacent to the beacon probe will experience a certain degree of disruption. Although the thiol adsorption is used to prevent non-specific adsorption of the immobilised oligonucleotide on the Au electrode, studies indicate that the thiol-backfilled Au surface is not completely defect-free. As observed from Figure 5.16, the complete replacement of Au-N by Au-S would be expected to reduce the Raman intensity for the Texas Red-labelled beacon probe in the case of the 9-mercapto-1-nonanol backfilling. The localised defects cause by Texas Red as a surface impurity among the ordered 9-mercapto-1nonanol packing might explain this different tendancy from the expection at the complete SAM substituion condition. Texas Red labels of beacon probe might have relatively more Texas Red adsorbed directly on Au as a surface impurity (Figure 5.17 a)) other than be completely substituted by the thiol SAM (Figure 5.17 b)), and hence reflects a overall higher Raman intensity in Figure 5.16 in the case of short-term (6 h) backfilling with 9-mercpto-1-nonanol. But the real reason for this is not clear currently.

As there are other intrinsic defects in the SAM, it is not easy to separate these defects individually in practical experiments. For example, the electrodeposited SSV Au structure is polycrystalline,

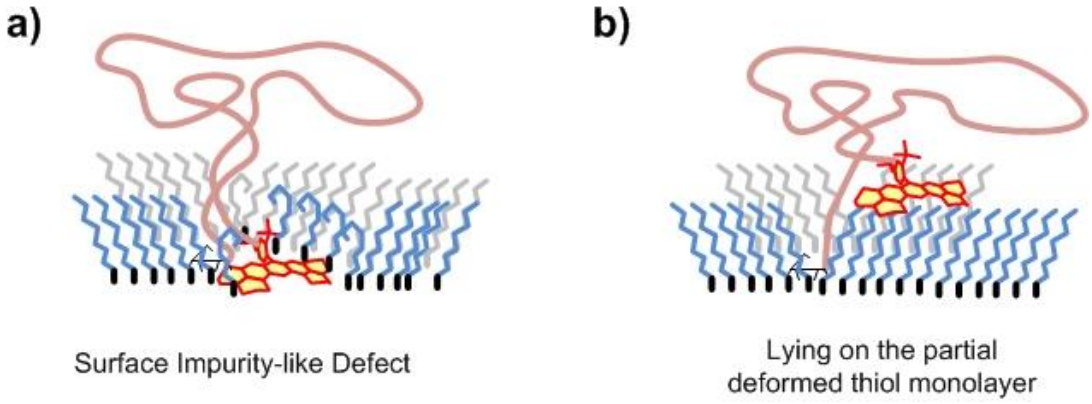

Figure 5.17 A schematic of ω-hydroxyl alkanethiols SAM near the Texas Red-labelled beacon probe. The mushroom-like chain represents the loop-stem shape of beacon probe. The waved chain stands for the ω-hydroxyl alkanethiol (the blue and grey colours are used for distinguishing the relative distance toward the viewpoint). The red ring cluster stands for the Texas Red label. a) The surface impurity-like defect is mainly formed from the thiols on the localised region of Texas Red label is less compact. The defect does not have adjacent alkene chains to provide a lateral support of van der Walls force to from the compact SAM. The resultant partial thiol disordered or collapsed defects around their boundary to the Texas Red. b) The thiol packing of localised region of Texas Red tag is defect-free and the Texas Red was purely substituted by thiol SAM which causes the Texas Red label lifted away from the Au surface.

and certainly, defects at crystal edges and step edges are inevitable. The deposited SSV structure is supposed not be able to maintain the intact atomic structure in a stringent cleaning method like piranha solution or electrochemical polishing for several tens of cycles[57]. Hamelin *et al.*[57] compared the capacitance the unconstructed Au(111) surface without and with holding the potential below -0.2 V, about 0.3 V positive to the onset of the hydrogen evolution, for 20 min in dilute (1 mM) perchloric acid. They reported the potential-induced hexagonal surface reconstruction was consistent with the literature[57]. Eberhardt *et al.*[58] indicated that the surface reconstruction depends on the anion adsorption of the supporting electrolyte, surface crystallinity and potential control. In the potential range -0.2 to -1.2 V scanned at 0.3 to 1 mV s^{-1} in this study, the chloride anion (as a strongly adsorbed anion) existed in the supporting electrolyte and the polycrystalline Au SSV surface, it is hardly to exclude the presence of the potential-induced surface reconstruction. The surface reconstruction may change the geometry of the Au nanostructure in the 10 nm scale[59]. Jäckel *et al.*[60] observed the evidence to support the speculation above using the single Au bowtie nanostructure modified with para-mercaptoaniline (pMA). The electrochemical SER spectra of pMA were aquired during the potential sweep started from zero, then scanned to -0.4 V and backed to 0.4 V. The ± 0.4 V cycling potential window did not indicate any *I-V* change. The SEM images and the SER spectra both suggests the electrochemically-induced surface roughening results in the ill-defined shape of the bowtie and the extra vibration modes (b_2) observed in SERS after the first potential sweep.

Two ways to investigate these effects are by increasing the mercaptoalkanol adsorption time to ensure equilibrium coverage or by changing the procedure used to co-adsorption method as mentioned in Section 3.2. We will discuss the effects of increased adsorption time first, and then examine the effect of co-adsorption of the Texas Red-labelled beacon probe and ω-hydroxyl alkanethiols.

The SSV substrates were fabricated as described Section 2.1 with a deposit thickness of 480 nm using the 600 nm nanosphere template. The SSV surfaces were separated from the same substrate to lower the nanosphere packing bias. The SSV surfaces were immersed into the solution containing 1 μM Texas Red-labelled beacon probe solution containing 0.5 M NaCl, 10 mM Tris buffer (pH 7.2) for 18 h. 1 μM ω-hydroxyl alkanethiol, with $HOCH_2(CH_2)_nSH$ with varied alkane length (n=1,3,5,8), was then added into the solution on the SSV surfaces and left for 24 h. The SSV surfaces were rinsed with copious amounts of 1 M NaCl, 10 mM Tris buffer (pH 7.2) before the Raman measurement. The Raman spectra were acquired in a homemade spectroelectrochemical

cell with 1 M NaCl, 10 mM Tris buffer (pH 7.2) as the supporting electrolyte. The Raman spectra were collected in the static mode using 633 nm excitation (2.3 mW) between 1180 to 1704 cm^{-1} using 25 s exposure during the 25 mV potential sweep. The potential was scanned from 0.0 to -1.2 V at 1 mV s^{-1}. The results are shown in Figure 5.18. An SSV surface immersed in 1 µM Texas Red solution containing 1 M NaCl, 10 mM Tris buffer (pH 7.2) for 18 h without passivation was also prepared as a control to compare the peak potential of the potential dependent Raman intensity.

The results shown in Figure 5.18 indicates that the Raman response of the 24 h backfilled 9-mercapto-1nonanol is less intense than that of 6 h backfilling adsorption. In all cases following backfilling exposure with ω-hyrdoxyl alkanethiols there is a gradual decrease in the peak intensity of the potential dependent Raman band at 1504 cm^{-1} accompanied with a negative shifted in the peak potential of the Raman intensity maximum as the alkyl chain length of the ω-hydroxyl alkanethiol increases. Another systematic change with the length of the alkane chain is in the onset

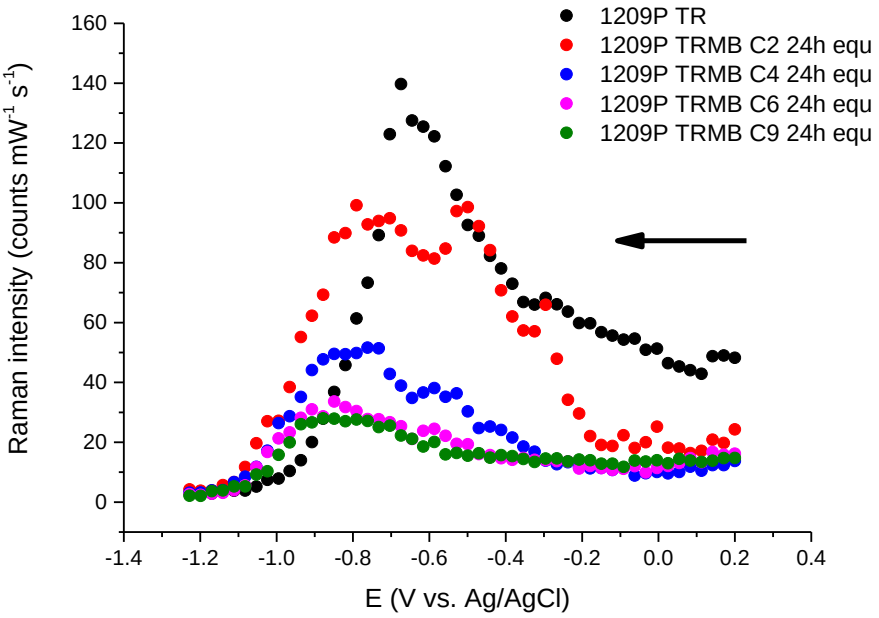

Figure 5.18 Intensity of 1504 cm^{-1} band of Texas Red on the Au SSV surfaces. SERS under linear sweep voltammetry of the Au electrodes modified with bare Texas Red (TR) without mercaptoalkanol adsorption and Texas Red-labelled beacon probe (TRMB) with backfilling with ω-hydroxyl alkanethiols, $HOCH_2(CH_2)_nSH$, with varied alkane length (n=1,3,5,8) for 24 h after 18 h probe immobilization. The SSV substrates were fabricated as described in Section 2.1 with deposit thickness of 480 nm for the 600 nm nanosphere template. The SSV surfaces were separated from the same substrate to lower the nanosphere packing bias. The arrow indicates the direction of potential sweeping.

potential of Raman intensity increasing ca. -0.15, -0.3, -0.4 and -0.55 V which shifts negative with the backfilled modification. However, the reason for the minor peaks at positive of the maximum Raman intensity which is also negative shifted as the alkyl chain length of ω-hydroxyl alkanethiols increasing is still not clear. Aseries of capacitance measurement were carried out to see if the minor peak could be related to the reductive desorption of alkanethiols or the potential dependent defects reported by Boubour *et al.*[111] and discussion at the beginning of Section 5.2.

The following impedance experiments were performed as described in Section 4.5 by using a 2 mm microdisc Au electrode (ALS, Japan). After cleaning, the Au electrode was immersed in the same Texas Red-labelled beacon probe solution for 18 h and backfilling exposure with different lengths of mercaptoalkanol for 24 h. After the modification steps, the Au electrodes were rinsed with copious amounts of 100 mM phosphate buffer (pH 7.0) before the impedance measurements. The supporting electrolyte, 100 mM phosphate buffer, was agitated with argon for 30 min to remove dissolved oxygen. The impedance measurement was made using a 10 mV sinusoidal perturbation at frequency 251.82 Hz over the potential range from 0.2 V to -1.2 V (vs. SCE). The capacitance was calculated as in Section 4.5.

The results are shown in Figure 5.19. For each of the mercaptoalkanol coated electrodes there is a mild shoulder increase in capacitance, Figure 5.19 a) and in the peaks of the corresponding derivative shown in Figure 5.19 b), that probably can be attributed to the reductive desorption of the ω-hydroxyl alkanethiol layers. The capacitance of the Texas Red labeled beacon probe backfilled with the mercatoalkanol reaches a value close to that for the bare Au at ca. -1.05 V suggest all the mercaptoalkanol is removed. The discrepency of the capacitance of the 9-mercapto-1-nonanol at the potential negative of -1.0 V is possiblely due to an error in the estimated area.

As the length of the alkane chain increases this feature shifted to move negative potential. The overall Raman response of the Texas Red-labelled beacon probe still reflects the peak intensity and the corresponding potential is related to the mercaptoalkanol chain length and the SAM packing. If one consider the complete substitution effect to explain the Raman intensity in the long-term mercaptoalkanol exposure, which gives a more compact packing around the Texas Red label, one would expect to observe an higher increase of Raman intensity at the potential negative of the onset of reductive desorption. Conversely, the Raman intensity maintains relatively low in the longer alkanethiol chain cases (C6 and C9) even for the potential negative of the onset of reductive desorption. This suggests that the ω-hydroxyl alkanethiol in the localised region of the Texas Red-labelled beacon probe does not completely diffuse away from the electrode surface. This counter-

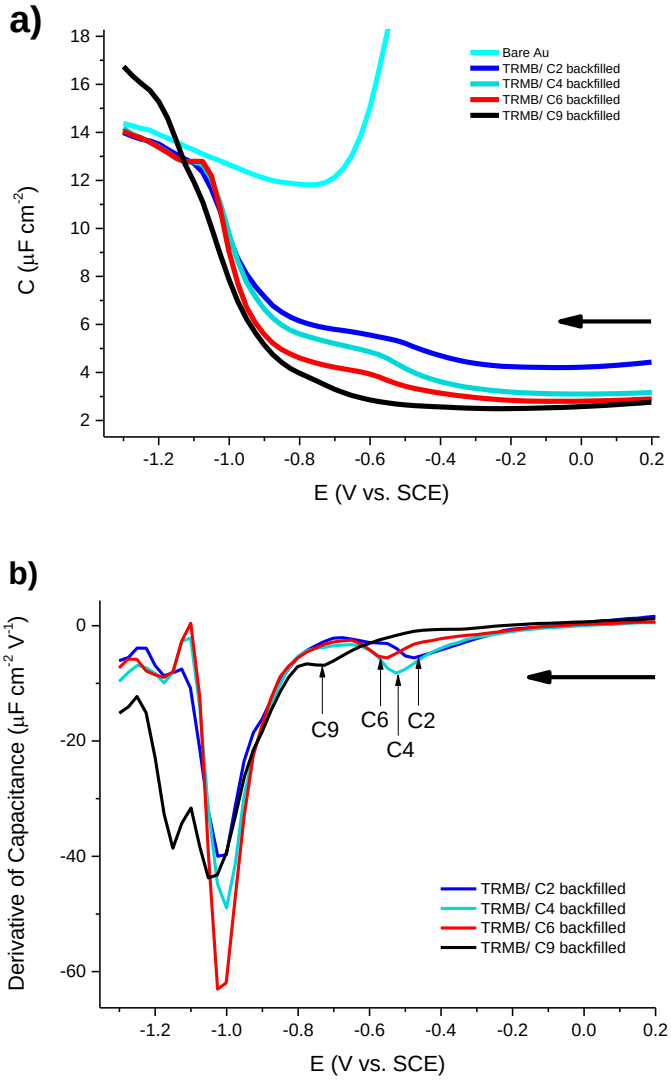

Figure 5.19 Capacitance measurement of Texas Red-labelled beacon probe backfilled passivation with the varied length of ω-hydroxyl alkanethiols. The impedance measurement was carried out on the Autolab PGSTAT 302 (Metrohm, Switzerland) on the 2 mm microdisc Au electrode (ALS, Japan). The supporting electrolyte 100 mM phosphate buffer and was agitated with Argon for 30 min to remove dissolved oxygen. The impedance measurement used a 10 mV sinusoidal perturbation at a frequency of 251.82 Hz calculation of capacitance was the same as Section 4.5. The arrow indicates the direction of potential sweeping.

intuitive speculation has been made and experimentally proved by Widrig *et al.*[30] They observed that the desorbed mercaptoalkane could re-adsorb at the Au electrode at potentials more positive than the potential for reduction of the original mercaptoalkane. Similar re-adsorption was observed in carboxylic and hydroxyl terminated alkanethiols[61]. The estimated quantity of the re-adsorption is proportion to the chain-length of the alkanethiol when the shorter alkane chains tends to diffuse away more from the electrode surface. Hence they concluded that the desorbed

alkanethiol stayed partially in the vicinity of the electrode surface after the reductive desorption. This desorption chracteristic can explain the maximum Raman intensity for the increasing alkyl chain length of bckfilled mercaptoalkanol maintain the decreasing tendency to the corresponding alkyl chain length even at the potential negative of the reductive desorption at ca. -0.9 V measured by the impedance spectroscopy.

The second peaks in the capacitance derivative at ca. -1.0 V seem to be consistent with the hydrogen evolution discussed in Section 4.5. Although the size and amount of the bubbles visually observed on the ω-hydroxyl alkanethiol passivated SSV surfaces are samller and fewer than that observed on Texas Red adsorbed SSV surfaces, we cannot completely exclude the contribution of hydrogen evolution in a neutral electrolyte (pH 7.2).

After comparing the short-term (6 h) and long-term (24 h) backfilling adsorption of mercaptoalkanol after the pre-immobilization of the Texas Red-labelled beacon probe and the relevant Raman response of Texas Red-labelled beacon probe under potential perturbation, a further preparation method of the Texas Red-labelled beacon probe and ω-hydroxyl alkanethiols was made by co-adsorption.

The SSV substrates were fabricated as described in Section 2.1. The SSV surfaces were separated from the same substrate to lower the nanosphere packing bias. The SSV surfaces were immersed into the solution containing 1 μM Texas Red-labelled beacon probe, 1 μM ω-hydroxyl alkanethiol, $HOCH_2(CH_2)_nSH$ with varied alkane length (n=1,3,5,8) individually for 16 h. The SSV surfaces were rinsed with copious amounts of 1 M NaCl, 10 mM Tris buffer (pH 7.2). The Raman spectra were acquired in the static mode using 633 nm excitation (2.3 mW) from 1180 to 1704 cm^{-1} using 25 s exposure during the 25 mV potential sweep. The potential was scanned from 0.0 to -1.2 V at 1 mV s^{-1}.

The results are shown in Figure 5.20. The potential dependent Raman intensity of the 1504 cm^{-1} band for the mercaptoalkanol of C2, C4 and C6 alkyl chain length has similar value when co-adsorbed with the the Texas Red-labelled beacon probe. In the case of the Texas Red-labelled beacon probe on the bare Au electrode, the potential of the Raman intensity maximum is positive to that of the probe co-adsorbed with the mercaptoalkanol, and the peak Raman intensity value is close to that observed in the C2, C4 and C6 (only 5- 10 counts mW s^{-1} less) mercaptoalkanol cases but not for the 9-mercapto-1-nonanol. The Raman intensity of co-adsorbed 9-mercapto-1-nonanol

with the Texas Red beacon probe behaved in quite a different way on the cathodic potential sweep with a steady and relatively low Raman intensity in the window from 0 to -1.2 V.

The self-assembled monolayer effects discussed in Section 5.2 suggests that the complete substitution of the Texas Red adsorption sites by the mercaptoalkanol SAM and formation of an

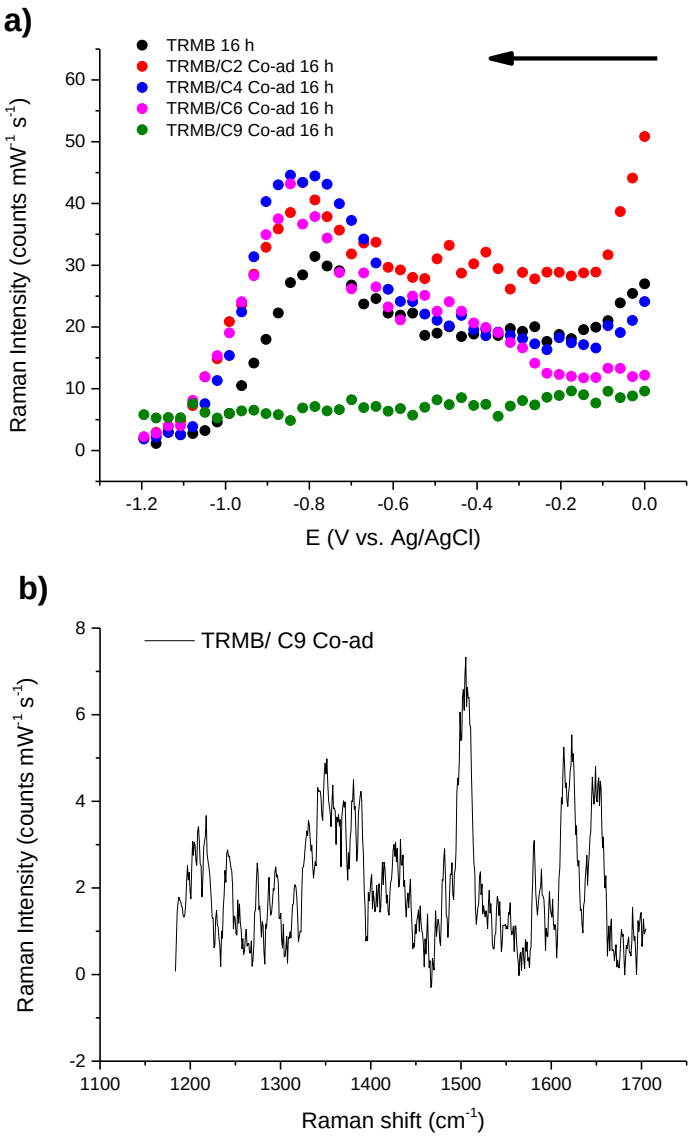

Figure 5.20 . a) The potential dependent Raman intensity change at 1504 cm^{-1} for the Texas Red-labelled beacon probe (TRMB) co-adsorbed with ω-hydroxyl alkanethiols of mercaptoethanol (C2), 4-mercapto-1-butanol (C4), mercaptohexanol (C6) and 9-mercapto-1-nonanol (C9) for 16 h. The SSV chips were separated from the same substrate to lower the nanosphere packing bias. b) Background-subtracted Raman spectrum of Texas Red-labelled beacon probe co-adsorbed with 9-mercapto-1-nonanol (C9). The spectra have been smoothed for a clarity of signal to noise ratio by using 5 points smoothing function of Origin ® v. 9.1 (OriginLab Inc, USA) The arrow indicates the direction of potential sweeping.

ionic insulating layer could not completely explain the case herein. Based on the complete substitution model, the Texas Red label may be lifted from surface and to lay on the SAM formed by the mercaptohexanol. This model seems to be able to explain the decrease of Raman intensity for the pre-adsorbed Texas Red beacon probe when backfilled with mercaptoalkanols (C2, C4, C6 and C9) at the open circuit po-tential. When an external potential was applied to the Texas Red beacon probe/ mercaptoalkanol surfaces prepared in the two step modification, the electrode modified by backfilling with the mercaptoalkanol during short duration (6 h) exhibit another feature of the potential dependent Raman intensity which cannot be explained by the complete substitution model. The suface impurity defects consider the Texas Red beacon probe as an impurity defect to the surrounding mercaptoalkanol packing and these defects co-exist with the complete substitution effect. When the backfilling extends to 24 h, the complete substitution model appears to be more evident to the resultant potential dependent Raman intensity. The intrinsic character of the desorbed mercaptoalkanols, that stay partially in the vincinity of the electrode surface, further separates the Texas Red from direct contact the Au surface.

The discrimination between the co-adsorbed ω-hydroxyl alkanethiols with alkyl chain length C2 to C6 is the Raman response in 0 to -0.5 V region and could be explained by stronger ionic insulation for the longer alkane length thiols. The electrode co-adsorbed prepared by the Texas Red-labelled beacon probe and mercaptoalkanols exhibit a different potential dependent Raman response from the two-step backfilled case (Texas Red-labelled beacon probe immobilized first, followed by the backfilling of mercaptoalkanols). The intrinsic difference between the backfilled and co-adsorption cases is, for the co-adsorption as mentioned in Section 3.2, there is a competitive adsorption between the two adsorbents. Conversely, in the two step backfilling preparation this simultaneous cooperates does not occur. Several authors[62–67] have studied the variation of backfilled and co-adsorption preparation in many respects including the surface inhomogenity between the two adsorbents. The key distinction between the two prepartions is probably due to the formation of a well-packed thiol cluster which has a stronger lateral attraction between the individual thiol alkane chain and requires a longer time (24 h) to achieve the dense packing at surface saturation.

The co-adsorption of the two adsorbates has been studied in several groups[66,68,69]. Based on the review of Smith *et al.*[70], indicates when two different adsorbates are mixed in solution and then exposed to a substrate, both species will adsorb on the surface. If the species differ enough in molecuar composition, they will aggreate into homogenous domains so as to maximize self-self interaction through van der Waals, hydroen bonding, or other interactions. However, may complex

factors arise when attempting to pattern molecules on a surface by simple solution-phase co-adsorption. The relative fractional surface coverages of the molecules will not necessarily be that of coadsorption solution; for example, a 1:1 mole ratio of adsorbates A and B will not necessarily yield a surface cmposition of 1:1 A:B. Factors that affect the competition for the surface include the relative solvation of the adsorbates by the solution, the sticky probability of each molecule, and the degree of the interaction between the molecule once they are adsorbed. Molecules that may be better solvated may not adsorb as quickly to the surface, while the comparatively less soluble molecules may either aggregate in solution or aggregate together on the surface, both situations where the molecules‘ self-interaction are maximal. This character of the aggregation of molecules imparting a particular property to the surface have been applied to make SAM-based sensors. Sensors for barbiturate and cholesterol have been created by capitalizing on the phase separartion between such analytes and *n*-alkanethiolated. Two-dimensional molecular imprinting has been

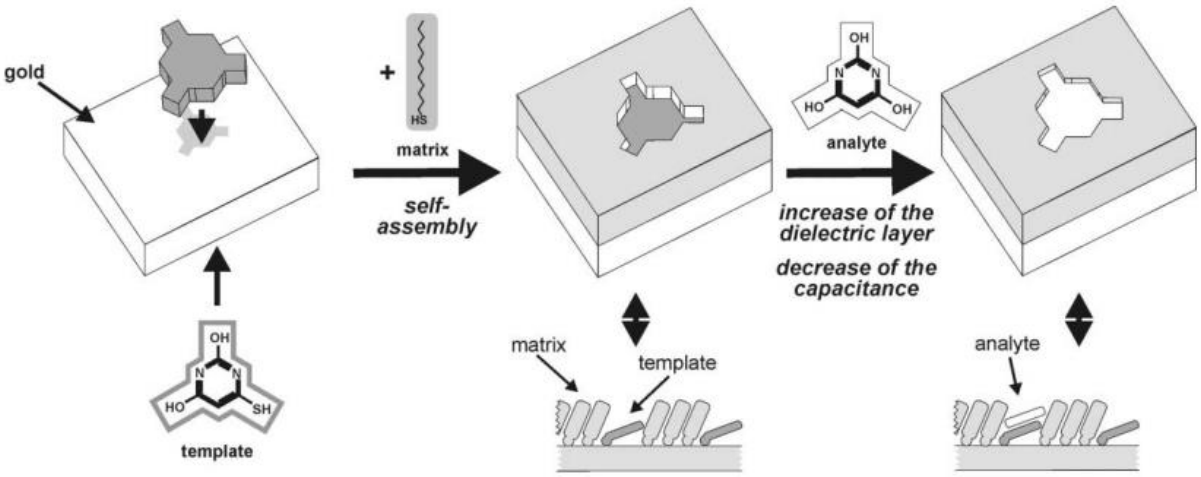

Figure 5.21 Suggested mechanism for preparation and operation of artificial chemoreceptors. The binding sites are formed by co-adsorption of template and matrix molecules. The template should have a shape similar to that of the analyte. Both the template and the matrix molecules must be able to bind to the surface strongly. As an example, co-adsorption of thiobarbiturate (template) and dodecanethiol (matrix) on the gold surface results in the formation of binding sites for barbiturate.(Reprinted with permission from Ref.[71]. © 1999 of John Wiley & Sons)

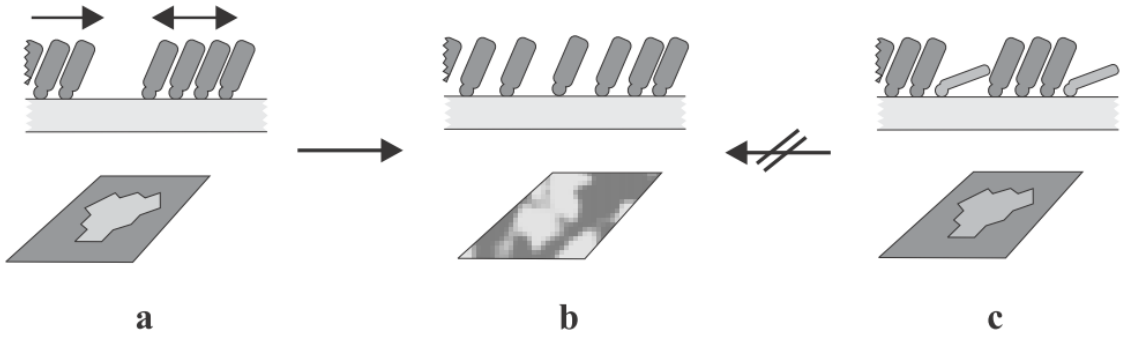

Figure 5.22 Schematic representation of the possibilities of building artificial receptors on a surface as viewed from above (below) and in cross section (above). By two-dimensional molecular imprinting the binding sites (a) can be distorted by lateral diffusion (b). The binding sites can be stabilized—as shown here for the first time—by using a template (c) in the monolayer..(Reprinted with permission from Ref.[71]. © 1999 of John Wiley & Sons)

used to create templates for analyte adsorption by coadsorbing an *n*-alkanethiolate with the analytes thiolated derives (i.e., thiobarbiturate, thiocholesterol)[71,72]. Mirsky *et al.*[71,73] fabricated the mix SAMs using the co-adsorption of thiobarbituric acid (the template) and dodecanethiol (the matrix) onto a gold substrate (Figure 5.21). The spreader-bar like imprinting used in their work is equivalent to the surface impurity like defect. The co-adsorption of the two components (thiobarbituric acid and dodecanethiol) reduced the lateral diffusion between the dodecanethiol and hence preserved the receptor site of barbituric acid for the following sensing as shown in Figure 5.22. The lateral diffusion of dodecanthiol is driven by the van der Waals interaction discussed in the formation process of SAM.

In contrast to the shorter alkane length of ω-hydroxyl alkanethiols, a very distinct potential-independent Raman response can be clearly seen in the 9-mercapto-1-nonanol co-adsorption case in the potential range 0 to -1.2 V. A significant blocking of the potential dependent Raman intensity can be observed and the Raman spectra are a relatively weak but the bands are distinguishable throughout the potential range. A representative Raman spectrum shown in Figure 5.20 b) shows a comparable intensity between the 1360 and 1504 cm^{-1} and a separated band 1620 next to the 1649 cm^{-1} band. There is no obvious explanation at the moment for the new band at 1620 cm^{-1}. The 1620 cm^{-1} band only can be resolved from the original intense 1649 cm^{-1} when the Raman intensity of Texas Red decreases to a low value. This suggests it is something other than the Texas Red is not resonant enhanced. This blocking of potential dependent Raman response can be interpreted as a

purely collective contribution of complete substitution and ionic insulation, and the surface impurity-like defect is not see for the co-adsorption with 9-mercapto-1-nonanol. This result can be compared with the backfilled case shown in Figure 5.18 a). Which shows a similar blocking effect at potential positive of -0.7 V. Miller *et al.*[74] indicates that the SAM structures have more defects when on the alkane length of the alkanethiol is shorter by observing voltametry of a redox indicator. Thus the length of alkanethiol increases (up to 9 in the case herein), the complete substitution effect can be different from the surface impurity-like defects in the case of shorter alkane chain.

From the perspective of the modification of the two states proposed in Figure 5.20, one can notice no single state can explain all the experimental results without considering ionic insulating. The surface impurity-like defects and the complete substitution effect interplay to varied extents in the overall Raman intensity under potential perturbation. The modification time, preparation methods (co-adsorption or two steps backfilled adsorption), the alkyl chain length of the ω-hydroxyl alkanethiol all have an effect on the resultant Raman spectra and intensity.

5.3 References

(1) Braun, S.; Salaneck, W. R.; Fahlman, M.*Adv. Mater.* **2009**, *21*, 1450.
(2) Sato, H.; Kawasaki, M.; Kasatani, K.; Katsumata, M. A.*J. Raman Spectrosc.* **1988**, *19*, 129.
(3) Du, H.; Fuh, R.-C. A.; Li, J.; Corkan, L. A.; Lindsey, J. S.*Photochem. Photobiol.* **1998**, *68*, 141.
(4) Iwata, K.; Weaver, W. L.; Gustafson, T. L.*J.Phys.Chem.* **1992**, *96*, 10219.
(5) Anema, J. R.; Brolo, A. G.; Felten, A.; Bittencourt, C.*J. Raman Spectrosc.* **2009**, *41*, 745.
(6) Nyquist, R. A.; Putzig, C. L.; Leugers, M. A.; McLachlan, R. D.; Thill, B.*Appl. Spectrosc.* **1992**, *46*, 981.
(7) Sears, W. M.*J. Chem. Phys.* **1981**, *75*, 1589.
(8) Palm, A.*J. Phys. Chem.* **1951**, *55*, 1320.
(9) Brandt, E. S.*Appl. Spectrosc.* **1988**, *42*, 882.
(10) Wang, J.; Zhang, P.; He, T.; Xin, H.; Liu, F.*J. Phys. Chem.* **1988**, *92*, 1942.
(11) Tuschel, D.*Spectroscopy* **2016**, *31*, 14.
(12) Furuya, K.; Torii, H.; Furukawa, Y.; Tasumi, M.*J. Phys. Chem. A* **2000**, *104*, 11203.
(13) Fujimoto, Y.; Katayama, N.; Ozaki, Y.; Yasui, S.; Iriyama, K.*J. Mol. Struct.* **1992**, *274*, 183.
(14) Dietze, D. R.; Mathies, R. A.*J. Phys. Chem. C* **2015**, *119*, 9980.
(15) Nion, A.; Jiang, P.; Popoff, A.; Fichou, D.*J. Am. Chem. Soc.* **2007**, *129*, 2450.
(16) Murphy, C. J.; Shi, X.; Jewell, A. D.; McGuire, A. F.; Bellisario, D. O.; Baber, A. E.; Tierney, H. L.; Lewis, E. A.; Sholl, D. S.; Sykes, E. C. H.*J. Chem. Phys.* **2015**, *142*.
(17) Rossel, F.; Brodard, P.; Patthey, F.; Richardson, N.V.; Schneider, W. D.*Surf. Sci.* **2008**, *602*, 24.
(18) Bartlett, P.; Mahajan, S.In *Advances in Electrochemical Science and Engineering: Bioelectrochemistry*; Alkire, R. C.; Kolb, D. M.; Lipkowski, J., Eds.; 2012; pp. 269–334.
(19) Lin, X. F.; Ren, B.; Yang, Z. L.; Liu, G. K.; Tian, Z. Q.*J. Raman Spectrosc.* **2005**, *36*, 606.
(20) Oklejas, V.; Sjostrom, C.; Harris, J. M.*J. Phys. Chem. B* **2003**, *107*, 7788.
(21) Brady, D. J.*Optical Imaging and Spectroscopy*; John Wiley & Sons, Inc.: Hoboken, NJ, USA, 2009.
(22) Wu, D. Y.; Li, J. F.; Ren, B.; Tian, Z. Q.*Chem. Soc. Rev.* **2008**, *37*, 1025.
(23) Jambrec, D.; Gebala, M.; LaMantia, F.; Schuhmann, W.*Angew. Chemie - Int. Ed.* **2015**, *54*, 15064.
(24) Kaiser, W.; Rant, U.*J. Am. Chem. Soc.* **2010**, *132*, 7935.
(25) Tymoczko, J.; Schuhmann, W.; Gebala, M.*ACS Appl. Mater. Interfaces* **2014**, *6*, 21851.
(26) Josephs, E.; Ye, T.*J. Am. Chem. Soc.* **2010**, *132*, 10236.
(27) Josephs, E.; Ye, T.*Nano Lett.* **2012**, *12*, 5255.
(28) Love, J. C.; Estroff, L. A.; Kriebel, J. K.; Nuzzo, R. G.; Whitesides, G. M.*Chem. Rev.* **2005**, *105*, 1103.
(29) Schwartz, D. K.*Annu. Rev. Phys. Chem.* **2001**, *52*, 107.
(30) Widrig, C. A.; Chung, C.; Porter, M. D.*J. Electroanal. Chem. Interfacial Electrochem.* **1991**, *310*, 335.
(31) Munakata, H.; Oyamatsu, D.; Kuwabata, S.*Langmuir* **2004**, *20*, 10123.
(32) Boubour, E.; Lennox, R. B.*J. Phys. Chem. B* **2000**, *104*, 9004.
(33) Boubour, E.; Lennox, R. B.*Langmuir* **2000**, *16*, 7464.
(34) Wink, T.; vanZuilen, S. J.; Bult, A.; vanBennekom, W. P.*Analyst* **1997**, *122*, 43R.
(35) Hagenstrom, H.; Schneeweiss, M. A.; Kolb, D. M.*Langmuir* **1999**, *15*, 7802.
(36) Torres, E.; Blumenau, A. T.; Biedermann, P. U.*Phys. Rev. B - Condens. Matter Mater. Phys.* **2009**, *79*, 1.
(37) Poirier, G. E.; Pylantt, E. D.*Science* **1996**, *272*, 1145.
(38) Dieringer, J. A.; McFarland, A. D.; Shah, N. C.; Stuart, D. A.; Whitney, A.V.; Yonzon, C. R.; Young, M. A.; Zhang, X.; VanDuyne, R. P.*Faraday Discuss.* **2006**, *132*, 9.
(39) Masango, S. S.; Hackler, R. A.; Large, N.; Henry, A.-I.; McAnally, M. O.; Schatz, G. C.; Stair, P. C.; VanDuyne, R. P.*Nano Lett.* **2016**, Article ASAP.
(40) Singh, A. K.; Khan, S. A.; Fan, Z.; Demeritte, T.; Senapati, D.; Kanchanapally, R.; Ray, P. C.*J. Am. Chem. Soc.* **2012**, *134*, 8662.

(41) Gersten, J.; Nitzan, A.*J. Chem. Phys.* **1980**, *73*, 3023.
(42) Goude, Z. E.; Leung, P. T.*Solid State Commun.* **2007**, *143*, 416.
(43) Yin, Y. D.; Gao, L.; Qiu, C. W.*J. Phys. Chem. C* **2011**, *115*, 8893.
(44) Rojas, R.; Claro, F.; Fuchs, R.*Phys. Rev. B* **1988**, *37*, 6799.
(45) Chang, R.; Leung, P. T.*Phys. Rev. B - Condens. Matter Mater. Phys.* **2006**, *73*, 1.
(46) Chung, H. Y.; Leung, P. T.; Tsai, D. P.*J. Chem. Phys.* **2013**, *138*.
(47) Ray, P. C.; Fan, Z.; Crouch, R. A.; Sinha, S. S.; Pramanik, A.*Chem. Soc. Rev.* **2014**, *43*, 30.
(48) Cole, R. M.; Baumberg, J. J.; DeGarcia Abajo, F. J.; Mahajan, S.; Abdelsalam, M.; Bartlett, P. N.*Nano Lett.* **2007**, *7*, 2094.
(49) Mahajan, S.; Cole, R. M.; Soares, B. F.; Pelfrey, S. H.; Russell, A. E.; Baumberg, J. J.; Bartlett, P. N.*J. Phys. Chem. C* **2009**, *113*, 9284.
(50) Su, G. J.; Yin, S. X.; Wan, L. J.; Zhao, J. C.; Bai, C. L.*Surf. Sci.* **2004**, *551*, 204.
(51) Wu, D. Y.; Hayashi, M.; Chang, C. H.; Liang, K. K.; Lin, S. H.*J. Chem. Phys.* **2003**, *118*, 4073.
(52) Porter, M. D.; Bright, T. B.; Allara, D. L.; Chidsey, C. E. D.*J. Am. Chem. Soc.* **1987**, *109*, 3559.
(53) Wu, D. Y.; Hayashi, M.; Lin, S. H.; Tian, Z. Q.*Spectrochim. Acta - Part A Mol. Biomol. Spectrosc.* **2004**, *60*, 137.
(54) Josephs, E.; Ye, T.*J. Am. Chem. Soc.* **2012**, *134*, 10021.
(55) Schönenberger, C.; Sondag-Huethorst, J. a. M.; Jorritsma, J.; Fokkink, L. G. J.*Langmuir* **1994**, *10*, 611.
(56) Aizenberg, J.; Black, A. J.; Whitesides, G. M.*Nature* **1998**, *368*, 868.
(57) Hamelin, A.; Stoicoviciu, L.; Edens, G. J.; Gao, X.; Weaver, M. J.*J. Electroanal. Chem.* **1994**, *365*, 47.
(58) Eberhardt, D.; Santos, E.; Schmickler, W.*J. Electroanal. Chem.* **1996**, *419*, 23.
(59) Tao, A. R.; Habas, S.; Yang, P.*Small* **2008**, *4*, 310.
(60) Jäckel, F.; Kinkhabwala, A. A.; Moerner, W. E.*Chem. Phys. Lett.* **2007**, *446*, 339.
(61) Finklea, H. O.In *Electroanalytical Chemistry: A Series of Advances Vol. 19*; Bard, A.; Rubenstein, I., Eds.; CRC Press: Boca Raton, Florida, 1996; pp. 109–335.
(62) Doneux, T.; DeRache, A.; Triffaux, E.; Meunier, A.; Steichen, M.; Buess-Herman, C.*ChemElectroChem* **2014**, *1*, 147.
(63) Arinaga, K.; Rant, U.; Tornow, M.; Fujita, S.; Abstreiter, G.; Yokoyama, N.*Langmuir* **2006**, *22*, 5560.
(64) Bain, C. D.; Biebuyck, H. A.; Whitesides, G. M.*Langmuir* **1989**, *5*, 723.
(65) Meunier, A.; Triffaux, E.; Bizzotto, D.; Buess-Herman, C.; Doneux, T.*ChemElectroChem* **2015**, *2*, 434.
(66) Folkers, J. P.; Laibinis, P. E.; Whitesides, G. M.*Langmuir* **1992**, *8*, 1330.
(67) Chidsey, C. E. D.; Bertozzi, C. R.; Putvinski, T. M.; Mujsce, A. M.*J. Am. Chem. Soc.* **1990**, *112*, 4301.
(68) Folkers, J. P.; Laibinis, P. E.; Whitesides, G. M.*J. Adhes. Sci. Technol.* **1992**, *6*, 1397.
(69) Folkers, J. P.; Laibinis, P. E.; Whitesides, G. M.; Deutch, J.*J. Phys. Chem.* **1994**, *98*, 563.
(70) Smith, R. K.; Lewis, P. a.; Weiss, P. S.*Prog. Surf. Sci.* **2004**, *75*, 1.
(71) Mirsky, V. M.; Hirsch, T.; Piletsky, S. A.; Wolfbeis, O. S.*Angew. Chemie - Int. Ed.* **1999**, *38*, 1108.
(72) Piletsky, S. A.; Piletskaya, E.V.; Sergeyeva, T. A.; Panasyuk, T. L.; El'Skaya, A.V.*Sensors Actuators, B Chem.* **1999**, *60*, 216.
(73) Mirsky, V. M.*TrAC - Trends Anal. Chem.* **2002**, *21*, 439.
(74) Miller, C.; Cuendet, P.; Gratzel, M.*J. Phys. Chem.* **1991**, *95*, 877.

Chapter 6 Conclusions and Future Work

Previous studies of the electrochemical SERS of Raman labelled oligonucleotides have clearly shown that the region where the Raman response decreases with increasing negative potential can be used to discriminate DNA sequence variations of single nucleotide polymorphisms[1,2] and short tandem repeats[3]. This study chose a 35 bp oligonucleotide that has 7 bp dsDNA of self-complementary pairing at the two ends and a 21 bp ssDNA loop in between to form a beacon probe. This is the first example of the investigation of the potential dependence of the Raman enhancement for a beacon probe. The 5' end of the beacon probe was modified with a hexaethylene glycol (HEG) linker and 3 disulfides to form 6 Au-S bond anchors on the Au surface. The 3' end was modified with Texas Red, using the NHS ester, as the Raman label on the beacon probe. The basic electrochemical SERS response of the Texas Red-labelled beacon probe exhibits similar Raman intensity variations during potential sweep from -0.3 to -1.2 V as the linear strand labelled DNA with the Texas Red at the 3' end. The recovery of the SERS signal after the cathodic potential scan for 1 h and 1 week showed that the immobilized beacon probe still stays on the SSV Au surface and that there is not significant desorption of its thiol anchor. The interpretation of the change in Raman intensity for the Texas Red is essentially consistent with studies reported by other groups based on assumed conformational changes during the potential scan. However, there is some uncertainty in the explanation of some of the experiments. For example, the increase in the Raman intensity for Texas Red between -0.3 to -0.9 V was explained as due to a change in the orientation of the Texas Red accompanied by the unwinding of the beacon probe. Since there are no other significant bands for Texas Red, except for the intense 1504 and 1648 cm^{-1} bands, that can be clearly observed, it is hard to discriminate between the contribution to the enhancement from conformation changes and from changes in the Raman label orientation.

The reasons for the reversible increase in the Raman intensity with potential had not been studied extensively in earlier work when compared with the studies of the decrease at more negative potential. In this work a series of experiments were carried out for Texas Red directly adsorbed on the Au SSV electrode. These experiments provide information on the behaviour of the Raman label and increase our understanding of the electrochemical system. Similar Raman intensity responses, increasing between -0.3 to -0.8 V and then decreasing between -0.9 to -1.2 V, were observed for the adsorbed Texas Red. To investigate the fundamental aspects of this, the electronic structure, the adsorbate orentaiton, the potential-tuning effect of the local surface plasmon resonance (LSPR), the effect of

excitation wavelength, the interference of hydrogen evolution, the electronic and vibrational Stark effects, and the charge transfer enhancement were all carefully examined and the most relavant factors for the potential dependent Raman enhancement determined.

The re-orientation of Texas Red during the potential sweep from 0.3 to -1.2 V was evaluated based on the Moskovits' selection rule, which compares the relative Raman intensity of the vibration modes of the out-of-plane bending and the in-plane bending. These two modes are normal to each other, and there was an increase of the ratio of Raman intensity between the two modes during the negatively potential scanning. This suggests the orientation of the aromatic plane of Texas Red is changing during the potential scan. Although we cannot exclude that the orientation change contributes to the overall potential dependent Raman enhancement, there is still lack of full correlation between the potential dependent Raman enhancement and re-orirntation ratio in the 0.1 to -0.3 V and -0.8 to -1.0 V regions. Hence the re-orientation of Texas Red cannot be completely attributed to the synchronised Raman intensity enhancement during the potential sweep.

The potential-tuning of the characteristic frequency of LSPR have been reported by many groups. According to the literature a negative potential sweep results in ca. 10 nm blue-shift in the LSPR in the case of 50 nm Au nanoparticles at -0.8 V as compared to 0.4 V. However, if there were a blueshift caused by the cathodic potential sweep for the SSV substrates in our studies, we would expect a decrease in Raman intensity from the maximum Raman enhancement based on the optimum substrates which is not observed. The experiments were further carried out by varying the deposit thickeness of the SSV substrate to tune the corresponding characteristic frequencies of the LSPR. No expected Raman decrease during potential sweep was noted as the deposit thickness, $\bar{t}$, ranged from 0.625 to 0.875. Ideally, the in-situ reflectance measurements are required on the SSV to support the interference. Consequently the resultant potential dependent Raman intensity cannot be explained on the basis of a blueshift of the LSPR caused by the cathodic potential scan.

The evolution of hydrogen results in generation of bubbles that merge irregularly on the surface and masks the observation of the electrochemical SER spectra. This interference can be delayed by changing to 0.1 M KOH as the supporting electrolyte. The decrease in the potential dependent Raman intensity for potentials negative of -1.0 V was thus extended to -1.2 V. However the masking effect of bubbles does not cause significant changes in the increase in the potential dependent Raman intensity.

Finally, the choice of excitation wavelength was found to be a significant factor. When it is shifted to the red (785 nm) relative to the electronic absorption maximum (λ_{max} 586 nm) of Texas Red, the potential dependent Raman enhancement is lower. In contrast, when the excitation (633 nm) is close to the λ_{max}, it results in enhanced Raman intensity dependence for Texas Red during the potential scan. This implies that the potential dependent Raman enhancement is correlated to the resonance Raman like scattering. There are two mechanisms which may both explain the potential dependent Raman enhancement. The first mechanism is the resonance Raman scattering triggered by the potential-shifted electronic Stark effect. The second is the chemical enhancement which contains chemisorption effects and charge transfer enhancement.

The energy gap associated with any electronic transition is much larger than that for normal vibrational levels, and consequently any electronic transition must encompass some associated vibration levels. Hence the electronic Stark effect triggered by the electric field will be accompanied by a vibrational Stark effect. This phenomenon has the same origin as the difference in the intensity of different vibration modes between normal Raman scattering and the resonance Raman scattering as discussed in Section 4.6. The resonance Raman enhancement occurs when the excitation wavelength is in resonance with an electronic transition of the molecule. Those vibrational modes that are coupled to this electronic transition will be resonantly enhanced and their Raman bands will appear much stronger relative to those bands for vibrational modes that are not coupled to the electronic transition. Consequently, Raman spectra obtained for the same molecule can appear different depending upon whether the laser excitation is in resonance with an electronic transition of the molecule or not[4]. However, the proportional shifts in frequency with applied potential, that are chracteristic of the vibrational Stark effect, are not observed in the case of Texas Red, 3,3'-diethylenecarbocyanine iodide (DTCI) and the Texas Red-labelled beacon probe. Hence the electronic Stark effect cannot be the reason of the potential dependent Raman enhancement.

The chemical enhancement, as reviewed by Tian and co-workers[5], contains the chemical binding (chemisorption) effect and charge transfer enhancement. The chemical binding is most obvious for strong bonding between the adsorbate and the metal surface, for example in the case of pyridine adsorbed on silver. The charge transfer enhancement, modeled by Lombardi and Birke[6,7], occurs when the excitation energy is close to, but less than, the electronic transition energy, then tuning of the electrochemical potential (Fermi level) of the metal electrode can create an intermediate state that couples with the electronic excited or ground state of the adsorbate molecule and finally results a

resonance like Raman enhancement. The CT enhancement is a photon-driven charge transfer (CT) between adsorbate and substrate, and a coupling effect between the electron–hole pair and adsorbed molecule. Based on the calculation of the orbital enegy level distribution, the relative position of the work function of the polycrystalline Au electrode, the excitation wavelength, and the observed potential of maximum Raman intensity, we could not exclude the contribution of CT enhancement to the potential dependent Raman enhancement in the case of Texas Red adsorbed on the Au SSV electrode. However in this work we did not carry out detailed calculations on the adsorbate (Texas Red)-metal clusters to investigate in detail the contribution of the chemical binding to the chemical enhancement. This could be the basis for future work in this area. Another point worth stating is that charge transfer phenomena[8] on the nanoscale driven by the photon[9], is not a short range effect that only occur on direct contact and chemical bonding to the metal surface. Our experimental results suggest that the CT enhancement can transfer through the self-assembly monolayer (SAM), formed by short alkyl chained mercaptoalkanols, but is blocked in the case of low permeability SAMs. However, the effect of defects for the short chain thiols which allow contact of Texas Red with the Au surface, cannot be ruled out completely and hence the binding effect and CT enhancement is still difficult to be realized experimentally.

The contribution of the excitation dependence for the Texas Red beacon probe was confirmed to be the critical factor in the potential dependent Raman enhancement in the case of the Texas Red-labelled, and Cy3-labelled, beacon probes.

The final factor explored in this study was the effect of the mercaptohexanol modification used to prevent the non-specific adsorption of the oligonucleotide at the Au surface. The conventional modification method used with mercaptohexanol is to backfill the surface after the immobilization of the oligonucleotide. However, several studies have indicated that this preparation method can result in an inhomogeneous distribution of the thiolated oligonucleotides[10]. Therefore the preparation of the surface by co-adsorption of mercaptohexanol and the Texas Red beacon probe was also studied. This co-adsorption method can reduce the surface coverage of the beacon probe and thus reduce non-specific intermolecular interations between adjacent probes on the Au surface. From the literature there are two possible packing states that may exist at the becon probe/mercaptoalkanol interface. There is a substitution state where the Au-S bonds of the mercaptoalkanol substitute for the Au-N bonds formed by the Texas Red at the Au surface and a surface impurity state. The surface impurity state is a defect that comes from the packing of the SAM around in the boudaries of the Texas Red and

the corresponding disruption in the mercaptoalkanol packing. These two states have been reported by Josephs *et al.*[11–13] to co-exist for the oligonucleotide/mercaptohexanol adsorbed on Au surfaces based on AFM measurements. The relative amounts of the two states may depend on the preparation method, the molar ratio of the oligonucleotide/mercaptohexanol and the time scale for packing.

The backfilled SAM modification was carried out in a two step modification. The Texas Red-labelled beacon probe was immobilized on the SSV substrates for 18 h first, then the substrates were immersed in the absence and presence of the mercaptohexanol for varied periods for the backfilling step from 1 h to 18 h. This result clearly show that the backfilling of mercaptohexanol has two effects on the Raman intensity compared to the absence of mercaptohexanol modification, on the Texas Red-labelled beacon probe adsorbed surface. The first is a decrease of the Raman intensity of Texas Red -0.3 to -0.6 V of the order of 550 counts mW^{-1} s^{-1} within the first 2 h. The second, is a minor decrease of the Raman intensity maximum, ca. 150 counts mW^{-1} s^{-1}, noted between -0.6 to -0.9 V in the following 2 to 6 h. No siginificant change of Raman intensity was formed over 6 to 18 h. The second decrease of Raman intensity in the presence of mercaptohexanol was proportional to the backfilling time and reached equilibrium in 18 h. This can be explained by two effects. The first is the complete replacement of Texas Red adsorption sites by Au-S thiolate, lifting up the Texas Red from the Au surface and increasing the distance from the metal surface. The second is the reduction in double layer capacitance by the formation of a compact monolayer, and hence the reduction in the electrostatic repulsion. These two factors collectively contribute to the resultant Raman response. When the potential was scanned into the Raman enhancement region, -0.6 V to -0.9 V, mercaptohexanol desorption became more evident and the potential dependent Raman enhancement, the intrinsic characteristic of Texas Red, begins to be observed.

Experiments were carried out using mercaptoalkanols with different alkyl chain lengths from C2, C4, C6 to C9. Two distinct immersion times, 6 h and 24 h, were used in order to compare short and long term packing of the mercaptoalkanol SAM. The Raman response during the potential sweep exhibited a transition pattern for both backfilling times (6 h and 24 h) as the alkyl chain length increased, except for the C9-mercaptoalkanol backfilling after 6 h. The most significant result was for the 24 h backfilling modification of the mercaptoalkanols. Two obvious features were observed. The first was that the maxmum is the Raman intensity gradually decreased from the C2—mercaptoalkanol to the C9-mercaptoalkanol accompanied by a second feature, a negative shift in the potential for the maximum Raman intensity. Comparison with the results for capacitance measurements at Au

microdisc electrodes suggest that the potential-induced defects and the subsequent reductive desorption of the mercaptoalkanol are changed during the potential sweep. The desorbed mercaptoalkanol does not complete diffuse away from the surface but stays in the vinicity of the interface at -0.8 V as has been reported by many authors. This plays a role in the explanation of the dependence of the Raman intensity on the alkyl chain length. The fact that the Raman intensity remains proportionaly low, even at -0.8 V when the C9-mercaptoalkanol is supposed to be desorbed, can be interpreted in terms of this effect.

The second preparation method, co-adsorption of the mercaptoalkanol with the labelled beacon probe in a 1: 1 molar ratio, was performed using the same mercaptoalkanols with chain lengths of C2, C4, C6 and C9. The results suggested that there is a surface impurity like defect formed and this may give an explanation for the resultant Raman intensity dependence. With the exception of the C9-mercaptoalkanol, all of the co-adsorbed mercaptoalkanols cause similar reductions in Raman intensity for the labelled beacon probe. This result suggests that the co-adsorption preparation method may produce the immobilized Texas Red-labelled beacon probe that is more like a surface impurity defect rather than being substituted by the mercaptoalkanol at the Au-N binding site on the Texas Red/Au interface. This might be explained if the co-adsorption preparation method reduces the lateral diffusion of the mercaptoalkanols and preserves the Texas Red/Au adsorption, an approach which also is applied in the molecular imprinting of sensors[14–16]. The C9-mercaptoalkanol coadsorbed with the beacon probe exhibits quite a different Raman reponse from the others. There was almost complete blocking but a weak, measurable signal (Raman intensity of the order of 10 counts $mW^{-1} s^{-1}$) was seen This suggests a nearly complete loss of the of the potential dependent Raman effect for the Texas Red label, presumably because the CT enhancement was blocked due to the low permeability of C9-mercaptoalkanol SAM.

Reviewing the overall work in this study, we present a new view point which differs from the focus on the oligonucleotide conformation change during the potential scan which has been studied by previous authors. The intrinsic behaviour of the Raman label exhibits a clear dependence on the relative energy difference between the electronic transition of the adsorbate and the excitation, the value of the electrode potential, and the adsorbate structure. Adsorption of mercaptoalkanols on the Au surface also plays a critical role and affects the resultant Raman intensity changes during the potential scan. Different preparation methods can change the relative ratio of the two proposed states, the substitution state and the surface impurity state, as discussed in the review of Love *et al.*[17] The resultant Raman

intensity needs to be considered together with these two effects, the oligonucleotide conformation, and the intrinsic electrochemical SERS behaviour of the Raman label in order to reach a better understanding on the electrochemical SERS of the beacon probe.

This study has tried to examine and explain the experimental results from the respect of the energy and the self-assembly monolayer aspects involved. However, there are still some unanswered questions to be explored. One of the most deserving of investigation is the behaviour of the C9-mercaptoalkanol which shows quite different packing from the short mercaptoalkanols. A second area for investigation is the use of Cy3 in electrochemical SERS. It might give more understanding to the different potential dependence of the Raman intensity between the Texas Red-labelled and the Cy3-labelled probe.

A final suggestion for further work is the interface dipole tuning of the work function of the metal and also the adsorbate. In a review Braun *et al.*[18] indicated that the adsorbed SAM would cause an interface dipole at the metal surface. Exploring this aspect will give more insight into the energy level alignments at the organic/metal interface and would further test the valdility of the CT enhancement suggested here. Hopefully, this may give a clearer link to the energetics of the oligonucleotide and give a better universal explanation of the phenomenon.

References

(1) Mahajan, S.; Richardson, J.; Brown, T.; Bartlett, P. N.*J. Am. Chem. Soc.* **2008**, *130*, 15589.
(2) Johnson, R. P.; Gao, R.; Brown, T.; Bartlett, P. N.*Bioelectrochemistry* **2012**, *85*, 7.
(3) Corrigan, D. K.; Gale, N.; Brown, T.; Bartlett, P. N.*Angew. Chemie - Int. Ed.* **2010**, *49*, 5917.
(4) Tuschel, D.*Spectroscopy* **2016**, *31*, 14.
(5) Wu, D. Y.; Li, J. F.; Ren, B.; Tian, Z. Q.*Chem. Soc. Rev.* **2008**, *37*, 1025.
(6) Lombardi, J. R.; Birke, R. L.; Lu, T.; Xu, J.*J. Chem. Phys.* **1986**, *84*, 4174.
(7) Lombardi, J. R.; Birke, R. L.*Acc. Chem. Res.* **2009**, *42*, 734.
(8) Adams, D. M.; Brus, L.; Chidsey, C. E. D.; Creager, S.; Creutz, C.; Kagan, C. R.; Kamat, P.V.; Lieberman, M.; Lindsay, S.; Marcus, R. A.; Metzger, R. M.; Michel-Beyerle, M. E.; Miller, J. R.; Newton, M. D.; Rolison, D. R.; Sankey, O.; Schanze, K. S.; Yardley, J.; Zhu, X.*J. Phys. Chem. B* **2003**, *107*, 6668.
(9) Lindstrom, C. D.; Zhu, X. Y.*Chem. Rev.* **2006**, *106*, 4281.
(10) Murphy, J. N.; Cheng, A. K. H.; Yu, H.-Z.; Bizzotto, D.*J. Am. Chem. Soc.* **2009**, *131*, 4042.
(11) Josephs, E.; Ye, T.*Nano Lett.* **2012**, *12*, 5255.
(12) Josephs, E.; Ye, T.*J. Am. Chem. Soc.* **2012**, *134*, 10021.
(13) Josephs, E.; Ye, T.*J. Am. Chem. Soc.* **2010**, *132*, 10236.
(14) Mirsky, V. M.; Hirsch, T.; Piletsky, S. A.; Wolfbeis, O. S.*Angew. Chemie - Int. Ed.* **1999**, *38*, 1108.
(15) Mirsky, V. M.*TrAC - Trends Anal. Chem.* **2002**, *21*, 439.
(16) Hirsch, T.; Kettenberger, H.; Wolfbeis, O. S.; Mirsky, V. M.*Chem. Commun.* **2003**, 432.
(17) Love, J. C.; Estroff, L. A.; Kriebel, J. K.; Nuzzo, R. G.; Whitesides, G. M.*Chem. Rev.* **2005**, *105*, 1103.
(18) Braun, S.; Salaneck, W. R.; Fahlman, M.*Adv. Mater.* **2009**, *21*, 1450.